LHCb 实验质子铅核对撞中 D^0 介子的核物质效应的研究

Nuclear matter effects of D^0 mesons in proton-lead collisions at LHCb

(申请清华大学理学博士学位论文)

培 养 单 位： 工程物理系

学　　科： 物 理 学

研 究 生： 王 剑 桥

指 导 教 师： 朱 相 雷　副教授

二〇二三年八月

LHCb 实验质子铅核对撞中 D^0 介子的核物质效应的研究

王剑桥

Nuclear matter effects of D^0 mesons in proton-lead collisions at LHCb

Dissertation submitted to

Tsinghua University

in partial fulfillment of the requirement

for the degree of

Doctor of Philosophy

in

Physics

by

Jianqiao Wang

Dissertation Supervisor: Associate professor, Xianglei Zhu

August, 2023

学位论文指导小组、公开评阅人和答辩委员会名单

公开评阅人名单

无（全隐名评阅）

答辩委员会名单

主席	CHEN SHAOMIN	教授	清华大学
委员	刘晓辉	教授	北京师范大学
	宋慧超	教授	北京大学
	杨振伟	教授	北京大学
	张黎明	副教授	清华大学
	朱相雷	副教授	清华大学
秘书	屈三强	助理研究员	清华大学

关于学位论文使用授权的说明

本人完全了解清华大学有关保留、使用学位论文的规定，即：

清华大学拥有在著作权法规定范围内学位论文的使用权，其中包括：（1）已获学位的研究生必须按学校规定提交学位论文，学校可以采用影印、缩印或其他复制手段保存研究生上交的学位论文；（2）为教学和科研目的，学校可以将公开的学位论文作为资料在图书馆、资料室等场所供校内师生阅读，或在校园网上供校内师生浏览部分内容；（3）根据《中华人民共和国学位条例暂行实施办法》及上级教育主管部门具体要求，向国家图书馆报送相应的学位论文。

本人保证遵守上述规定。

作者签名：王剑桥　　导师签名：朱松雪

日　　期：2023.5.22　　日　　期：2023.5.22

摘 要

在夸克胶子等离子体（QGP）新物态中，夸克和胶子处于色禁闭被解除的自由状态。重离子碰撞是在实验室中研究 QGP 的唯一手段。与质子-质子碰撞相比，重离子碰撞中的粒子产生会受到由 QGP 产生造成的热核物质（HNM）效应影响，还会受到因重核内禀属性或其他与 QGP 产生无关的冷核物质（CNM）效应影响。一般认为，质子-重核（pA）碰撞中 HNM 效应可以忽略，因此 pA 碰撞是研究 CNM 效应的有效手段。而近些年越来越多的实验证据显示，高多重数的 pA 对撞中也可能会有 QGP 产生，但需要更多实验测量对此进行检验。

大型强子对撞机在 2016 年进行了每核子对质心系能量为 8.16 TeV 的质子-铅核（pPb）碰撞，LHCb 实验在前向（质子方向）和后向快度分别采集了积分亮度为 $12.2 \pm 0.3\,\text{nb}^{-1}$ 和 $18.6 \pm 0.5\,\text{nb}^{-1}$ 的数据。利用该数据，本文精确测量了碰撞中瞬发 D^0 介子的双微分产生截面，测量覆盖的横动量范围是 $p_\text{T} < 30\,\text{GeV}/c$ 以及质心系快度范围分别为 $1.5 < y^* < 4.0$（前向）和 $-5.0 < y^* < -2.5$（后向）。将该截面与同能量质子-质子（pp）碰撞数据进行比较得到了瞬发 D^0 介子的核修正因子。在前向快度，核修正因子显著小于 1 且与核部分子分布函数（nPDF）这一 CNM 模型计算基本一致，确认 CNM 效应的存在；最低横动量（$p_\text{T} < 1\,\text{GeV}/c$）数据低于 nPDF 计算结果，暗示在小动量分数（$x \sim 10^{-5}$）可能存在更强的核遮蔽效应或额外的部分子能损。在后向快度（$-3.5 < y^* < -2.5$）的高 p_T 区间（$p_\text{T} > 6\,\text{GeV}/c$），核修正因子相对于 nPDF 计算有显著性 $2.0 - 3.8\sigma$ 的压低，暗示 $x \sim 0.01$ 的反遮蔽效应可能弱于 nPDF 模型预言或存在其他末态效应。前后向截面比的测量结果也印证了 D^0 介子产生截面的前后向不对称和高横动量 nPDF 计算与数据的偏离。本文还计算了 8.16 TeV 和 5.02 TeV 的 pPb 对撞中瞬发 D^0 截面比，与 nPDF 计算相符。

为了探究在 pPb 对撞中是否存在 HNM 效应，本论文还利用同样的数据测量了瞬发 D^0 介子的集体流。利用二粒子关联的方法，本文给出了 D^0 介子和带电粒子的 $(\Delta\eta, \Delta\phi)$ 关联函数，观察到了它们的长程关联（“嵴”）。对长程关联函数的傅立叶展开，本文初步得到了包含 D^0 介子和带电粒子贡献的椭圆流（$V_2^{D^0-h}$）和三角流（$V_3^{D^0-h}$）。发现后向高多重数事例在中等 p_T 区间（$1 < p_\text{T} < 5\,\text{GeV}/c$），$V_2$ 显著大于零。而 V_3 较小。这些结果暗示后向高多重数事例中粲夸克可能参与部分子集体运动。后续将结合带电粒子集体流的测量结果，得到最终的 D^0 介子集体流的结果。

关键词： 重离子对撞；核物质效应；重味粒子；产生截面；集体流

ABSTRACT

Quark-gluon plasma (QGP) is a matter state where the colour confinement is removed and the quark and gluon can be considered as free particles. Heavy-ion collisions provide unique opportunities to study QGP in the laboratory. Compared to pp collisions, particle production in heavy-ion collisions can be affected by hot nuclear matter (HNM) effects, as well as cold nuclear matter (CNM) effects, where HNM effects are induced by the formation of QGP, and CNM effects originate from the intrinsic properties of nuclei or other effects not related to QGP. It is generally believed that HNM effects are negligible in pA collisions; thus, these collisions are considered as excellent probes for investigating CNM effects. However, more experimental signatures suggest the possible existence of QGP in pA collisions. Further investigations are required to validate this assumption.

The Large Hadron Collider has conducted pPb collisions at a centre-of-mass energy per nucleon pair of $\sqrt{s_{\rm NN}} = 8.16\,\text{TeV}$ in 2016. The LHCb detector collected pPb data for both forward (direction of the proton beam) and backward rapidity regions, corresponding to integrated luminosities of $12.2 \pm 0.3\,\text{nb}^{-1}$ and $18.6 \pm 0.5\,\text{nb}^{-1}$, respectively. With these data, the double-differential cross-section of prompt D^0 production is determined with high precision in a transverse momentum region of $p_{\rm T} < 30\,\text{GeV}/c$, and a centre-of-mass rapidity region of $1.5 < y^* < 4.0$ (forward) and $-5.0 < y^* < -2.5$ (backward). The nuclear modification factor of prompt D^0 mesons is derived by comparing the cross-section in pPb collisions with that in pp collisions. Significant suppression of the nuclear modification factor compared to unity is observed at forward rapidity, which agrees with the prediction from nPDF models and confirms the existence of CNM effects. A stronger suppression than the nPDF calculations is observed for the lowest transverse momentum region of $p_{\rm T} < 1\,\text{GeV}/c$ at forward rapidity, hinting at a stronger shadowing than predicted at Bjorken-$x \sim 10^{-5}$, or underlying energy loss. At backward rapidity, a suppression with a significance of $2.0 - 3.8$ standard deviations compared to nPDF expectations is found in the kinematic region of $p_{\rm T} > 6\,\text{GeV}/c$ and $-3.25 < y^* < -2.5$, corresponding to $x \sim 0.01$. This result indicates a weaker anti-shadowing effect than the model or additional final-state effects at backward rapidity. The measured forward-backward production ratio also suggests the production asymmetry between forward and backward rapidities, where the discrepancy between data and nPDF models is also found. The production ratio between

8.16 TeV and 5.02 TeV in pPb collision is also measured which shows a good agreement with nPDF calculations.

The prompt D^0 collective flow is also measured with the LHCb pPb data at $\sqrt{s_{\rm NN}} =$ 8.16 TeV, which aims to investigate underlying HNM effects in pPb collisions. The two-particle correlation method is employed in this analysis and the $(\Delta\eta, \Delta\phi)$ correlation function of D^0 with charged particle pairs is measured. The structure of the near-side ridge is observed. The elliptic flow $V_2^{D^0-h}$ and triangle flow $V_3^{D^0-h}$ are extracted via the Fourier expansion on the long-range correlation function. The measured V_2 and V_3 values include the contributions from $v_n^{D^0}$ and v_n^h. For V_2, positive values are observed for $1 < p_{\rm T}(D^0) < 5$ GeV/c and high-multiplicity intervals, hinting at the collectivity of charm quarks in high-multiplicity pPb events, while the V_3 values are too small to determine. More work on the charged particle flow measurement is in progress for achieving final results on D^0 collective flow.

Keywords: heavy-ion collision; nuclear matter effect; heavy-flavour particle; production cross-section; collective flow

TABLE OF CONTENTS

LIST OF FIGURES

LIST OF TABLES

LIST OF SYMBOLS AND ACRONYMS

SM	Standard Model
QED	Quantum Electrodynamics
QCD	Quantum Chromodynamics
pQCD	pertubative Quantum Chromodynamics
DIS	Deep Inelastic Scattering
QPM	Quark-Parton Model
PDF	Parton Distribution Function
QGP	Quark-Gluon Plasma
IP	Impact Parameter
MC	Monte Calo
HNM	Hot Nuclear Matter
CNM	Cold Nuclear Matter
nPDF	nuclear Parton Distribution Function
DGLAP	Dokshitzer–Gribov–Lipatov–Altarelli–Parisi
BFKL	Balitsky-Fadin-Kuraev-Lipatov
FCEL	Full Coherent Energy Loss
CGC	Colour Glass Condensate
LO	Leading Order
SPS	Super Proton Synchrotron
LHC	Large Hadron Collider
LHCb	Large Hadron Collider beauty
CERN	European Organisation for Nuclear Research
RHIC	Relativistic Heavy Ion Collider
BNL	Brookhaven National Laboratory
ZYAM	Zero Yield At Minimum
LEP	Large Electron-Positron collider
PSB	Proton Synchrotron Booster
PS	Proton Synchrotron
LS	Long Shutdown
VELO	VErtex LOcator
RICH	Ring Imaging CHerenkov detector
TT	Tracker Turicesis

T-station	Tracking station
SPD	Scintillation-Pad Detector
PS	Pre-shower
ECAL	Electromagnetic CALorimeter
HCAL	Haronic CALorimeter
PID	Particle IDentification
HPD	Hybrid Phton Detector
PV	Primary Vertex
SMOG	System for Measuring Overlap with Gass
IT	Inner Tracker
OT	Outer Tracker
ST	Silicon Tracker
NN	Neural Network
DLL	Delta Log Likelihood
PMT	PhotoMultiplier Tube
MWPC	Multi-Wire Proportional Chambers
MVA	Multiple-Variable Analysis
L0	Level-0
HLT	High-Level Trigger
EFF	Event Filter Farm
RTA	Real-Time Analysis
DST	Data Summary Tape
VD	Vertex Displacement
FD	Flight Distance
DoCA	Distance of the Closest Approach
DIRA	DIRection Angle
CB	Crystal Ball
BKGCAT	BacKGround CATegories
TOS	Trigger On System
TIS	Trigger Independent of System
MLP	Multi-Layer Perceptron
HM	High Multiplicity
LM	Low Multiplicity
ROC	Receiver Operating Characteristic

CHAPTER 1 INTRODUCTION

1.1 Theoretical overview

1.1.1 The standard model

The fundamental constituents of matter can be described by the Standard model (SM). It describes the elementary particles making up the Universe and the interactions between them and has been well verified by experiments. The elementary particles and their classification in the SM is shown in Fig. 1.1. In this figure, the elementary particles include both fermions and bosons. The fermions, which are all spin−1/2 particles, as well as their anti-particles, are the building blocks for matter. They can be classified into quarks and leptons. The quark was first proposed by Gellmann and Zweig [2-3]. In the quark model, quarks are the constituents making up hadrons. Different quarks are indicated with the quantum number *flavour*. At the beginning, only three types of quark are included, namely the up quark

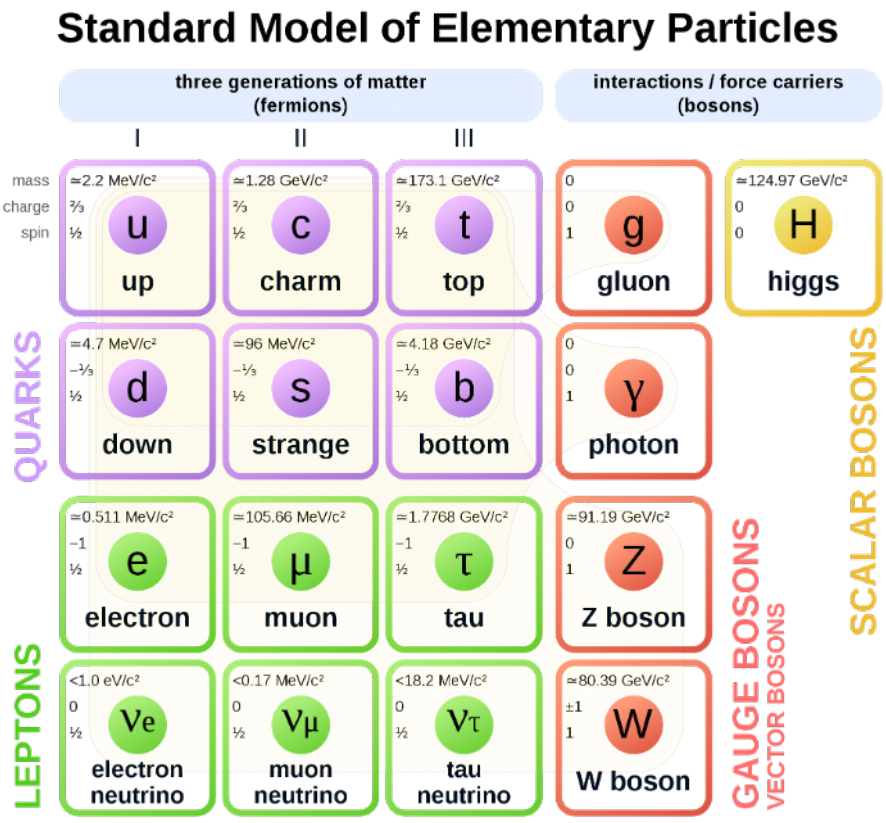

Figure 1.1 Elementary particles and their classification in the standard model. This figure is taken from the Wikipedia [1].

Table 1.1 Properties of the four fundamental forces and the corresponding force-carrying bosons.

Force	Strength [fm]	Boson		Spin	Mass [GeV/c^2]
Strong	1	Gluon	g	1	0
Electromagnetic	10^{-3}	Photon	γ	1	0
Weak	10^{-8}	W boson	$W^{\pm}$	1	80.4
		Z boson	Z	1	91.2
Gravity	10^{-37}	Graviton	G	2	0

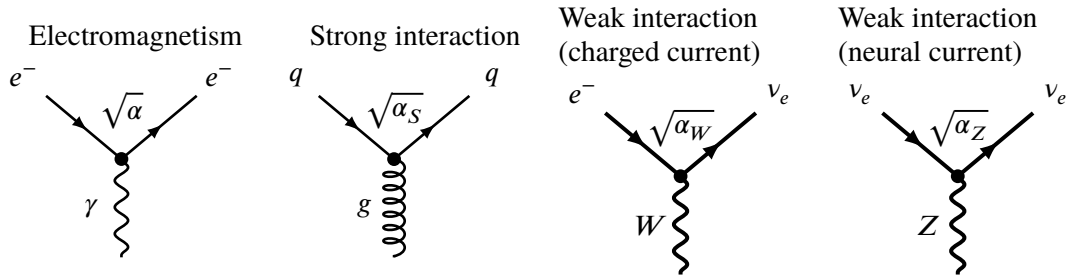

Figure 1.2 Typical interaction vertices for four gauge bosons in the standard model. The diagrams are taken from Ref. [9].

(u), down quark (d) and strange quark (s), which are also called light (flavour) quarks due to their small rest masses. The charm quark (c)[4-5], bottom / beauty quark (b)[6] and top quark (t)[7] were then observed successively and are called heavy quark oppositely. The quarks can be paired into three generations, including an *up-type* one with $+\frac{2}{3}$ electric charge and a *down-type* with $-\frac{1}{3}$, and the quark mass increases as the generation. There are also three generations of leptons in the SM, which are the electron (e), muon (μ) and tau (τ), as well as their corresponding neutrinos ν_e, ν_μ and ν_τ. The three charged leptons all have electric charge of -1, while the neutrinos are neutral particles, which are found to have very tiny but non-zero masses via the neutrino oscillation phenomena[8].

Another species of elementary particles are bosons, including four gauge bosons and the Higgs boson. Currently, the SM has embodied three of four fundamental interactions of nature, which are the strong interactions, the electromagnetic interactions and weak interactions. The observed gauge bosons are all spin-1 particles carrying the forces. Table 1.1 summarises the properties of the gauge bosons and the interactions. The undiscovered propagator for gravity *graviton* is also included. The interaction between particles are implemented via exchanging these gauge bosons. With the Feynman diagrams, the coupling can be described by the vertices as Fig. 1.2 shows. The electromagnetic interaction can be well described by the Quantum Electrodynamics (QED), which is the quantisa-

tion of charged particles and electromagnetic field. All particles with electric charges can participate in this interaction and almost all the macroscopic electromagnetic phenomena can be classified into this interaction. The strength of the interaction can be characterised by the dimensionless coupling constant α, also known as the fine structure constant, with $\alpha \approx 1/137$. The Quantum Chromodynamics (QCD) is a non-Abelian gauge field theory describing the strong interaction. It has a similar concept *colour charge* as the electric charges in the QED. While there are three different colour charges and not only the quarks but also the gluons themselves carry colour charges, which leads to different properties between strong and electromagnetic interaction. The strong interaction also has its own coupling constant $\alpha_S \sim 1$. Thus the strong interaction is stronger than the electromagnetic interaction within the force range. The propagators for the weak interaction are massive $W^{\pm}$ and Z bosons, which couple the processes with and without electric charge variation respectively, namely the charge current and neural current. All the fermions carry the weak interaction charge and participate in the weak interaction. In the 1960s, the weak interaction is unified into the electromagnetic interaction with the electroweak model by Glashow, Salam and Weinberg, which gives precise prediction on the properties of Z bosons and verified by experimental measurements[10]. The final building block for the SM is the Higgs boson, which was proposed by Englert and Higgs[11-16] to explain the origin of the particle rest masses. Its discovery[17-18] at the LHC is the great success of the SM.

1.1.2 Quark-parton model

The deep inelastic electron-proton scatterings, where the energy of electrons are high enough to break up protons, suggest that protons consist of more fundamental particles. Fig. 1.3 shows an electron-proton inelastic scattering of $e^- p \to e^- X$, and the four-momenta of each particles or virtual photon are given. Four Lorentz-invariant variables are introduced to describe the process as

$$Q^2 \equiv -q^2 \ , \ x \equiv \frac{Q^2}{2p_2 \cdot q} \ , \ y \equiv \frac{p_2 \cdot q}{p_2 \cdot p_1} \ , \nu \equiv \frac{p_2 \cdot q}{m_p} \ . \tag{1.1}$$

The deep inelastic scattering (DIS) cross-section can be described with two dimensionless structure functions $F_1(x, Q^2)$ and $F_2(x, Q^2)$,

$$\frac{\mathrm{d}^2\sigma}{\mathrm{d}x\mathrm{d}Q^2} \approx \frac{4\pi\alpha^2}{Q^4} \left[(1-y) \frac{F_2\left(x, Q^2\right)}{x} + y^2 F_1\left(x, Q^2\right) \right] \ , \tag{1.2}$$

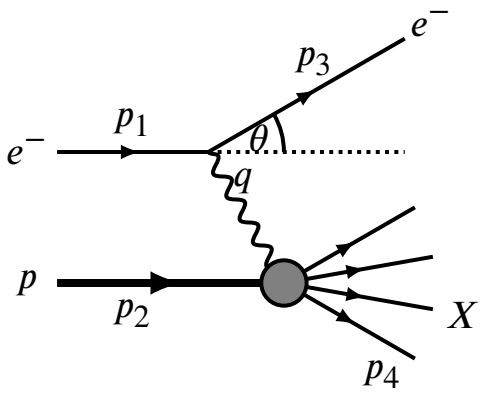

Figure 1.3 Sketch for the electron-proton inelastic scattering. The figure is taken from Ref. [9].

where four-momentum transfer $Q^2 \gg m_p^2 y^2$ is assumed. F_1 and F_2 reveal the interaction between the magnetic moments of the electron and nucleon, and between the electric charges of the electron and nucleon respectively. The DIS experiments suggested two interesting properties of structure functions[19-20]. The first one is the *Bjorken scaling*

$$F_1(x, Q^2) \to F_1(x)\ ,\ F_2(x, Q^2) \to F_2(x)\ , \tag{1.3}$$

which means that the structure functions are almost independent of Q^2. The second is the *Callan-Gross relation* which reveals the relation between F_1 and F_2

$$F_2(x) = 2xF_1(x). \tag{1.4}$$

These observations are predicted by the quark-parton model (QPM) proposed by Feynman. The model considered the electron-proton DIS as the elastic scattering with point-like *partons*. The calculation with QED naturally gives Eq.. 1.3 and 1.4

$$F_2^{ep}(x, Q^2) = 2xF_1^{ep}(x, Q^2) = x \sum_i Q_i^2 q_i^p(x)\ . \tag{1.5}$$

The Bjorken-x can then be interpreted as the momentum fraction of the parton, Q_i is the charge of the parton and $q_i^p(x)$ is the parton distribution function (PDF), which represents the x distribution of the parton in proton. The form of PDFs reflects the dynamics of proton and the interactions between partons. The PDFs of u and d quarks inside protons are measured in DIS experiments, which gives a integration of $\int x \sum q_i(x) \mathrm{d}x \simeq 0.5$. It indicates that not only valence quarks, but also gluons and sea quarks from the pair production process $g \to q\bar{q}$ of virtual gluons, contribute to the momentum of proton. Although later QCD was proposed and quarks and gluons were observed experimentally, the concept of partons, structure functions and PDFs are still important in describing the proton structure and the processes involving nucleons. Because perturbative QCD (pQCD) is not appli-

cable for such calculation, experimental input is needed for the obtaining knowledge of PDFs. The DIS of electron / neutrino and proton is still an important tool to investigate the PDFs of quarks, while the PDF of gluons can be studied from high-energy proton-proton (pp) collisions.

1.1.3 Quantum chromodynamics

The conventional hadrons include *mesons* and *baryons*, which are formed with a quark and an anti-quark, and three quarks, respectively. This fact suggests that extra degree of freedom and constraint may exist. Nambu introduced the colour charge to represent it, which includes three different types, namely the red (R), green (G) and blue (B). The colour charge plays a similar role of the electric charge. Therefore, the QCD Lagrangian density can be written following the form of QED as

$$\mathcal{L}_{\mathrm{QCD}} = \bar{q}^{\alpha}(i\gamma^{\mu}D_{\mu\alpha\beta} - m\delta_{\alpha\beta})q^{\beta} - \frac{1}{4}F^{a}_{\mu\nu}F^{\mu\nu}_{a} \,, \tag{1.6}$$

where the Einstein's summation convention is followed for repeated indices, and the summation over α and β goes from 1 to 3 and a goes from 1 to 8 in Eq. 1.6. q^{α} is the quark field with the quark mass m. γ^{μ} is the Dirac-γ matrix. The deviation symbol $D_{\mu\alpha\beta}$ is the covariant deviation acting on the quark field

$$D_{\mu\alpha\beta} = \partial_{\mu}\delta_{\alpha\beta} + igt^{a}_{\alpha\beta}A^{a}_{\mu} \,, \tag{1.7}$$

where g is the dimensionless coupling constant for QCD which can be related to the strong coupling constant with $\alpha_S = g^2/4\pi$. t^a is the generators of the SU(3) group, also known as the Gellman Matrices. and A^a_μ is the gluon field. The Gellman Matrices are eight traceless 3×3 Hermition matrices satisfying the communication and normalisation relation

$$[t^a, t^b] = if_{abc}t^c, \; tr(t^a t^b) = \frac{1}{2}\delta^{ab} \,, \tag{1.8}$$

where f_{abc} is the structure constant. $F^a_{\mu\nu}$ is the gluon field intensity derived from the gluon field A^a_μ by

$$F^{a}_{\mu\nu} = \partial_{\mu}A^{a}_{\nu} - \partial_{\nu}A^{b}_{\mu} - gf_{abc}A^{b}_{\mu}A^{c}_{\nu} \,. \tag{1.9}$$

The gluons are massless thus their mass terms do not appear in the QCD Lagrangian, which gives the SU(3) gauge symmetry of the Lagrangian. Different from the U(1) symmetry of QED, the SU(3) group is non-Abelian or noncommutative. This gives an extra (the third) term in the gluon field density and generates the gluon self-interaction vertices. Two main features of QCD can be developed further. The first one is the *colour*

confinement, that is to say, the particles are in the colour-singlet state and coloured objects cannot propagate as free particles. It is supported by the experimental evidence that single free quarks have never been observed. Thus, the coloured quarks may be confined in a meson with a combination of $R\bar{R}$ $B\bar{B}$ or $G\bar{G}$, or in a baryon with a combination of three different colours RGB. Exotic hadrons with more than three valence quarks are also predicted to exist in similar way, where the possible candidates for tetraquarks[21] ($q\bar{q}q\bar{q}$) and pentaquarks[22] ($q\bar{q}qqq$) are also discovered by experiments.

Another important feature is the *asymptotic freedom*, originating from the running coupling constant α_S. The coupling constants do depend on the energy scale Q^2 or the characteristic distance. In the case of QED, it is known as *screening* effect, which is attribute to the virtual charged-particle pairs produced by the vacuum that can neutralises the electromagnetic interactions with increasing distance. When it comes to QCD, virtual gluon pairs can also be produced due to the gluon self-interactions, which dominate the screening effects caused by virtual quark pairs. Thus, the QCD interaction strength increases with distance or decreases with Q^2. This anti-screening effect of the strong force can be approximately described by linear function $V(\boldsymbol{r}) \sim \kappa r$. Quantitatively, the exact dependence of α_S on Q^2 can be obtained by considering the contributions from the tree diagram and all loop diagrams of QCD vertices, and using the technique of *renormalisation* to avoid the integral divergency in the calculation. Due to the higher-order loop-diagram related to the four-vector currents can be cancelled, only corrections on gluon propagators need to be considered, as shown in Fig. 1.4. Then the evolution of α_S with Q^2 is calculated to be:

$$\alpha_s\left(Q^2\right) = \frac{\alpha_s\left(\mu^2\right)}{1 + \frac{\alpha_s\left(\mu^2\right)}{12\pi}\left(33 - 2n_f\right)\ln\left(Q^2/\mu^2\right)}, \tag{1.10}$$

where μ is the energy scale chosen in the renormalisation such that $\alpha_S(\mu^2)$ can be determined from experimental measurements. n_f is the number of quark flavours that can contribute to vacuum fluctuation in corresponding Q^2, given by $|Q| > 2m_f$. Since $n_f \leq 6$, α_S always decreases with increasing Q^2, in contrast to the electromagnetic α. That is what asymptotic freedom refers to. α_S can be measured indirectly through various processes in experiments, whose results are compared to theoretical calculations in Fig. 1.5.

This evolution of α_S has consequently lead to more interesting conclusions. In the QPM, the quarks are treated as free particles in DIS. This approximation does give reasonable results as its strong interactions with other quarks become small at the corresponding

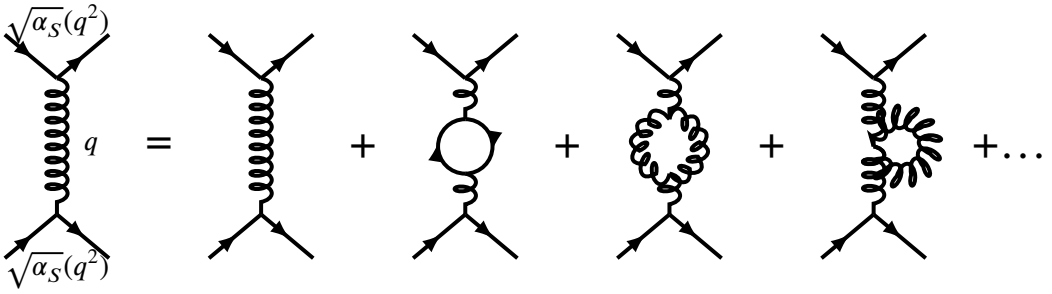

Figure 1.4 Feynman diagrams for QCD vertices in renormalisation, taken from Ref. [9].

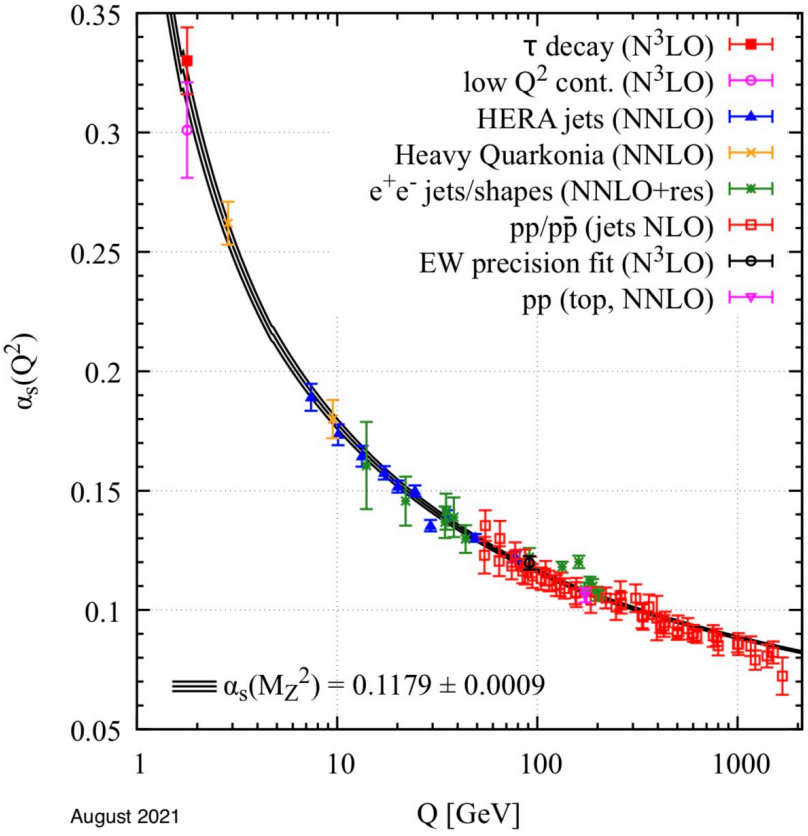

Figure 1.5 Theoretical calculation and experimental measurements on α_S as a function of Q, taken from Ref. [23].

large Q^2. The value of α_S is also important for perturbative calculations in QCD (pQCD). At low energy scale or large distance scale, α_S is close to 1. Thus perturbation theory is not applicable. To overcome this difficulty, the lattice gauge theory was proposed by Wilson[24], which quantises the gauge filed on a discrete lattice in 4-dimensional Euclide space-time and has been a powerful tool for handling low energy QCD problems. The α_S fortunately goes down to ~ 0.1 for the typical energy scale in high-energy collisions where perturbative theory can be used again, though higher-order terms are not negligible. The QCD scale Λ_{QCD} can be derived from Eq. 1.10 to characterise this, defined as

$$\Lambda_{\mathrm{QCD}} \equiv \mu \exp\left[-\frac{6\pi}{(33-2n_f)\alpha_S(\mu^2)}\right] . \tag{1.11}$$

Then evolution of α_S can then be rewritten in the form

$$\alpha_s\left(Q^2\right) = \frac{12\pi}{(33-2n_f)\ln(Q^2/\Lambda^2_{\mathrm{QCD}})} . \tag{1.12}$$

The Λ_{QCD} has a typical value of $\sim 300\,\mathrm{MeV}$ for $n_f = 4$. The perturbative region ($Q \lesssim \Lambda_{\mathrm{QCD}}$) and non-perturbative region ($Q \gg \Lambda_{\mathrm{QCD}}$) can be classified by this parameter. A new matter state, the quark-gluon plasma (QGP), is also expected to exist at high energy scale or small distance as the consequence of asymptotic freedom, which has been one of the main topics of nuclear physics.

1.1.4 Quark-gluon plasma

Quark-gluon plasma is a matter state where the colour confinement is removed and quarks and gluons can be considered as free particles. The existence of QGP state can be seen from the QCD phase diagram in the temperature T and baryon chemical potential μ_B space in Fig. 1.6, which is derived from QCD models[25-26]. QGP can be formed in the environment of extremely high temperature or large baryon number density. When the temperature or net baryon density goes down, it will transit into ordinary hadronic matter with dramatic changes in thermodynamic properties. The solid line represents the boundary of the sharp first-order phase transition at intermediate or high net baryon density regions. While for the low μ_B case, lattice QCD calculations predict that they will instead experience a continuous transition called *smooth crossover* around the temperature of $145-163\,\mathrm{MeV}$[28], shown as the dashed line in the diagram. The point separating two boundaries is the so called *critical point*, which is also estimated by lattice calculations with $T_{\mathrm{c}} \sim 159\,\mathrm{MeV}$ and $\mu_{\mathrm{c}} \sim 360\,\mathrm{MeV}$[29] and has not been verified by experiments.

The study of QGP has aroused general interests due to many aspects. The Big Bang

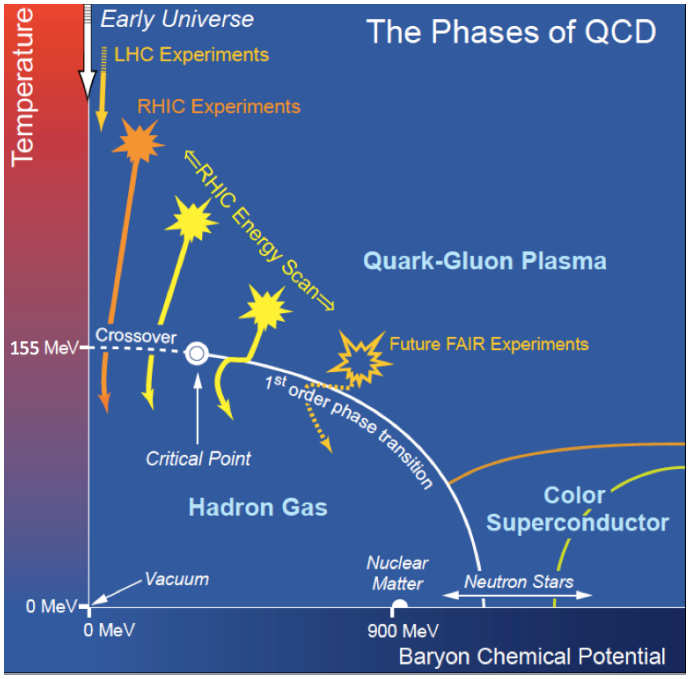

Figure 1.6 Schematic QCD phase diagram from theoretical calculations, taken from Ref. [27]. The temperature and baryon chemical potential that various heavy-ion experiments and the early Universe can reach are also shown.

model has been the most popular theory that describes the origin and evolution of the early Universe. According to this model, the Universe takes the state of QGP at the primordial time ($\sim 10^{-6}$s) of formation. As the Universe cools down in the inflation, it experiences the phase transition across the *crossover* line in Fig. 1.6. The coloured quarks and gluons are confined into hadrons via the *hadronisation*. Thus, QGP relates the investigation of the *maximum* and *minimum*, which is not only important for the test of the non-perturbative QCD, but also meaningful for in the study of the early Universe.

1.1.5 Heavy-ion collisions

As shown in Fig. 1.6, the extreme condition for the creation of the QGP can also be reached in high-energy relativistic heavy-ion collisions, which provide unique opportunities to study QGP in laboratories. Multiple scatterings occur in the collision of two heavy ions, and a large amount of energy will be deposited in the collision region. Fig. 1.7 illustrates the stages of the dynamical evolution of relativistic heavy-ion collisions, which can be roughly divided into the flowing stages:

(a) Initial stage

The heavy nucleus (Pb, Au, *etc.*) can be considered as a ball rather than a point. In high-energy collisions, the two nuclei are accelerated to high velocity close to that

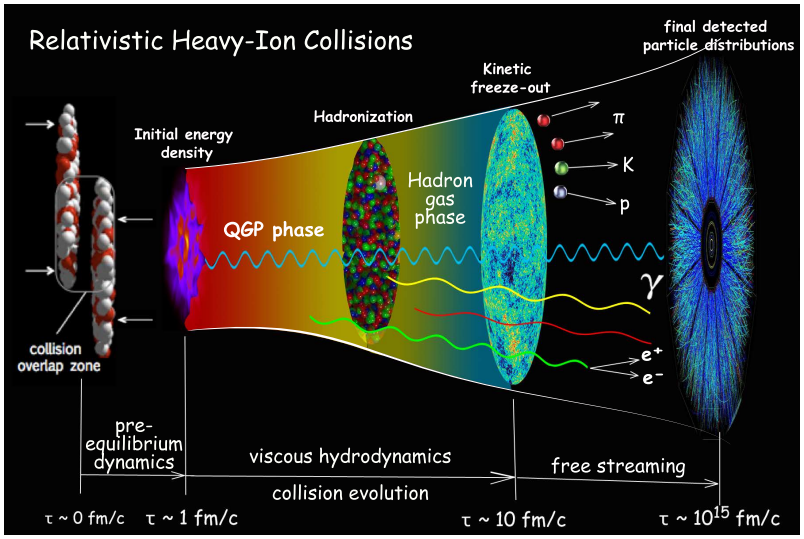

Figure 1.7 Illustration of the space-time evolution of high-energy heavy-ion collisions, taken from Ref. [30].

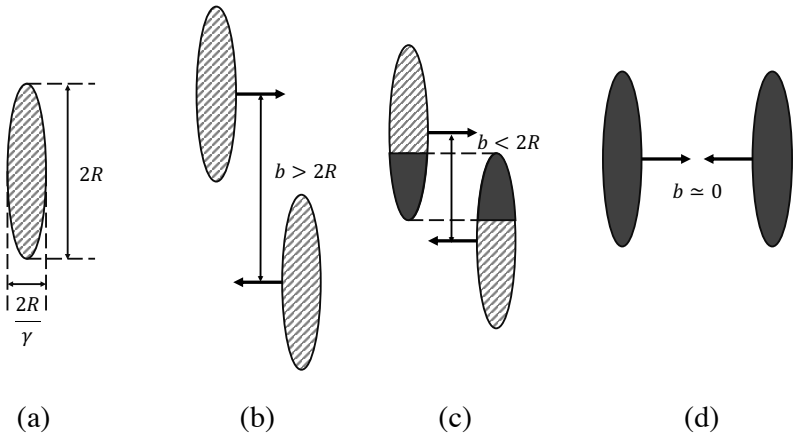

Figure 1.8 Sketch of the high-energy collisions of two nuclei, (a) a single nucleus, (b) ultra-peripheral collision, (c) peripheral collision, (d) central collision. The sub-figures (b) (c) (d) are taken from Ref. [31].

of light c. Therefore, the ball can be seen as flat disks in the centre-of-mass frame due to Lorentz contraction, as shown in Fig. 1.8. It is essential to investigate on the collision geometry in this step, because it significantly influences the collision dynamics. The collision geometry can be characterised via the transverse distance between the centre of two incoming nuclei, b, *i.e.* the impact parameter (IP). In ultra-peripheral collisions of the case b in Fig. 1.8, the two nuclei do not overlap and can interact via the electromagnetic field surrounding them. While for the cases (c) and (d) in Fig. 1.8, the nucleons can be classified into *participants* and *spectators*, depending on whether they are inside the overlap region or not.

The semi-classical Glauber model [32] was proposed to describe such collisions with

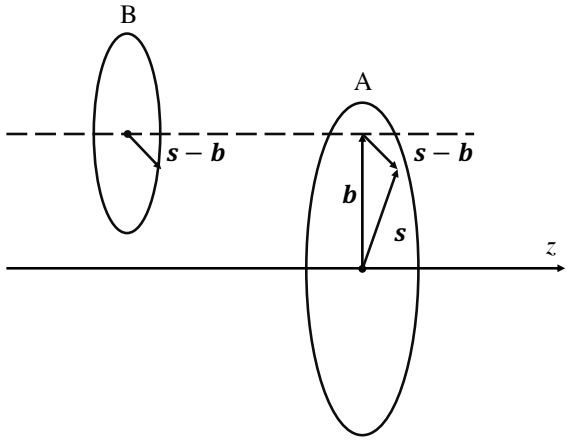

Figure 1.9 Collision geometry for nucleus A and B, where the vector $\boldsymbol{b}$ and $\boldsymbol{s}$ are inside the transverse plane perpendicular to the beam direction z. The figure is taken from Ref. [31].

two parameters, the number of binary nucleon-nucleon collisions, N_{coll}, and the number of participating nucleons, N_{part}. These two parameters can not be measured directly and can be related to the impact parameter b according to this model. Considering a more general collision of two different nuclei A and B, as shown in Fig. 1.9, where the nuclei are assumed not to deflect due to the high energy. $\boldsymbol{b}$ is the vector of the IP and $\boldsymbol{s}$ is the vector of a certain point inside the transverse plane. Then, the *nuclear overlap function* $T_{AB}(\boldsymbol{b})$ is defined as

$$T_{AB}(\boldsymbol{b}) = \int \mathrm{d}^2\boldsymbol{s}\; T_A(\boldsymbol{s}) T_B(\boldsymbol{s}-\boldsymbol{b})\,, \tag{1.13}$$

where T_A and T_B are the thickness function, obtained by integrating the probability per unit volume $\rho_A(z,\boldsymbol{s})$ over the beam direction

$$T_A(\boldsymbol{s}) = \int \mathrm{d}z\; \rho_A(z,\boldsymbol{s})\,, \tag{1.14}$$

and the ρ_A is normalised to unity. So the normalisation to unity also holds for T_A, T_B and T_{AB}. The probability of the inelastic scattering between A and B can be given as

$$\frac{\mathrm{d}^2\sigma^{\text{in}}_{AB}}{\mathrm{d}b^2} = 1 - \left(1 - \sigma^{\text{in}}_{\text{NN}} T_{AB}(\boldsymbol{b})\right)^{AB}\,, \tag{1.15}$$

as well as N_{part} and N_{coll}, as functions of $\boldsymbol{b}$

$$\begin{aligned} N_{\text{part}}(\boldsymbol{b}) = A \int \mathrm{d}^2\boldsymbol{s}\; T_A(\boldsymbol{s}) \left[1 - \left(1 - \sigma^{\text{in}}_{\text{NN}} T_B(\boldsymbol{s}-\boldsymbol{b})\right)^B\right] \\ + B \int \mathrm{d}^2\boldsymbol{s}\; T_B(\boldsymbol{s}-\boldsymbol{b}) \left[1 - \left(1 - \sigma^{\text{in}}_{\text{NN}} T_A(\boldsymbol{s})\right)^A\right]\,, \end{aligned} \tag{1.16}$$

$$N_{\text{coll}}(\boldsymbol{b}) = AB\sigma^{\text{in}}_{\text{NN}} T_{AB}(\boldsymbol{b})\,. \tag{1.17}$$

The $\sigma_{\mathrm{NN}}^{\mathrm{in}}$ is the cross-section for inelastic nucleon-nucleon scatterings, which can be measured via experiments. The calculation is usually implemented through the Monte Calo (MC) simulation. This model considers the nucleus-nucleus collisions as a superposition of nucleon-nucleon interactions and is widely used in the theoretical calculations of reaction cross-sections.

(b) Pre-equilibrium and thermalisation

In this period, The nucleons are stopped by the nuclear matter of another nucleus, which can be characterised by the *nuclear stopping power* depending on the nucleus geometry and collision energy. The virtual quanta and the gluon fields will be highly excited, and after a certain time, de-excite to a large amount of quarks and gluons. These partons then experience interactions and a local equilibrated QGP will be created. The time τ_0, when the system reaches local equilibrium in the local rest frame, is approximated to be $\lesssim 1$ fm/c. The matter state in the period of $0 < \tau < \tau_0$ is call the *pre-equilibruim state*. A large amount of entropy will also be created in this process.

This stage provides initial conditions for the evolution of QGP so it arouses many interests. There have been many models to describe the mechanism of the pre-equilibrium and thermalisation, which can be classified to coherent and incoherent models. One of the coherent models is the colour-string breaking model[33]. In this model, the two colliding nuclei pass through each other. The wounded nucleons in the nuclei will be colour excited and colour strings will form between the two neclei, where the colour strings are considered as coherent colour fields. These colour fields will cause the $q\bar{q}$ and gg pair production according to the Schwinger mechanism[34]. The produced quarks and gluon pairs will then interact with each other and form QGP that reaches the local thermal equilibrium. This evolution can be described with the relativistic Boltzmann equation. For the incoherent model, the equilibrated QGP originates from the minijets which are produced in incoherent superposition of parton collisions. Then pQCD can be applied in the calculation on minijet production[35], and the relativistic Boltzmann equation can be used for the calculation of the equilibrium process. Several simulation models for heavy-ion collisions, such as HIJING[36], are based on the incoherent model. Unfortunately, current models have not yet quantitatively described the whole process of pre-equilibrium and thermalisation due to the involved time-dependent and non-perturbative processes.

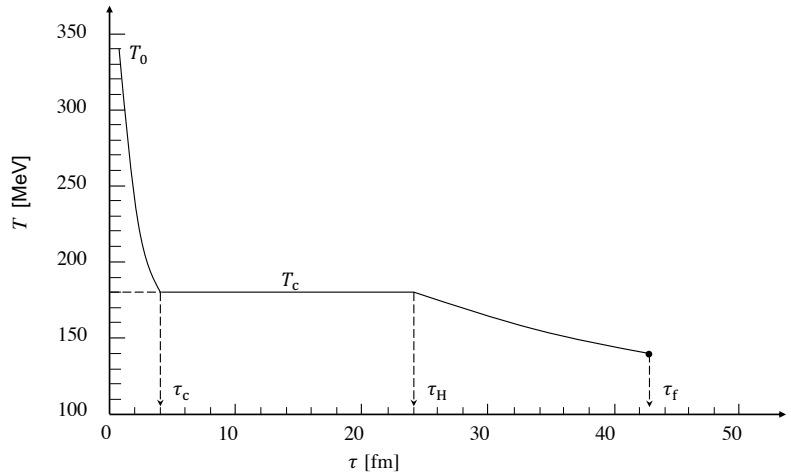

Figure 1.10 Time evolution of the temperature of the QGP created in the heavy-ion collisions, assuming the initial temperature T_0 to be $\sim 2T_c$. This figure is taken from Ref. [31].

(c) Hydrodynamic evolution

After the thermalisation reached at τ_0, the system will transfer into the QGP phase, considering that the temperature is larger than the first-order phase transition or cross-over temperature $T_0 > T_c$. Since the system is in local thermal equilibrium, the subsequent evolution can be described with relativistic hydrodynamics [37-40]. The time evolution of its temperature is illustrated in Fig. 1.10, assuming an initial temperature of $T_0 \sim 2T_c$. The temperature first falls to T_c in a very short time. The volume at the same time expands rapidly as a consequence of the decrease of entropy density, where the QGP can be considered as the *perfect fluid* and the entropy is conserved. Though the short lifetime makes it difficult for direct measurements, the formation of QGP does influence the final-state observables.

After the expansion, the system will experience a first-order phase transition at $\tau = \tau_c$ to the hadron gas phase, where the temperature stays at T_c. The system is in a mixed phase for $\tau_c < \tau < \tau_H$. There have been great interests on how the hadrons are created from the quarks and gluons, which is the so called *hadronisation*. The typical mechanism for hadronisation in e^+e^-, $p\bar{p}$ and pp collisions is the fragmentation[41-42]. In these collisions, high-energy $q\bar{q}$ pairs are produced first, and then radiate soft gluons. These gluons produce more $q\bar{q}$ pairs, which can also radiate gluons subsequently. In this successive process, the quark and anti-quark may combine to form colour-singlet hadrons and back-to-back jets are created. These hadrons typicallly have a momentum fraction $z < 1$ of the original partons. Consider a hadron h with momentum p hadronised from a parton i with p_i, where $p = zp_i$. The inclusive

production cross-section of this hadron $E\mathrm{d}^3\sigma_h/\mathrm{d}^3p$ can be given by[43]

$$E\frac{\mathrm{d}^3\sigma_h}{\mathrm{d}^3p} = \sum_i \int_0^1 \frac{\mathrm{d}z}{z} E_i \frac{\mathrm{d}^3\sigma_i}{\mathrm{d}^3p_i} D_{i\to h}(z)\,, \tag{1.18}$$

where $E_i\mathrm{d}^3\sigma_i/\mathrm{d}^3p_i$is the invariant production cross-section of the parton i, and $D_{i\to h}(z)$ is the fragmentation function. $D_{i\to h}(z)\mathrm{d}z$ can also be interpreted as the number of the hadron h in the momentum interval $[zp_i, (z+\mathrm{d}z)p_i]$ from the parton i with momentum p_i. This mechanism has been well established for predicting the production of hadrons with large transverse momentum p_T. Nevertheless the $D_{i\to h}(z)$ can only given by phenomenological models or experimental input. An alternative model for hadronisation is *quark recombination*[44] or *quark coalescence*[45]. When three quarks, or a quark and an anti-quark, have overlapping wavefunctions in position and velocity space, they will combine to form a baryon or a meson. Thus, the produced hadrons always have larger momenta than the original quarks. A simplified model gives the cross-section for coalescence as

$$E\frac{\mathrm{d}^3N_\mathrm{M}}{\mathrm{d}^3p} \propto \int_{\Sigma_\mathrm{f}} p^\mu \mathrm{d}\Sigma_\mu \int_0^1 \mathrm{d}x w\left(r; xp_\mathrm{T}\right) \bar{w}\left(r; (1-x)p_\mathrm{T}\right) \left|\phi_\mathrm{M}(x)\right|^2, \tag{1.19}$$

$$\begin{aligned} E\frac{\mathrm{d}^3N_\mathrm{B}}{\mathrm{d}^3p} \propto & \int_{\Sigma_\mathrm{f}} p^\mu \mathrm{d}\Sigma_\mu \int_0^1 \mathrm{d}x \int_0^{1-x} \mathrm{d}x' \\ & \times w\left(r; xp_\mathrm{T}\right) w\left(r; x'p_\mathrm{T}\right) w\left(r; \left(1-x-x'\right)p_\mathrm{T}\right) \left|\phi_\mathrm{B}\left(x, x'\right)\right|^2 . \end{aligned} \tag{1.20}$$

Here Σ_f is the hyper-surface where the coalescence takes place and $r \in \Sigma_\mathrm{f}$, $w\left(r; xp_\mathrm{T}\right)$ and $\bar{w}\left(r; xp_\mathrm{T}\right)$ are the phenomenological phase-space distribution of quarks and anti-quarks respectively, x and x' are the lightcone momentum fraction of quarks, $\phi_\mathrm{M}(x)$ and $\phi_\mathrm{B}(x)$ are the lightcone wave functions of mesons and baryons. Due to the high quark density and the large number of produced minijets in the pre-equilibrium stage of the nucleus-nucleus collisions, quark coalescence plays a more important role than in the *pp* collisions. This also provides us with a probe into the phase transition of QGP, which will be discussed in Sec. 1.1.6 afterwards. After the phase transition, the nuclear matter go through a new hydrodynamic evolution in the hadron gas phase within the time interval $\tau_\mathrm{H} < \tau < \tau_\mathrm{f}$, which can be described with a similar method as the evolution of the QGP phase, or with more sophisticated hadronic transport models like ultrarelativistic quantum molecular dynamics model[46]. The system continues to cool down and expand, until the thermal equilibrium is broken at τ_f.

(d) Freeze-out and post-equilibrium

After τ_f, mean free paths of the constituent hadrons are larger than the scale of the hadron gas. The chemical freeze-out first happens after which inelastic scatterings between particles finish and the numbers of each particles species are maintained. Then the kinetic freeze-out occurs as the elastic scatterings also finish. A large numbers of hadrons, especially protons, kaons and pions, will be emitted and finally detected by the experimental facilities.

1.1.6 Nuclear matter effects

As described in the section above, the QGP has a very short lifetime $\sim 7\,\mathrm{fm}/c$ [47], which makes it difficult to detect and measure directly. However, its existence does influence the evolution of the collision systems and finally change the distributions of the produced final-state particles. According to the Glauber model, nucleus-nucleus collision can be seen as the superposition of nucleon-nucleon collisions. Thus, pp collision is a good baseline for studying the hot-dense nuclear matter in heavy-ion collisions. The comparison can be quantified as the ratio *nuclear modification factor* R_{AA}, neglecting the difference between proton and neutrons

$$R_{AA}\left(N_{\mathrm{part}}, \sqrt{s_{\mathrm{NN}}}\right) = \frac{1}{\langle N_{\mathrm{coll}}(\boldsymbol{b})\rangle} \frac{\sigma_{AA}\left(N_{\mathrm{part}}, \sqrt{s_{\mathrm{NN}}}\right)}{\sigma_{pp}\left(\sqrt{s}\right)} . \tag{1.21}$$

The $\sigma_{AA}\left(N_{\mathrm{part}}, \sqrt{s_{\mathrm{NN}}}\right)$ and $\sigma_{pp}\left(\sqrt{s}\right)$ are the cross-sections for a species of particle in AA collisions and pp collisions respectively, corresponding to the same centre-of-mass energy $\sqrt{s}$ (centre-of-mass energy per nucleon pair $\sqrt{s_{\mathrm{NN}}}$ for heavy-ion collisions). $\langle N_{\mathrm{coll}}(\boldsymbol{b})\rangle$ is the average number of equivalent nucleon-nucleon collisions at the IP of b, which is commonly obtained from MC simulation. A factor with non-unity will be observed if nuclear matter effects exist. In addition to the formation of QGP, the difference on intrinsic properties and interactions between protons and heavy nuclei can also affect the measurements. According to different sources, these effects can be classified into hot nuclear matter (HNM) effects and cold nuclear matter (CNM) effects.

1.1.6.1 Hot nuclear matter effects

The hot nuclear matter effects originate from the formation of QGP, and the corresponding observables are also considered as the QGP signatures. These signatures can be detected via different probes, such as hadrons and jets. Some typical HNM effects that

are important for experimental measurements will be introduced below.

- Parton energy loss

  When high-energy partons are created in the collision, it will lose energy in several processes. The first process happens throughout its hadronisation when successive radiations happen and jets are produced. The jets can be detected if the collision energy is high enough no matter what the collision system (e^+e^-, $p\bar{p}$ or pp) is. Another significant one originates from its interaction with QGP, so it can only occur in AA collisions. When passing through QGP, fast partons interact with the quarks and gluons in the medium and emit gluons. Theoretical calculations[48-49] give a comparable energy loss per unit length with the former one in the transverse direction. This will cause the suppression or deflection of jets, which is also known as *jet quenching*[50-53]. Jet quenching is one of the most important signature for QGP and provides an excellent probe for studying the space structure of QGP.

- Strangeness enhancement

  In high-energy pp collisions, the yield of strange quark pairs $s\bar{s}$ is calculated to be 10-20% of that of $u\bar{u}$ or $d\bar{d}$ pairs[54]. While in AA collisions, the gluon fusion process $gg \to s\bar{s}$ in QGP can also contribute to the strangeness production. The copious gluons in QGP and significantly lower production threshold for strange quarks will lead to an enhanced production of strange particles, in particular for those with multiple s quarks. Therefore, strangeness enhancement is also considered as a QGP signature[55].

- Charmonium suppression

  The suppression of J/ψ meson production is predicted in AA collisions as a consequence of the Debye screening effect in QGP[56]. At zero temperature, the $c\bar{c}$ pairs are confined in charmonium by the binding energy, which can be described as[56]

  $$V(r) = \sigma r - \frac{\alpha_{\text{eff}}}{r}\,, \tag{1.22}$$

  The parameters σ and α_{eff} are introduced to characterise the intense of string and coulombic interactions. As the temperature increases to $\sim T_c$, the string intense will disappear and the colour-screened coulombic potential will dominate the bounding energy, which can be given as[57]

  $$V(r) = -\frac{\alpha_{\text{eff}}}{r} \exp\left(-\frac{r}{r_D(T)}\right), \tag{1.23}$$

  and r_D is the screening radius. At $T \approx 1.2T_c$, r_D will be too small to hold the bound

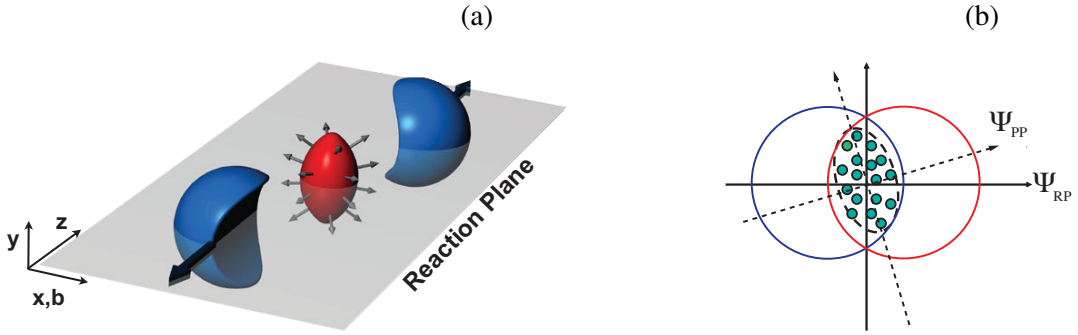

Figure 1.11 Sketch for non-central AA collisions (left) and the projection to the $x-y$ (transverse) plane (right). The figures are taken from Ref. [61].

states[56]. In addition, the high-density light quarks and gluons can also break the $c\bar{c}$ bound states in QGP. Open-charm mesons (D mesons) will be produced instead[58].

- Collective flow

  The hydrodynamic evolution of the QGP will induce collective motions of produced final-state particles, which is called the *collective flow*. The first one is the radial flow originating from the QGP transverse expansion[59]. For hadrons, the radial flow will be superposed to the hadron thermal emission and thus lead to a modification of their transverse mass M_{T} spectrum compared to that in pp collisions, where M_{T} is defined as $M_{\mathrm{T}}^2 = p_{\mathrm{T}}^2 + M^2$.

  Another type of flow, *anisotropic flow*, is an important QGP signature expected to be observed in non-central AA collisions. The sketch for non-central AA collisions is shown in Fig. 1.11, where the red part symbolises the participants and blue parts symbolise the spectators. The beam direction is defined as z axis, the IP vector $\boldsymbol{b}$ is defined as x axis. The $x-z$ plane is then defined as the *reaction plane* Ψ_{RP}. According to the relativistic Euler equation, the pressure gradient, which is steeper along x axis, can lead to a stronger collective expansion in this direction. Consequently, an anisotropic elliptic distribution of particle production will be observed in their transverse azimuthal distribution[60]. This anisotropy can be quantified by the Fourier coefficients of the azimuthal particle distribution function[62]

$$E\frac{\mathrm{d}^3N}{\mathrm{d}p^3} = \frac{1}{2\pi}\frac{\mathrm{d}^2N}{p_{\mathrm{T}}\mathrm{d}p_{\mathrm{T}}\mathrm{d}y}\left(1+2\sum_{1}^{\infty}v_n\cos[n(\phi-\Psi_{\mathrm{R}})]\right), \tag{1.24}$$

  where ϕ is the azimuthal angle of the particle momentum and Ψ_r is that of Ψ_{RP} in the laboratory frame (against the participant plane Ψ_{PP} in Fig. 1.11b). The v_2, also known as the *elliptic flow*, is sensitive to the equation of state of QGP and particularly helpful to extract its sound velocity c_s[61].

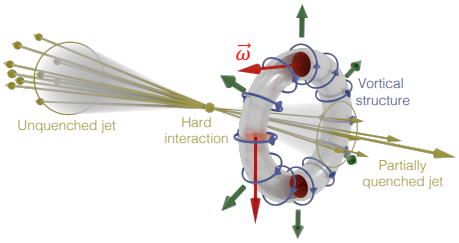

Figure 1.12 Illustration of the generation of a vortical structure caused by a jet quenching, where one of the jets is quenched while another not. The figure is taken from Ref. [64].

- Hydrodynamic vorticity

  When back-to-back jets are produced and one of them are partially quenched by QGP, a vortical structure of *smoke ring* can be produced during the thermalisation of the quenched jet[63], as illustrated in Fig. 1.12. The vorticity will finally be transferred into polarisation of produced particles due to angular momentum conservation. This interesting phenomenon can not only confirm the thermalisation of the quenched jets, but also probe the shear viscosity of QGP[64].

- Hadronisation from quark coalescence

  As described in the phase transition of the QGP, the quark coalescence can also contribute to the hadronisation mechanism in addition to the fragmentation. Because constituent quarks have smaller momentum than the produced hadron in the coalescence, it will dominate the hadron production at intermediate p_{T}. Thus, an enhanced baryon-to-meson ratio will be observed in this region[44-45]. Taking the collective flow of constituent quarks into consideration, the anisotropic distribution of mesons and baryons is also expected, A simplified model gives the baryon and meson v_2 as[65]

$$v_{2,\mathrm{M}}(p_{\mathrm{T}}) \simeq 2v_{2,q}(p_{\mathrm{T}}/2)\ ,\ v_{2,\mathrm{B}}(p_{\mathrm{T}}) \simeq 3v_{3,q}(p_{\mathrm{T}}/3)\ , \tag{1.25}$$

  which is also a probe to the coalescence picture in hadronisation.

1.1.6.2 Cold nuclear matter effects

The CNM effects are often related to the intrinsic properties of nuclei or multiple scatterings between nucleons. They can also significantly change the particle production in heavy-ion collisions. Thus, a complete understanding of heavy-ion collisions requires the understanding of these effects. In AA collisions, it is always difficult to distinguish the QGP signatures from these CNM effects. These effects could be studied in other collision systems involving heavy nuclei, such as pPb, where the system size is assumed to be too

small to create QGP. Similar to AA collisions, the Glauber model can also be used to compare pA collisions with the equivalent measurements in pp collisions. Considering that the size of heavy nuclei is much larger than that of proton, an approximated parametrisation of $T_{AB}(b)$ in the form of sharp-cutoff function can be given as[66]

$$T_{AB}(b) = \frac{3}{2\pi R^3}\sqrt{R^2 - b^2}\,\theta(R-b)\,, \tag{1.26}$$

and by averaging N_{coll} over b

$$\langle N_{\text{coll}}\rangle = \frac{1}{\sigma_{\text{NN}}^{\text{in}}}\int \mathrm{d}b\; 2\pi b A T_{AB}(b)\sigma_{\text{NN}}^{\text{in}} = A\,, \tag{1.27}$$

and thus the nuclear modification factor R_{pA} can be defined as

$$R_{pA}\left(\sqrt{s_{\text{NN}}}\right) = \frac{1}{A}\frac{\sigma_{pA}\left(\sqrt{s_{\text{NN}}}\right)}{\sigma_{pp}\left(\sqrt{s}\right)}\,, \tag{1.28}$$

if the collision geometry is neglected. Current understanding of CNM effects includes the following:

- Modification of parton densities

  As described in the QPM, the structure function F_2 reveals the proton dynamics and determines the cross-sections of the processes involving protons. The assumption that F_2 differs between bound and free nucleons was predicted[67-68] and were supported by DIS experiment results from the European Muon Collaboration (EMC)[69]. The ratio of parton densities, or the ratio of the nuclear PDF (nPDF) over the PDF, is defined as

  $$R_i^A(x,Q^2) \equiv \frac{f_i^A(x,Q^2)}{A f_i^{\text{nucleon}}(x,Q^2)}\,, \tag{1.29}$$

  where i runs for each parton flavour (valence quarks, sea quarks or gluons). An illustration of the $R_i^A(x,Q^2)$ dependence on x in a certain Q^2 region is shown in Fig. 1.13, where roughly four structures are included:

  - Shadowing region, $R_i^A < 1$ for $x \lesssim 0.1$. This suppression at small x can be attributed to the hadronic behaviour of the virtual photon at high energy[71]. The hadronic component of the virtual photon will interact several times with nucleons in the nucleus[72]. The details for handling the hadronic interactions of the virtual photon with partons varies across models. One common model is the parton fusion[67]. The partons with $x < 0.1$ that sharing the same transverse coordinate can have overlapped wavefunctions in space and interact

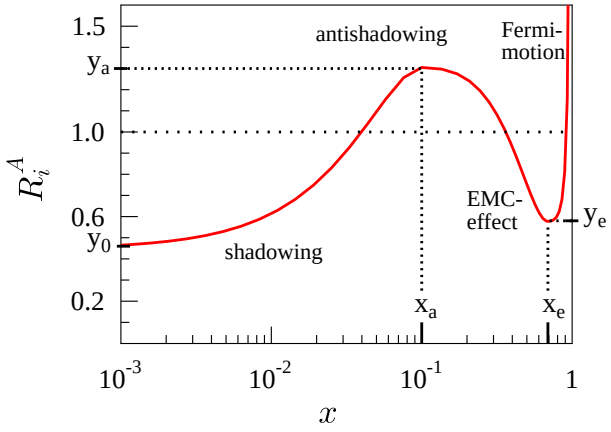

Figure 1.13 Illustration of the $R_i^A(x)$ in a certain Q^2 region. The figure is taken from Ref. [70]
.

with each other. The number of soft partons that photons can interact with at small x will consequently be proportional to $A^{\frac{2}{3}}$.

- Antishadowing region, $R_i^A > 1$ for $0.1 \lesssim x \lesssim 0.3$. This phenomenon was also predicted by the parton fusion[67]. The parton fusion can not change the total momentum carried by the partons. The enhancement will occur at larger x region due to the redistributed parton densities.
- EMC region, $R_i^A < 1$ for $0.3 \lesssim x \lesssim 0.8$. This difference was first observed in the DIS experiment by the EMC in the measurement of $F_2(\mathrm{Fe})/F_2(\mathrm{D})$ for $x > 0.3$[69]. There have been many models attempting to explain the experiment results, such as the contribution from the pion field in nuclei[73-74], or the modification of the nucleon radius in nuclei[75].
- Fermion motion region, $R_i^A > 1$ for $x \gtrsim 0.8$. As its name implies, this effect originates from the Fermion motion inside the nucleus[76]. The Fermion motion can lead to a high-momentum tail of the nucleon that will contribute to the structure function[77].

The Dokshitzer–Gribov–Lipatov–Altarelli–Parisi (DGLAP) evolution equations[78-80] is a powerful tool to study the Q^2 evolution of R_i^A at energy scales large enough for perturbative calculation. Nowadays, various descriptions of the nPDF, such as nCTEQ15[81], EPPS16[82], EPPS21[83], nNNPDF2.0[84] and nNNPDF3.0[85], have been made based on DGLAP equations, parametrised with the experimental input of different types[70]. A comparison on the $R_{\mathrm{uV}}^{\mathrm{Pb}}$ and $R_{\mathrm{dV}}^{\mathrm{Pb}}$ (valence u and d quark) are shown in Fig. 1.14. The typical involved data are from

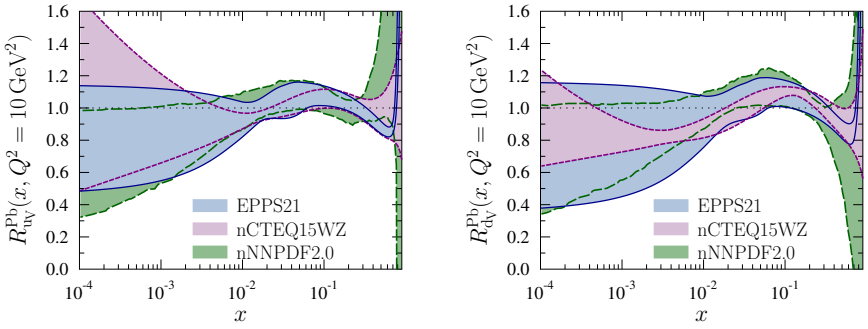

Figure 1.14 Results on the $R_{\mathrm{uV}}^{\mathrm{Pb}}$ and $R_{\mathrm{dV}}^{\mathrm{Pb}}$ from EPPS21[83], nCTEQ15[81] and nNNPDF2.0[84] models. The figure is taken from Ref. [83].

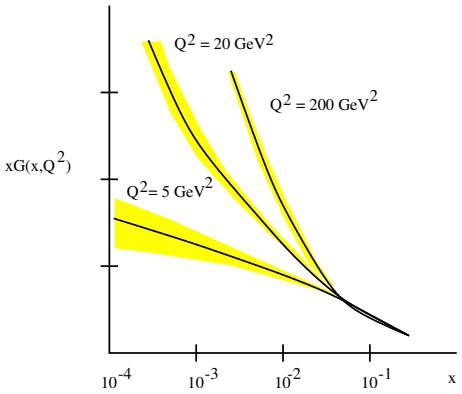

Figure 1.15 Gluon structure function $xG(x, Q^2)$ measured in electron-proton DIS experiments. The figure is taken from Ref. [86].

the deep inelastic lA scatterings, Drell-Yan dilepton, inclusive π meson, dijet and heavy-flavour production in pA collisions.

- Gluon saturation

  In the DIS experiments, the contribution from gluons $xG(x, Q^2)$ was found to dominate the proton momentum. The $xG(x, Q^2)$ shows a rapid growth with increasing Q^2 in small x ($x < 10^{-2}$) regions as presented in Fig. 1.15. A qualitative explanation can be given following the case of nuclear shadowing. At sufficiently large Q^2 or small x, the parton density becomes large and the interactions between them grow stronger[86]. As Q^2 increases, the number of gluons will not keep increasing. They will overlap, interact with each other and finally saturate[87-88]. That is to say, the gluons transfer into a system called *colour glass condensate* (CGC). The *colour* refers to the colour charges carried by gluons. The *glass* means that the system is similar to the glass in the real world, which evolves very slowly. And the *condensate* indicate that the high-density gluons have formed a multiparticle Bose-Einstein condensate state. Fig. 1.16 shows a *phase diagram* for QCD. Along the horizontal axis

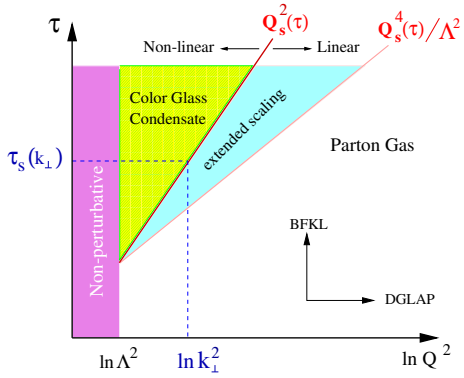

Figure 1.16 QCD evolution in the two-dimensional space of $\ln(Q^2)$ and $\tau \equiv \ln(1/x)$. The figure is taken from Ref. [86].

with the increasing Q^2, the QCD evolution can be described with DGLAP[78-80] equations. And the Balitsky-Fadin-Kuraev-Lipatov (BFKL)[89-91] equations give the evolution with decreasing x where gluon density increases rapidly. As the x continues decreasing, the gluon recombination[88] will take place. The Balitsky-Kovchegov (BK) equation[92-93] was developed to describe the QCD evolution in the saturation region, which gives the boundary of the region with

$$Q_s^2(x) \sim \alpha_S(Q_s^2) N_c \frac{xG(x, Q_s^2)}{\pi R^2} . \tag{1.30}$$

Here the R is the radius of the hadron and $Q_s(x)$ is called the saturation scale. When applied to heavy nuclei, $g(x, Q_s^2) \to Ag(x, Q_s^2)$ and $R \to RA^{1/3}$ and Q_s^2 shows an $A^{1/3}$ dependence. Therefore, the gluon saturation will be observed more easily in heavy nuclei.

- Cronin effect

  This effect was first observed when measuring the hadron production in pA collisions at the Fermi National Accelerator Laboratory[94]. The measured p_{T} spectrum was found to be broadened. An illustration of R_{pA} as a function of p_{T}, which is now also called the *Cronin ratio*, is presented in Fig. 1.17. An enhancement of $R_{pA}(p_{\mathrm{T}})$ can be observed at intermediate p_{T}, and the ratio will asymptotically go down to unity with p_{T} increases towards $infty$. The Cronin effect can be attributed to the initial-state multiple elastic scattering. Theoretical models of soft hadronic rescatterings[96-97], soft partonic rescatterings[98] and hard partonic rescatterings[99-100] are proposed to explain this effect in different p_{T} regions.

- Cold nuclear matter energy loss

  In pA collisions, partons should experience multiple parton scatterings, as shown in Fig. 1.18. Throughout this process, partons will emit gluons and thus loss energy.

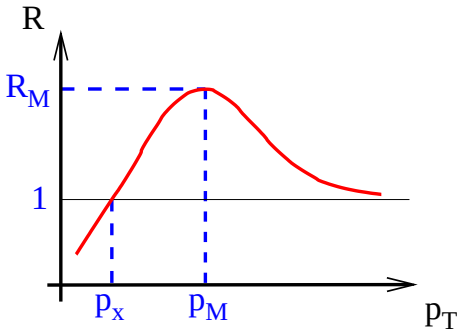

Figure 1.17 Illustration of the $R_{pA}(p_{\mathrm{T}})$ shape arising from the Cronin effect. The figure is taken from Ref. [95].

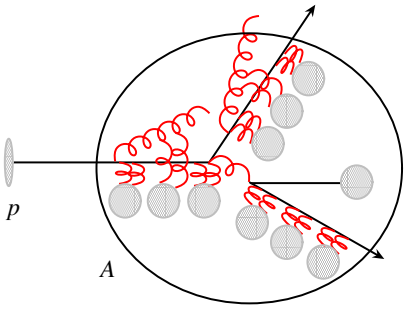

Figure 1.18 Schetch for the multiple parton scattering in the nuclear rest frame. The figure is taken from Ref. [101].

These processes can be classified into different types depending on how the parton propagation is modified and when the scatterings happen, which will also give various corrections to the nuclear cross-section[101] (or R_{pA}). The elastic scatterings, as mentioned in the Cronin effect, will lead to enhanced R_{pA} at intermediate p_{T}. While inelastic scatterings can cause the suppression at all p_{T}. These scatterings can also take place in the intial or final state, which will result in energy loss in the nucleus before or after the large Q^2 hard scatterings[102]. The momentum fraction x of partons in the nucleus can also be used to characterise the scatterings. When x is small, the incident particles interact with the partons coherently. The calculation from the fully coherent energy loss (FCEL)[103] gives an energy loss proportional to the incoming parton energy, which consequently predicts a suppression for all kinds of hadrons in pA collisions compared to binary pp collisions at forward rapidity. While for the backward rapidity region where x is large, the incoherent energy loss dominates. The R_{pA} is expected to be enhanced due to the contributions from the incoherent double scatterings[104].

- Initial-state correlation

  The elliptic flow v_2 was assumed to originate from the hydrodynamic evolution of

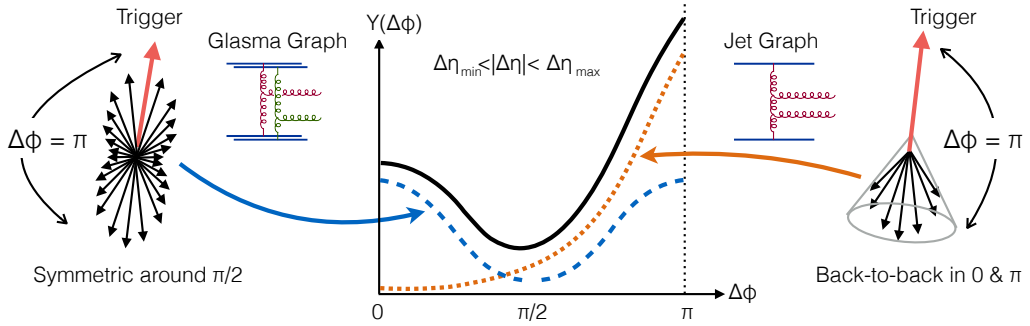

Figure 1.19 Cartoon for long-range two particle azimuthal correlation function $Y(\Delta\phi)$ and the contributions from di-jet and glamsa graphs. The figure is taken from Ref. [117].

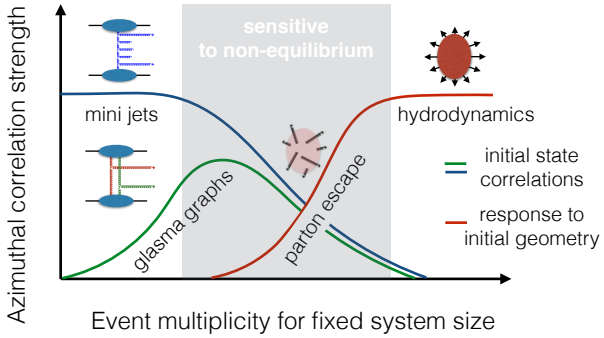

Figure 1.20 Illustration of the contributions on azimuthal correlation strength from inital- and final-state effects in small systems versus event multiplicity. The figure is taken from Ref. [117].

QGP in heavy-ion collisions. However, unexpected large v_2 (long-range azimuthal correlation) is also observed in small collision systems, such as pp, pA, dA and ^{3}HeA collisions[105-114]. Except for the assumption that QGP droplets may be created in high-multiplicity pA collisions[115-116], there are also models that successfully reproduce the observed long-range azimuthal correlation in small systems with the CGC effective field theory, which attributes the collectivity to the initial-state correlation[117-118]. An qualitatively illustration of the theoretical model is shown in Figs. 1.19 and 1.20. For low-multiplicity events, the correlation originating from the di-jets dominates the correlation function. These back-to-back structure will result in a peak at $\Delta\phi = \pi$. As the multiplicity increases, the *glasma graph* will give a symmetric structure at $\Delta\phi \sim \pi/2$, which originates from the multiple parton processes, and can be calculated in the CGC framework[117]. When the multiplicity becomes extremely high, the final-state effects will finally take place and the hydrodynamic expansion of the QGP will be the dominant contribution. Corresponding

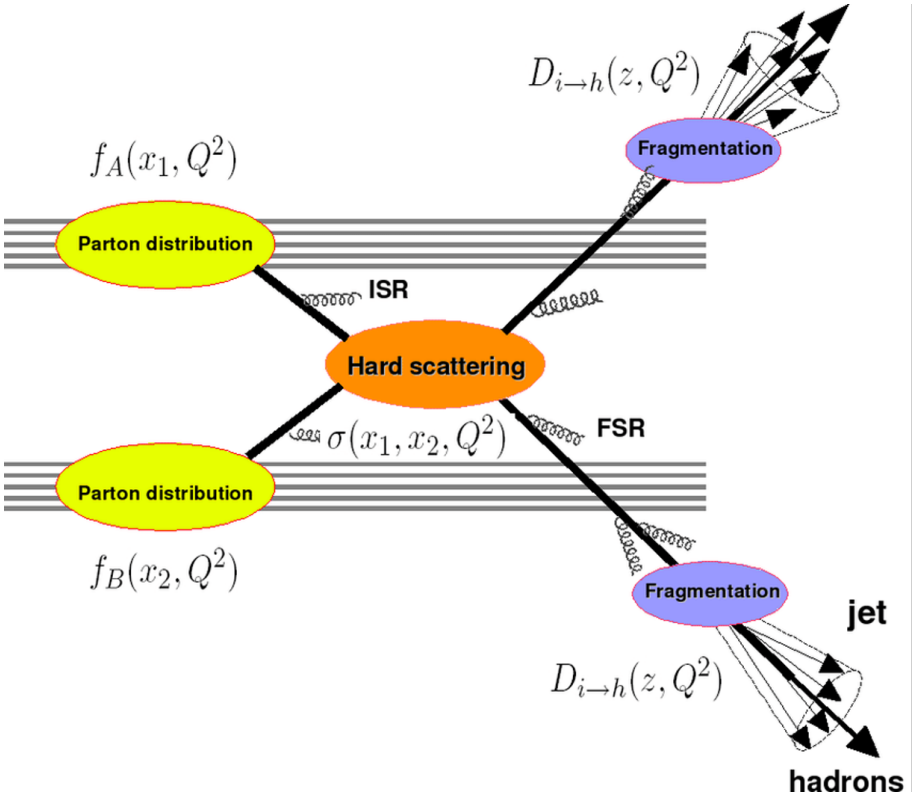

Figure 1.21 Sketch for the heavy-flavour production in heavy-ion collisions.

calculations[118] also predict that such elliptic flow v_2 will not vary with particle masses in pA collisions.

1.1.7 Charm hadron in heavy-ion collisions

Charm hadrons have been considered as an excellent probe for investigating nuclear matter effects in heavy-ion collisions. The charm quarks have a mass of $m_c = 1.27\,\mathrm{GeV}/c$[119] and are produced in hard processes of the collisions. The dynamical scales for these hard processes are much larger than Λ_{QCD}[101], so perturbative calculations can be applied to them. The ground-state open-charm mesons have a lifetime of $\tau \sim 1$ ps, which allows them experience the whole time evolution of QGP. For D^0, $D^{\pm}$ mesons, they have a binding energy of $\sim$ hundreds MeV. This energy is close to the dynamic scales of the nuclear matter created in relativistic collisions[101]. Thus, the fragmentation and dissociation of D mesons are sensitive to the medium properties in the collisions.

The process for the production of heavy flavour particles can be illustrated with the cartoon in Fig. 1.21. The heavy-flavour production is controlled by the initial conditions, the hard scattering cross-sections and the fragmentation functions, where the initial-state and final-state rescatterings may affect the process in heavy-ion collisions additionally.

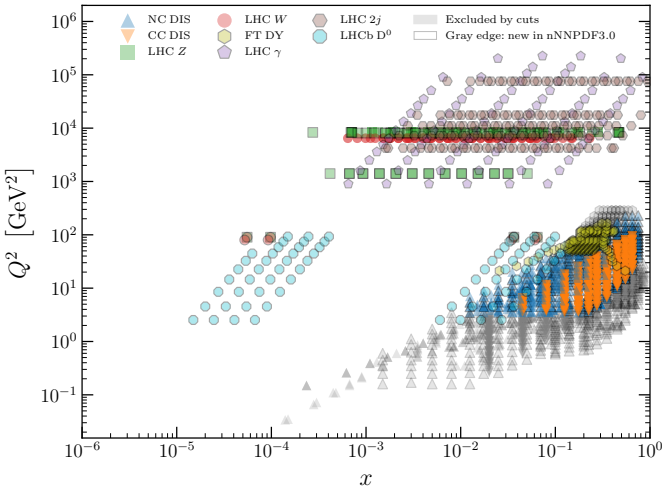

Figure 1.22 Kinematic coverage in the (x, Q^2) space for the nNNPDF3.0 analysis. The figure is taken from Ref. [85].

The pQCD gives the hadronic cross-section in the form[120]

$$\sigma_{\text{hadronic}} = \sigma_{\text{partonic}}\left(x_i, z_j\right) \otimes \left\{\prod_i f_{i,h_i}\left(x_i\right)\right\} \otimes \left\{\prod_j D_{h_j/j}\left(z_j\right)\right\} . \tag{1.31}$$

Here $f_{i,h_i}(x_i)$ is the PDF of parton i in the hadron h_i, $D_{h_j/j}(z_j)$ is the fragmentation function of parton j into hadron h_j and σ_{partonic} is the partonic cross-section. The $\otimes$ is the convolution performed over the internal kinematic variables in the process.

In the pp collisions at high energy, the heavy-flavour processes are driven by gg luminosity[121]. So the heavy-flavour cross-sections are sensitive to the gluon PDFs. In other words, the measurements of the heavy-flavour production provides important information on the PDFs. When it comes to pA collisions, the comparison between the measured cross-sections in pp and pA collisions can greatly improve the knowledge the gluon nPDF f_A^g. By making the ratio R_g^A, the terms from hard scatterings and hadronisation can be canceled. It had been predicted that the D^0 production cross-sections measured with pPb data collected by the LHCb experiment at forward rapidity ($2 < \eta < 5$) can provide significant constraints for nPDF parametrisations in the shadowing region of $x < 10^{-3}$[122]. This has been verified for the determination of EPPS21[83] and nNNPDF3.0[85] nPDFs, where their previous analysis[82,84] did not include LHCb prompt D^0 results[123]. The kinematic coverage of the involved data for Ref. [85] in the (x, Q^2) space is shown in Fig. 1.22, where the prompt D^0 data cover both shadowing and antishadowing regions. And the improvement on the gluon nPDFs in small x regions, when including LHCb D^0 data, can be seen in Fig. 1.23.

In the calculation of heavy-flavour production, the energy loss in the cold nuclear

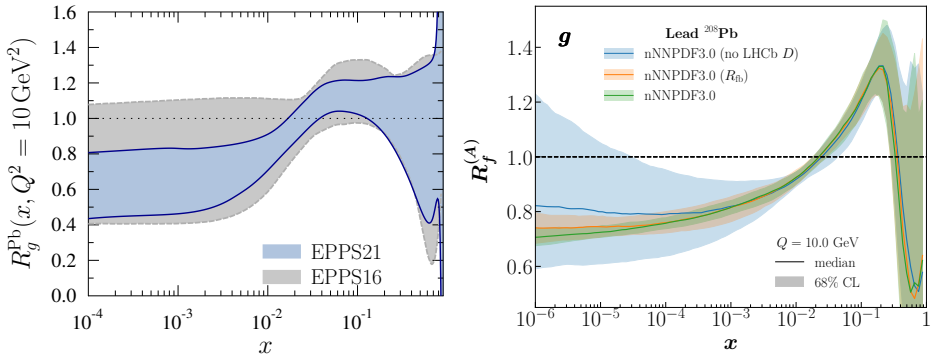

Figure 1.23 Comparison of $R_g^{\rm Pb}(x, Q^2 = 10\,{\rm GeV}^2)$ between (left) EPPS21[83] and EPPS16[82], and (right) between nNNPDF3.0[85] with and without including LHCb prompt D^0 results[123]. For the left panel, EPPS21 includes extra uncertainties of free-protons with respect to EPPS16. For the right panel, the blue band represents the nNNPDF3.0 without the D^0 measurement, the red one represents the nNNPDF3.0 involving the measured D^0 forward-backward production ratio $R_{\rm FB}$ and the green one represents the nNNPDF3.0 involving the measured D^0 $R_{p\rm Pb}$. The left figure is taken from Ref. [83] and the right figure is adapted from Ref. [85].

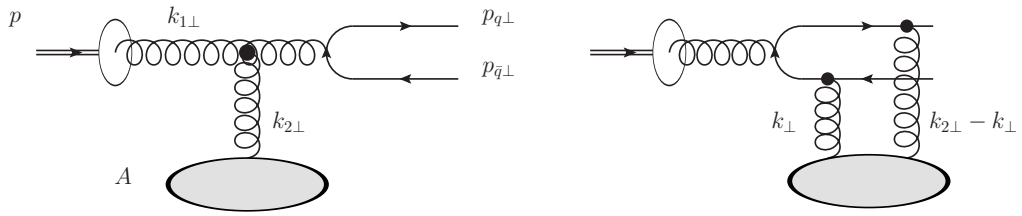

Figure 1.24 Leading order diagrams of the $c\bar{c}$ pair production in the pA collisions. The $c\bar{c}$ pairs split (left) after and (right) before the multiple scatterings. The $k_{i\perp}$ and $p_{i\perp}$ represent the transverse momenta of the gluons and quarks respectively. The blobs symbolise the multiple scatterings with the gluon fields in the nuclei. The figure is taken from Ref. [124].

matter can be implemented in the PDF of partons in nuclei $f_{q,g/N}$ in Eq. 1.31. The radiative energy loss ΔE of the parton is proportional to the energy E as well as the single scattering probability L/λ, corresponding to an average parton energy loss $\sim$ 10% for large nuclei such as Au and Pb. This energy loss gives a modification on the x as[101]

$$\epsilon = \frac{\Delta E}{E} \propto \frac{L}{\lambda} = \kappa A^{1/3}\,, \tag{1.32}$$

$$f_{q,g/N}(x) \to f_{q,g/N}(\frac{x}{1-\epsilon})\,. \tag{1.33}$$

This energy loss will lead to suppressed heavy-flavour production at forward rapidity.

The CGC framework also provides a description on the heavy-flavour production at forward rapidity. In the leading order (LO), the formation of $c\bar{c}$ pairs in pA collisions can be illustrated in the diagrams in Fig. 1.24. The two diagrams include the $c\bar{c}$ pair splitting after and before the multiple scattering with the nucleus. The pair production cross-section

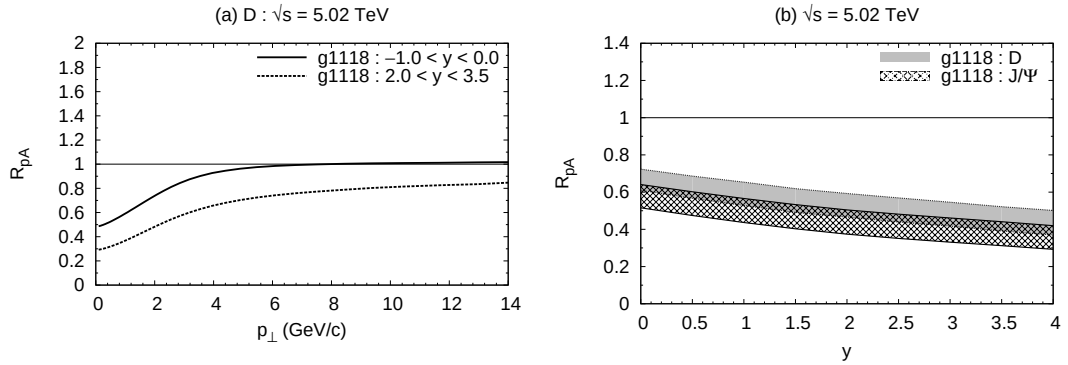

Figure 1.25 Nuclear modification factor R_{pA} as a function of (left) transverse momentum $p_\perp$ and (right) rapidity y for D mesons and J/ψ mesons. The figure is taken from Ref. [125].

in pA collisions is given as[124-125]

$$\frac{\mathrm{d}\sigma_{q\bar{q}}}{\mathrm{d}^2p_{q\perp}\mathrm{d}^2p_{\bar{q}\perp}\mathrm{d}y_q\mathrm{d}y_{\bar{q}}} = \frac{\alpha_S^2}{16\pi^2 C_F}\int\frac{\mathrm{d}^2k_\perp}{(2\pi)^2}\frac{\Xi_{\mathrm{coll}}\left(\boldsymbol{k}_{2\perp},\boldsymbol{k}_\perp\right)}{k_{2\perp}^2}x_1G\left(x_1,\mu\right)\phi_{A,x_2}^{q\bar{q},g}\left(\boldsymbol{k}_{2\perp},\boldsymbol{k}_\perp\right)\,, \tag{1.34}$$

where $p_\perp$ and $k_\perp$ denote the transverse momentum of quarks and gluons respectively, $C_F = (N_c^2-1)/(2N_c)$, Ξ_{coll} is the relevant hard matrix element, $xG(x,\mu)$ is the collinear gluon distribution function with the factorisation scale μ, and $\phi_{A,x_2}^{q\bar{q},g}$ is the tree-point function of the nucleus. The single heavy quark production is then derived by integrating over the anti-quark phase space.

$$\frac{\mathrm{d}\sigma_q}{\mathrm{d}^2p_{q\perp}\mathrm{d}y_q} = \int\mathrm{d}^2p_{\bar{q}}\mathrm{d}y_{\bar{q}}\frac{\mathrm{d}\sigma_{q\bar{q}}}{\mathrm{d}^2p_{q\perp}\mathrm{d}^2p_{\bar{q}\perp}\mathrm{d}y_q\mathrm{d}y_{\bar{q}}}\,. \tag{1.35}$$

And the heavy meson production cross-section can be obtained by convoluting the quark cross-section with the fragmentation function

$$\frac{\mathrm{d}\sigma_h}{\mathrm{d}^2p_{h\perp}\mathrm{d}y} = f_{q\to h}\int_{z_{\min}}^1\mathrm{d}z\frac{D_q^h(z)}{z^2}\frac{\mathrm{d}\sigma_q}{\mathrm{d}^2p_{q\perp}\mathrm{d}y_q}\,, \tag{1.36}$$

where z relates the transverse momemtum of the hadron h and quark q with $p_{h\perp} = zp_{q\perp}$. The factor $f_{q\to h}$ is the branching ratio of heavy quark q fragmenting into the meson h, which can be obtained from experimental measurements. Throughout this calculation, a main difference between pp and pA collisions is the choice for the saturation scale,

$$Q_{s,A}^2(x_0) = A^{1/3}Q_{s,p}^2(x_0)\,, \tag{1.37}$$

which will modify the calculation of $\phi_{A,x_2}^{q\bar{q},g}$. The calculated R_{pA} for D meson as a function of transverse momentum $p_\perp$ and rapidity y is shown in Fig. 1.25. A suppression compared to unity is also predicted at forward rapidity, which corresponds to small x regions. This

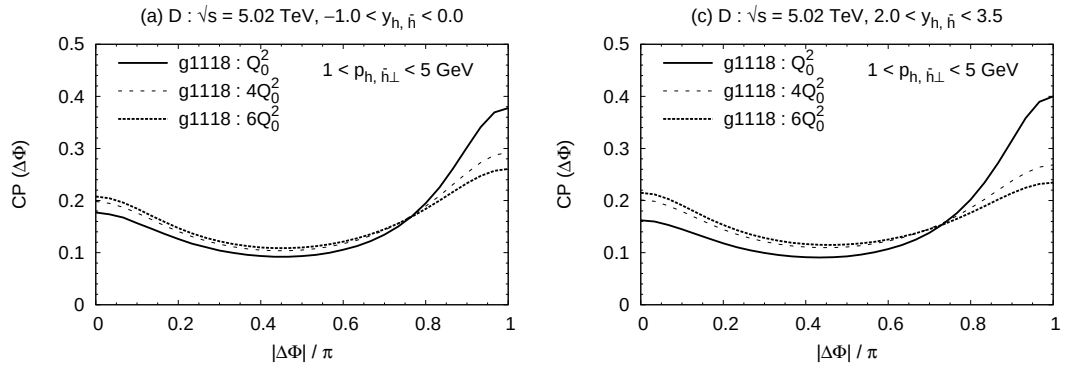

Figure 1.26 Nuclear modification of the azimuthal correlation of $D^0\overline{D}^0$ pair production in pA collsions. The figure is taken from Ref. [125].

calculation presents a more suppressed J/ψ production, which originates from the multiple scatterings of the produced $c\bar{c}$ pairs with the gluons in the target.

Some theories, for instance Refs. [101,125], also predict the particle correlation for heavy-quark pairs. The azimuthal correlation between opposite sign $D^0\overline{D}^0$ pairs $|\Delta\Phi|$ ($D^0\overline{D}^0$) are calculated by the CGC calculation for both pp and pA. Its nuclear modification is shown in Fig. 1.26. A gradually suppressed away-side ($|\Delta\Phi| \sim \pi$) peak is predicted with the increasing saturation scale in nuclei, as a consequence of the enhanced multiple scatterings and saturation effects in heavy nuclei. Corresponding measurements on (open-) charm pair productions are also conducted with the LHCb pp and pPb data [126-127].

The theoretical models introduced above describe the hadronisation ($q \to h$) with the fragmentation function $D(z)$, where its form is often parametrised with

$$D_q^h = (\alpha + 1)(\alpha + 2)z^\alpha(1 - z)\,. \tag{1.38}$$

In small collision systems, the fragmetation mechanism is assumed to dominate the hadronisation, while the quark coalescence is considered as the signature of the QGP in AA collisions. Experimental results on strange[128] and exotic[129-130] heavy-flavour particles indicate that hadronisation mechanism other than parton fragemetation in the high-multiplicity pp or pPb events. Measurements of the baryon-to-meson ratio, for instance Λ_c^+/D^0 ratio[131] will significantly improve the knowledge of hadronisation in small systems. The heavy-flavour hadron v_n can also be modified from quark coalescence as shown in Eq. 1.25.

1.2 Experimental overview

There have been many experimental facilities that aim to study nuclear physics with data collected from heavy-ion collisions. These facilities include the Super Proton Synchrotron (SPS) and Large Hadron Collider (LHC) at European Organisation for Nuclear Research (CERN), and Relativistic Heavy Ion Collider (RHIC) at Brookhaven National Laboratory (BNL). The SPS is a fixed-target experiment that mainly collects pp, pA and AA data. The choices for heavy-nuclei beam can be O, S and Pb for heavy-ion collisions at $\sqrt{s_{\mathrm{NN}}} \sim 10\,\mathrm{GeV}$. The RHIC collects pp, dAu, CuCu, AuAu and UU data, and the energy can reach up to $\sqrt{s_{\mathrm{NN}}} = 200\,\mathrm{GeV}$. The energy scan can also be performed at RHIC by changing the $\sqrt{s_{\mathrm{NN}}}$ below $20\,\mathrm{GeV}/c$, which can serve for the search of the critical point of the QCD phase diagram, as shown in Fig. 1.6. The LHC can accelerate the beams up to $\sqrt{s} = 13\,\mathrm{TeV}$ for pp collisions, $\sqrt{s_{\mathrm{NN}}} = 8.16\,\mathrm{TeV}$ for pPb collisions and $\sqrt{s_{\mathrm{NN}}} = 5.02\,\mathrm{TeV}$ for PbPb collisions till now. The fixed target experiments can also be performed with the LHCb detector[132-133], where the inert gases act as target nuclei. This section will review some selected recent results with the pPb data from the LHC, which is closely related to the motivation of studying the cold and possible hot nuclear matter effects in the pPb collisions of this thesis.

1.2.1 Heavy-flavour production in pPb collisions

The LHCb experiment has provided precise measurements with pPb data at $\sqrt{s_{\mathrm{NN}}} =$ 5.02 TeV and 8.16 TeV at forward and backward rapidity, especially for heavy-flavour particles. The production cross-section of J/ψ, $\psi(2S)$ and Υ mesons were first measured at $\sqrt{s_{\mathrm{NN}}} = 5.02\,\mathrm{TeV}$ [123,134-135]. The nuclear modification factor $R_{p\mathrm{Pb}}$ of prompt and nonprompt J/ψ mesons was measured in Ref. [134] as a function of y. The result with updated reference of J/ψ production cross-section at $\sqrt{s} = 5.02\,\mathrm{TeV}$ in pp [136] is shown in Fig. 1.27. A significant suppression is observed at forward (positive) rapidity, which is also reproduced by calculations incorporating nPDF models[70,137] as well as the FCEL prediction[138]. The results are limited by the large uncertainties especially at backward (negative) rapidity, so new measurements with improved statistics are implemented with data at $\sqrt{s_{\mathrm{NN}}} = 8.16\,\mathrm{TeV}$[139]. For the forward rapidity, $R_{p\mathrm{Pb}}$ of prompt J/ψ mesons shows a rising trend versus p_{T} and the suppression is weakened at high p_{T} as shown in Fig. 1.28. While the data points at backward rapidity is consistent with unity except for low-p_{T} regions. The results show good agreement between 5.02 TeV and 8.16 TeV results

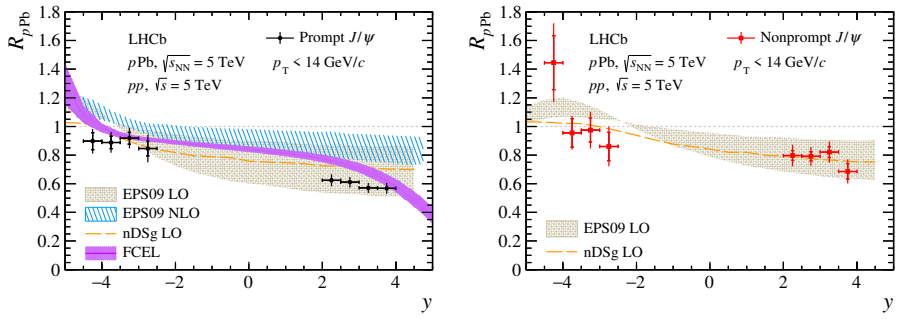

Figure 1.27 Nuclear modification factor $R_{p\mathrm{Pb}}$ as a function of rapidity y for (left) prompt and (right) nonprompt J/ψ mesons at $\sqrt{s_{\mathrm{NN}}} = 5.02\,\mathrm{TeV}$. The error bars represent the quadric sum of the statistical and systematic uncertainties. The figures are taken from Ref. [136].

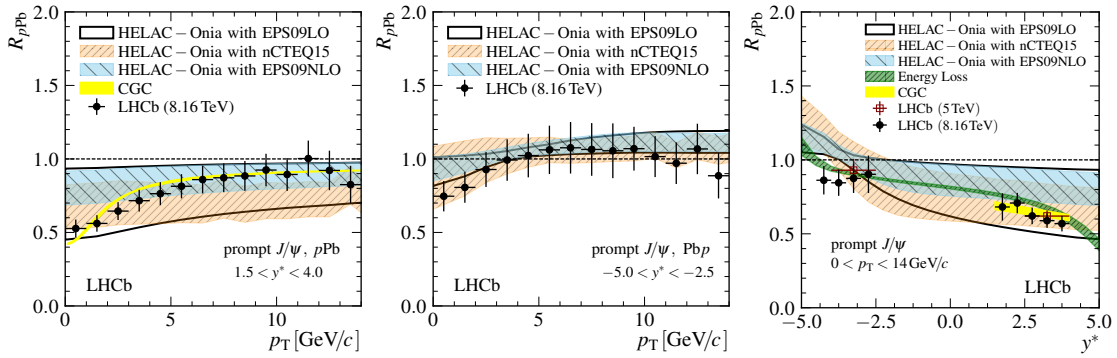

Figure 1.28 Nuclear modification factor $R_{p\mathrm{Pb}}$ of prompt J/ψ mesons (left and middle) as a function of transverse momentum p_{T}, and (right) as a function of rapidity y at $\sqrt{s_{\mathrm{NN}}} = 8.16\,\mathrm{TeV}$. The error bars represent the quadric sum of the statistical and systematic uncertainties. The figures are taken from Ref. [139].

and the theoretical calculations of nPDFs and CGC are also consistent with the measurements. The production of nonprompt J/ψ mesons is expected to be different from prompt components, but similar to B-hadrons. Thus, a comparison between nonprompt J/ψ and B^+ $R_{p\mathrm{Pb}}$[140] has been made in Fig. 1.29. This figure shows good agreement between two particles, and agreement with nPDF calculations. Both two particles indicate a suppression at forward rapidity, while an agreement with unity is found for backward rapidity.

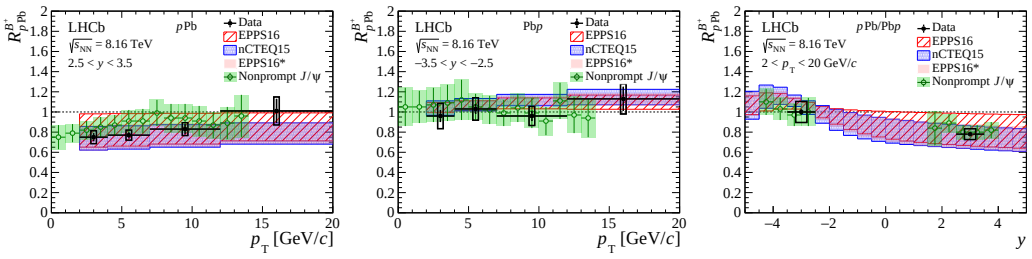

Figure 1.29 Nuclear modification factor $R_{p\mathrm{Pb}}$of B^+ and nonprompt J/ψ mesons (left and middle) as a function of transverse momentum p_{T}, and (right) as a function of rapidity y at $\sqrt{s_{\mathrm{NN}}} = 8.16\,\mathrm{TeV}$. The error bar represent the statistical uncertainties and boxes represent the quadric sum of the statistical and systematic uncertainties. The figures are taken from Ref. [140].

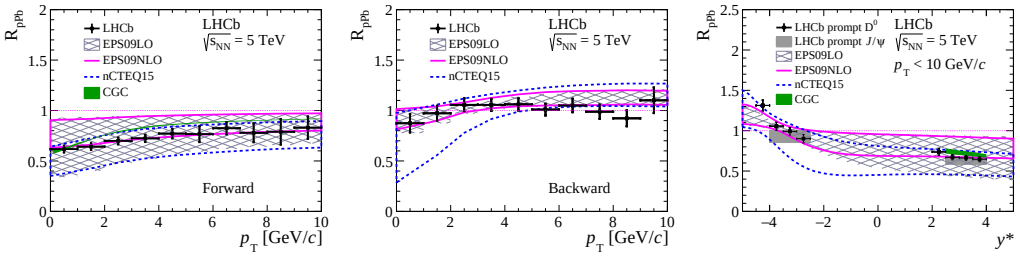

Figure 1.30 Nuclear modification factor $R_{p\mathrm{Pb}}$ of prompt D^0 mesons (left and middle) as a function of transverse momentum p_T, and (right) as a function of rapidity y at $\sqrt{s_\mathrm{NN}} = 5.02\,\mathrm{TeV}$. The error bars represent the quadric sum of the statistical and systematic uncertainties. The figures are taken from Ref. [123].

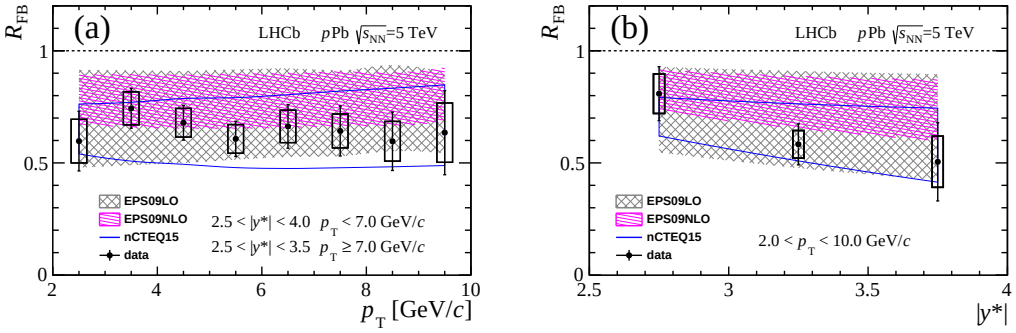

Figure 1.31 Forward-backward production ratio R_FB of prompt Λ_c^+ baryons as a function of (left) p_T and (right) y. The error bars represent the quadric sum of statistical and systematic uncertainties and the boxes represent the systematic uncertainties. The figures are taken from Ref. [131].

The prompt D^0 [123] and Λ_c^+ [131] production are also measured with pPb collision data at $\sqrt{s_\mathrm{NN}} = 5.02\,\mathrm{TeV}$. $R_{p\mathrm{Pb}}(D^0)$ versus p_T and y are shown in Fig. 1.30. The results show similar shape with $R_{p\mathrm{Pb}}$ of prompt J/ψ mesons, and agree with theoretical calculations. It is remarkable that the uncertainty of this measurement is much smaller than the error band of the theoretical calculations [70,81], where the dominate uncertainty of the calculation originates from the nPDFs. So this result is used as the input for the parametrisation of nPDFs, which has greatly reduced the uncertainty of the nPDFs both in the shadowing and anti-shadowing regions [83,85,141] as described in Sec. 1.1.7. Due to the absence of the production cross-section of the prompt Λ_c^+ baryons in pp collisions, the forward-backward production ratio R_FB is presented instead of $R_{p\mathrm{Pb}}(\Lambda_c^+)$. The result in Fig. 1.31 suggests significant production asymmetry between forward and backward rapidities. The main results from this measurement is the prompt Λ_c^+-over-D^0 production ratio $R_{\Lambda_c^+/D^0}$. The measured ratio presented in Fig. 1.32 corresponds to a value of ~ 0.3, which agrees with the nPDF predictions [70,81] but deviates from the ALICE result at midrapidity [142]. Neglecting the large uncertainties, this discrepancy may originate from the different particle

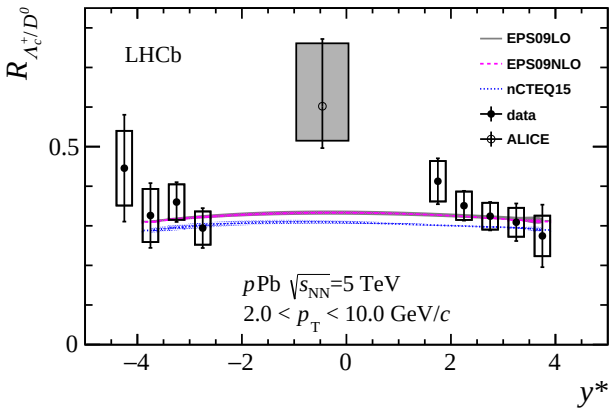

Figure 1.32 Prompt Λ_c^+-over-D^0 production ratio $R_{\Lambda_c^+/D^0}$ as a function of y. The error bars represent the quadric sum of statistical and systematic uncertainties and the boxes represent the systematic uncertainties. The figure is taken from Ref. [131].

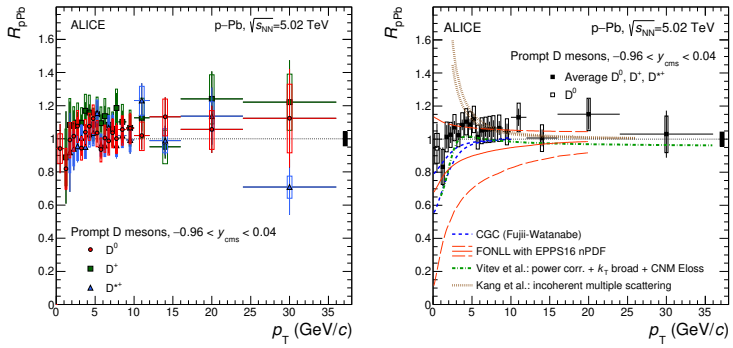

Figure 1.33 Nuclear modification factor $R_{p\mathrm{Pb}}$ of (left) non-strange D^0,D^+,D^* mesons and (right) the average value as a function of p_T at midrapidity. The error bars represent the statistical uncertainties, the boxes represent the systematic uncertainties and the black-filled box at $R_{p\mathrm{Pb}} = 1$ represents the normalisation uncertainty. The figures are taken from Ref. [146].

multiplicities between forward and mid rapidities.

The measurements of prompt D-meson production at midrapidity are also performed by the ALICE experiment [143-146]. Fig. 1.33 shows the $R_{p\mathrm{Pb}}$ results of prompt D^0, D^+, D^* mesons. An consistence with unity is suggested, where the strong enhancement below 4 GeV/c predicted by the incoherent multiple scattering[104] is not seen.

1.2.2 Collective flow in small systems

The collective flow and flow parameters have been defined above in Eq. 1.24, where the direction of the reaction plane in the laboratory Ψ_{RP} remains unknown. Mathematically, Ψ_{RP} of an event can be determined with the harmonics of the flow as

$$\Psi_{\mathrm{RP}}^{(n)} = \frac{1}{n}\left(\arctan\frac{\sum_i w_i \sin n\phi_i}{\sum_i w_i \cos n\phi_i}\right), \tag{1.39}$$

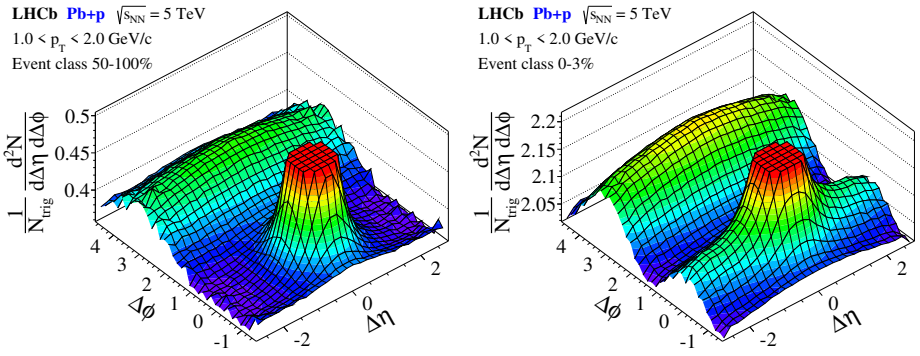

Figure 1.34 Two-particle correlation functions of charged particles (p,K,π) at backward rapidity in the (left) low and (right) high-multiplicity events. The figures are taken from Ref. [114].

where summation goes over the particles in this event and the w_i is the weight of ith particle. Nevertheless, this relation holds only if the anisotropic flow dominates the particle angular distribution, and a good resolution of angle is needed. The event plane detector[147], which has been equipped in both forward and backward direction of the STAR experiment, is designed to measure the azimuthal patterns of emitted particles and determines the direction of the reaction plane for each event with this method.

This method is infeasible for single-arm detectors, where the acceptance does not cover a solid angle of 2π, or in small collision systems, where the reaction plane is hard to define. The *multiple-particle correlation* method can be adopted to overcome the difficulty[148]. Take the two particle correlation function for instance. The equation holds that

$$\left\langle e^{in(\phi_1-\phi_2)}\right\rangle_{D_1\times D_2} = v_n(D_1)v_n(D_2) + \left\langle e^{in(\phi_1-\phi_2)}\right\rangle_c \ . \tag{1.40}$$

The second term on the right hand represents the *non-flow correlation*, corresponding to an order of $\mathcal{O}(1/N)$ where N is the number of the particles in an event. This method is also called *cumulant* and the correlation can be extended to more particles, where non-flow contribution can be significantly suppressed[149-150].

The two-particle correlation function in Eq. 1.40 can be written in another form as

$$\frac{\mathrm{d}N_{\mathrm{pair}}}{\mathrm{d}\Delta\phi} \propto \left(1 + \sum_{n=1}^{\infty} 2v_n^2 \cos n\Delta\phi\right) . \tag{1.41}$$

The measured v_n^2 with this method also inevitably contains non-flow contribution. The contribution can be observed in the two-dimensional correlation function $\frac{1}{N_{\mathrm{trigger}}}\frac{\mathrm{d}^2N_{\mathrm{pair}}}{\Delta\eta\Delta\phi}$, as shown in Fig. 1.34. There are several prominent structures in the correlation functions.

- Near-side peak (jet peak, short-range correlation) at ($\Delta\eta \sim 0, \Delta\phi \sim 0$). The jet peak is induced by the particles produced in the same jet-like process as shown in

Fig. 1.19. Thus, the appearance of the peak do not depend on collision systems and will be enhanced with increasing p_{T} of trigger particles. It always dominates the correlation functions so they are truncated in Fig. 1.34.

- Near-side ridge (ridge, long-range correlation) at ($|\Delta\eta| \gtrsim 1.5, \Delta\phi \sim 0$). As mentioned above, the existence of the long-range correlation indicates the v_2 of of the particle, which has been observed in AA collisions[151-152]. This statement can be explained by projecting the correlation function to the $\Delta\eta$ axis. Then the ridge will account for a non-zero v_2 in Eq. 1.41. A prominent difference between the two panels in Fig. 1.34 is the existence of the ridge in the right panel, indicating that only high-multiplicity pPb events show similar behaviours with events in PbPb collisions.
- Away-side ridge at ($\Delta\phi \sim \pi$). This away-side ridge can be attribute to the momentum conservation in the collisions. The sum of the particle p_{T} will remains zero in both laboratory and centre-of-mass frames. Two particles in back-to-back jets respectively will have $\Delta\phi \sim \pi$ while $\Delta\eta$ can be of any value. Thus the away-side ridge can be observed in all measured $\Delta\eta$ range.

By integrating over the long-range regions, the dominate non-flow contribution can be excluded. The obtained $\frac{\mathrm{d}N}{\mathrm{d}\Delta\phi}$ in Ref. [114] is shown in Fig. 1.35. The baselines of correlation functions are shifted to zero with zero-yield-at-minimum (ZYAM) method[153-154]. The ridge is observed for both forward and backward rapidities and its strength significantly increases with event activities.

There exist other more non-flow contributions in addition to the jet peak. The Bose-Einstein correlation, the correlation between two particles short-time resonance decays (*e.g.* $\Delta \rightarrow p\pi$), will influence the measured correlation function[155]. The electromagnetic and strong interactions between particles can also give slight modification to the correlation. Ref. [156] summarise the methods to deal with the non-flow subtraction, which will be discussed afterwards.

This method can also be adopted to measure the flow of identified particles, where Eq. 1.41 can be modified as

$$\frac{\mathrm{d}N^{ab}_{\mathrm{pair}}}{\mathrm{d}\Delta\phi} \propto \left(1 + \sum_{n=1}^{\infty} 2v_n^a v_n^b \cos n\Delta\phi\right) . \tag{1.42}$$

The v_2 of strange and charm particles is measured with this method by CMS experiment in pPb collisions[157] at $\sqrt{s_{\mathrm{NN}}} = 8.16\,\mathrm{TeV}$, and the non-flow contributions are further

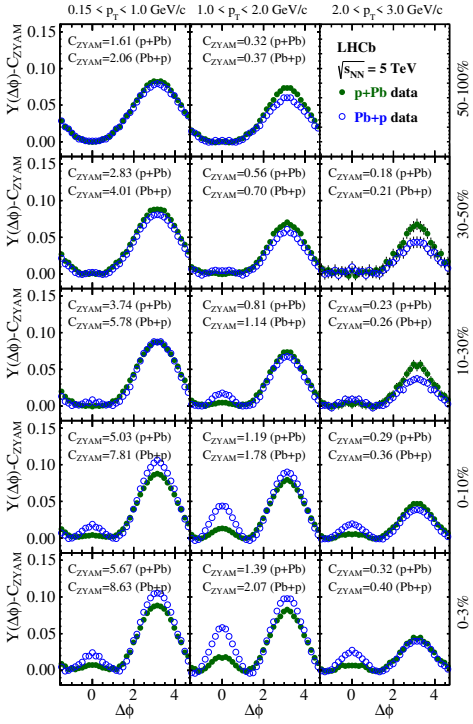

Figure 1.35 One-dimensional correlation function as a function of $\Delta\phi$ in long-range regions ($2 < |\Delta\eta| < 2.8$). All kinematic intervals, event activities and both forward and backward rapidities are included. The figures are taken from Ref. [114].

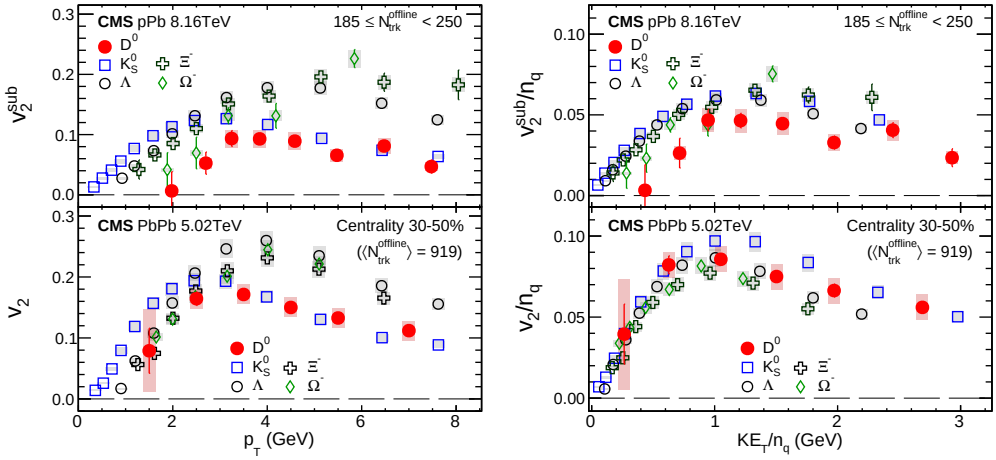

Figure 1.36 Left: v_2^{sub} as a function of p_{T} for D^0 mesons and strange hadrons in (top) high-multiplicity pPb events at $\sqrt{s_{\text{NN}}} = 8.16\,\text{TeV}$ and (bottom) non-central PbPb events at $\sqrt{s_{\text{NN}}} = 5.02\,\text{TeV}$. Right: v_2^{sub}/n_q as a function of transverse kinetic energy per constituent quark KE_{T}/n_q. The figures are taken from Ref. [157].

subtracted to get v_2^{sub}. The results are shown in Fig. 1.36 and are compared to v_2 from PbPb collisions at $\sqrt{s_{\text{NN}}} = 5.02\,\text{TeV}$[158-159]. Significant positive v_2 of strange and charm hadrons is observed in high-multiplicity pPb events which shares similar trend versus p_{T} with non-central PbPb events. To compared with the Eq. 1.25 from the coalescence model, the n_q scaled v_2 as a function of transverse kinetic energy per constituent quark KE_{T}/n_q

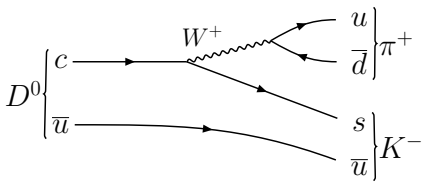

Figure 1.37 Feynman diagram of $D^0 \to K^-\pi^+$ decay.

is also derived, where $KE_{\mathrm{T}} = M_{\mathrm{T}} - m$. A broken v_2/n_q scaling is found for D^0 mesons, indicating a weaker collective behaviour of charm quarks compared to light quarks in small systems.

1.3 Motivation for this thesis

This thesis will focus on studying the cold and hot nuclear matter effects experimentally in pPb collisions. The probe selected in this thesis is the D^0 meson, which is the most produced heavy-flavour particle in the collisions. The properties of the D^0 meson is described in detail in PDG2022[23]. It has a mass of $m_0 = (1864.48 \pm 0.05)\,\mathrm{GeV}/c^2$, a lifetime of $\tau = (0.4103 \pm 0.0010)\,\mathrm{ps}$ and quantum numbers of $I(J^P) = \frac{1}{2}(0^-)$. The valence quarks of the D^0 meson is $c\bar{u}$, and one of the most frequently used decay channel for D^0 reconstruction is $D^0 \to K^-\pi^+$, of which the Feynman diagram is shown in Fig. 1.37. It is a Cabbibo-favoured weak decay having a branching fraction of $(3.947 \pm 0.030)\%$. The final-state K,π particles are all long-lived charged hadrons, which are convenient for full reconstruction.

The first part of the thesis is the measurements on the D^0 production cross-section and $R_{p\mathrm{Pb}}$ in pPb collisions at $\sqrt{s_{\mathrm{NN}}} = 8.16\,\mathrm{TeV}$. Compared to other experiments, the LHCb detector have clear advantages in measurements of heavy-flavour production, and also provide good separation between prompt and secondary particles. For the D^0 mesons, it can been seen from Fig. 1.38 that the LHCb detector can achieve an excellent signal purity. This is also evident from the measured $R_{p\mathrm{Pb}}$ results in Fig. 1.30 and 1.33. The heavy-ion experiments in LHCb detector also have unique kinematic coverage, as shown in Fig. 1.39. Compared to pPb data at $\sqrt{s_{\mathrm{NN}}} = 5.02\,\mathrm{TeV}$, the 8.16 TeV data will have $\sim$ 20 times of statistics. This will hopefully help to provide a better constraint on the nPDF models. With the increasing energy, the measurement can reach a more smaller x down to $\sim 10^{-6}$, where possible gluon saturation is also expected to occur[160]. It is also worth investigating whether final-state effects exists in the heavy-flavour production

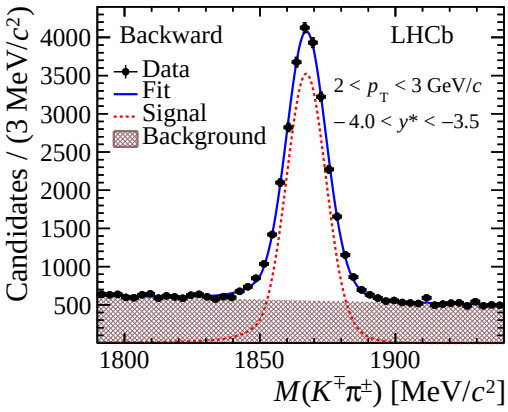

Figure 1.38 Invariant-mass distribution of D^0 mesons in pPb collisions at $\sqrt{s_{\rm NN}} = 5.02$ TeV from LHCb detector. The left figure is taken from Ref. [123] .

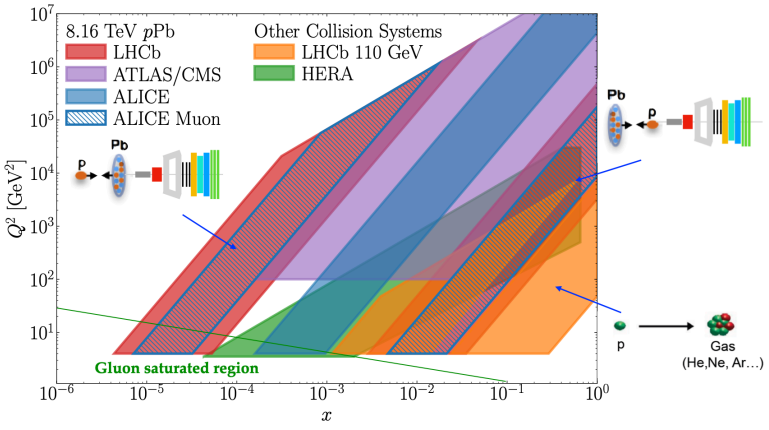

Figure 1.39 Kinematic coverage in (x, Q^2) space of different heavy-ion experiments. For the LHCb detector, both forward and backward pPb data and fixed-target data are included.

in small systems, using the data set with high statistics.

The study of collective flow of D^0 mesons offer insights into the underlying QGP formation or hot nuclear matter effects in pPb collisions. Though more and more similarities between high-multiplicity pPb and PbPb collisions are found, such as the observed large elliptic flow described above as well as the evidence of the strangeness enhancement[128] and the quark coalescence[129-130], it is still under discussion whether these phenomena are related to the QGP[115,117-118,161-162], as the hard probe *jet quenching* has never been observed in small systems and the measurement is rather difficult to perform. Current results on collective flow focused on the midrapidity region, so it is essential improve the knowledge in forward regions (both forward and backward rapidities). The second part of the thesis will measure the D^0 collective flow at forward rapidities in small system, which will be among the first flow measurements with LHCb data.

CHAPTER 2 LHCB EXPERIMENT

The Large Hadron Collider beauty (LHCb) detector[132-133] is a high-precision detector designed for studying particles containing charm and beauty quarks. Its primary motivation is to explore the new physics beyond the SM indirectly, by providing precise measurements on *CP* violation and searching for very rare decays. Due to its strong capabilities in particle and vertex reconstruction, the LHCb experiment has now become a general-purposed program. It has made great contributions to various fields, including hadron spectroscopy, heavy-ion physics, electroweak physics, *etc.*

2.1 Large Hadron Collider

The Large Hadron Collider (LHC)[163] is a two-ring superconducting hadron accelerator and collider located at CERN near Geneva. It is the most powerful accelerator in the world and has been the most important facility for the experimental particle physics. The predecessor of the LHC was the Large Electron-Positron Collider (LEP). In 2000, the LEP was closed and its tunnel was used by the LHC. The structure of the LHC is illustrated in Fig. 2.1. Protons are first obtained from hydrogen atoms that stored in a bottle, and then accelerated to 50 MeV by LINAC2 and injected into proton synchrotron booster (PSB). Afterwards protons experience successive accelerations, first to 1.4 GeV by PSB, to 45 GeV by proton synchrotron, and to 450 GeV by SPS. Finally, proton beam is transferred to the 26.7 km-circumference LHC in two opposite directions. The energy of protons is designed to be 7 TeV at most, corresponding to $\sqrt{s} = 14$ TeV. Each proton beam has a large number of bunches (2808) with a bunch spacing of 25 ns, where each bunch contains 10^{11} protons. The peak instantaneous luminosity can reach $\mathcal{L} = 10^{34}\,\mathrm{cm}^{-2}\mathrm{s}^{-1}$, which results in a high possibility for the processes of interest.

This facility can also be used to accelerate lead ions. The lead atoms will first be ionised by an electron current to around Pb^{29+}, and accelerated to 4.2 MeV per nucleon. Then the ions will be stripped to Pb^{54+} and accelerated to 72 MeV per nucleon in the low energy ion ring (LEIR). The ions will experience further acceleration and ionisation, and finally reach an energy of 2.56 TeV per nucleon in the LHC.

There are four main experiments at the LHC. The ATLAS[165] and CMS[166] experiments, which take data with the highest luminosity, are two general-purposed experiments

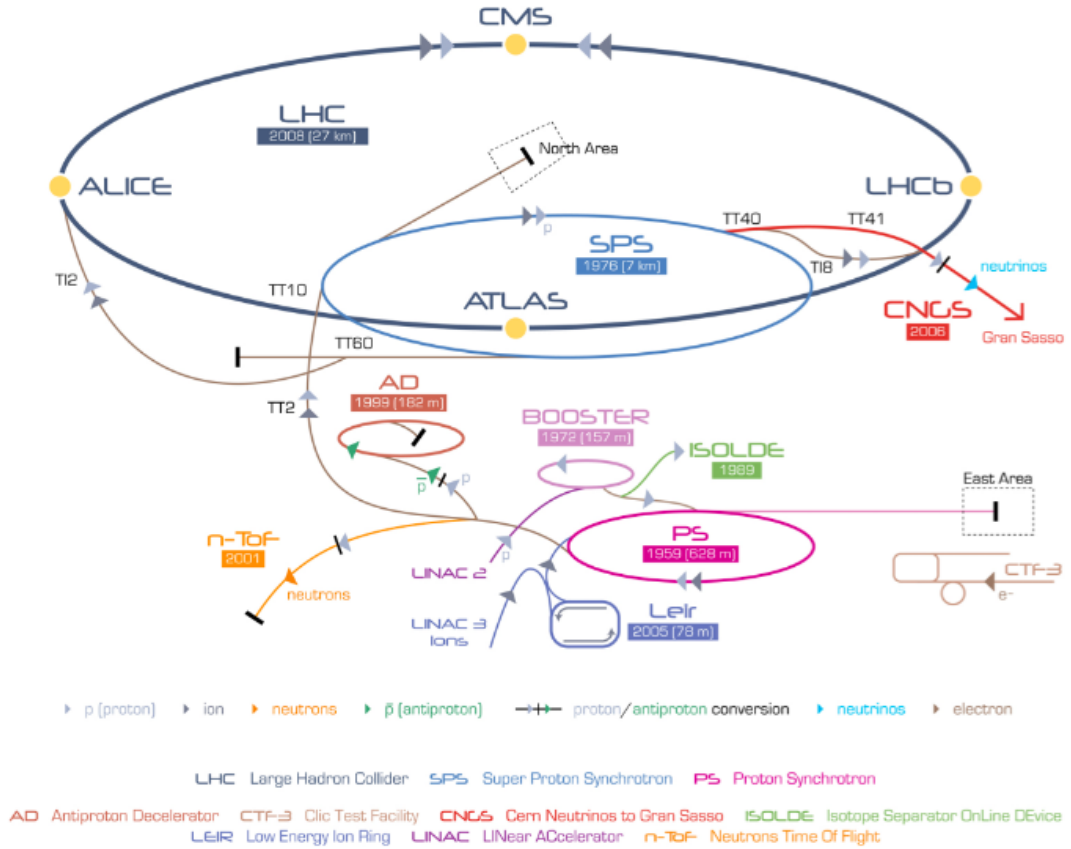

Figure 2.1 Sketch of the CERN accelerator complex and the experiments at the LHC. The figure is taken from Ref. [164].

and have made great contributions to the observation of the Higgs boson[17-18]. The LHCb detector[132], is designed for studying heavy-flavour particles. It aims at a peak instantaneous luminosity of $\mathcal{L} = 10^{32}\,\mathrm{cm}^{-2}\mathrm{s}^{-1}$. The ALICE experiment is a dedicated heavy-ion experiments, taking data at a luminosity of $\mathcal{L} = 10^{-27}\,\mathrm{cm}^{-2}\mathrm{s}^{-1}$ for nominal PbPb operations. There were also two smaller experiments, the LHCf experiment[167] which aims to calibrate the hadron interaction models for Extremely High-Energy Cosmic-Rays, and the TOTEM experiment[168] which focuses on the measurement of the total pp cross-section and the investigation of the elastic and diffractive pp scattering.

The LHC first produced the pp collisions at $\sqrt{s} = 0.9\,\mathrm{TeV}$ in November 2009. From 2010, the LHC started its Run1 operation for pp collisions at $\sqrt{s} = 7\,\mathrm{TeV}$ in 2010 and 2011, and $\sqrt{s} = 8\,\mathrm{TeV}$ in 2012 and 2013. The heavy-ion data of PbPb collisions at $\sqrt{s_{\mathrm{NN}}} = 2.76\,\mathrm{TeV}$ were also produced in 2012 and 2013. In early 2013, the LHC started to run pPb collisions at $\sqrt{s_{\mathrm{NN}}} = 5.02\,\mathrm{TeV}$, when the LHCb experiment also started to collect heavy-ion data. After Run1, the LHC went into a long shutdown (LS1) in order to increase the beam energy and instantaneous luminosity. The following Run2 operation started in 2015 and finished in 2018, which mainly collected pp data at $\sqrt{s} = 13\,\mathrm{TeV}$. Another pp

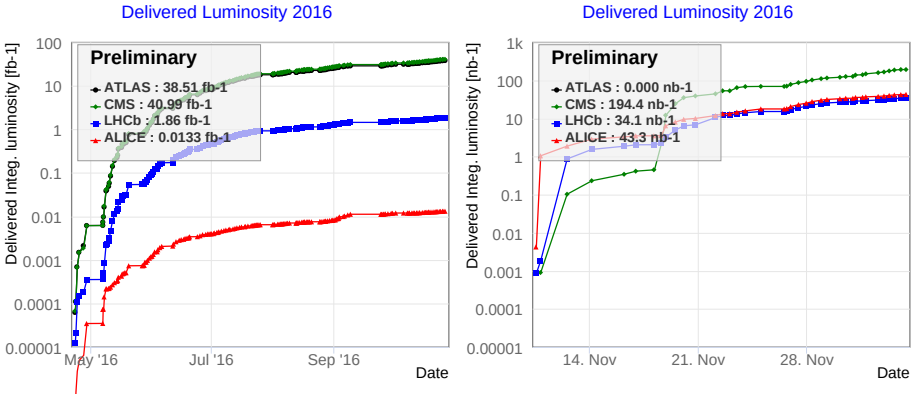

Figure 2.2 Delivered integrated luminosity for ALICE, CMS, LHCb, ALICE experiments in 2016, for both (left) proton runs and (right) ion runs. The figure is taken from Ref. [169].

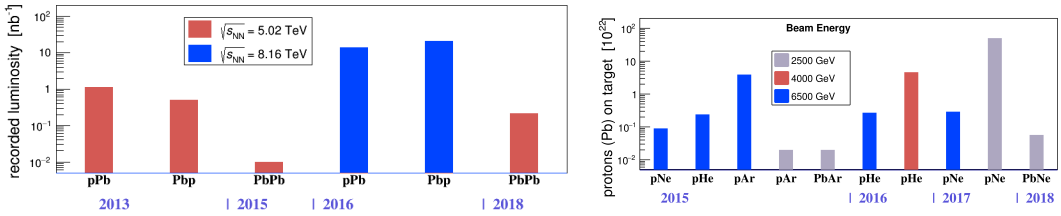

Figure 2.3 Summary of LHCb heavy-ion data from (left) collider mode and (right) fixed-target configurations during Run1 and Run2. pPb and Pbp refer to the data collected in forward and backward configurations, respectively.

sample at $\sqrt{s_{\rm NN}} = 5.02\,\text{TeV}$ was also recorded in order to provide reference for heavy-ion collisions. For heavy-ion collisions in Run2, both PbPb data at $\sqrt{s_{\rm NN}} = 5.02\,\text{TeV}$ and pPb data at $\sqrt{s_{\rm NN}} = 8.16\,\text{TeV}$ were recorded. The delivered integrated luminosities for p and Pb beams with time in 2016 are shown in Fig. 2.2. During Run2, the LHCb detector collected both the pPb and PbPb data. The LHCb heavy-ion data samples are summarised in Fig. 2.3, where data from fixed-target experiments are also included.

2.2 LHCb Detector

The LHCb detector is a single-arm spectrometer dedicated to heavy-flavour physics. It covers the forward region of 15 mrad to 300 (250) mrad in horizontal (vertical) plane, corresponding to a pseudorapidity range of approximately $2 < \eta < 5$. With this design, the LHCb detector can ideally accept 25% of the produced $b\bar{b}$ pairs with only 1.8% solid angle coverage, according to the simulation shown in Fig. 2.4.

The layout of the LHCb detector in Run1 and Run2 is presented in Fig. 2.5. It contains a vertex locator (VELO), two ring imaging Cherenkov detectors (RICH1 and RICH2), a tracker turicensis (TT), the dipole magnet, three tracking stations (T-stations, T1-T3), five muon stations (M1-M5), a scintillation-pad detector (SPD), a pre-shower (PS), an electro-

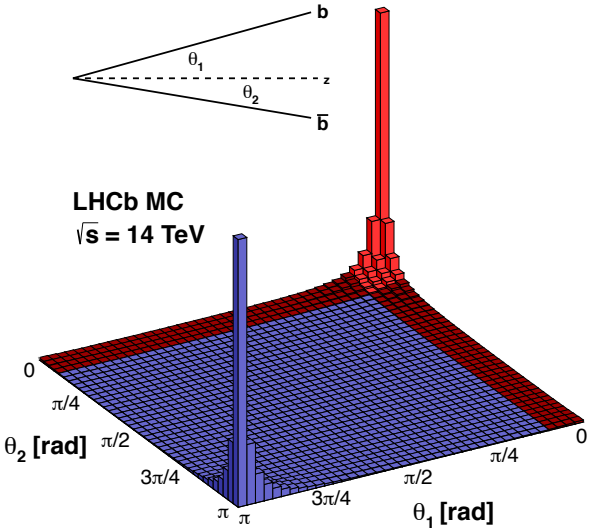

Figure 2.4 Angular distribution of $b\bar{b}$ pairs in pp collisions at $\sqrt{s}$ =14 TeV, obtained from the simulation with PYTHIA8 and CTEQ6 NLO. The figure is taken from Ref. [170].

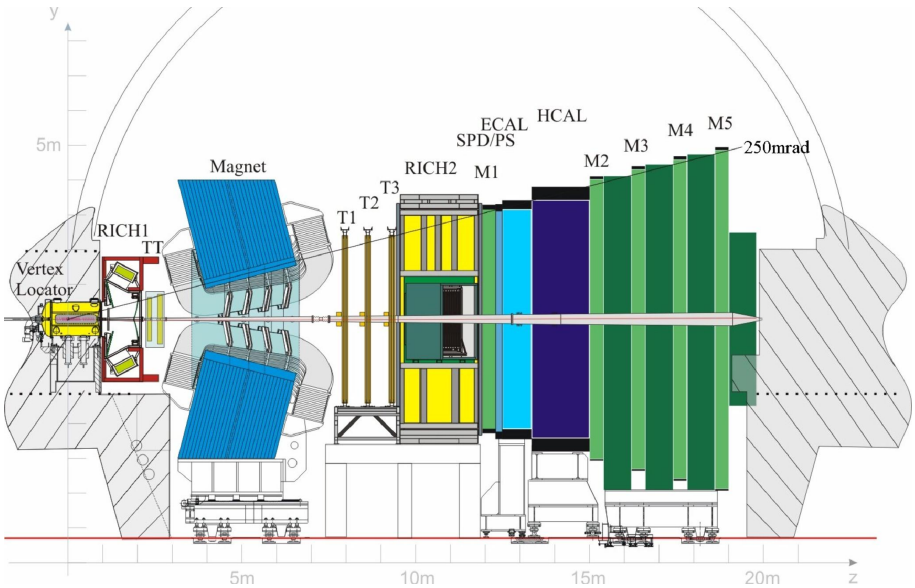

Figure 2.5 Layout of the LHCb detector. The z axis is defined as the beam direction, and x (horizontal), y (vertical) are defined to form a right-handed coordinate system. The figure is taken from Ref. [133].

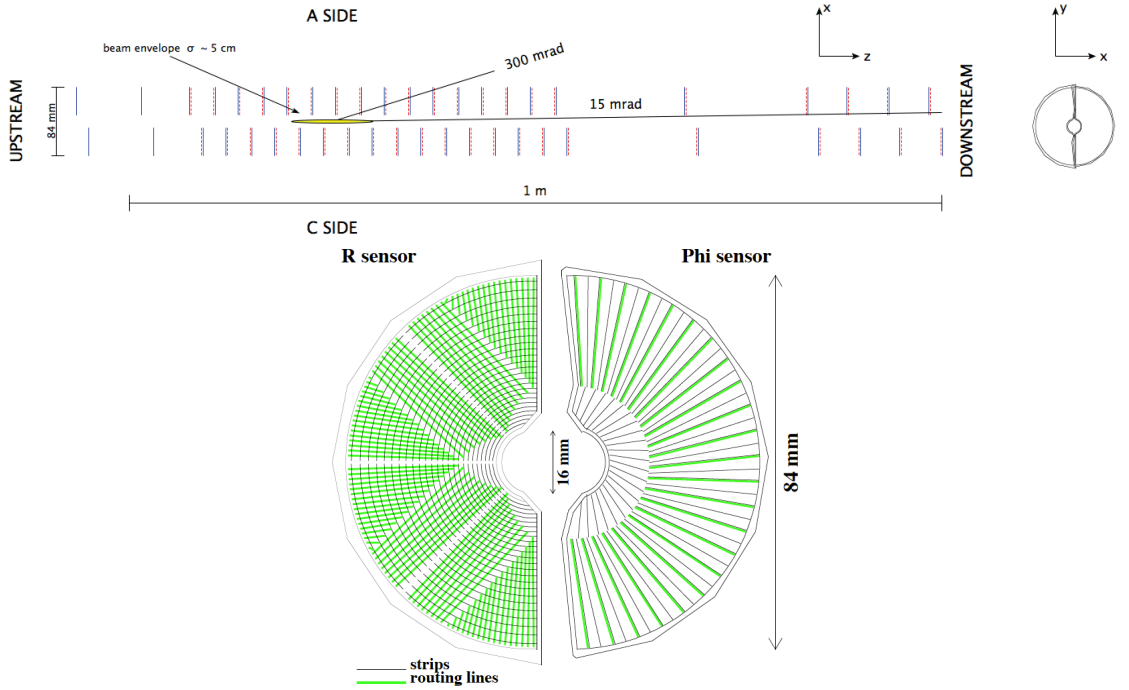

Figure 2.6 (top) Layout of the LHCb VELO at $y = 0$ in the xz plane and (bottom) of an R and Φ sensor. The figures are taken from Ref. [171].

magnetic calorimeter (ECAL), and a hadronic calorimeter (HCAL). These sub-detectors can be roughly classified into the tracking system, the particle identification (PID) system and the trigger system. These sub-detectors play important roles in reconstruction and identification of particles, and thus resulting in a high signal purity and a good resolution of mass, decay time and kinematic information.

2.2.1 Tracking system

The tracking system comprises the VELO, the four planar tracking stations TT and T1-T3 and the dipole magnet.

2.2.1.1 Vertex locator

The VELO[171] is a silicon microstrip detector located around the interaction region, as shown in the top panel of Fig. 2.6. It is placed in a vacuum vessel and uses a CO_2 cooling system. The VELO consists of 42 semi-circular silicon modules, where each contains an R sensor and a Φ sensor designed for the measurement of radial distance r and azimuthal angle respectively. The arrangement of the modules can be seen in Fig. 2.6, These sensors are arranged along and only 7 mm from the LHC beams. Due to this close distance, the two halves of the VELO have to be separated when injecting beams. After the beams get stable, the two halves are closed with a small overlap, in order to ensure a full coverage in

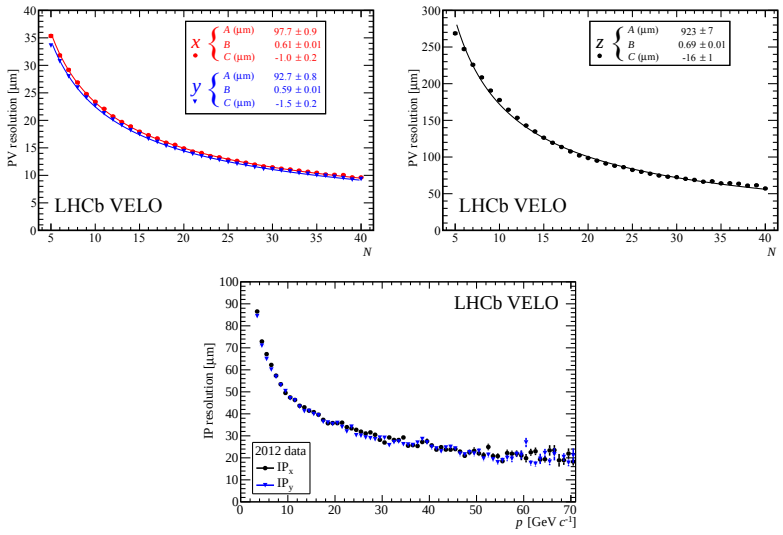

Figure 2.7 Resolution of the PV position as a function of number of tracks in (top left) x, y direction and (top right) z direction, and (bottom) the resolution of the impact parameter as a function of particle momentum. The figures are taken from Ref. [171].

azimuth. Between data-taking periods, the position of the VELO in xy plane are flexible in order to make sure that it is located at the centre of the beam interaction region.

The VELO is designed to cover the LHCb acceptance[172], that is to say, the tracks with a polar angle of $15 < \theta < 300$ mrad will leave at least three hits in the VELO stations. The VELO detector is important for the efficient reconstruction of events with multiple-track final states. It provides the direction information on tracks and can help to recognise the pattern and reject fake tracks efficiently. The vertex reconstruction is another key function of the VELO. The accuracy of the primary vertex (PV) reconstruction is first guaranteed by the small distance to the beam, which minimises the displacement before hitting the VELO. The VELO can also reconstruct tracks in backward directions in order to improve the PV reconstruction. It also provides precise reconstruction of displaced vertices, and thus can be used for the determination of flight distance and decay time of particles. This gives the LHCb detector the capability to implement lifetime measurements and time-dependent analyses, for instance, the $B_s^0 - \overline{B}_s^0$ oscillation frequency[173].

The VELO detector has been running smoothly and providing high-precision measurements since the beginning of LHCb data taking, with an average signal-to-noise ratio of about 20 : 1 and a track finding efficiency of better than 98%[171]. The resolution of the PV position varies with the event multiplicity, as shown in Fig. 2.7, within a range of $\sim 10 - 35\,\mu$m for PV_x, PV_y, and $\sim 50 - 300\,\mu$m for PV_z. The resolution of the IP, defined as the distance between the track and the PV closest to it, is also presented in Fig. 2.7, which shows a decreasing trend versus p_T. The resolution of the measured decay

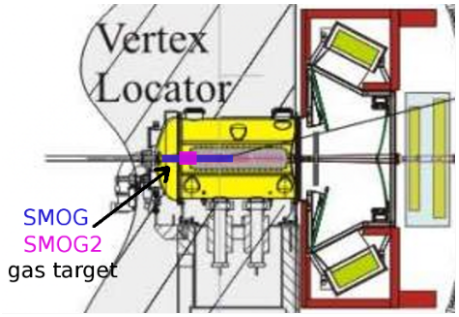

Figure 2.8 Illustration of the internal gas target in the VELO detector. The figure is taken from Ref. [174].

time is $\sim$ 50 fs, which is much smaller than the typical lifetime of ground-state charm ($\sim 200 - 1000$ fs) and beauty hadrons ($\sim$ 1500 fs).

The VELO also offers the possibility to perform beam-gas collisions in the LHC. It is achieved by placing an internal gas target in the VELO detector, which is called the *system for measuring overlap with gas* (SMOG)[174] as shown in Fig. 2.8. This system was originally designed for a precise measurement of luminosities [175-177], and it also provides unique opportunities for heavy-ion physics, cosmic ray physics and nucleon structure[174,178-179]. A large varieties of fixed-target samples, in the configuration of p/Pb beams and noble gases targets, has been collected during LHCb Run2 as summarised in Fig. 2.3.

2.2.1.2 Tracking turicensis

The TT is a p^+-on-n silicon microstrip detector, located upstream of the LHCb dipole magnet and placed in a thermally and electrically insulated detector volume with constant temperature[132]. It has four detection layers, each organised in an $(x - u - v - x)$ arrangement, where the two x strips are placed vertically, and u, v strips are rotated by a stereo angle of $\mp 5^\circ$ with respect to x strips respectively. This ensures an efficient 3D reconstruction of tracks. The layout of the third layer is shown in the left panel of Fig. 2.9. This design ensures that the sensors cover the full acceptance of the LHCb detector and the read-out hybrids are located out of the active area. The fundamental structure of the layer is the half module, which is illustrated in the right panel of Fig. 2.9. It comprises seven silicon sensors and two or three font-end hybrids. Each silicon microstrip sensor is 9.64 cm wide, 9.44 cm long and 500 µm thick. The K sectors are arranged closest to the beam while L sectors are furthest away.

The main considerations of the design including spatial resolution, hit occupancy, signal-shaping time, single-hit efficiency, radiation damage, material budget and the cost

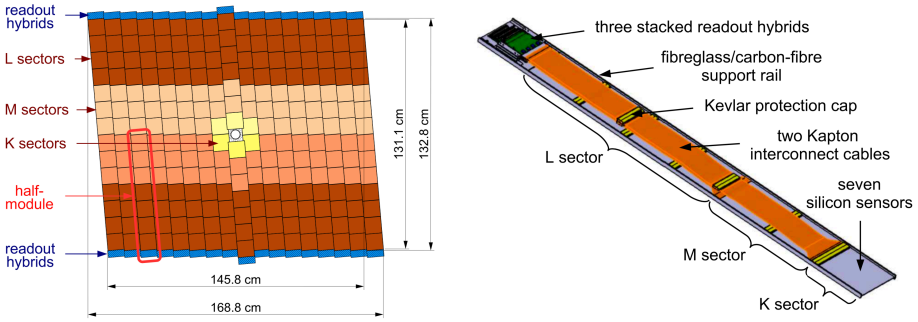

Figure 2.9 Layout of (left) the third (v) detection layer and (right) a half module (with four L sectors, two M sectors and one K sector) of the TT detector. The figures are taken from Ref. [132].

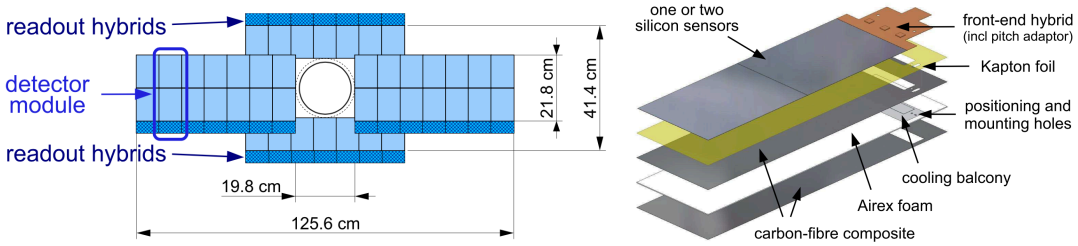

Figure 2.10 Layout of (left) the x detection layers in four detector boxes in the second IT station and (right) a two-sensor IT module. The figures are taken from Ref. [132].

of readout channels. The hit efficiency is finally measured to be greater than 97%, and the hit resolution is 53.4 µm on average.

2.2.1.3 Tracking stations

The T stations are three planar detectors located downstream of the dipole magnet. It contains an inner part (Inner tracker, IT) and an outer part (Outer tracker, OT) which employ different designs.

The IT stations are silicon microstrip detectors, so they are developed together and share common design choices. The IT and TT stations are together known as the silicon trackers (ST). Each of the three IT stations contains four detector boxes that places in four directions around the beam pipe. The detector boxes all have four detector layers arranged in $(x-u-v-x)$ structure. The x detection layers in four detector boxes are illustrated in the left panel of Fig. 2.10. Each detection sensor consists of seven modules, where the left and right have two silicon sensors and one read-out hybrid while the above and below ones have one sensor and one read-out hybrid. The layout of the IT module is also presented in Fig. 2.10. The thickness of the sensors is designed to improve the signal-to-noise ratio, which varies between one-sensor and two-sensor modules and is also different from that of the silicon sensors in the TT. Other parts are similar to that of the TT. The hit efficiency is found to be greater than 98%, with a hit resolution of 54.9 µm.

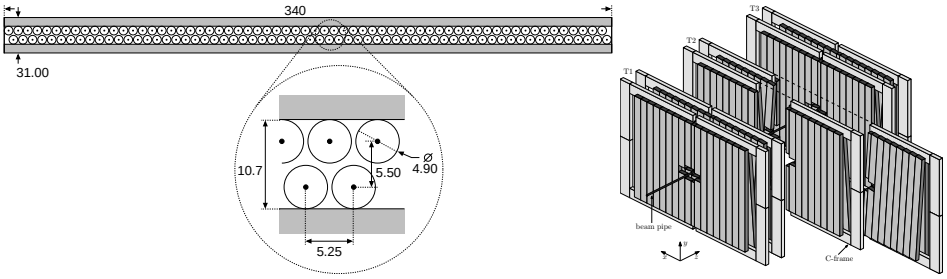

Figure 2.11 (left) Cross-section of straw-tube modules and (right) the arrangement of the straw-tube modules in the LHCb OT station. The figures are taken from Ref. [180].

The OT stations are a drift chamber detector constructed from 12 double layers of gaseous straw tubes[180]. The gases will be ionised when charged tracks travel through it. The straw tubes are filled with a mixture of 70% Ar, 28.5% CO_2 and 1.5% O_2 in order to reduce the drift time down to less than 50 ns and improve the radiation tolerance. The cross-section of a modules and its arrangement are illustrated in Fig. 2.11. The modules comprise two layers of 64 straw tubes. Then four modules are arranged in the $(x-u-v-x)$ structure similar to that of TT and IT stations. The three stations have an area of about 5×6 m^2 covering the outer part of the LHCb acceptance. The space close to the beam pipe is left for IT stations, as shown in Fig. 2.11. During the LHCb data taking, the drift time was found to be at most 35 ns[133]. The average hit efficiency is 99.2% and the single hit resolution is 205 µm, close to the design value of 200 µm.

2.2.1.4 Magnet

The dipole magnet in LHCb detector, used for deflecting the charged tracks and measuring their momenta, is placed between TT and T stations. A warm magnet is employed instead of the super-conducting magnet to avoid the very high cost and long construction time[132]. The two coils are placed symmetrically in the vertical direction providing strong magnetic field in this direction, as illustrated in the left panel of Fig. 2.12. The magnet is controlled via the magnet control system which supplies the power and monitors the parameters. It provides an integrated magnetic field of 4 T $\cdot$ m along the z axis, while in xy plane a non-uniformity of $|B|$ less than 1% is found. The measured B_y as a function of z is given in the right panel of Fig. 2.12. The precision of the magnetic field determination is estimated by measuring the magnetic field with different Hall probes, where a relative uncertainty of about 4×10^{-4} is seen.

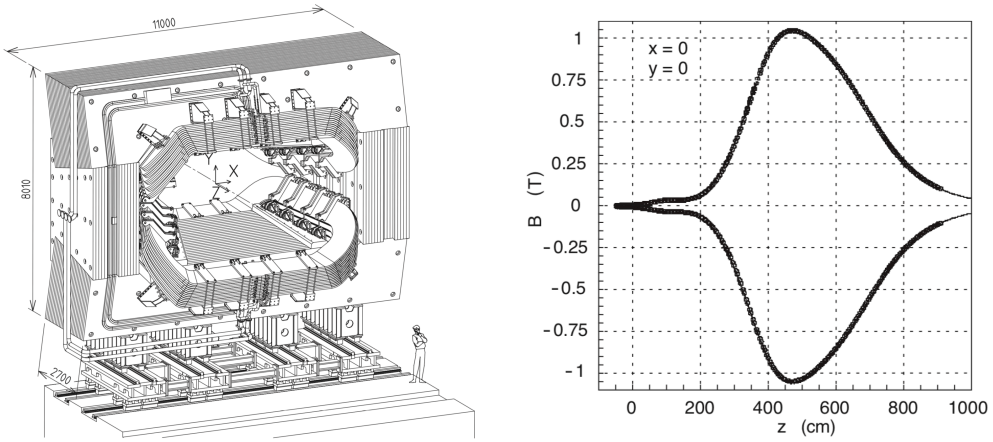

Figure 2.12 (left) Illustration of the structure of the LHCb dipole magnet and (right) variation of the measured vertical magnetic field strength B_y along the z axis. The figures are taken from Ref. [132].

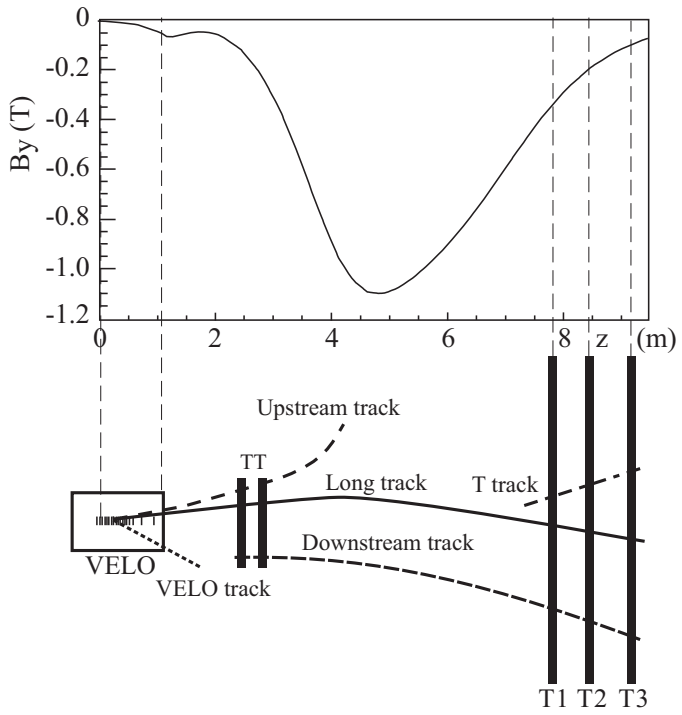

Figure 2.13 Illustration of tracks of different types in LHCb detector. The corresponding magnet field strength is also plotted for reference. The figure is taken from Ref. [133].

2.2.2 Track reconstruction

The LHCb tracking system provides an excellent reconstruction of charged tracks with the hit information from the sub-detectors. Before introducing the track finding method, it is essential to give the definition of different track types in the LHCb experiment. There are five main types of tracks, which are illustrated in Fig. 2.13.

- **Long tracks** This type of track, shown as the solid line in Fig. 2.13 travels the

full tracking system. Their trajectories can be detected in both the VELO and the T stations while optionally in the TT. Long tracks have the best momentum and position resolution among all track types, so they are the most important and widely used tracks for physics analyses.

- **Upstream tracks** These tracks have hits in the VELO and TT. They are in general soft particles that deflected by the magnetic field out of the LHCb acceptance. Because these tracks pass through the RICH1 detector, they can be used to learn its PID performance.
- **Downstream tracks** Downstream tracks are the tracks that go through the TT and T stations. Most of them are the final states of long-lived particles that decay outside the VELO. They are often used for the reconstruction of strange K_S^0 and Λ particles.
- **VELO tracks** They are tracks that only transverse the VELO detector due to their large polar angle. They only carry orientational information as they do not pass through the dipole magnet. VELO tracks are important for the PV reconstruction. Tracks in backward directions are also included in this type, also know as *back tracks*.
- **T tracks** These tracks only pass through the T stations. They are mostly the secondary particles produced from the multiple scatterings. They can be used for study the performance of RICH2 detector.

  The reconstruction of long tracks begins with straight-line trajectories reconstructed in the VELO[133]. These trajectories are required to have at least three hits both in R sensors and in Φ sensors respectively. Then the reconstructed VELO tracks are combined with the information from T stations with methods described in Refs.[181-182]. For a final step of long track reconstruction, their trajectories can be extrapolated to match the hits in TT, in order to achieve a better momentum resolution. The upstream tracks are also reconstructed from VELO tracks. Their trajectories are matched with hits in the TT instead of T stations. At least three hits in TT are needed for the matching. The downstream tracks reconstruction starts with the T tracks. Extrapolation is performed with the T tracks through the dipole magnet to search for the possible match in the TT. After the track finding, the tracks are further fitted with a Kalman Filter[183] incorporating the modification from multiple scattering and energy loss. The clone track which has two many common hits with another track will be removed. An example of track reconstruction from the

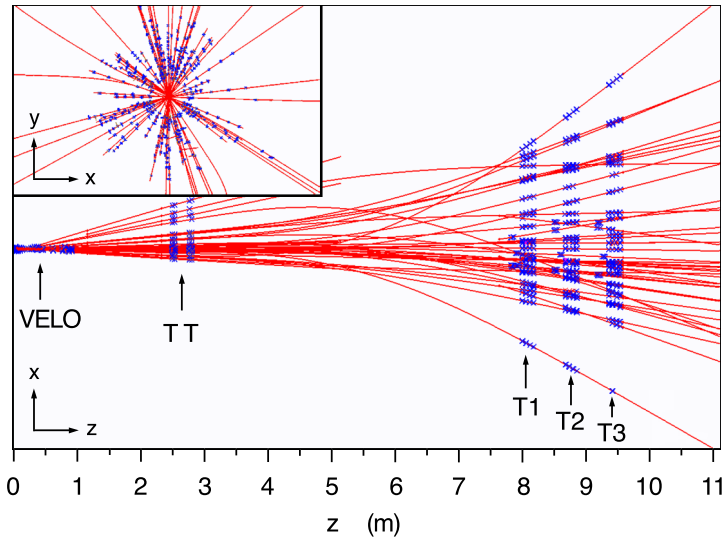

Figure 2.14 Illustration of the hits and the reconstructed tracks in an event. The figure is taken from Ref. [133].

hits in an event is shown in Fig. 2.14. The quality of the track can be estimated either from the fit via the χ^2 per degree of freedom (χ^2/ndf), or from the multivariate technique with neural network (NN)[184]. These estimators are often used for the fake track reduction. The relative resolution of particle momentum $\Delta p/p$ is estimated to be $0.4\% - 1.0\%$ for a momentum range of $5 - 200\,\text{GeV}/c$ with the combined tracking system for long track.

The track finding efficiency is defined to describe the possibility that tracks passing through the tracking systems are reconstructed. It is measured with a data-driven tag-and-probe method[185-186]. The *tag* leg is a full reconstructed long track, while another *probe* leg is partially reconstructed. The probe track can then be used to match a fully reconstructed track. The fraction of matched ones is defined as the tracking finding efficiency. The calibration is usually performed with $J/\psi \to \mu^+\mu^-$ samples. The results are presented in Fig. 2.15 and efficiencies greater than 95% are obtained. In this thesis, the tracking efficiency will also be estimated with $K^0_S \to \pi^+\pi^-$ samples, where the details will be described in the next chapter.

2.2.3 Particle identification system

The PID in LHCb experiment is achieved with four sub-detectors: the Cherenkov detectors, the calorimeter system and the muon stations. The PID system provides excellent capabilities in distinguishing different species of charged particles. The neural particles, including photons and π^0 mesons, can also be reconstructed and identified with calorime-

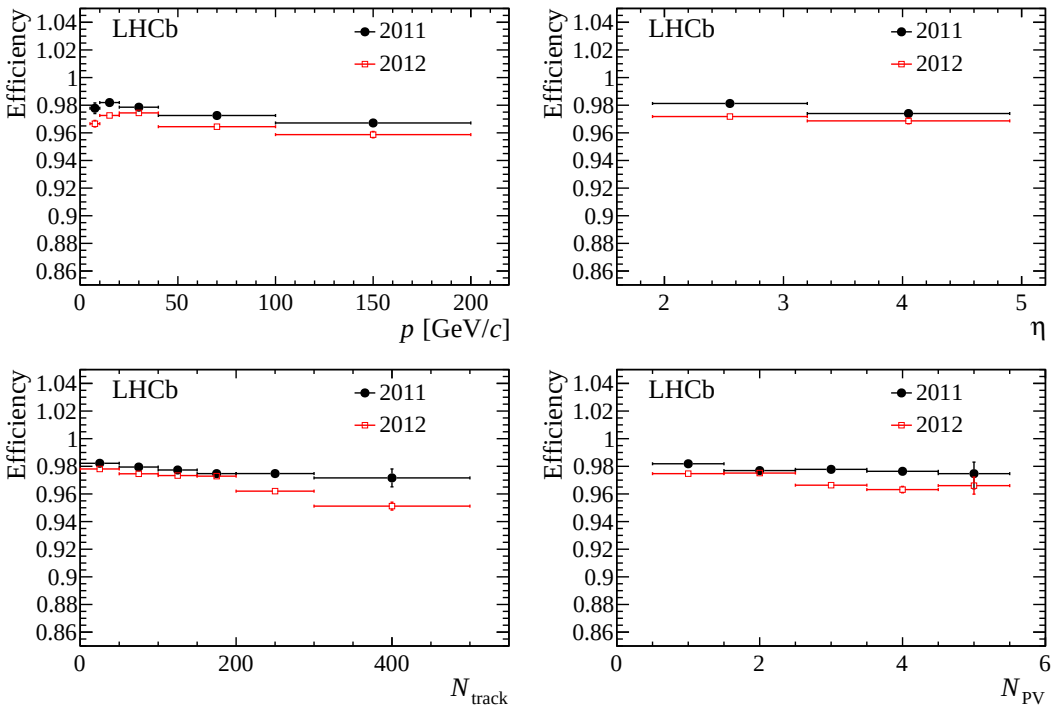

Figure 2.15 Measured track finding efficiency of LHCb 2011 and 2012 data as a function of the (top left) momentum p, (top right) pseudorapidity η, (bottom left) number of tracks N_{track} and (bottom right) number of primary vertices N_{PV}. The error bars shown the statistical uncertainties. The figures are taken from Ref. [133].

ter systems.

2.2.3.1 Cherenkov detectors

The two Cherenkov detectors, RICH1 and RICH2, provide excellent identification of charged p,K, π hadrons. The principle for such detector is the Cherenkov radiation. Charged particle passing through a particular medium will emit Cherenkov photons when its velocity is larger than the speed of light in this medium. The measured Cherenkov angle, given by $\theta_{\text{C}} = \arccos(c/n\upsilon)$, depends only on the particle velocity rather than the momentum. The particle species can then be determined by comparing θ_{C} with the momentum measured by tracking detectors. Fig. 2.16 shows the relation between the reconstructed θ_C and the momentum for charged p, K, π, μ particles in the C_4F_{10} medium.

In order to cover the full momentum region, RICH1 and RICHI2 are responsible for the identification of soft particles ($2 < p < 40\,\text{GeV}/c$) with $25 < \theta < 300$ mrad and hard ($15 < p < 100\,\text{GeV}/c$) particles with $15 < \theta < 120$ mrad, respectively. Then different radiator materials of C_4F_{10} and CF_4 are chosen to satisfy the requirements for RICH1 and RICH2, respectively. The layout of two detectors is presented in Fig. 2.17.

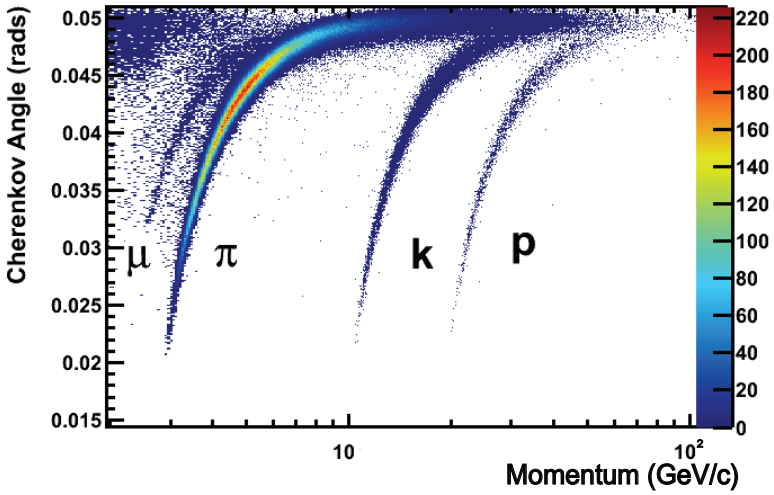

Figure 2.16 Dependence of the Cherenkov angle on the particle momentum for four different species of charged particles. The material of the radiator is the C_4F_{10}. The figure is taken from Ref. [187].

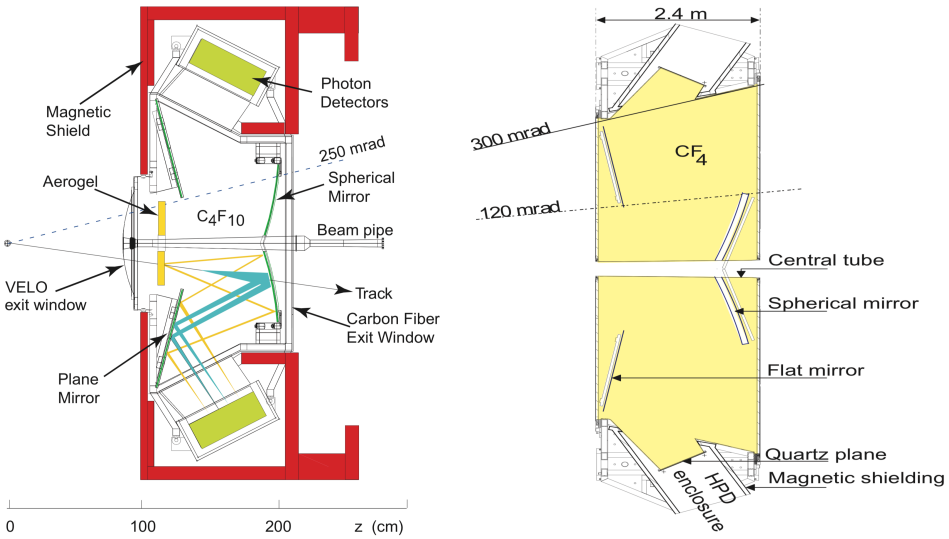

Figure 2.17 Layout of (left) the RICH1 detector in side view and of (right) the RICH2 detector in top view. The figures are taken from Ref. [132].

RICH1 is placed between the VELO and TT detectors and is very close to the beam pipe, while RICH2 is located downstream the T stations. Extra large iron boxes are employed in RICH1 for magnetic shield, because the measurement on the soft particles will largely affected by the magnetic field. The two detectors share similar optical systems. After the Cherenkov photons are produced, they will first be focused by the spherical mirror, and then reflected out of the LHCb acceptance to the hybrid photon detector (HPD). The recorded patterns on the planes of HPDs will be further used to determine the Cherenkov angles.

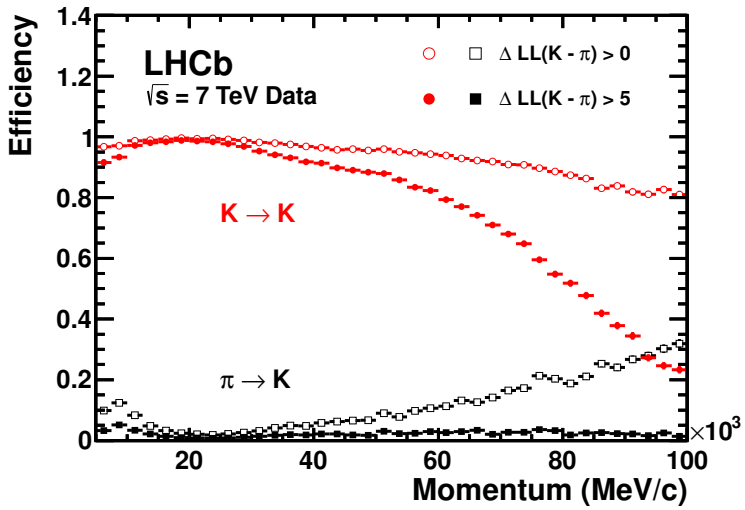

Figure 2.18 The measured PID efficiency and $\pi \to K$ misidentification rate on data as a function of the momentum. The figure is taken from Ref. [133].

The estimator for charged particle identification is developed from the log-likelihood algorithm using the information from RICH and tracking detectors[188]. The likelihood value will be calculated with the mass hypothesis to p, K, π, e, μ. The delta log likelihood ($\Delta \log \mathcal{L}$, DLL) with respect to $\mathcal{L}_\pi$, is often used to determine the particle species. The DLL variables are widely used for PID in LHCb analyses[123,131,140] and are adopted for K/π identification in D^0 reconstruction in this thesis. The PID performance can be studied with $K^0_S \to \pi^+\pi^-$, $\Lambda \to p\pi^-$ and $D^* \to D^0\pi^+$ samples using the tag-and-probe method. The efficiency and purity of K/π separation is shown in Fig. 2.18. By requiring a selection of $\mathrm{DLL}_{K-\pi} > 5$, the PID efficiency will be $\sim 90\%$ on average with a high purity of $\sim 97\%$. The information from RICH detectors is also helpful to improve the performance of e or μ identification with calorimeter or muon systems.

2.2.3.2 Calorimeter system

The calorimeter system comprises the SPD, the PS, the ECAL and the HCAL. The layout of the system is shown in Fig. 2.19. It is located between two muon stations M1 and M2. The SPD and PS are both scintillator cells which are separated by a thin lead layer. The SPD distinguishes between charged and neural particles by comparing the deposited energy with the expectation[189]. Then PS further contributes to the separation of electrons, photons and π^0 mesons. The ECAL has a structure of *shashlik*, which is a widely used technology in experiments. It is a sampling scintillator/lead structure, where the scintillator layers act as active materials and the lead layers act as the absorber. It

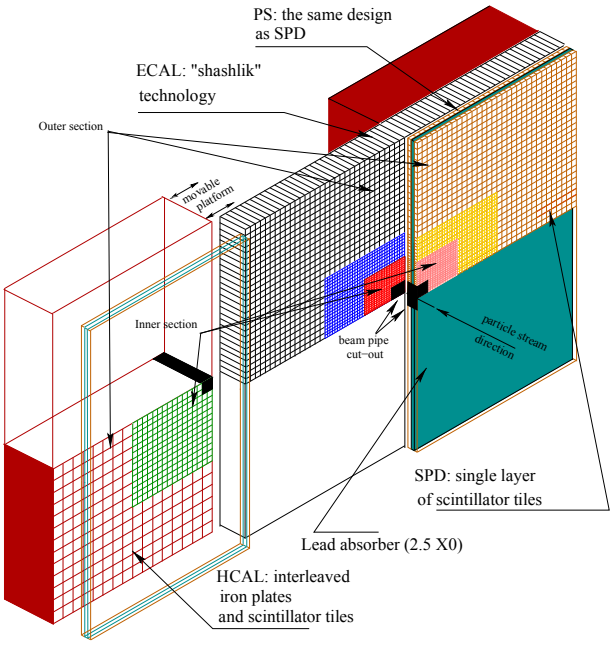

Figure 2.19 Layout of the LHCb calorimeter system. The figure is taken from Ref. [189].

provides the information on the transverse energy E_{T} of electron, photon and neural pions, which can also be used as the trigger for signals with electrons or photons in final states. The HCAL has a sampling structure of iron and scintillator tiles, which can ideally measure the hadron E_{T}. Due to the limited space, its thickness (5.6 nuclear interaction length) is insufficient for stopping all the hadrons. Thus, its capability of measurement is limited. However, HCAL plays an important role in the trigger for decays with hadronic final states, which will be introduced in detail afterwards. For all the four detectors, the wavelength-shifting fibres are employed to transmit the light from the shower of the particles to the photomultiplier tubes (PMT).

Photons can be reconstructed by two methods with the calorimeter system. Firstly, photons can be reconstructed from e^-e^+ pairs with common vertices, if they are converted in detector materials Secondly, the non-converted photons can be directly reconstructed with the ECAL information. Converted photons show a better energy resolution (4-5 MeV) compared to non-converted photons, which enables the separation of different χ_{cj} states[190]. The π^0 mesons can also be reconstructed in two ways. The low E_{T} ones mostly decay into two well separated photon pairs. These pions are known as the resolved π^0 mesons. While for high energy π^0 mesons, the decay products can not be separated, which are denoted a merged pions.

The calorimeter system also provides good e/h and γ/π^0 identification. By requir-

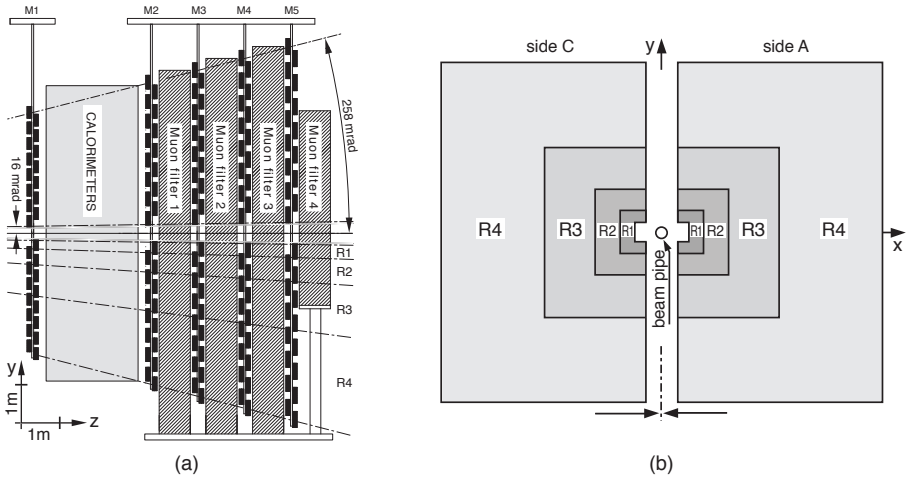

Figure 2.20 (left) Side view and (right) front view of muon stations. The figure is taken from Ref. [191].

ing suitable selection, an electron reconstruction efficiency of $(91.9 \pm 1.3)\%$ with a mis-identification rate of $(4.5 \pm 0.1)\%$ can be achieved[189]. A signal efficiency of 95% for non-converted photons can be obtained while rejecting 50% merged π^0 contaminations.

2.2.3.3 Muon stations

The muon stations M1-M5 are designed for the trigger, identification and track reconstruction of muons. They are all constructed from multi-wire proportional chambers (MWPC)[191]. Each of them contains two halves which are movable to get close to the beam pipe. The layout of the stations is shown in Fig. 2.20. M1 is located before the calorimeter system, which can significantly improve the p_{T} resolution in online reconstruction. The M2-M5 are placed in most downstream of the LHCb detector where most of other species of particles are stopped. A typical value of $0.35 - 0.55\%$ for muon momentum resolution can be achieved by matching the long tracks with hits in muon stations.

A binary selection IsMuon can be used to estimate whether a track is a muon. It is based on whether hits on muon stations and calorimeters can be found in the region around the extrapolated track[192]. The efficiency and mis-identification rate is given in Fig. 2.21. After this loose selection, the muon PID can be further improved with two methods. The first approach computes the combined likelihood with the information from the muon stations, calorimeters and RICH detectors, where the algorithm is similar to that for charged hadrons. Another estimator is the ProbNN_{μ}, derived from the multivariate analysis (MVA) toolkit [193], shows an even better background rejection compared to the DLL_{μ} variable given by the former approach[133]. Therefore, it has been utilised by more

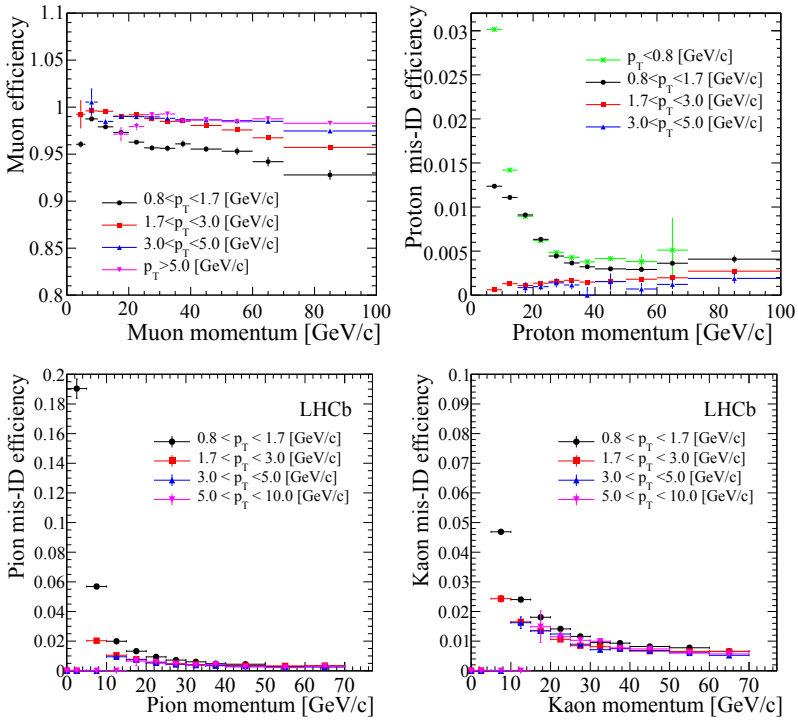

Figure 2.21 (top left) Muon efficiency and mis-identification rate to (top right) protons, (bottom left) pions and (bottom right) kaons as a function of particle momentum and transverse momentum. The figures are taken from Ref. [133].

LHCb measurements with muon final states[136,139].

2.2.4 Trigger system

The trigger system of LHCb experiment is designed to reduce the event rate and to select the events of interest efficiently. The bunch crossing rate of the pp collisions is 40 MHz, while the event rate of $b\bar{b}$ pairs is estimated to be $\sim$ 100 kHz at a luminosity of $2 \times 10^{32}\,\mathrm{cm}^{-2}\mathrm{s}^{-1}$ [132]. The reduction of event frequency is realised via two levels of triggers, namely the level-0 (L0) trigger and high level trigger (HLT). The schematic illustration of LHCb trigger both in Run1 and Run2 is shown in Fig. 2.22.

2.2.4.1 Level-0 trigger

The L0 trigger is a hardware trigger which aims to reduce the event frequency to $\sim$ 1 MHz with which all sub-detectors can be read out. It contains three independent units: the L0-calorimeter trigger, L0-muon trigger and L0-pileup trigger. The L0-calorimeter is based on the measured E_{T} of 2×2 cells in the ECAL and HCAL[133]. High-energy charm or beauty decay products are used to trigger the event. The information from hits in PS and SPD will be used further to classify the triggers into `L0Hadron`, `L0Photon`

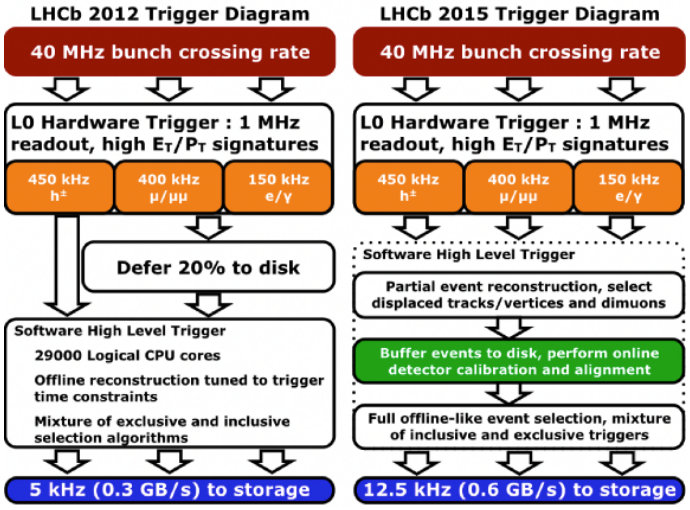

Figure 2.22 Flow chart of the LHCb trigger strategy in (left) Run1 and (right) Run2. The figures are taken from Ref. [194].

and `L0Electron`. The L0-muon trigger is dedicated to searching for high-p_{T} muons. The hits in five muon stations can be used to reconstruct muons with a momentum resolution of $\sim$ 25%[195]. The trigger decision is made by comparing the largest muon p_{T} with `L0Muon` threshold, or comparing the product of the largest two muon p_{T} with `L0DiMuon` threshold. The L0-pileup trigger is used for the measurement of the luminosity with the information from the VELO detector[196]. After this, the information will be collected by a L0 decision unit to make the final L0 trigger decision, where overlapped decisions are also allowed.

2.2.4.2 High level trigger

The HLT is a software trigger implemented in the event filter farm (EFF). The HLT makes use of the information of all the sub-detectors to apply more delicate selections online and reduce the event rate down to less than 1 GB/s for storage.

The HLT is composed of two stages, namely HLT1 and HLT2. The HLT1 reconstructs long tracks and primary vertices using the information from the tracking systems, where simplified algorithms are used due to time and storage limit. Fake tracks rejection can be performed and particles with high p_{T} and large IP will be selected. The HLT2 will then perform full event reconstruction incorporating all available information from LHCb sub-detectors. The track reconstruction will be repeated with more complicated algorithms, and all types of tracks will be taken into consideration. The reconstruction based on RICH detectors, calorimeters and muon stations will also be implemented to obtain all species of particles ($p, K, \pi, e, \mu, \gamma, \pi^0$) with PID information. There have been $\sim$ 20 HLT1 and

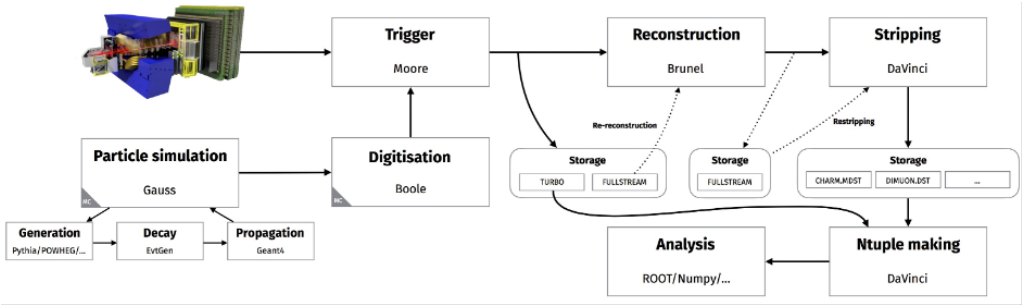

Figure 2.23 Flow chart of the offline data processing with LHCb software framework.

$\sim$ 500 HLT2 trigger lines in total serving for various physical processes of interests for Run2.

Due to the great improvement on the computing power and reconstruction algorithm, there have been significant development on the online reconstruction in LHCb Run2, as shown in Fig. 2.22. With the application of real-time analysis (RTA)[197-198], the LHCb detector has managed to store events of interest more efficiently, with a much reduced data size. In Run2, the output of the HLT1 will be buffered into disks first, and an asynchronous processing by HLT2 will begin. More offline-like reconstruction and selection can be performed in the process.

2.2.5 LHCb data acquisition

Before the data tuples for analysis is accessible, the output of the LHCb hardware need to be processed with the LHCb software framework[199-200], as illustrated in Fig. 2.23. As mentioned above, the LHCb data will experience the two-step software HLT, which is carried out by the Moore software. Then two types of data streams are stored in data tapes and provided for physics analyses. The full stream, which is adopted both in Run1 and Run2, persists the full event information if it passes the triggers. Such data have a quite huge size and are difficult for analysers to utilise them directly. Further steps of (re-)reconstruction by Brunel and offline data processing (*stripping*) with DaVinci are needed, according to the requirements from analysers. Then the stripped data will be stored in the data summary tape (DST) format, which can finally be processed and saved to the ROOT files suitable for further analysis.

Another `turbo` stream[201], supported by the RTA technique, is only adopted in Run2. Thanks to the efficient real-time reconstruction online, it has a much smaller data size but higher signal-to-background ratio. It also saves a lot of time for offline reconstruction and can be directly processed DaVinci into ROOT tuples via DaVinci. As

the `turbo` model has been evolving throughout Run2, there are three different types of `turbo` data that satisfy different physics targets.

- `Turbo`: Only the reconstruction on candidates and the cascaded decay products are performed after the candidates are triggered by HLT2.
- `Turbo++`/ `PersistReco`: When a candidate is triggered, the reconstruction of all the long and downstream tracks in the associated event will be performed. These data can be used for reconstruction with particle combinations, *e.g.*, a D^0 and π combination to a D^* candidate. This will result in a larger data size compared to `Turbo` data.
- `TurboSP` (`Turbo` with selective persistence): Similar to `Turbo++`, while selections are also applied to the associated tracks and vertices of trigger candidates.

The acquisition of simulation samples is also presented in Fig. 2.23. The data taking in hardware level is replaced by the simulation software framework GAUSS. The *pp* collision and the particle production are described with PYTHIA 8[202-203] with a specific LHCb configuration[204]. The software EVTGEN[205] is used to describe the decays of unstable particles, where the radiation of final-state particles is generated by PHOTOS[206]. The interaction of the produced particles with detectors, as well as the detector response, is described with GEANT4 toolkit[207-208], and its implementation in the LHCb detector is introduced in Ref. [209]. The LHCb experiment also provides the simulation samples for *p*Pb collisions based on EPOS-LHC generator[210], where the generated particles are embedded into minimum-bias *p*Pb events before the modeling of their decays. A better description of the detector occupancies can be achieved with the application of EPOS.

CHAPTER 3 DATA AND SIMULATION SAMPLES

The data sample used for the two analyses is the pPb collisions at $\sqrt{s_{\mathrm{NN}}} = 8.16\,\mathrm{TeV}$ collected by the LHCb detector in Run2, where the energy of the proton beam and lead beam are 6.5 TeV and 2.65 TeV, respectively. Both two collision configurations are included, denoted pPb and Pbp which are illustrated in Fig. 3.1. The pPb and Pbp cover the positive (forward, Fwd) and negative (backward, Bwd) rapidity regions, respectively, with the positive z-axis defined as the direction of the proton beam. And y^*, the rapidity in the centre-of-mass frame, is related to the rapidity in the laboratory frame with y_{lab} by $y^* = y_{\mathrm{lab}} - 0.465$ for pPb collisions.

The integrated luminosity is $12.2 \pm 0.3\,\mathrm{nb}^{-1}$ for pPb data and $18.6 \pm 0.5\,\mathrm{nb}^{-1}$ for Pbp. The corresponding data stream is `Turbo++`, so the full events associated to the triggered D^0 candidates are recorded. Thus, the two-particle correlation function can be measured with the sample.

The `L0` trigger of `L0SPD` requires at least one hit in the SPD. It is fully efficient *minimum-bias* trigger. The HLT1 lines, `Hlt1TrackMVADecision` and `Hlt1TwoTrackMVADecision` are designed to selected events with one or two hadrons from charm decays. The HLT2 line is the `Hlt2CharmHadD02KPi_XSecTurbo` for measuring the D^0 production cross-section. The explicit selection criteria in HLT2 are listed in Table 3.1 and are the same for both pPb and Pbp data. The χ^2_{IP} is defined as the difference in the vertex-fit χ^2 of a given PV reconstructed with and without a certain track or particle under consideration. It is strongly correlated with IP and, together with IP, is frequently used for the discrimination of prompt and secondary particles in LHCb analyses. The DoCA is the distance of the closest approach between two final state tracks, and the DIRA is the direction angle between the track momentum and vertex displacement. The χ^2/ndf(vtx) is the χ^2 per

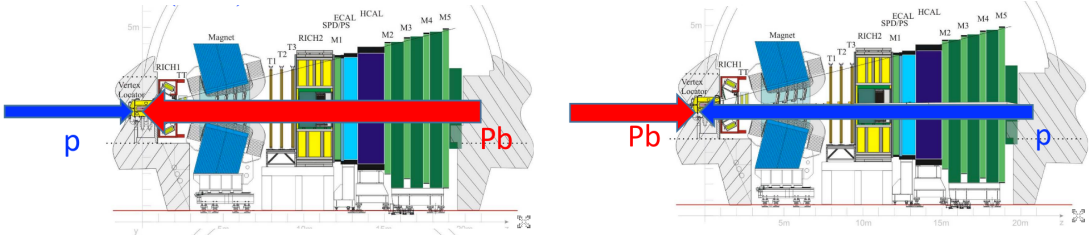

Figure 3.1 Illustration of two collision configurations (pPb and Pbp) for LHCb proton-lead data.

Table 3.1 HLT2 selection on the D^0 candidates.

Quantity	Selections
p_{T} (track)	$> 250\,\mathrm{MeV}/c$
χ^2_{IP}(track)	> 16
χ^2/ndf(track)	< 3
p(track)	$p > 2\,\mathrm{GeV}/c$
$\mathrm{DLL}_{K-\pi}(K^-)$	> 5
$\mathrm{DLL}_{K-\pi}(\pi^+)$	< 5
p_{T} (track)	$p_{\mathrm{T}}(\mathrm{max}) > 500\,\mathrm{MeV}/c$
p_{T} (D^0)	> 0
DoCA	DoCA(max) $< 1.0\,\mathrm{mm}$
M($D^0 \to K^-\pi^+$)	$1775 < m(D^0) < 1955\,\mathrm{MeV}/c^2$
DIRA	$< 17.3\,\mathrm{mrad}$
χ^2/ndf(vtx)	< 10
χ^2(VD)	> 49

degree of freedom in the D^0 end vertex fit and the χ^2(VD) is the χ^2 of the vertex displacement (VD, or flight distance, FD). In data, both prompt and non-prompt D^0 candidates are included. Prompt mesons are those directly produced in proton-lead collisions or from strong decays of excited charm hadrons, rather than from decays of beauty hadrons (non-prompt or from-b).

The MC simulation samples include 10M $D^0 \to K^-\pi^+$ & $\overline{D}^0 \to K^+\pi^-$ decays from EPOS+Pythia 8 simulation for both configurations, used for calculating efficiencies. The simulation samples can also be used to get the information of prompt D^0 mesons, such as the distribution of kinematic variables. Wherein, 4M of the simulations are labeled *multiplicity-fixed*, which improve the number of pill-up in order to provide a better simulation on the event multiplicity of data. It is implemented by placing multiple EPOS events (three for pPb and four for Pbp) in the same PV. The rest 6M of the samples, in which the number of pill-up is two, are denoted as *multiplicity-unfixed*. Another 2M sample for high-p_{T} D^0 candidates are also required in order to reduce the uncertainties from limited simulation sample size. Besides, the non-prompt D^0 mesons are simulated by 3M $B^+ \to \overline{D}^0\pi^+$ for both pPb and Pbp. These samples will served for discriminating the prompt and non-prompt components, as described later in Sec. 4.3. Generator-level MC samples, generated by GAUSS without further simulation on detector response, are also

produced to investigate the LHCb acceptance of decay products from D^0 signals.

CHAPTER 4 PROMPT D^0 PRODUCTION MEASUREMENT

This chapter presents the measurement of production D^0 meson production with pPb collisions data at $\sqrt{s_{\rm NN}}$ =8.16 TeV collected by the LHCb detector. The double differential cross-section of prompt measurement is determined in the kinematic range of $0 < p_{\rm T} < 30\,\text{GeV}/c$ and $1.5 < y^* < 4.0$ ($-5.0 < y^* < -2.5$) for forward (backward) rapidity. The nuclear modification factor is derived, taking the cross-section in pp collisions as the reference. The results are compared with theoretical calculations from nPDF, CGC and FCEL models. The forward-backward production ratio and the cross-section ratio between 8.16 TeV and 5.02 TeV are also given and compared with nPDF predictions.

4.1 Cross-section definition

The double differential cross-section for prompt D^0 production is measured as a function of y^*, the rapidity in the nucleon-nucleon center-of-mass frame, and $p_{\rm T}$, the transverse momentum with respect to the beam direction. The differential cross-section in a given ($p_{\rm T}$, y^*) interval is defined as

$$\frac{{\rm d}^2\sigma}{{\rm d}p_{\rm T}{\rm d}y^*} \equiv \frac{N(D^0 \to K^\mp\pi^\pm) + N(\overline{D}^0 \to K^\pm\pi^\mp)}{\mathcal{L} \times \varepsilon_{\rm tot} \times \mathcal{B}(D^0 \to K^\mp\pi^\pm) \times \Delta p_{\rm T} \times \Delta y^*}\,, \tag{4.1}$$

where $N(D^0 \to K^\mp\pi^\pm)$ and $N(\overline{D}^0 \to K^\pm\pi^\mp)$ are the D^0 and $\overline{D}^0$ signal yields, $\mathcal{L}$ is the integrated luminosity, $\varepsilon_{\rm tot}$ is the total efficiency, $\mathcal{B}(D^0 \to K^\mp\pi^\pm) = (3.96 \pm 0.03)\%$ is the sum of branching fractions for the decays $D^0 \to K^-\pi^+$ and $D^0 \to K^+\pi^-$ [23], where the branching fraction of $D^0 \to K^+\pi^-$ channel is two orders of magnitude smaller than that of $D^0 \to K^-\pi^+$. $\Delta p_{\rm T}$ and Δy^* are the $p_{\rm T}$ and y^* interval widths, respectively. The D^0 mesons are reconstructed through the $D^0 \to K^-\pi^+$ and the doubly Cabibbo-suppressed $D^0 \to K^+\pi^-$ decay channels and their charge conjugates. Throughout the analysis, the measurements are for the combined sample of D^0 and $\overline{D}^0$ mesons. The measurement is performed within a $p_{\rm T}$ range of $0 < p_{\rm T} < 30\,\text{GeV}/c$, and a y^* range of $1.5 < y^* < 4.0$ ($-5.0 < y^* < -2.5$) for forward (backward) rapidity. The signal yields and the total efficiency are determined in each kinematic interval.

Table 4.1 Offline selections for D^0 candidates.

Quantity	Selections
η	$2 < \eta < 5$
p_{T} (track)	$> 400\,\mathrm{MeV}/c$
IP(track)	$< 3\,\mathrm{mm}$
ProbNNghost(track)	< 0.3
p(track)	$3.2 < p < 100\,\mathrm{GeV}/c$
$\mathrm{DLL}_{K\pi}(\pi^+)$	< 0
$m(D^0)$	$1815 < m(D^0) < 1915\,\mathrm{MeV}/c^2$
$\log_{10}\chi^2_{\mathrm{IP}}(D^0)$	$-5 < \log_{10}\chi^2_{\mathrm{IP}}(D^0) < 5$
Decay time	$0.5 < \tau < 10\,\mathrm{ps}$

4.2 Offline selection

Several additional selection criteria are applied offline as shown in Table 4.1, following previous D^0 analysis at $\sqrt{s_{\mathrm{NN}}} = 5.02\,\mathrm{TeV}$[123], in order to improve signal-to-noise ratio. Both tracks are required to be in the acceptance of LHCb detector $2 < \eta < 5$. The transverse momentum of K^- and π^+ are required to be larger than $400\,\mathrm{MeV}/c$. The IP for both tracks are tightened to be less than 3 mm to remove the background tracks originating from the interactions of final-state particles with the detector. The MVA variable from NN is used to select high-quality tracks. The momenta of K^- and π^+ are required to be in the range $3.2 < p < 100\,\mathrm{GeV}/c$, which is the fiducial region of tracking and PID calibration. A tighter PID selection $\mathrm{DLL}_{K-\pi} < 0$ is applied to π^+. A signal window of invariant-mass within $[1815, 1915]\,\mathrm{MeV}/c^2$ and $\log_{10}\left(\chi^2_{\mathrm{IP}}\right)$ within$[-5, 5]$ for D^0 is set for the convenience of mass and $\log_{10}\left(\chi^2_{\mathrm{IP}}\right)$ fit. The lifetime of the D^0 candidates is limited to be within $[0.5, 10]\,\mathrm{ps}$, which is roughly $(1 - 20) \times \tau(D^0)$.

4.3 Signal yield

Extended unbinned maximum likelihood fit is performed in each kinematic interval to get the inclusive D^0 signal yield. A linear combination of a Crystal Ball (CB) function[211] and a Gaussian function is used to describe the shape of $M(K\pi)$ invariant-mass distribution

$$fr \times f_{\mathrm{CB}} + (1 - fr) \times \mathrm{Gaussian}\,, \tag{4.2}$$

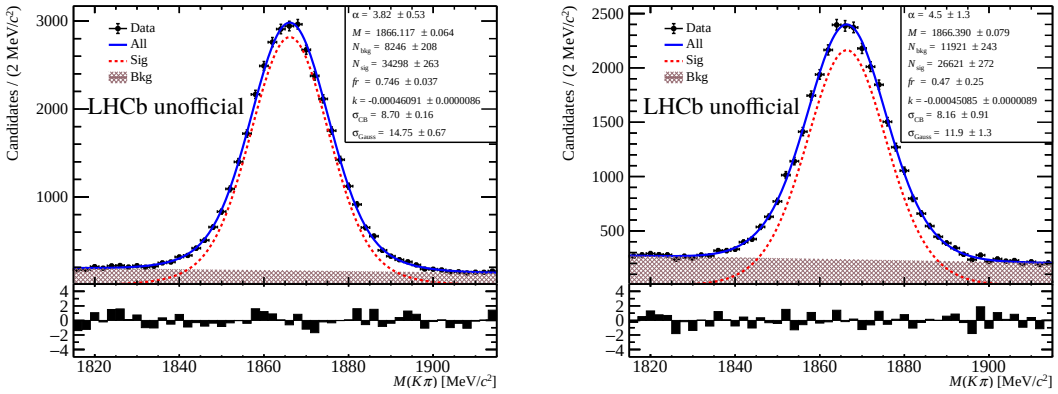

Figure 4.1 Fit to $M(K\pi)$ distribution in kinematic interval of $2.5 < p_{\mathrm{T}} < 3.0\,\mathrm{GeV}/c$ for (left) forward ($3.50 < y^* < 3.75$) and (right) backward ($-4.75 < y^* < -4.50$) rapidity intervals.

where fr is the fraction of the CB function and the CB function is defined as

$$f_{\mathrm{CB}}(x; M, \sigma, \alpha, n) = \begin{cases} \frac{\left(\frac{n}{|\alpha|}\right)^n e^{-\frac{1}{2}\alpha^2}}{\left(\frac{n}{|\alpha|} - |\alpha| - \frac{x-M}{\sigma}\right)^n}, & \text{if } \frac{x-M}{\sigma} < -|\alpha|\,, \\ \exp\left(-\frac{1}{2}\left(\frac{x-M}{\sigma}\right)^2\right), & \text{if } \frac{x-M}{\sigma} \geq -|\alpha|\,. \end{cases} \tag{4.3}$$

In this function, n and α are used to describe the *tail* originating from the radiative cascade transition and n is fixed to 1 from physics constraint due to the bremsstrahlung. M and σ are the mean value and standard deviation of this Gaussian-like function. The CB and Gaussian function are required to share a common mean value. A linear function is used to describe the shape of background. This invariant mass fit is performed in the mass window $M(D^0) \pm 50\,\mathrm{MeV}$ as listed in Table 4.1. Examples are shown in Fig. 4.1 for both forward and backward rapidities. Inclusive D^0 yields scaled with interval width are obtained in this step, as shown in Fig. 4.2.

To get prompt D^0 yields from total yields, the distribution of $\log_{10}\left(\chi^2_{\mathrm{IP}}\right)$is fitted in the similar way as previous analysis[131]. On average non-prompt D^0 mesons have larger IP than prompt D^0 mesons due to the flight distance of B hadrons. To suppress the background component, an *sPlot* method[212] is performed using the fit result from $M(K\pi)$ fit. So the $\log_{10}\left(\chi^2_{\mathrm{IP}}\right)$ distribution of weighted data contains only prompt D^0 component and non-prompt components. The distribution function describing the shape of each

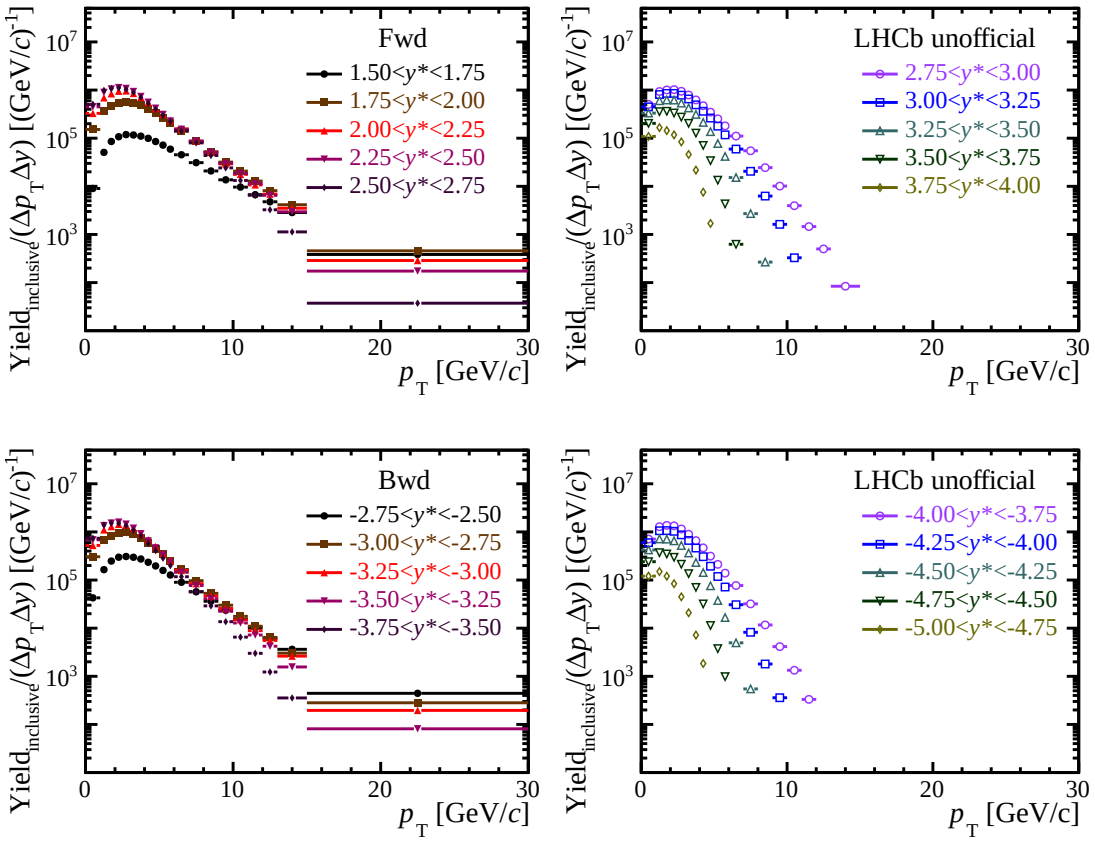

Figure 4.2 Inclusive D^0 yields as a function of p_{T} and y^* obtained from $M(K\pi)$ fit for (top) forward and (bottom) backward rapidities. The error bars show the statistical uncertainties.

component is the Bukin function[213] as follows:

$$\mathcal{P}(x;\mu,\sigma,\epsilon,\rho_L,\rho_R) = \begin{cases} \exp\left\{ \frac{(x-x_1)\epsilon\sqrt{\epsilon^2+1}\sqrt{2\ln 2}}{\sigma\left(\sqrt{\epsilon^2+1}-\epsilon\right)^2 \ln\left(\sqrt{\epsilon^2+1}+\epsilon\right)} + \rho_L \left(\frac{x-x_1}{\mu-x_1}\right)^2 - \ln 2 \right\} & x \le x_1, \\ \exp\left\{ -\left[\frac{\ln\left(1+2\epsilon\sqrt{\epsilon^2+1}\frac{x-\mu}{\sigma\sqrt{2\ln 2}}\right)}{\ln\left(1+2\epsilon^2-2\epsilon\sqrt{\epsilon^2+1}\right)} \right]^2 \times \ln 2 \right\} & x_1 < x < x_2, \\ \exp\left\{ \frac{(x-x_2)\epsilon\sqrt{\epsilon^2+1}\sqrt{2\ln 2}}{\sigma\left(\sqrt{\epsilon^2+1}-\epsilon\right)^2 \ln\left(\sqrt{\epsilon^2+1}+\epsilon\right)} + \rho_R \left(\frac{x-x_2}{\mu-x_2}\right)^2 - \ln 2 \right\} & x \ge x_2. \end{cases} \tag{4.4}$$

$$x_1 = \mu + \sigma\sqrt{2\ln 2}\left(\frac{\epsilon}{\sqrt{\epsilon^2+1}} - 1\right), x_2 = \mu + \sigma\sqrt{2\ln 2}\left(\frac{\epsilon}{\sqrt{\epsilon^2+1}} + 1\right).$$

This function is an asymmetric Gaussian-like function, where μ and σ are the mean and standard deviation, ϵ describes the asymmetry, ρ_L and ρ_R parametrise the left and right tails, respectively. For both configurations, ρ_L and ρ_R of prompt component, as well as ϵ, ρ_L and ρ_R of non-prompt component, are fixed to the values obtained from the fit to simulation samples, where both prompt ($D^0 \to K^-\pi^+$) and non-prompt ($B^+ \to \overline{D}^0\pi^+$)

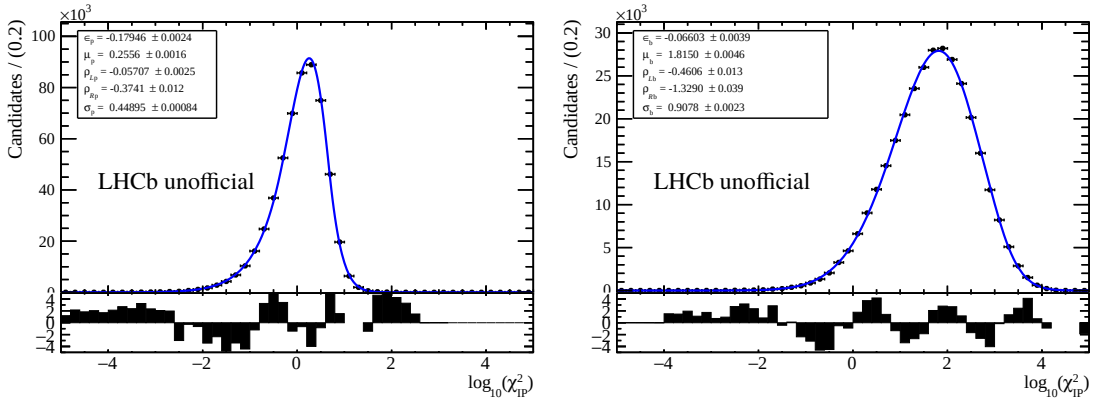

Figure 4.3 Fit result of (left) prompt and (right) non-prompt D^0 simulation samples for forward data in the kinematic range of $0 < p_T < 30\,\text{GeV}/c$ and $1.5 < y^* < 4.0$.

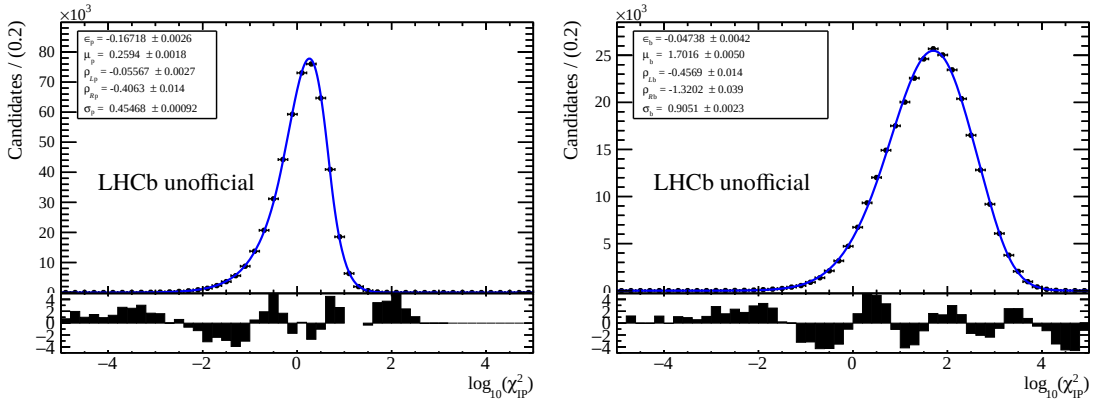

Figure 4.4 Fit result of (left) prompt and (right) non-prompt D^0 simulation samples for backward data in the kinematic range of $0 < p_T < 30\,\text{GeV}/c$ and $-5.0 < y^* < -2.5$.

samples are both included. The fit results in fully kinematic regions are shown in Fig. 4.3 (prompt) and 4.4 (non-prompt), where the parameters for prompt and non-prompt shapes are denoted as $(*)_p$ and $(*)_b$, respectively. Other parameters are allowed to vary and are determined from $\log_{10}\left(\chi^2_{IP}\right)$ fit, of which the examples are shown in Fig. 4.5 for both forward and backward regions.

From the fit of second step, the prompt D^0 yield in the invariant-mass window of $[1815, 1915]\,\text{MeV}/c^2$ and $\log_{10}\left(\chi^2_{IP}\right)$ window of $[-5, 5]$ can be directly obtained, as summarised in Fig. 4.6. There may be some D^0 signal candidates outside invariant-mass window or $\log_{10}\left(\chi^2_{IP}\right)$ window. This effect will be considered in the evaluation of selection efficiencies. The fraction of prompt component f_{prompt} is shown in Fig. 4.7.

4.4 Efficiency

In this analysis, total efficiency ε_{tot} is composed of four parts, the geometrical acceptance efficiency ε_{acc} , the reconstruction and selection efficiency $\varepsilon_{\text{rec\&sel}}$, the PID effi-

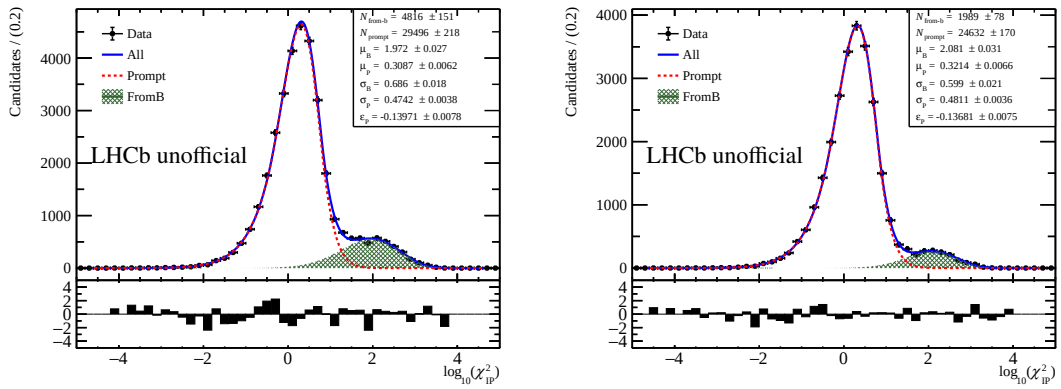

Figure 4.5 Fit to $\log_{10}\left(\chi^2_{\mathrm{IP}}\right)$ distribution in kinematic interval of $2.5 < p_{\mathrm{T}} < 3.0\,\mathrm{GeV}/c$ for (left) forward ($3.50 < y^* < 3.75$) and (right) backward ($-4.75 < y^* < -4.50$) rapidity intervals.

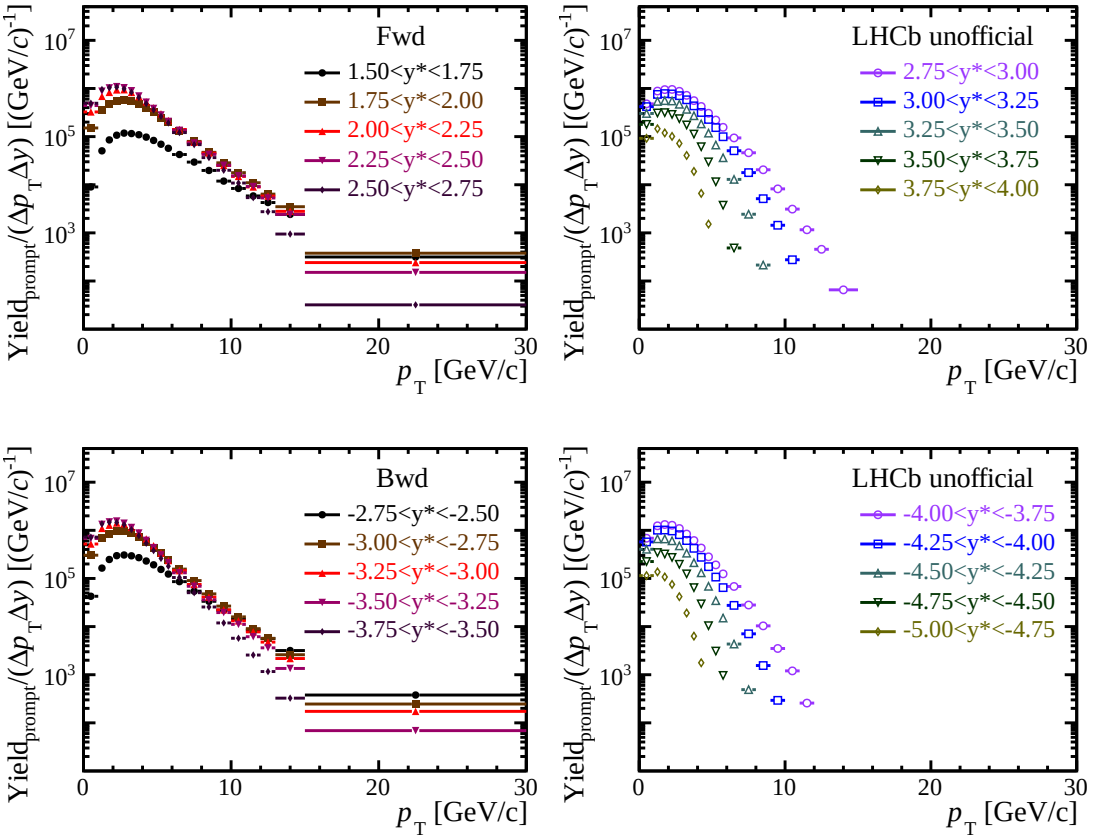

Figure 4.6 Prompt yields obtained from $\log_{10}\left(\chi^2_{\mathrm{IP}}\right)$ fit in (top) forward and (bottom) backward rapidity intervals. The error bars show the statistical uncertainties.

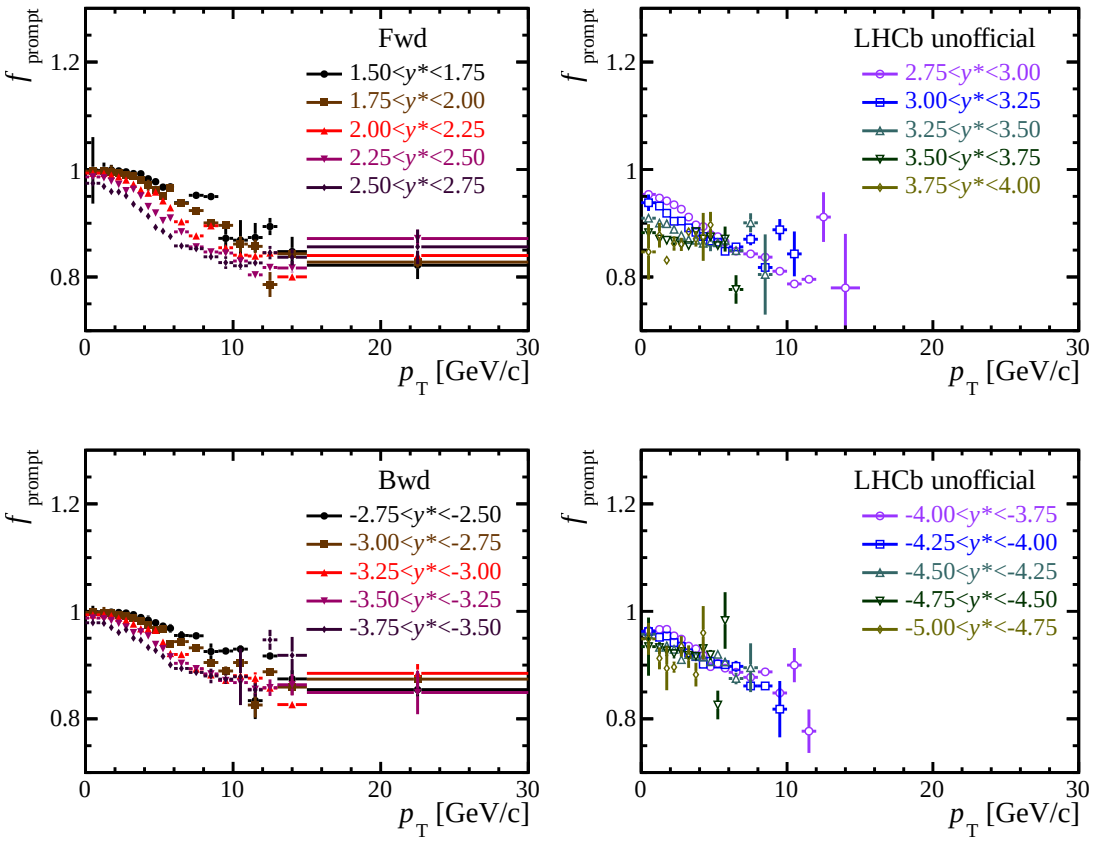

Figure 4.7 The fraction of non-prompt D^0 component from fit for (top) forward and (bottom) backward, The error bars show the statistical uncertainties.

ciency ε_{PID} and trigger efficiency $\varepsilon_{\text{trigger}}$. The total efficiency is obtained by multiplying these four parts:

$$\varepsilon_{\text{tot}} = \varepsilon_{\text{acc}} \times \varepsilon_{\text{rec\&sel}} \times \varepsilon_{\text{PID}} \times \varepsilon_{\text{trigger}} \,. \tag{4.5}$$

The four efficiencies are calculated in each kinematic interval and the detail are introduced in the following sections.

4.4.1 Validation of the simulation sample

It has been confirmed that LHCb simulation describes data well in Run2 according to LHCb early measurements performed in 2015, which were performed for open-charm [214] and J/ψ mesons [215] in pp collisions at $\sqrt{s_{\text{NN}}} = 13$ TeV. To be specific for this analysis, the parameters used for D^0-candidate selection are compared, as they determines whether efficiencies are calculated correctly, including p_{T}(track), χ^2_{IP}(track), χ^2/ndf(track), p(track), $p_{\text{T}}(D^0)$, $y^*(D^0)$, DoCA, DIRA, χ^2/ndf(vtx), χ^2(VD), $\tau(D^0)$. They are shown in Figs. 4.8, 4.9, 4.10, 4.11. The data samples are weighted with *sWeight* from $M(K\pi)$ fit and simu-

lation samples are weighted with nVeloClusters from multiplicity correction which will be discussed afterwards. Due to the extra simulation sample with $p_{\mathrm{T}}(D^0) > 8\,\mathrm{GeV}/c$, only $p_{\mathrm{T}} < 8\,\mathrm{GeV}/c$ are compared. Most of the variables show similar distribution between data and simulation, except for track χ^2/ndf. For them the requirement is χ^2/ndf(track) < 3 as Table 3.1 shows, which accepts almost all the events. Therefore, the mismatch between data and simulation does not have significant effects. The slight difference between $p_{\mathrm{T}}(D^0)$ and $y^*(D^0)$ is also neglected due to the tight binning scheme of this measurement. For detector occupancies (multiplicity variables), special corrections are made when calculating the reconstruction and selection efficiency.

4.4.2 Geometrical acceptance efficiency

The $\varepsilon_{\mathrm{acc}}$ is defined as

$$\varepsilon_{\mathrm{acc}} \equiv \frac{D^0 \text{ with } K^-\pi^+ \text{ in LHCb acceptance}}{\text{Generated } D^0} \,. \tag{4.6}$$

In this equation the signal acceptance is defined a range of polar angle θ of $[10, 400]$ mrad with respect to the beam direction. So a generator level simulation sample for prompt $D^0 \to K^-\pi^+$ decay without geometrical acceptance requirement for the decay products is used to estimate $\varepsilon_{\mathrm{acc}}$ for D^0 mesons in both forward and backward rapidity intervals. The $\varepsilon_{\mathrm{acc}}$ as a function of p_{T} and y^* is shown in Fig. 4.12. The results are summarised in Tables A.1 and A.2 in Appendix A.1.

4.4.3 Reconstruction and selection efficiency

The reconstruction and selection efficiency is defined as

$$\varepsilon_{\mathrm{rec\&sel}} = \frac{\sum D^0 \text{in acceptance, reconstructed and selected}}{D^0 \text{ with } K^-\pi^+ \text{ in LHCb acceptance}} \,. \tag{4.7}$$

This efficiency include two parts, the efficiencies of reconstructing the two long π and K tracks and the refined selections of the D^0 signals. The selection criteria are listed in the Table 4.1, but PID requirements on DLL are excluded as these quantities are not well simulated in simulation. The data sample for calculating $\varepsilon_{\mathrm{rec\&sel}}$ is the MC truth-matched $D^0 \to K^-\pi^+$ decays in full MC simulated pPb events. To correct the differences between data and MC simulation, corrections for truth matching matching algorithm, track reconstruction, and multiplicity distributions are considered, which are shown separately in the following.

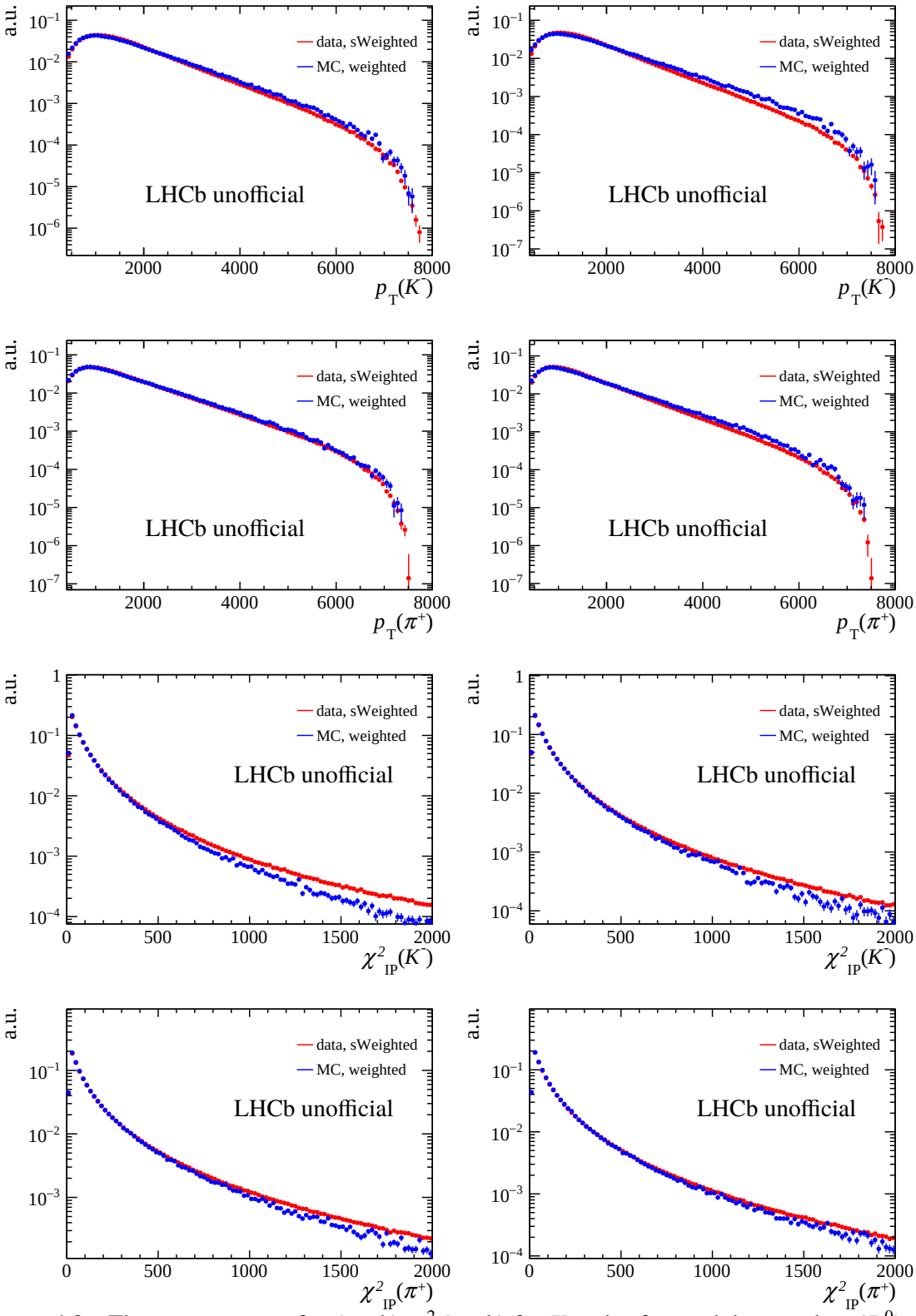

Figure 4.8 The comparisons of p_T(track), χ^2_{IP}(track) for K and π for candidates with $p_T(D^0) < 8$ GeV/c. The data are weighted with *sWeight* from $M(D^0)$ fit and simulations are weighted with nVeloClusters. Left for Fwd and right for Bwd.

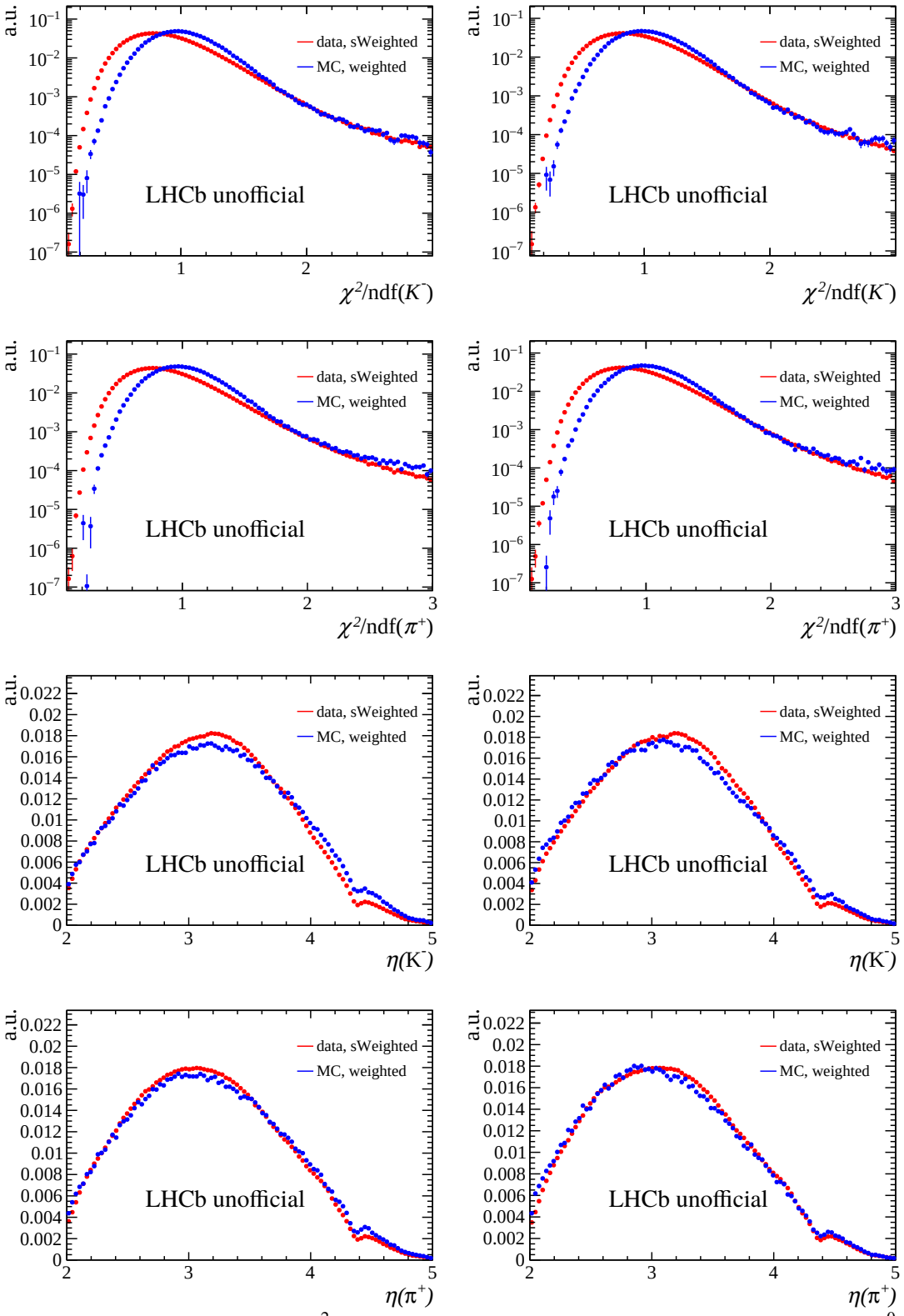

Figure 4.9 The comparisons of χ^2/ndf(track), η(track) for K and π for candidates with $p_T(D^0) < 8$ GeV/c. The data are weighted with *sWeight* from $M(D^0)$ fit and simulations are weighted with nVeloClusters. Left for Fwd and right for Bwd.

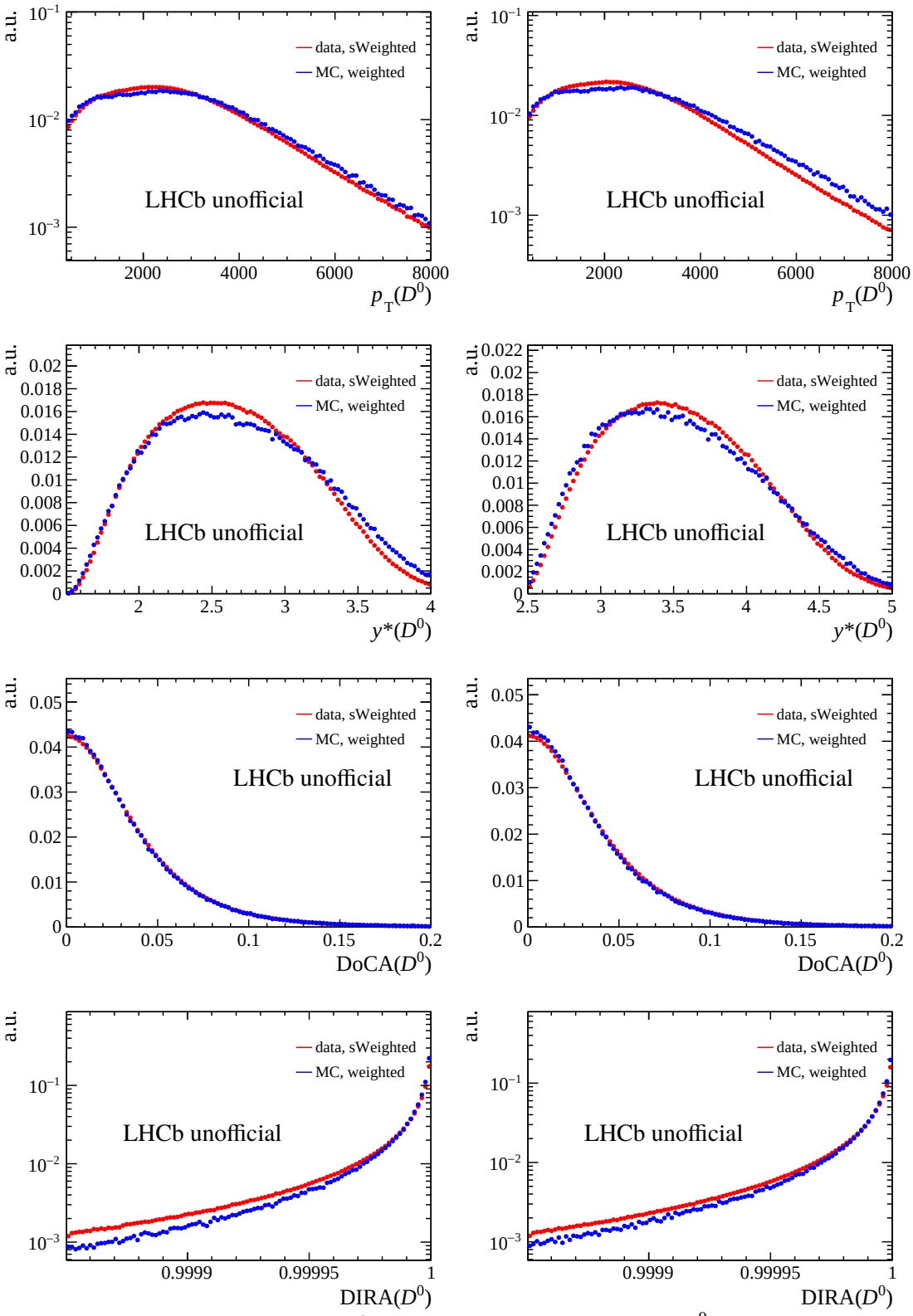

Figure 4.10 The comparisons of p_T, y^*, DoCA and Direction Angle for D^0 mesons for candidates with $p_T(D^0) < 8$ GeV/c. The data are weighted with *sWeight* from $M(D^0)$ fit and simulations are weighted with nVeloClusters. Left for Fwd and right for Bwd.

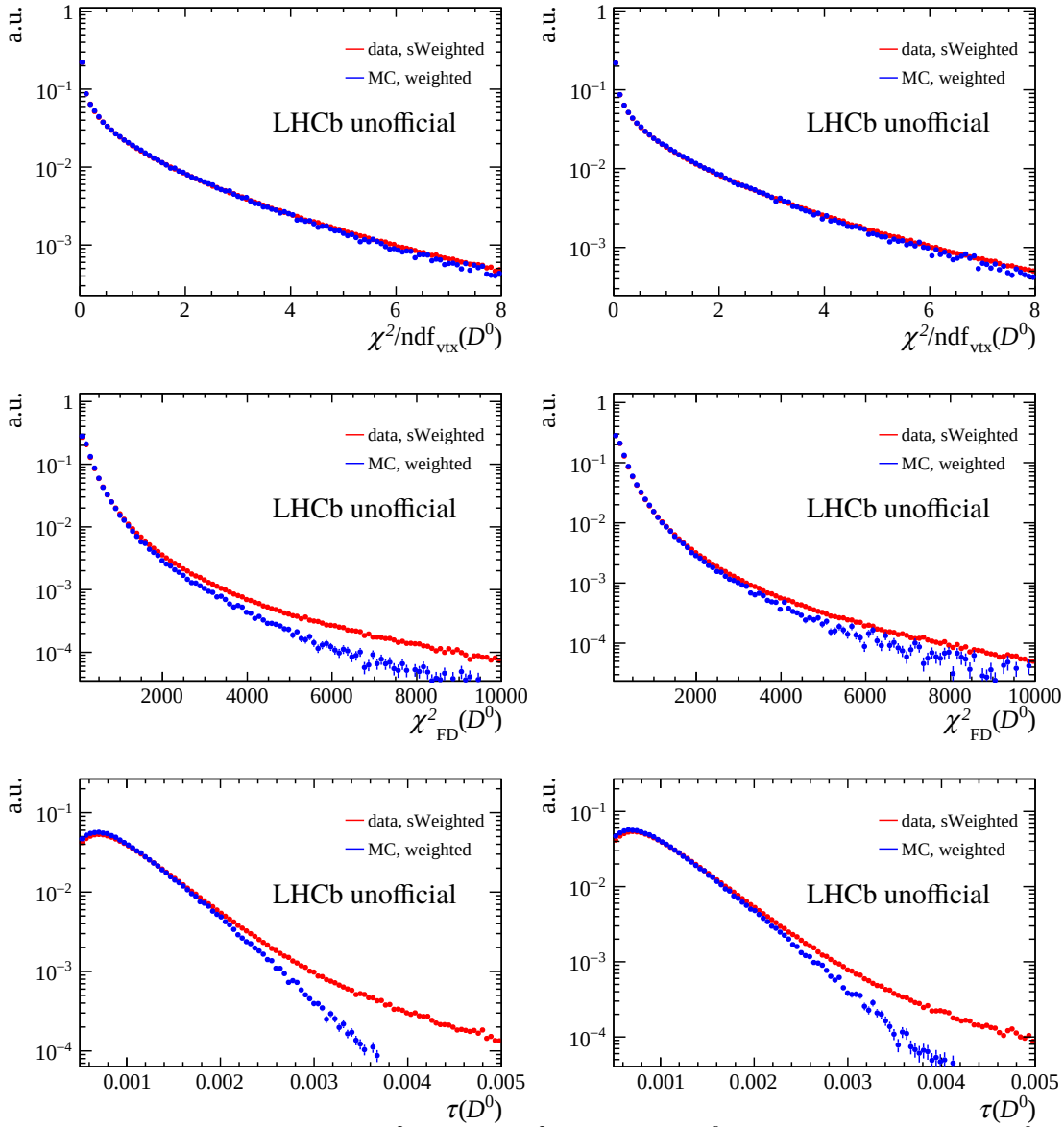

Figure 4.11 The comparisons of χ^2/ndf(vtx), χ^2(VD) and $\tau(D^0)$ for candidates with $p_{\mathrm{T}}(D^0) < 8$ GeV/c. The data are weighted with *sWeight* from $M(D^0)$ fit and simulations are weighted with nVeloClusters. Left for Fwd and right for Bwd.

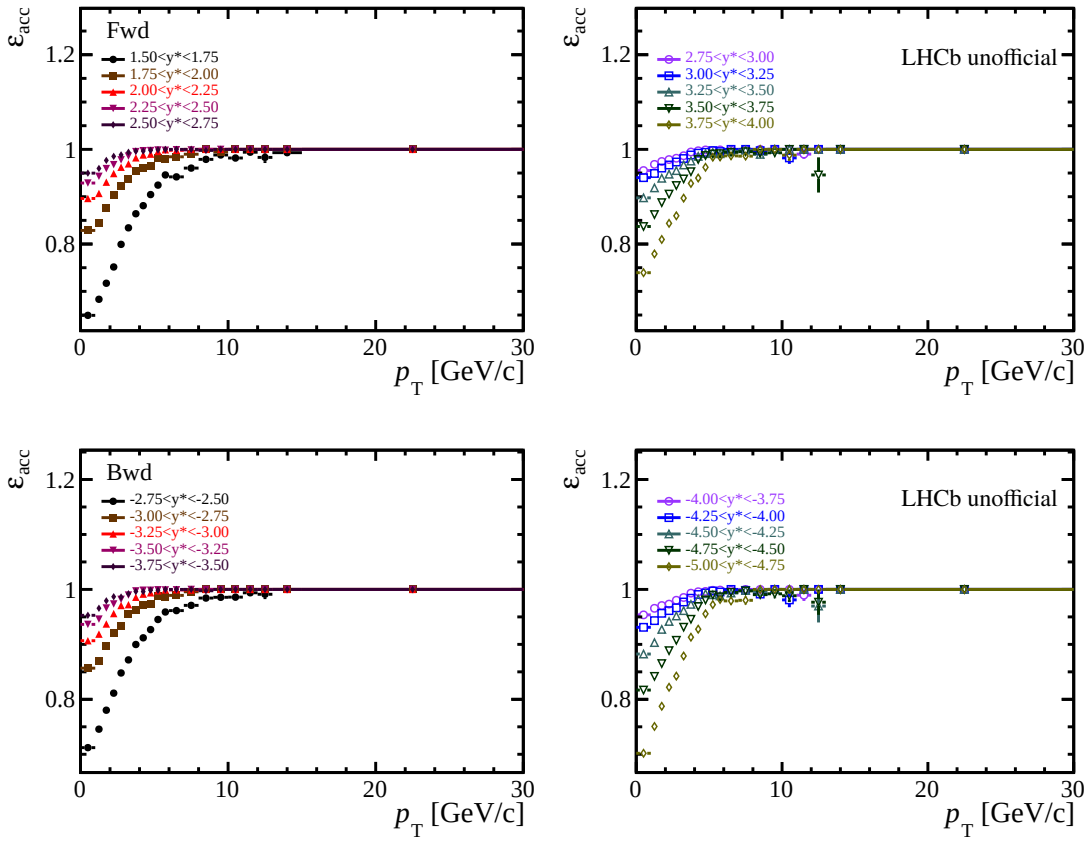

Figure 4.12 Geometrical acceptance efficiency ε_{acc} as a function of p_{T} and y^* of prompt D^0 meson for (top) forward and (bottom) backward data. The error bars show the statistical uncertainties.

4.4.3.1 Truth matching correction

The signals in the simulation are picked out by truth matching requirements, which include D^0, K, π ID requirements and background categories (BKGCAT) requirements from matching algorithm `(D0_BKGCAT==0||D0_BKGCAT==50)`, where 0 refers to signal and 50 refers to *low-mass background* originating from partial reconstruction of signals. This matching algorithm, which requires at least 70% matched hits between the reconstructed and MC true tracks, occasionally flags the signal track as a fake track (ghost). This effect can be investigated by plotting the $M(K\pi)$ distribution of those D^0 candidates not truth-matched but passing the selections. A peak around the D^0 mass can be seen from the blue points in Fig. 4.13. A Gaussian signal plus a linear background is used to fit this mass spectrum. The ratio of the number of D^0 signal in this peak over the truth-matched D^0 signal is calculated. Since the fraction is small, it is calculated with unbinned simulation samples. The fit gives a fraction of $(1.23 \pm 0.05)\%$ for forward and $(1.14 \pm 0.05)\%$ for backward rapidities. Since the effect would result in an underestimate

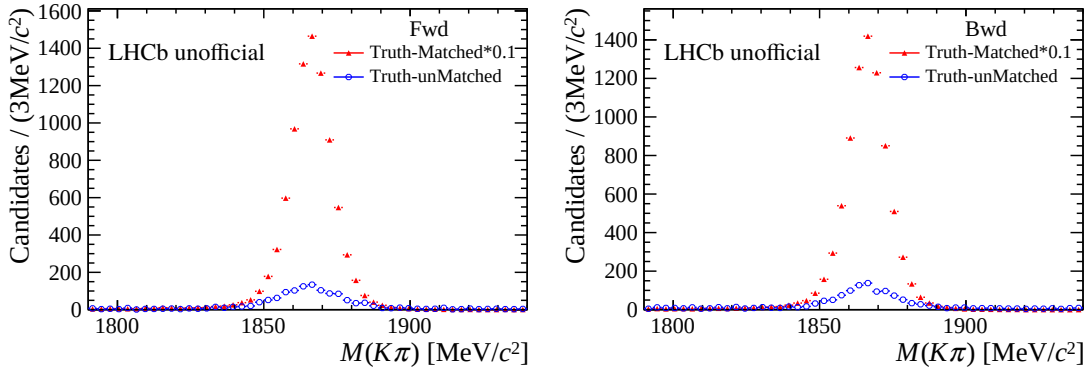

Figure 4.13 The $M(K\pi)$ distribution of truth-matched and truth-unmatched D^0 mesons for (left) forward and (right) backward simulations. Matched peak is scaled down by a factor of 0.1 for comparison.

of the efficiency, the total efficiency should be multiplied by a factor of 1.0123 for forward and 1.0114 for backward rapidities, while the uncertainties are negligible.

4.4.3.2 Track reconstruction correction

The track finding efficiency, as described in the LHCb tracking system, is known to be different between data and simulation. Therefore, the tracking efficiencies obtained with simulation have to be corrected for this difference. The correction tables for pPb samples are given as a function of track momentum (p) and pseudo-rapidity (η) as in Fig. 4.14, which was studied in b-hadron production in pPb collisions at $\sqrt{s_{\rm NN}} = 8.16\,\text{TeV}$[140]. The calibration was performed using a tag-and-probe method with detached $J/\psi \to \mu^+\mu^-$ decays constructed in the `Turbo` stream in both data and simulation. Uncertainty in these tables will be considered in systematic uncertainties detailed in the next section. To take the efficiency into account, the definition of $\varepsilon_{\rm rec\&sel}$ in Eq. 4.7 is modified as:

$$\varepsilon_{\rm rec\&sel} = \frac{\sum_{D^0\text{reconstructed and selected}} w_i(p_{K^-}, \eta_{K^-}) \times w_i(p_{\pi^+}, \eta_{\pi^+})}{D^0 \text{ with } K^-\pi^+ \text{ in LHCb acceptance}}\,, \tag{4.8}$$

where the w_i is weight given by the correction table. In this correction, the uncertainties are large in low-momentum regions due to the lack of statistics in calibration samples. This leads to large uncertainties for D^0 efficiencies in low-$p_{\rm T}$ and low-y intervals. To reduce these uncertainties, a new calibration with minimum-bias $K^0_{\rm S} \to \pi^+\pi^-$ data and simulation samples are performed, using the same tag-and-probe method[216]. In this calibration, a tag leg and a probe leg is combined to get the $K^0_{\rm S}$ signal. The tag leg is required to be a long track while the probe leg can be of any type (upstream / downstream / long). Selections are applied to the tag leg and $K^0_{\rm S}$ candidates to reduce the background which are listed in Table 4.2. In order to reduce the bias caused by the selections, only a

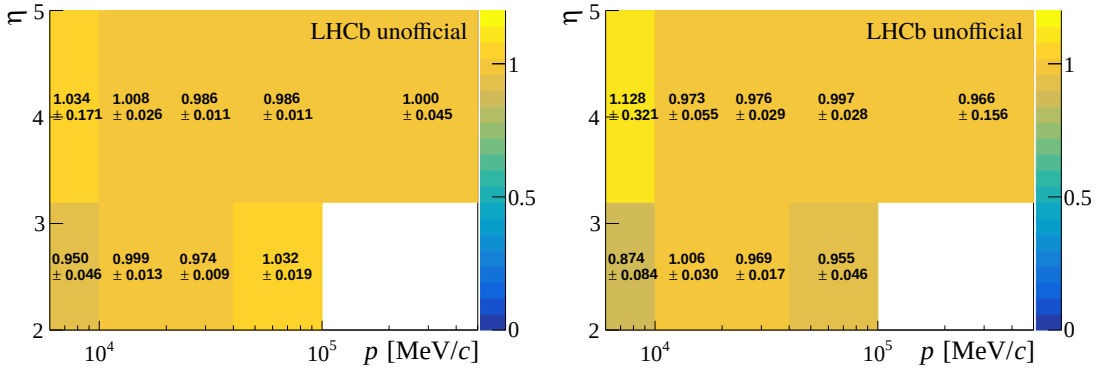

Figure 4.14 Tracking efficiency correction table calibrated in b-hadron production measurement in pPb at $\sqrt{s_{\rm NN}} = 8.16\,\text{TeV}$ [140] for forward (left) and backward (right) configurations.

Table 4.2 Selections on K^0_S candidates in the tracking calibration.

Variable	Selection
χ^2/ndf(vtx)	< 10
χ^2(FD)(K^0_S)	> 100
$\chi^2_{\rm IP}(K^0_S)$	< 1
DoCA(K^0_S)	< 1 mm
cos(DIRA(K^0_S))	> 0.9995
η(probe)	$2 < \eta < 5$
$\chi^2_{\rm IP}$(probe)	> 30
$p_{\rm T}$(probe)	$> 200\,\text{MeV}/c$
p(probe)	$2 < p < 500\,\text{GeV}/c$
PIDK(tag)	< 5
PIDp(tag)	< 5
p(tag)	$> 2\,\text{GeV}/c$
$p_{\rm T}$(tag)	$> 500\,\text{MeV}/c$
$\chi^2_{\rm IP}$(tag)	> 30
χ^2/ndf(tag)	< 3
GP(tag)	< 0.4

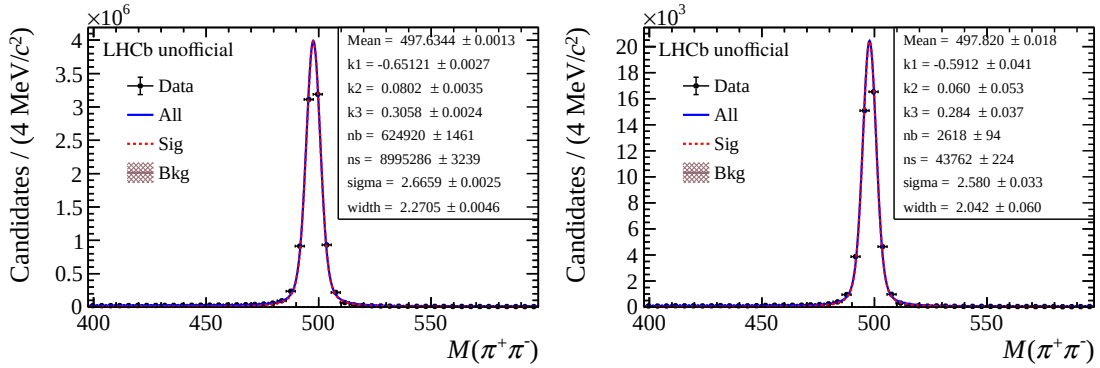

Figure 4.15 $M(\pi^+\pi^-)$ distribution and the fit in kinematic interval of $2 < p < 10\,\text{GeV}/c, 3.2 < \eta < 5$ for K^0_S candidates with long probe leg for (left) data and (right) simulation at forward rapidity.

few kinematic constraints are added to the probe leg. The $\varepsilon_{\text{VELO}}$ and the ε_{T} are defined as the track finding efficiency of the VELO and the T stations. They are multiplied to get the $\varepsilon_{\text{long}}$, *i.e.* the track finding efficiency. The three efficiencies are defined as the equation below

$$\varepsilon_{\text{VELO}} = \frac{N(\text{Long})}{N(\text{Downstream}) + N(\text{Long})}\,, \tag{4.9}$$

$$\varepsilon_{\text{T}} = \frac{N(\text{Long})}{N(\text{Upstream}) + N(\text{Long})}\,, \tag{4.10}$$

$$\varepsilon_{\text{long}} = \varepsilon_{\text{VELO}} \times \varepsilon_{\text{T}}\,, \tag{4.11}$$

where N refers to the K^0_S yields with a probe leg of certain track type. The yields are obtained from the fit of $M(\pi^+\pi^-)$ around the K^0_S mass, where the signal is modeled with a Breit-Wigner function[23] convoluted with a Gaussion and the background with a three-order polynomial. Figs. 4.15, 4.16 and 4.17 show the fit results for the kinematic interval of $2 < p < 10\,\text{GeV}/c, 3.2 < \eta < 5$ for long, upstream and downstream probe leg, respectively.

Take the yields from the fit into Eq. 4.11, the $\varepsilon_{\text{Long}}$ is calculated and shown Fig. 4.18. The tracking correction table can be obtained by comparing the ε(data) with ε(MC):

$$w = \frac{\varepsilon_{\text{long}}(\text{data})}{\varepsilon_{\text{long}}(\text{MC})}\,, \tag{4.12}$$

which is shown in Fig. 4.19. Finally, the two correction tables are combined by choosing the values with smaller uncertainties, which is shown in Fig. 4.20.

4.4.3.3 Multiplicity correction

The LHCb reconstruction efficiency depends strongly on the detector occupancy, which can be evaluated with multiple detector multiplicity variables. However, the dis-

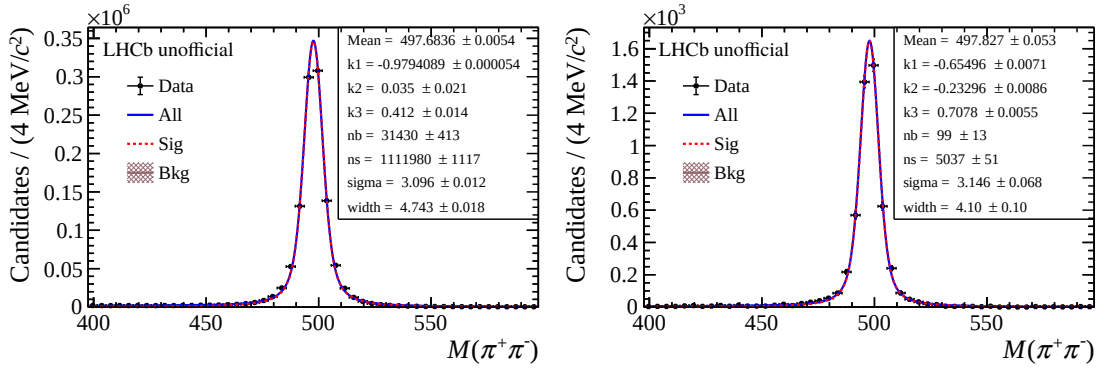

Figure 4.16 $M(\pi^+\pi^-)$ distribution and the fit in kinematic interval of $2 < p < 10\,\text{GeV}/c, 3.2 < \eta < 5$ for K^0_S candidates with upstream probe leg for (left) data and (right) simulation at forward rapidity.

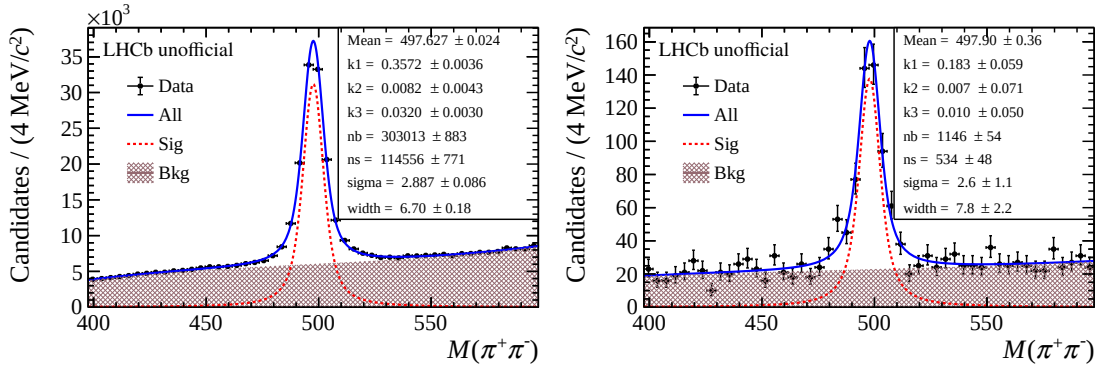

Figure 4.17 $M(\pi^+\pi^-)$ distribution and the fit in kinematic interval of $2 < p < 10\,\text{GeV}/c, 3.2 < \eta < 5$ for K^0_S candidates with downstream probe leg for (left) data and (right) simulation at forward rapidity.

tributions of these variables in simulation are different from those in data. Thus, the D^0 reconstruction efficiencies should be calculated after correcting the distributions of these variables. The multiplicity variables considered for the correction is the number of hits in the VELO (nVeloClusters), the number of the reconstructed long tracks (nLongTracks) and the number of the hits in the TT stations (nTTClusters). Their distributions in data and simulation are shown in Fig. 4.21, where the data distribution is weighted with the *sWeight* from the D^0 invariant-mass fit. To reproduce the distributions in data, the multiplicity distributions in simulation are weighted. Samples for $p_T(D^0) < 8\,\text{GeV}/c$ and $p_T(D^0) > 8\,\text{GeV}/c$ are considered separately in the weighting as shown in Figs. 4.22 and 4.23. The multiplicity weights are assigned to each event both before and after selection. The average values of the three $\varepsilon_{\text{rec\&sel}}$ obtained from weighting on the three multiplicity variables are used as the final results. The efficiencies are shown in Fig. 4.24, with all the corrections incorporated. The numerical values are listed in Tables A.3 and

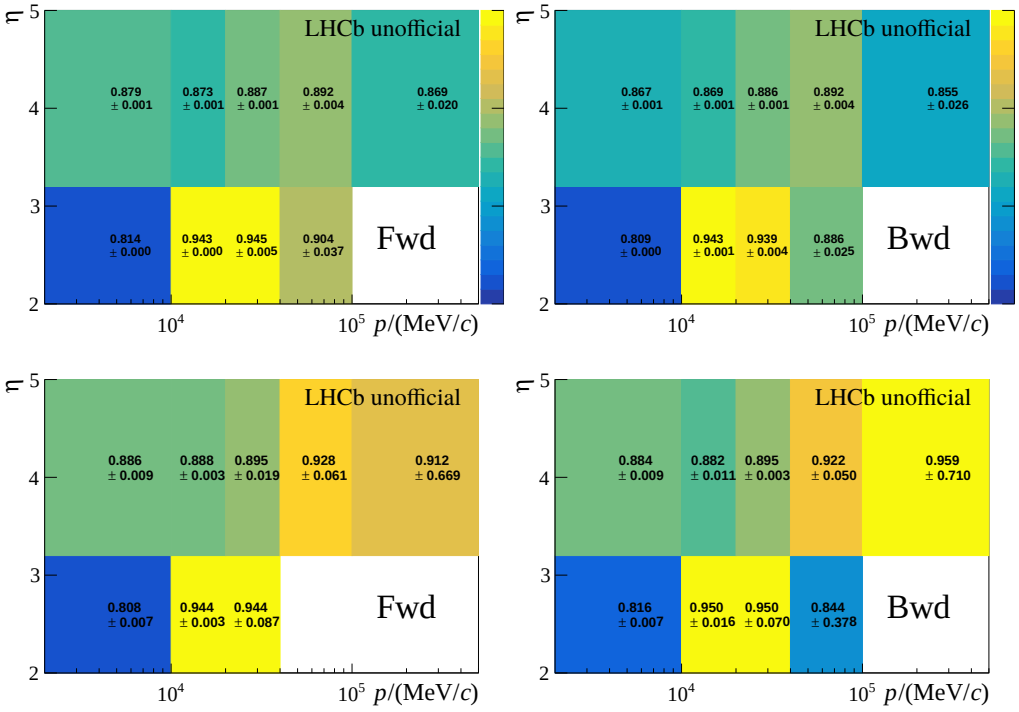

Figure 4.18 Long track reconstruction efficiency $\varepsilon_{\text{Long}}$ as a function of p(probe) and η(probe) for (top) data and (bottom) simulation. Left is for the forward rapidity and right for the backward.

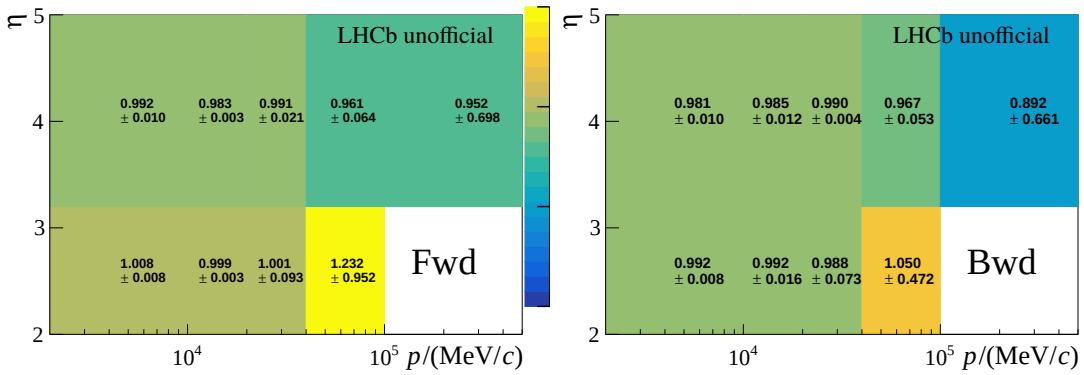

Figure 4.19 Tracking correction table from the calibration with minimum-bias $K^0_S \to \pi^+\pi^-$ samples for (left) forward and (right) backward configurations.

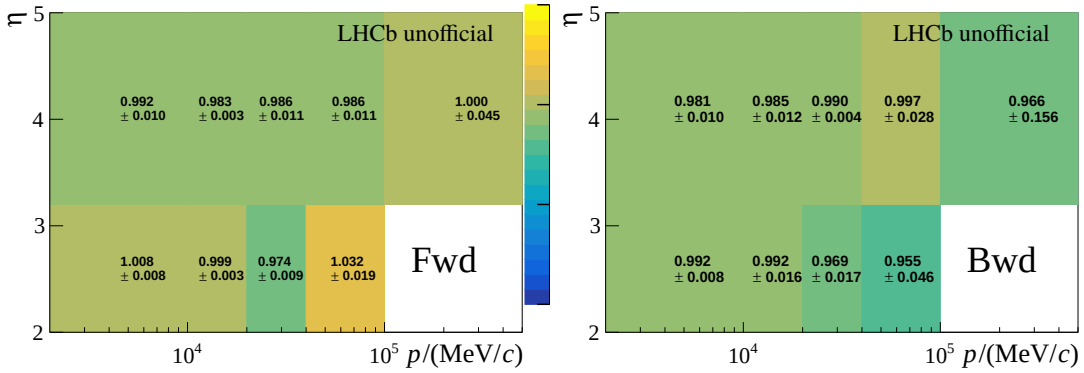

Figure 4.20 Tracking correction table table combined from the calibrations with $J/\psi \to \mu^+\mu^-$ and $K^0_S \to \pi^+\pi^-$ samples.

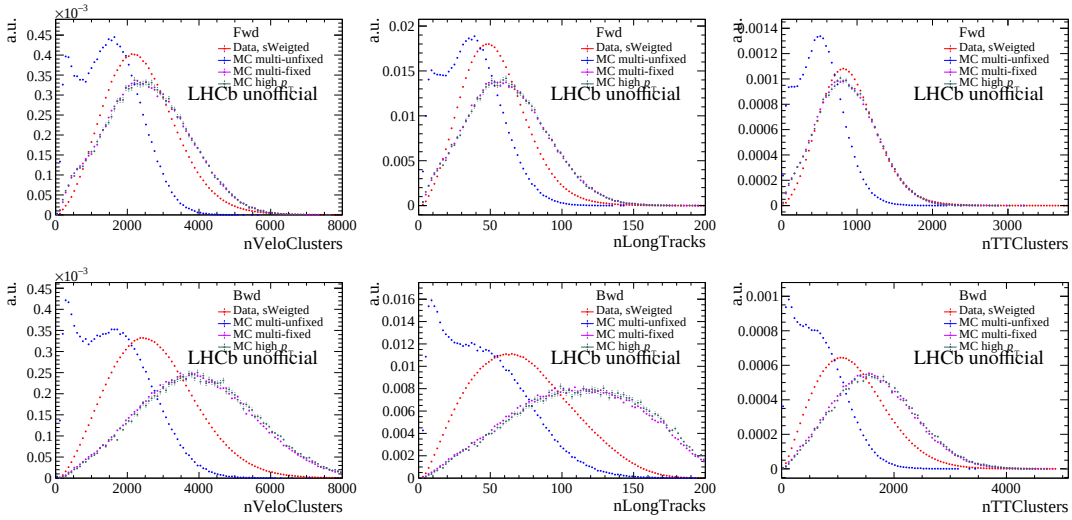

Figure 4.21 Comparisons of data and MC simulation distribution of (left) nVeloClusters, (middle) nLongTracks and (right) nTTClusters. The data have been weighted with *sWeight* from the D^0 invariant-mass fit and the simulations include multiplicity-unfixed samples (in full kinematic intervals), multiplicity-fixed samples (in full kinematic intervals) and multiplicity-fixed samples for $p_T(D^0) > 8\,\text{GeV}/c$. Forward comparisons are shown on the top and backward on the bottom.

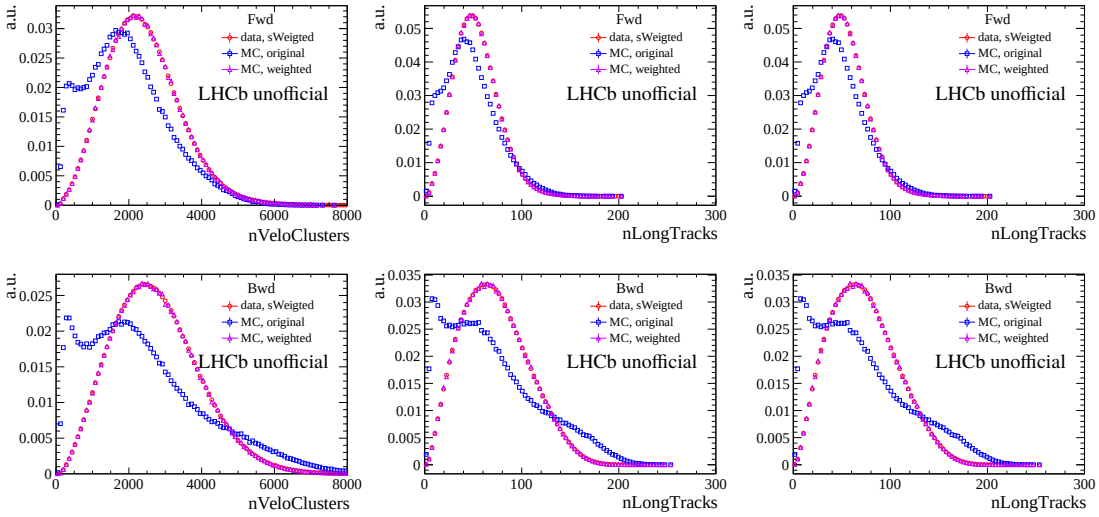

Figure 4.22 The distributions of (left) nVeloClusters, (middle) nLongTracks and (right) nTTClusters for data and simulation samples with $p_{\mathrm{T}}(D^0) < 8\,\mathrm{GeV}/c$. Weighted MC simulations, including both multiplicity-fixed and multiplicity-unfixed samples, are also shown, almost overlapping with the data. Forward comparisons are shown on the top and backward on the bottom.

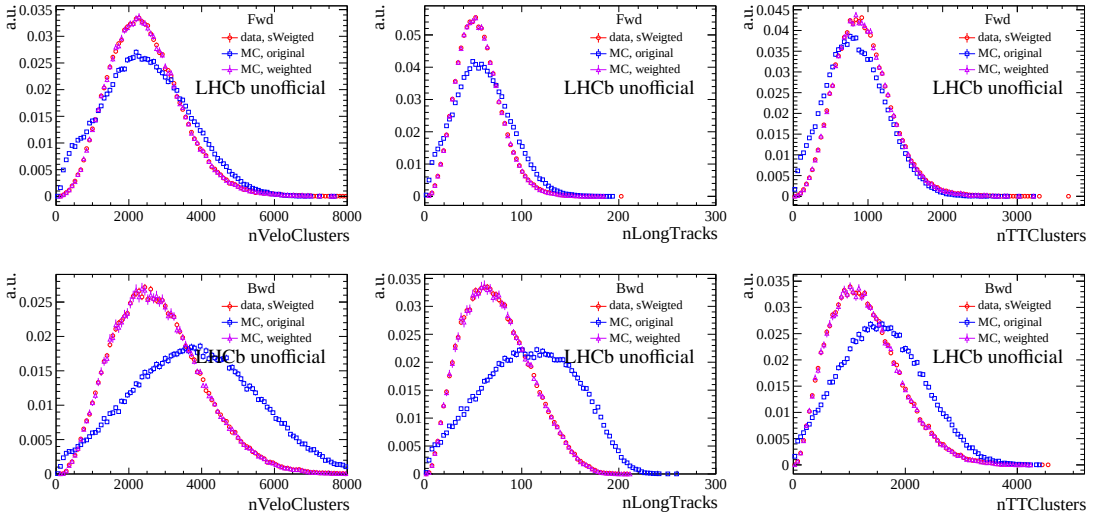

Figure 4.23 Distributions of (left) nVeloClusters, (middle) nLongTracks and (right) nTTClusters for data and simulation samples with $p_{\mathrm{T}}(D^0) > 8\,\mathrm{GeV}/c$. Weighted MC simulations, including both multiplicity-fixed and multiplicity-unfixed samples, are also shown, almost overlapping with the data. Forward comparisons are shown on the top and backward on the bottom.

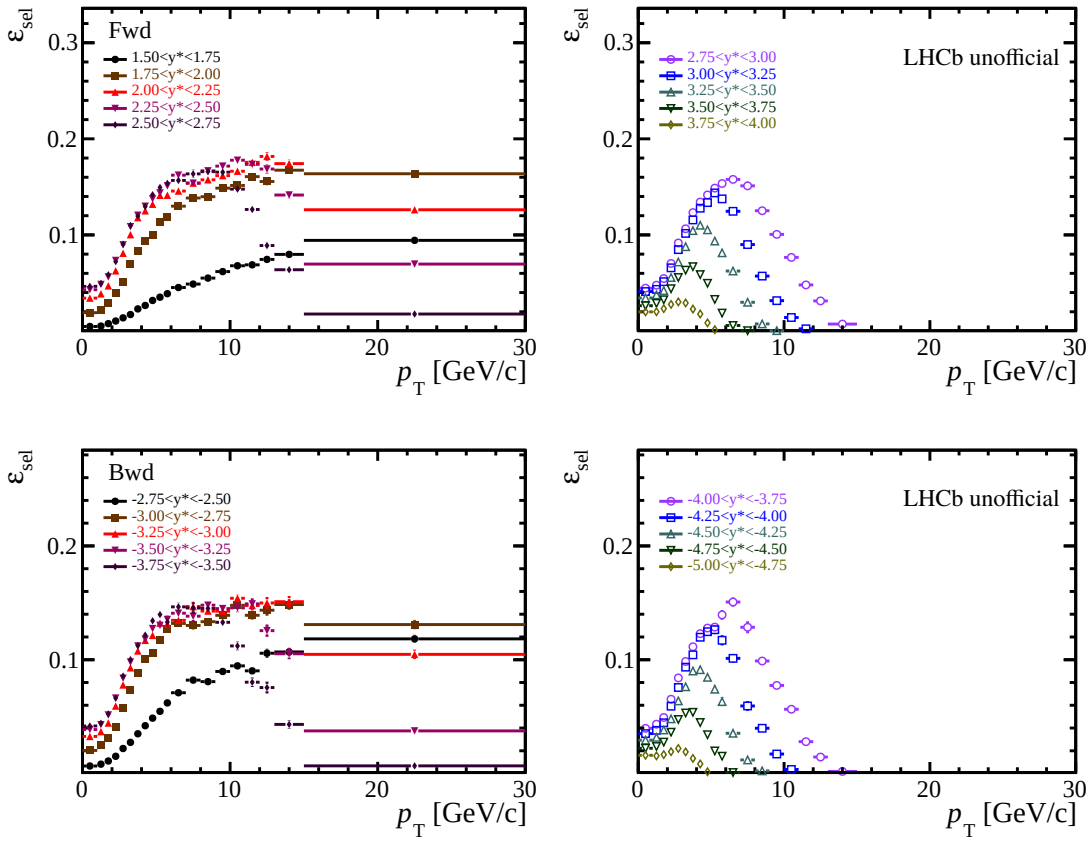

Figure 4.24 Reconstruction and selection efficiency $\varepsilon_{\text{rec\&sel}}$ as a function of p_T and y^* of prompt D^0 meson for (top) forward and (bottom) backward samples with all corrections considered. The error bars show the statistical uncertainties.

A.4.

4.4.4 PID efficiency

The PID efficiency ε_{PID} is defined as the efficiency of the PID requirements on the two hadron tracks in D^0 selection. The ε_{PID} is determined using the single track PID efficiency obtained from data convolved with the kinematic distributions in *sWeight* data in each D^0 kinematic interval according to the formula

$$\varepsilon_{\text{PID}} \equiv \frac{\sum_i^N sWeight_i}{\sum_i^N sWeight_i \Big/ \left(\varepsilon_K(p_i^K, \eta_i^K, \text{nSPDHits}) \times \varepsilon_\pi(p_i^\pi, \eta_i^\pi, \text{nSPDHits})\right)}, \tag{4.13}$$

where N is the number of the events in the *sWeight* data samples, and the nSPDHits is the number of hits in the SPD detector. In Tables 3.1 and 4.1, the selections are $\text{DLL}_{K-\pi}(K^-) > 5$ and $\text{DLL}_{K-\pi}(\pi^+) < 0$ for K and π candidates respectively. Because PID variables are not well described by simulations, a data-driven tag-and-probe method[217-218] is employed instead. The PID efficiency ε_K and ε_π as functions of p, η

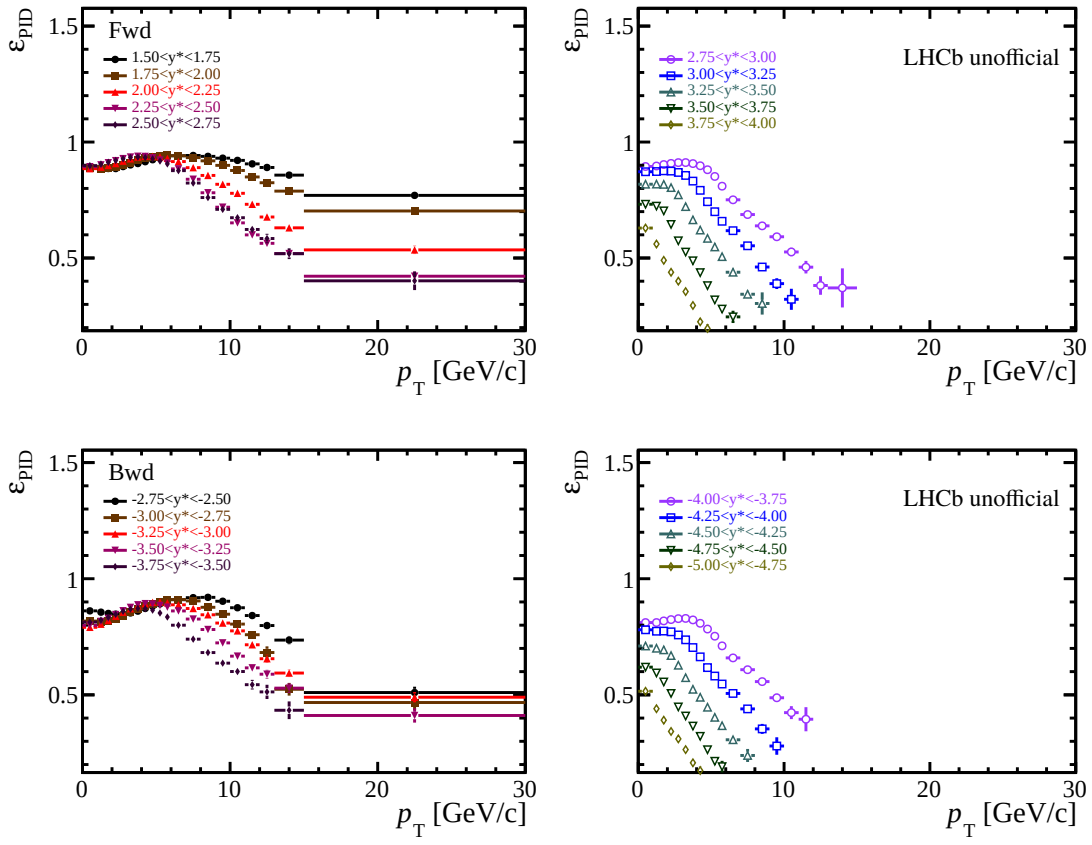

Figure 4.25 PID efficiency ε_{PID} as a function of p_{T} and y^* of prompt D^0 meson for forward (top) and backward (bottom) configurations. The error bars show the statistical uncertainties.

and nSPDHits (also known as the PID calibration table) can be obtained from the package `PIDCalib` of URANIA. The efficiencies are evaluated for between forward and backward samples separately. Then Eq. 4.13 can be applied for getting the ε_{PID} as shown in Fig. 4.25 and listed in Tables A.5 and A.6 in Appendix A.1. The uncertainties of in ε_K and ε_π given by `PIDCalib` will be considered as systematic uncertainties as discussed in the next section.

4.4.5 Trigger efficiency

In LHCb experiment, Run 2 data are required to pass the trigger on signal (TOS) of HLT1 and HLT2, where TOS refers to trigger on selection. Since the `L0SPD` trigger is fully efficient with 100% efficient for D^0 events and HLT2 efficiency has been considered in other offline selection efficiencies, only HLT1 selections need to be considered in $\varepsilon_{\text{trigger}}$. The $\varepsilon_{\text{trigger}}$ is defined as

$$\varepsilon_{\text{trigger}}(p_{\text{T}}, y^*) \equiv \frac{D^0 \text{ TOS of HLT1 in interval } (p_{\text{T}},y^*)}{D^0 \text{ selected in interval } (p_{\text{T}},y^*)}\,, \tag{4.14}$$

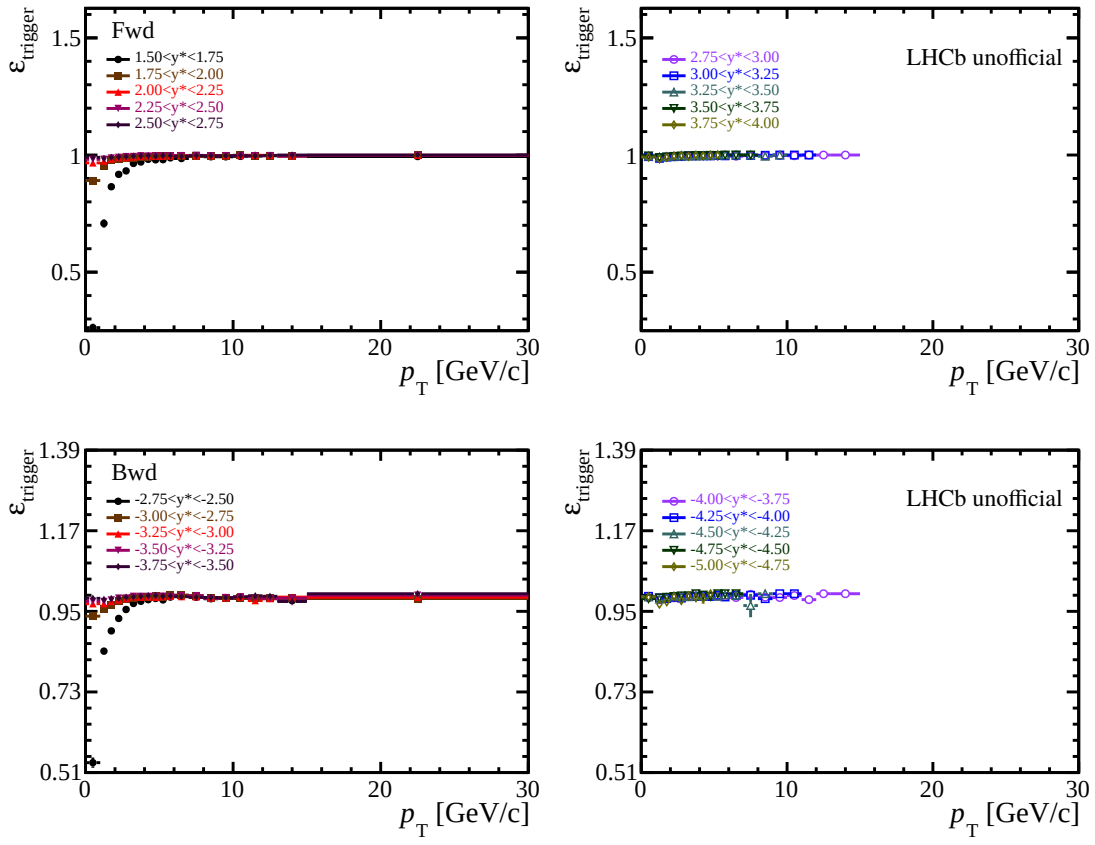

Figure 4.26 Trigger efficiency $\varepsilon_{\text{trigger}}$ as a function of p_T and y^* of prompt D^0 meson for (top) forward and (bottom) backward samples. The error bars show the statistical uncertainties.

where tracking correction and multiplicity corrections are applied to both numerator and denominator. Benefiting from the offline-like online selections in trigger, the HLT1 efficiency can be calculated with the simulation sample. The trigger requirement `(D0_Hlt1TrackMVADecision_TOS1 || D0_Hlt1TwoTrackMVADecision_TOS)` is applied to the selected D^0 events. The result is shown in Fig. 4.26 while the numerical results are listed in Tables A.7 and A.8 in Appendix A.1. This efficiency can also be evaluated with a data-driven method named *TISTOS*[219]. A cross-check is performed and will be discussed in the systematic uncertainty section 4.5.2.

4.4.6 Total efficiency

The total efficiencies ε_{tot} are obtained directly from the multiplication of the efficiencies in Eq. 4.5. The results are shown in Fig. 4.27 and listed in Table A.9 and A.10 in Appendix A.1. The uncertainties are due to simulation sample size, which are considered uncorrelated between intervals.

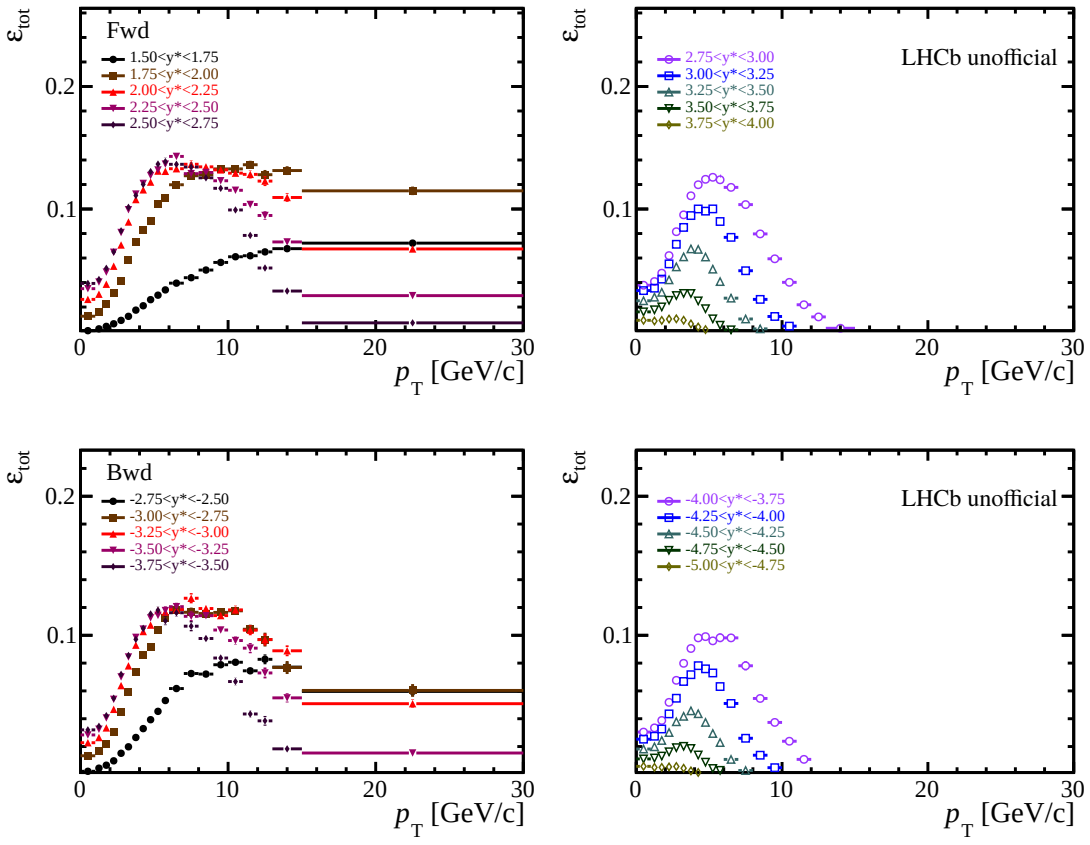

Figure 4.27 Total efficiency ε_{tot} as a function of p_{T} and y^* of prompt D^0 meson for (left) forward and (right) backward configurations.

4.5 Systematic uncertainties

The systematic uncertainties are evaluated separately for the forward and backward configurations, if not specified, due to very different environments in the two kinematic regions.

4.5.1 Signal yield determination

In this analysis, the prompt D^0 signal yields are determined through a two-step fit, and the uncertainties for each step are estimated separately. For the $M(K\pi)$ fit, the signal shape is switched from the sum of a CB function and a Gaussian to the sum of two CB functions. To see how these changes affect the final results, $\log_{10}\left(\chi^2_{\text{IP}}\right)$ fit is also performed to get the prompt yields. The maximum of the differences are treated as the systematic uncertainties, which are shown in Fig. 4.28. For most of the bins, the uncertainties are less than 7%.

For the estimation of systematic uncertainty originating from the $\log_{10}\left(\chi^2_{\text{IP}}\right)$ fit, multiple variations in this fit are performed. In the default $\log_{10}\left(\chi^2_{\text{IP}}\right)$ fit the ρ_L and ρ_R for prompt component and the ρ_L, ρ_R and ϵ for non-prompt component are fixed from simu-

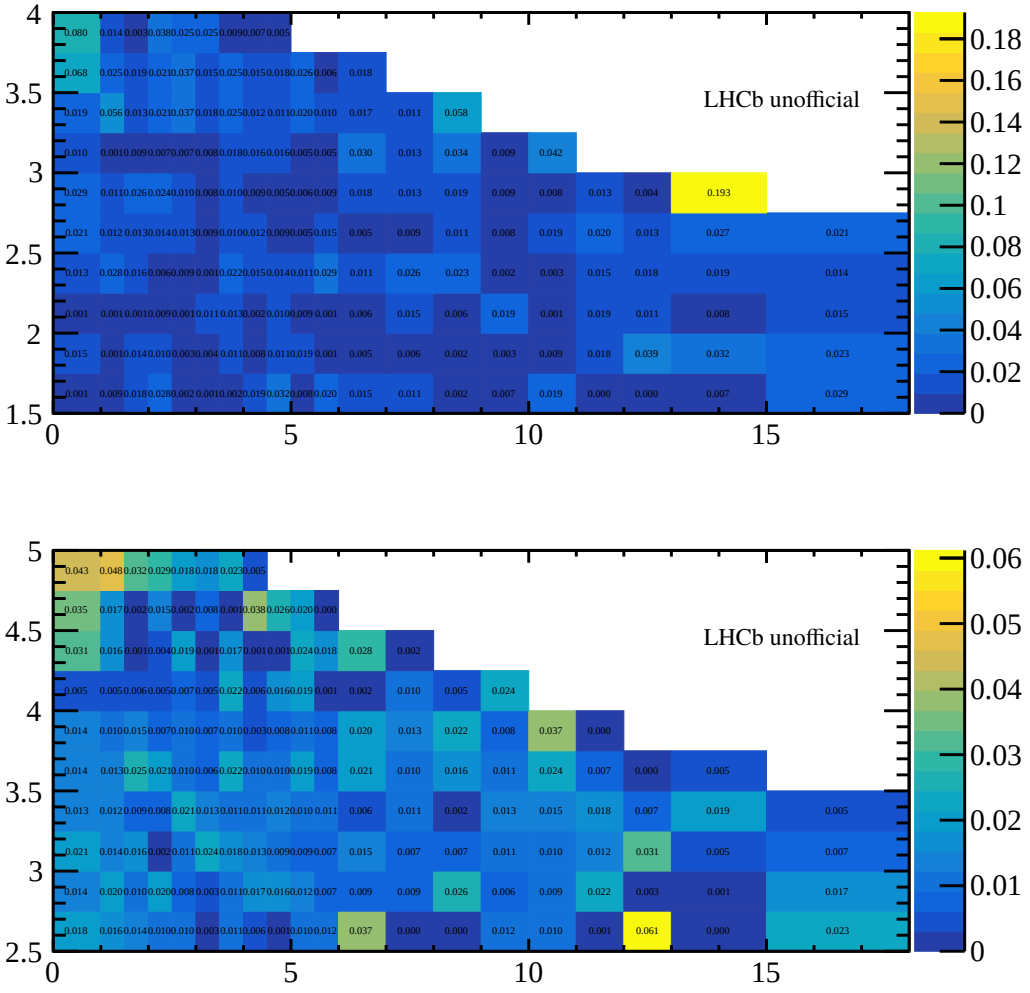

Figure 4.28 Relative systematic uncertainties of $M(K\pi)$ fit as a function of p_{T} and y^* for (top) forward and (bottom) backward configurations. The p_{T} range of the rightmost intervals is folded from $15-30\,\mathrm{GeV}/c$ to $15-18\,\mathrm{GeV}/c$.

lations. These values are changed to one sigma away from the default values. The default shape of non-prompt $\log_{10}\left(\chi^2_{\mathrm{IP}}\right)$ Bukin function is changed to a Gaussian to evaluate the uncertainty on this shape. Besides, a two-dimensional sideband fit method is used to determine the prompt signal yield. In this method, the background $\log_{10}\left(\chi^2_{\mathrm{IP}}\right)$ distribution is estimated with the kernel density function[220] out of the $M(K\pi)$ signal window. And the fit is performed on the two-dimensional $(M(K\pi), \log_{10}\left(\chi^2_{\mathrm{IP}}\right))$ distribution, where prompt and from-b D^0 candidates and background are all included. The differences between the default results obtainted in Section 4.3 and these results are calculated and their maximum are considered as the systematic uncertainty from the $\log_{10}\left(\chi^2_{\mathrm{IP}}\right)$ fit. The uncertainties in this step are summarised in Fig. 4.29, found to be less than 7% for low p_{T} bins while larger for high p_{T} bins. The systematics uncertainties in both steps are considered uncorrelated between forward and backward data.

4.5.2 Efficiency

In the estimation of the efficiencies, the values are provided with error bars, which are treated as the systematic uncertainties due to limited simulation sample size, as shown in Fig. 4.30.

The uncertainties in tracking correction table should be propagated into the result of efficiencies. To evaluated this, 100 toy samples of tracking tables are generated from Gaussian distributions, of which the μ is the mean value and σ the error bar for each bin. These samples are used to evaluate the efficiencies. The standard deviations of these efficiencies for each D^0 interval is treated as systematic uncertainties. An additional uncertainty of 1.1%(1.4%) is assigned to the K (π) due to the hadronic interactions of these particles with the detector. This uncertainty is dominated by the uncertainty on the material budget and full correlation between kaons and pions is assumed, yielding a total uncertainty of 2.5%[123] for D^0 efficiencies, independent of p_{T} and y^*. Besides, different methods used for the tracking correction[186] will introduce an uncertainty at the level of 0.8% per track and 1.6% on total for this analysis. The result, obtained by adding the aforesaid terms in quadrature, is shown in Fig. 4.31.

For the multiplicity corrections, three different variables are applied in the weighting of simulation samples. The standard deviation for the three efficiency tables are taken as the systematic uncertainties, which are determined in each kinematic bin. The results are shown in Fig. 4.32.

For PID efficiencies, the uncertainties originated from those in the PID calibration

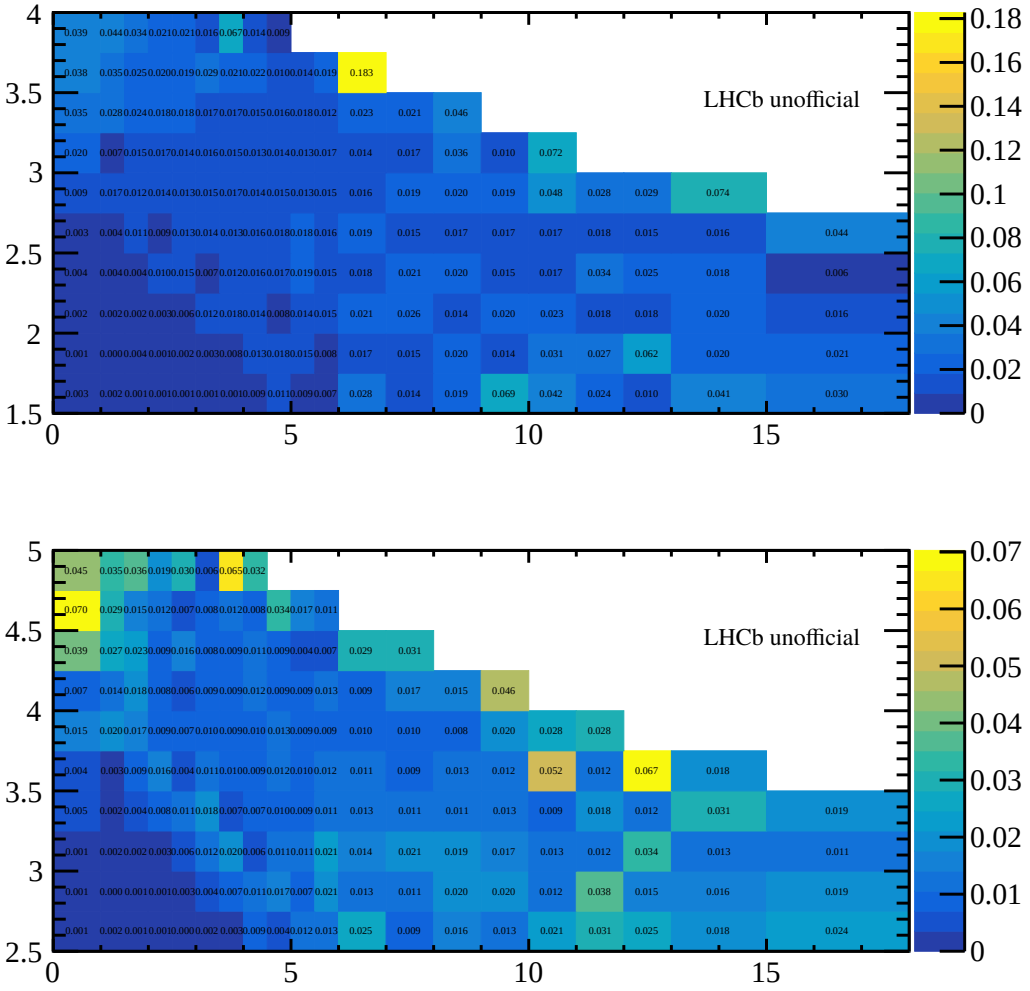

Figure 4.29 Relative systematic uncertainties of $\log_{10}\left(\chi^2_{\mathrm{IP}}\right)$ fit as a function of p_{T} and y^* for (top) foward and (bottom) backward configurations. The p_{T} range of the rightmost intervals is folded from $15-30\,\mathrm{GeV}/c$ to $15-18\,\mathrm{GeV}/c$.

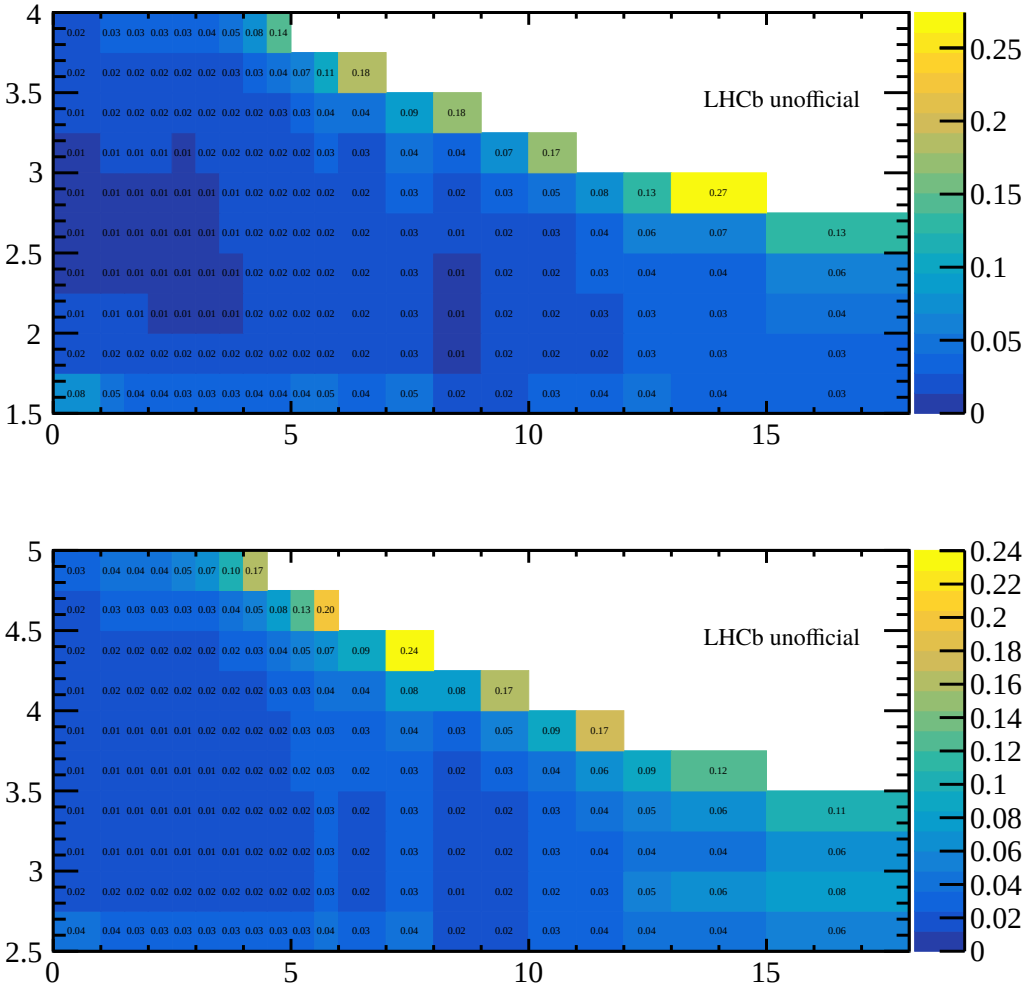

Figure 4.30 Relative systematic uncertainties due to limited simulation sample size as a function of p_{T} and y^* for (top) forward and (bottom) backward configurations. The p_{T} range of the rightmost intervals is folded from $15-30\,\mathrm{GeV}/c$ to $15-18\,\mathrm{GeV}/c$.

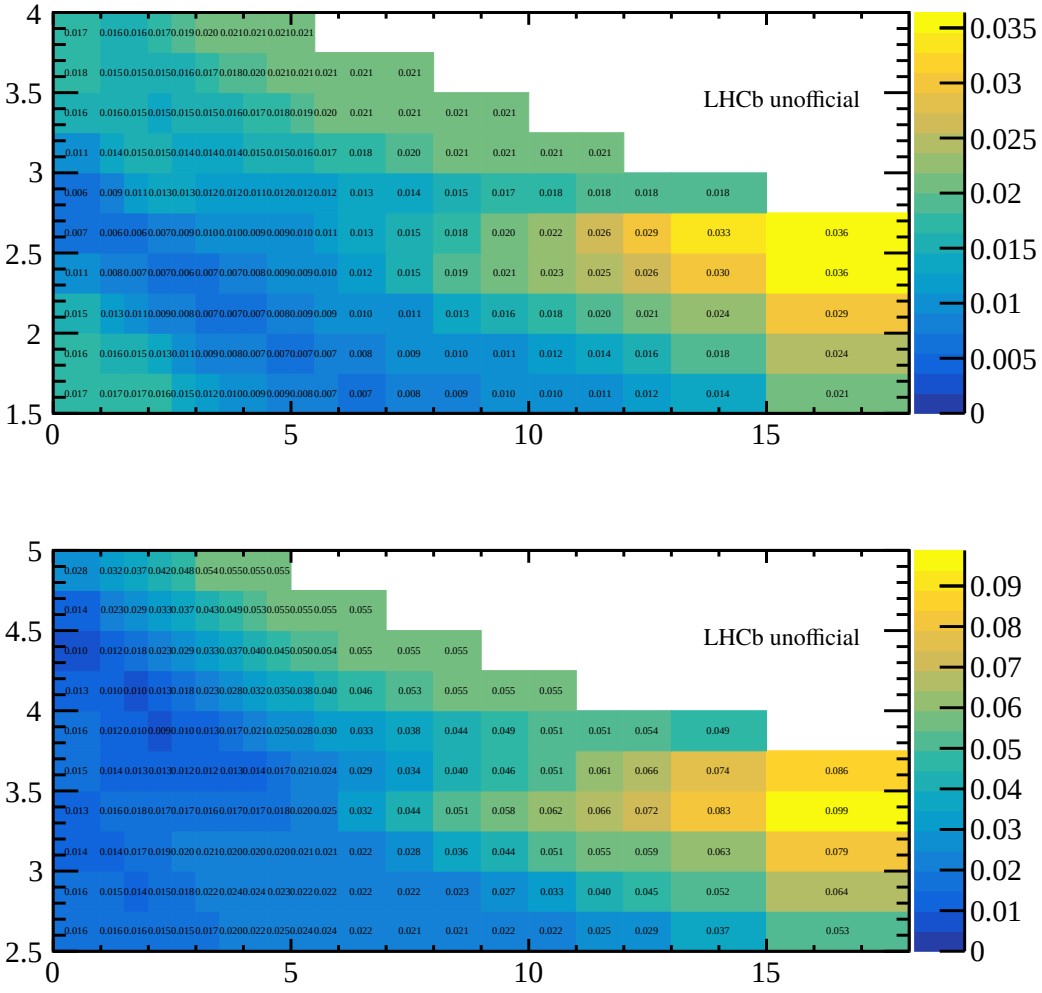

Figure 4.31 Relative systematic uncertainties from tracking correction as a function of p_{T} and y^* for (top) forward and (bottom) backward configurations. The p_{T} range of the rightmost intervals is folded from $15-30\,\mathrm{GeV}/c$ to $15-18\,\mathrm{GeV}/c$.

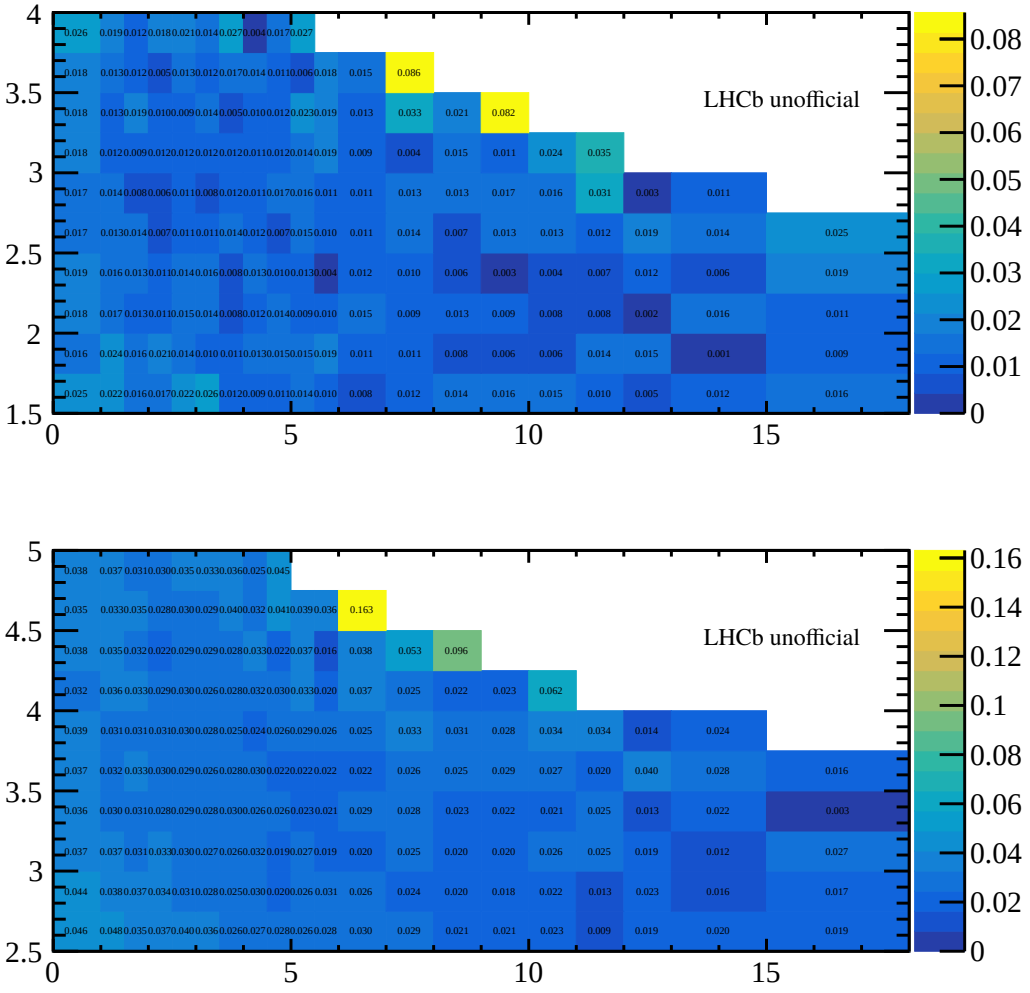

Figure 4.32 Relative systematic uncertainties from multiplicity correction as a function of p_{T} and y^* for (top) forward and (bottom) backward configurations. The p_{T} range of the rightmost intervals is folded from $15 - 30\,\mathrm{GeV}/c$ to $15 - 18\,\mathrm{GeV}/c$.

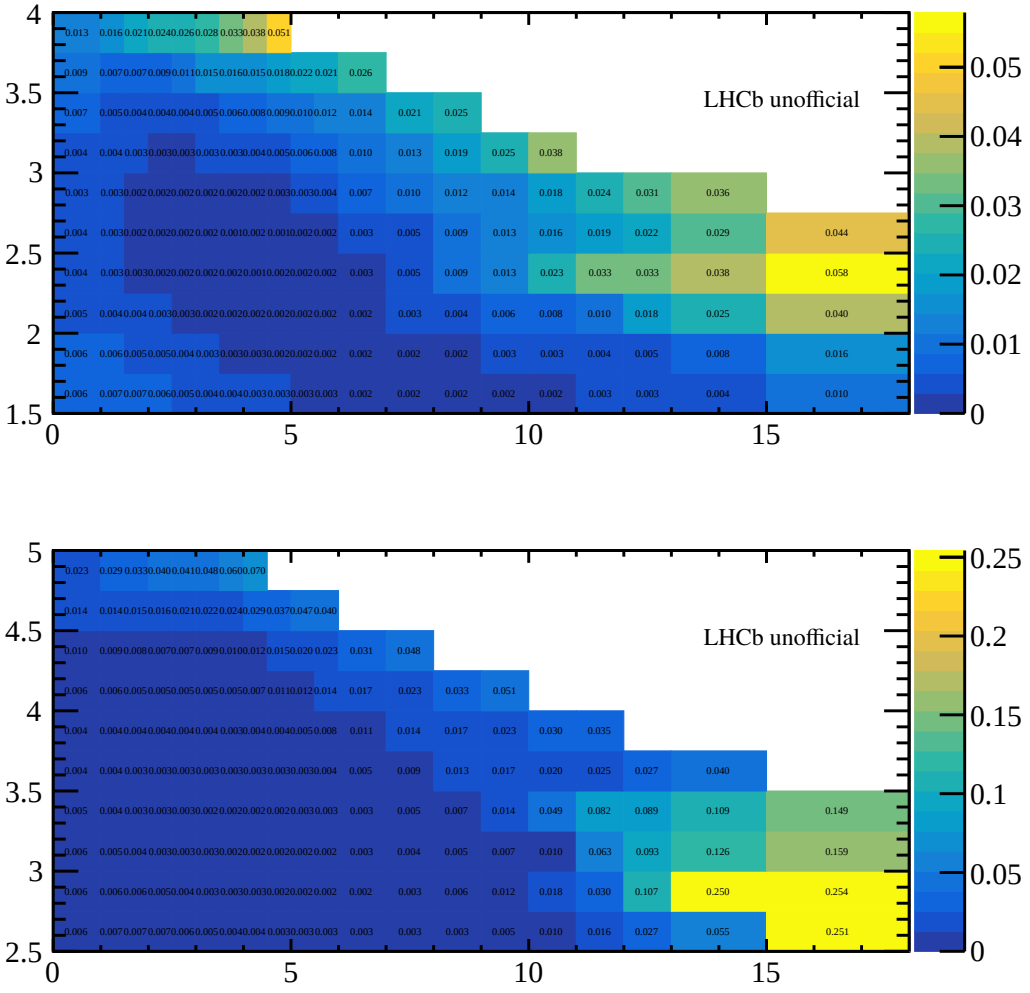

Figure 4.33 Relative systematic uncertainties from the K/π PID calibration table as a function of p_{T} and y^* for (top) forward and (bottom) backward configurations. The p_{T} range of the rightmost intervals is folded from $15-30\,\mathrm{GeV}/c$ to $15-18\,\mathrm{GeV}/c$.

tables can be evaluated with the same method as tracking uncertainty, which is shown in Fig. 4.33. The default multiplicity variable of the PID calibration table is nSPDHits. For the estimation of the systematic uncertainties in PID efficiency due to multiplicity variable choice, this variable is changed to nVeloClusters and the difference is taken as the uncertainties, which is shown in Fig. 4.34.

For trigger (HLT1) efficiency, another data-driven method *TISTOS* is used to cross-check the default efficiency calculated with simulation samples, as well as to estimate the systematic uncertainty. The triggered events in the LHCb experiment can be classified into three categories. The first one is the TOS as mentioned before. Another one, where the trigger objects are not associated with the signal candidates, is tagged as trigger independent of signal (TIS). There exist also events triggered by both TIS and TOS (TIS&TOS).

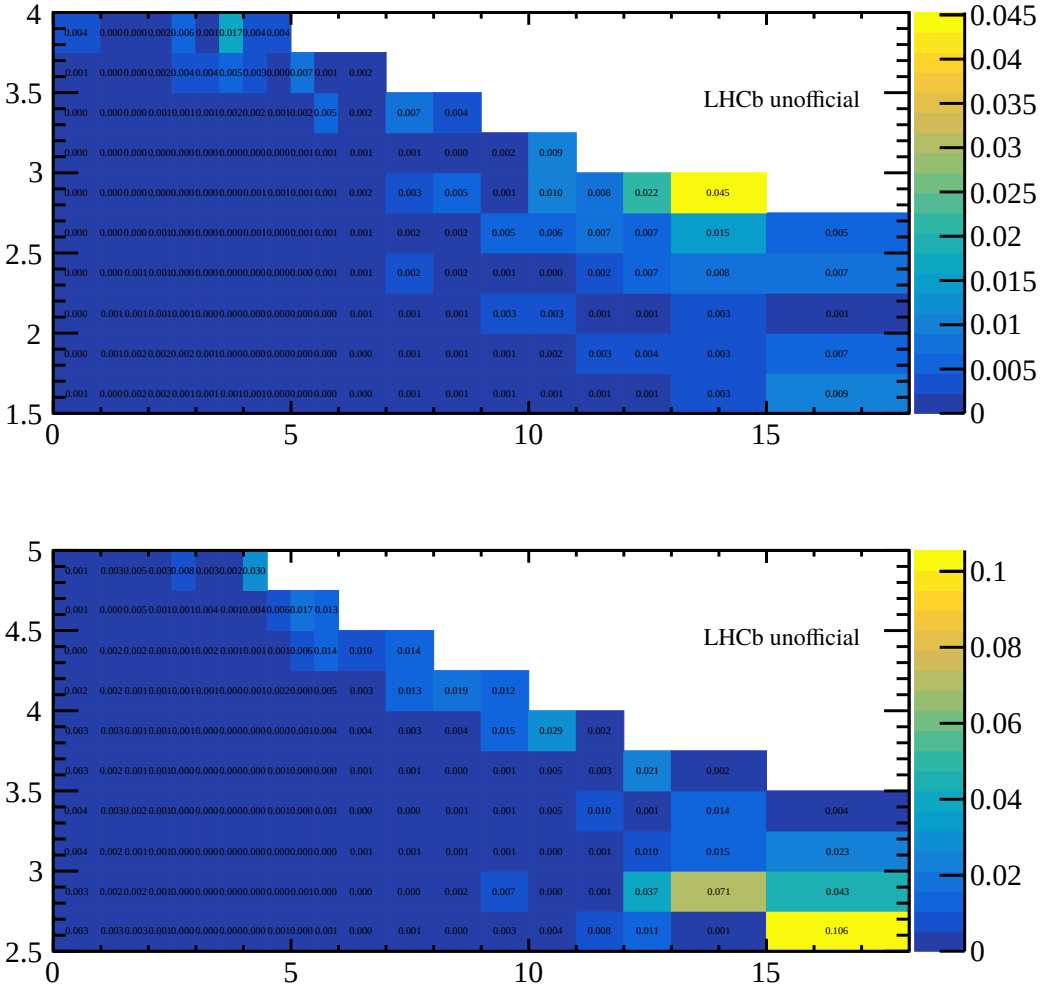

Figure 4.34 Relative systematic uncertainties from the multiplicity variable chosen in the PID calibration table as a function of p_{T} and y^* for (top) forward and (bottom) backward configurations. The p_{T} range of the rightmost intervals is folded from $15-30\,\mathrm{GeV}/c$ to $15-18\,\mathrm{GeV}/c$.

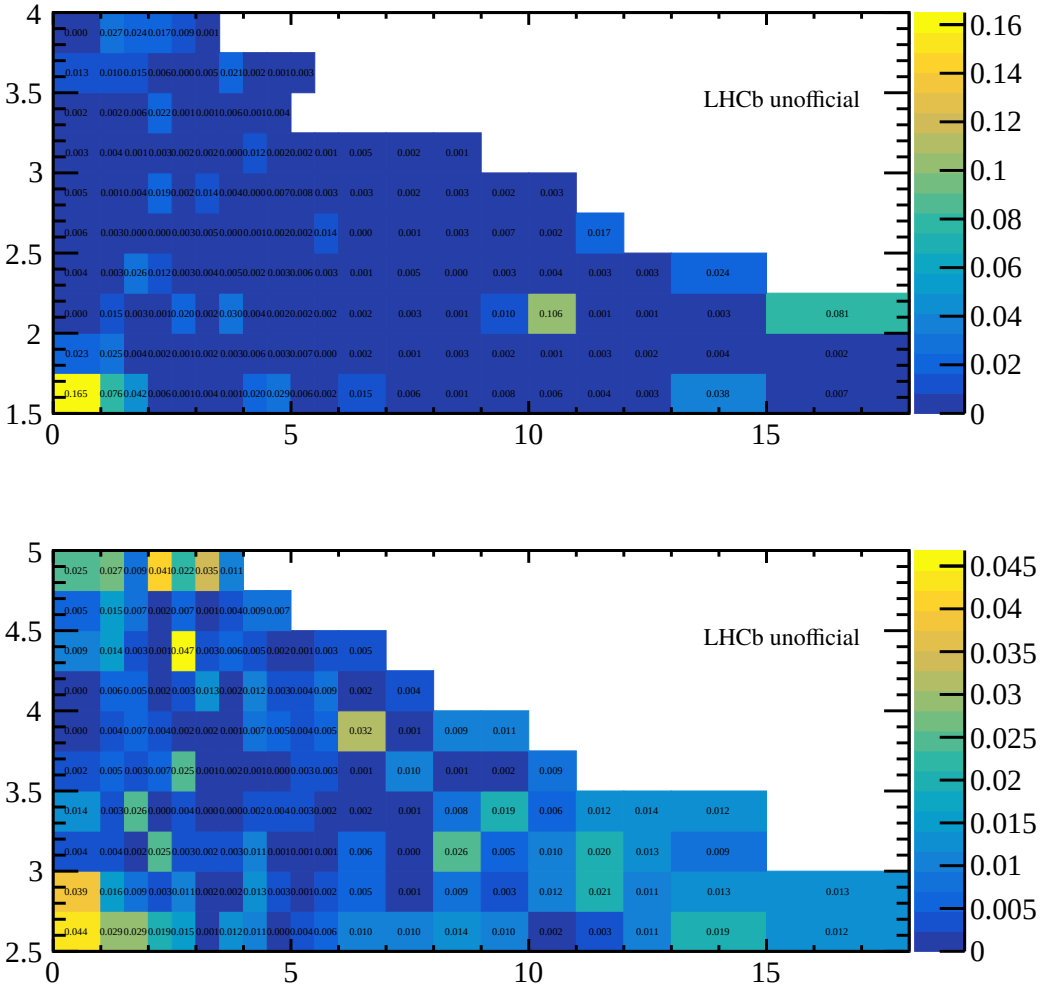

Figure 4.35 Relative systematic uncertainties of trigger efficiency as a function of p_{T} and y^* for (top) forward and (bottom) backward configurations. The p_{T} range of the rightmost intervals is folded from $15-30\,\mathrm{GeV}/c$ to $15-18\,\mathrm{GeV}/c$.

Considering that TIS and TOS are uncorrelated, the $\varepsilon^{\mathrm{TOS}}$ can be evaluated with

$$\varepsilon^{\mathrm{TOS}} = N^{\mathrm{TIS\&TOS}}/N^{\mathrm{TIS}} \,. \tag{4.15}$$

To avoid possible biases, the minimum-bias pPb and Pbp data samples are used to reconstruct D^0 candidates, and the yields N are obtained from the two step fit used above. The corresponding uncertainties can then be obtained by comparing the efficiencies obtained from these two different methods, as presented in Fig. 4.35.

4.5.3 Other systematics

The relative uncertainty of the luminosity is 2.6% for forward and 2.5% for backward data samples, respectively. The relative uncertainty of the branching fraction

Table 4.3 Systematic uncertainties considered in this measurement, in %. The range indicates the minimum and the maximum value among the two-dimensional p_T and y^* intervals. The systematic uncertainties due to simulation sample size, mass fit and $\log_{10}\left(\chi^2_{IP}\right)$ fit are uncorrelated across the intervals. The other sources of systematic uncertainties are fully correlated between different intervals.

Uncertainty source	Forward [%]	Backward [%]
Tracking calibration	3.0 – 4.7	3.1 – 10.7
PID	0.2 – 6.9	0.2 – 26.5
Trigger efficiency	0.0 – 16.5	0.0 – 4.7
Multiplicity correction	0 – 9	0 – 16
Luminosity	2.6	2.5
Branching fraction	0.8	0.8
Mass fit	0.0 – 19.3	0.1 – 6.1
$\log_{10}\left(\chi^2_{IP}\right)$ fit	0.3 – 19.5	0.4 – 7.0
Simulation sample size	1 – 40	1 – 26
pp interpolation	3.4 – 17.5	3.4 – 28.8

$\mathcal{B}(D^0 \to K^-\pi^+)$ is 0.8%.

4.5.4 Summary of systematic uncertainties

The systematic uncertainties in each step are added in quadrature to get the total uncertainties, summarised in Table 4.3. The systematic uncertainty from pp interpolation in the calculation of $R_{p\mathrm{Pb}}$ is also included, which will be explained later.

4.6 Results

4.6.1 Production cross-section

The measured double-differential cross-section of prompt D^0 mesons is shown in Fig. 4.36. The total prompt D^0 production cross-section, obtained by integrating the double-differential measurements, is $297.6 \pm 0.6 \pm 14.0\,\mu$b in the kinematic range of $0 < p_T < 30\,\mathrm{GeV}/c$ and $1.5 < y^* < 4.0$ for the forward rapidity region, and $315.2 \pm 0.2 \pm 17.8\,\mu$b in the kinematic range of $0 < p_T < 30\,\mathrm{GeV}/c$ and $-5.0 < y^* < -2.5$ in the backward rapidity region. The first uncertainties are statistical and the second systematic. Numerical values for the double-differential cross-section are listed in the Tables A.17 and A.18 in Appendix A.3. The one-dimensional differential cross-sections $\mathrm{d}\sigma/\mathrm{d}p_T$ and $\mathrm{d}\sigma/\mathrm{d}y^*$ can be obtained by integrating the double-differential

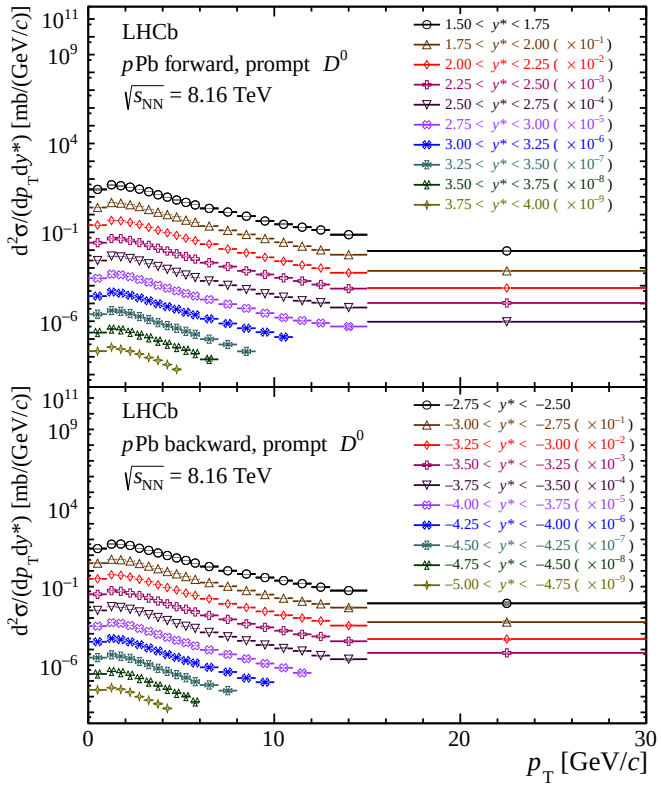

Figure 4.36 Double-differential cross-sections of prompt D^0 mesons in pPb collisions in the (top) forward and (bottom) backward rapidity regions. To display the differential cross-section values in different rapidity intervals, multiplicative factors of 10^{-n} are used with n increasing with rapidity value. The uncertainties are smaller than the symbol size.

cross-section along another dimension. For the $d\sigma/dp_T$, two different integral regions are considered, which are $1.5 < y* < 4.0$ and $2.5 < y^* < 4.0$ at forward rapidity, and $-5.0 < y* < -2.5$ and $-4.0 < y^* > -2.5$ at backward rapidity. The results are presented in Fig. 4.37 and the numerical values are listed in Tables 4.4, 4.5, 4.6, 4.7, 4.8 and 4.9.

4.6.2 Nuclear modification factor

The nuclear modification factor $R_{p\mathrm{Pb}}$ as a function of p_T and $y*$ can be defined as.

$$R_{p\mathrm{Pb}}(p_T, y^*) \equiv \frac{1}{A} \frac{d^2\sigma_{p\mathrm{Pb}}(p_T, y^*)/(dp_T dy^*)}{d^2\sigma_{pp}(p_T, y^*)/(dp_T dy^*)}, \tag{4.16}$$

where $A = 208$ is the mass number of the lead nucleus and σ_{pp} is the prompt D^0 production cross-section in pp collisions at $\sqrt{s} = 8.16\,\mathrm{TeV}$. An interpolation between LHCb measurements at $\sqrt{s} = 5.02\,\mathrm{TeV}$ and $\sqrt{s} = 13\,\mathrm{TeV}$ [214,221] is performed to obtain $d^2\sigma_{pp}(p_T, y^*)/(dp_T dy^*)$, using a power-law function $\sigma(\sqrt{s}) = p_0 \left(\sqrt{s}\right)^{p_1}$. A linear function is also considered. An example is shown in Fig. 4.38 The interpolation uncer-

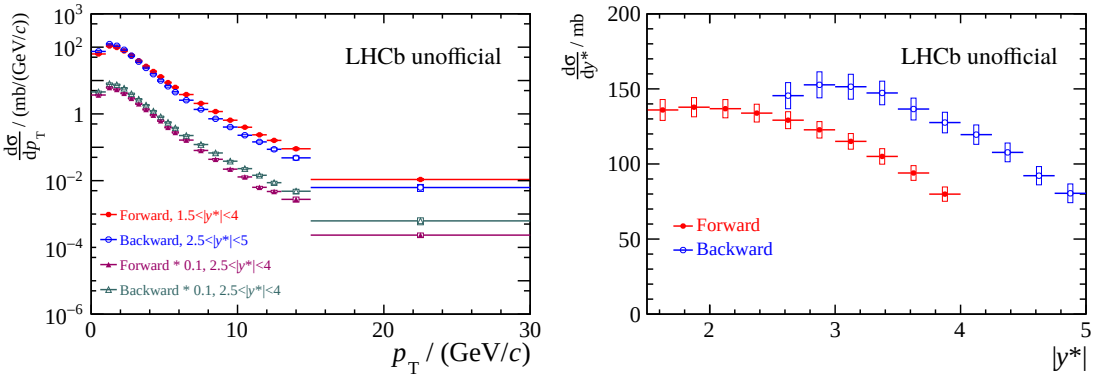

Figure 4.37 One-dimensional prompt D^0 production cross-sections (left) $\mathrm{d}\sigma/\mathrm{d}p_\mathrm{T}$ and (right) $\mathrm{d}\sigma/\mathrm{d}y^*$ in pPb collisions for forward and backward rapidities. The error bars show the statistical uncertainties and the boxes show the systematic uncertainties.

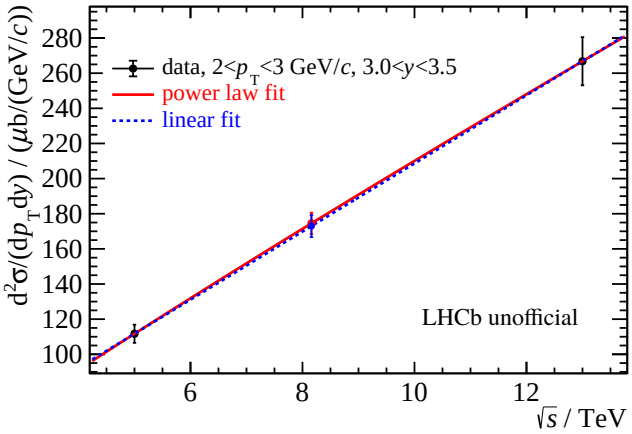

Figure 4.38 Interpolation of D^0 cross-sections in pp collision at $\sqrt{s} = 8.16\,\mathrm{TeV}$ with a power function and a linear function, in the kinematic range $2 < p_\mathrm{T} < 3\,\mathrm{GeV}/c$ and $3.0 < y^* < 3.5$. The data points are LHCb results at 5,13 TeV in pp collisions.

Table 4.4 One-dimensional cross-sections $\mathrm{d}\sigma/\mathrm{d}p_\mathrm{T}$ for prompt $D^0 + \overline{D}^0$ mesons as a function of p_T in forward rapidity regions, integrated over $1.5 < y^* < 4.0$. The first uncertainty is statistical, the second is the component of the systematic uncertainty that is uncorrelated between bins and the third is the correlated component.

	Forward
p_T/(GeV/c)	$(\mathrm{d}\sigma/\mathrm{d}p_\mathrm{T})$/(mb/(GeV/$c$))
(0.0,1.0]	$62.59 \pm 0.59 \pm 0.94 \pm 2.93$
(1.0,1.5]	$108.31 \pm 0.19 \pm 1.21 \pm 4.95$
(1.5,2.0]	$97.84 \pm 0.16 \pm 0.87 \pm 4.36$
(2.0,2.5]	$77.08 \pm 0.14 \pm 0.69 \pm 3.40$
(2.5,3.0]	$56.66 \pm 0.10 \pm 0.48 \pm 2.53$
(3.0,3.5]	$39.18 \pm 0.08 \pm 0.31 \pm 1.74$
(3.5,4.0]	$26.70 \pm 0.07 \pm 0.26 \pm 1.17$
(4.0,4.5]	$18.66 \pm 0.06 \pm 0.18 \pm 0.81$
(4.5,5.0]	$12.98 \pm 0.05 \pm 0.15 \pm 0.57$
(5.0,5.5]	$8.68 \pm 0.03 \pm 0.10 \pm 0.38$
(5.5,6.0]	$6.24 \pm 0.03 \pm 0.08 \pm 0.27$
(6.0,7.0]	$3.81 \pm 0.02 \pm 0.06 \pm 0.17$
(7.0,8.0]	$2.06 \pm 0.01 \pm 0.03 \pm 0.09$
(8.0,9.0]	$1.18 \pm 0.01 \pm 0.02 \pm 0.05$
(9.0,10.0]	$0.65 \pm 0.01 \pm 0.01 \pm 0.03$
(10.0,11.0]	$0.40 \pm 0.01 \pm 0.01 \pm 0.02$
(11.0,12.0]	$0.24 \pm 0.00 \pm 0.00 \pm 0.01$
(12.0,13.0]	$0.16 \pm 0.00 \pm 0.00 \pm 0.01$
(13.0,15.0]	$0.09 \pm 0.00 \pm 0.00 \pm 0.00$
(15.0,30.0]	$0.01 \pm 0.00 \pm 0.00 \pm 0.00$

tainty comprises the difference between the two interpolation models, and the propagated total uncertainties from the pp measurements, and typically amounts to 3% (5%) at forward (backward) rapidity. The interpolation is performed within the common measured kinematic range of $p_\mathrm{T} < 10\,\mathrm{GeV}/c$ and $2.0 < y < 4.5$ for 5.02 and 13 TeV pp results, hence $R_{p\mathrm{Pb}}$ is measured in that range.

The nuclear modification factor of the D^0 meson as a function of p_T is displayed in Fig. 4.39, where eight panels report the results in different y^* subintervals of $\Delta y^* = 0.5$ and the two left panels are in the common range between the forward and backward rapidity coverage, $2.5 < |y^*| < 4$. The numerical values are given in Tables 4.10 and 4.11.

Table 4.5 One-dimensional cross-sections $\mathrm{d}\sigma/\mathrm{d}p_\mathrm{T}$ for prompt D^0 + $\overline{D}^0$ mesons as a function of p_T in backward rapidity regions, integrated over $-5.0 < y^* < -2.5$. The first uncertainty is statistical, the second is the component of the systematic uncertainty that is uncorrelated between bins and the third is the correlated component.

	Backward
p_T/(GeV/c)	$(\mathrm{d}\sigma/\mathrm{d}p_\mathrm{T})$/(mb/(GeV/$c$))
(0.0,1.0]	$74.50 \pm 0.09 \pm 0.96 \pm 4.31$
(1.0,1.5]	$123.66 \pm 0.18 \pm 1.20 \pm 6.95$
(1.5,2.0]	$110.11 \pm 0.18 \pm 0.96 \pm 6.04$
(2.0,2.5]	$83.55 \pm 0.12 \pm 0.63 \pm 4.50$
(2.5,3.0]	$55.35 \pm 0.08 \pm 0.41 \pm 3.02$
(3.0,3.5]	$36.86 \pm 0.06 \pm 0.29 \pm 2.00$
(3.5,4.0]	$23.86 \pm 0.06 \pm 0.23 \pm 1.30$
(4.0,4.5]	$15.47 \pm 0.05 \pm 0.15 \pm 0.86$
(4.5,5.0]	$10.02 \pm 0.03 \pm 0.10 \pm 0.53$
(5.0,5.5]	$6.71 \pm 0.03 \pm 0.08 \pm 0.37$
(5.5,6.0]	$4.48 \pm 0.02 \pm 0.06 \pm 0.24$
(6.0,7.0]	$2.57 \pm 0.01 \pm 0.04 \pm 0.15$
(7.0,8.0]	$1.36 \pm 0.01 \pm 0.02 \pm 0.08$
(8.0,9.0]	$0.71 \pm 0.01 \pm 0.01 \pm 0.04$
(9.0,10.0]	$0.40 \pm 0.00 \pm 0.01 \pm 0.02$
(10.0,11.0]	$0.23 \pm 0.00 \pm 0.00 \pm 0.02$
(11.0,12.0]	$0.15 \pm 0.00 \pm 0.00 \pm 0.01$
(12.0,13.0]	$0.09 \pm 0.00 \pm 0.00 \pm 0.01$
(13.0,15.0]	$0.05 \pm 0.00 \pm 0.00 \pm 0.01$
(15.0,30.0]	$0.01 \pm 0.00 \pm 0.00 \pm 0.00$

The $R_{p\mathrm{Pb}}$ as a function of p_T in different y^* sub-intervals with $\Delta y^* = 0.25$ is also given in Fig. 4.40 and 4.41 for forward and backward rapidites, respectively. A significant suppression of the cross-section in pPb collisions, with respect to that in pp collisions scaled by the lead mass number, is observed at forward rapidity as well as at backward rapidity up to $y^* \sim -3.5$, confirming the existence of CNM effects in D^0 production in pPb collisions.

The $R_{p\mathrm{Pb}}$ results are compared with several theoretical calculations. The HELAC-Onia approach[222-223] is based on a data-driven modeling of the scattering at partonic level folded with the free proton PDFs[224]. The calculations are first tuned by fitting the

Table 4.6 One-dimensional cross-sections $\mathrm{d}\sigma/\mathrm{d}p_\mathrm{T}$ for prompt $D^0 + \overline{D}^0$ mesons as a function of p_T in forward rapidity regions, integrated over the common rapidity region of $2.5 < |y^*| < 4.0$. The first uncertainty is statistical, the second is the component of the systematic uncertainty that is uncorrelated between bins and the third is the correlated component.

	Forward
p_T/(GeV/c)	$(\mathrm{d}\sigma/\mathrm{d}p_\mathrm{T})$/(mb/(GeV/$c$))
(0.0,1.0]	$36.83 \pm 0.39 \pm 0.78 \pm 1.71$
(1.0,1.5]	$61.65 \pm 0.16 \pm 0.97 \pm 2.76$
(1.5,2.0]	$54.15 \pm 0.15 \pm 0.66 \pm 2.40$
(2.0,2.5]	$41.49 \pm 0.09 \pm 0.52 \pm 1.82$
(2.5,3.0]	$29.29 \pm 0.08 \pm 0.38 \pm 1.31$
(3.0,3.5]	$20.09 \pm 0.06 \pm 0.23 \pm 0.90$
(3.5,4.0]	$13.58 \pm 0.06 \pm 0.20 \pm 0.62$
(4.0,4.5]	$9.18 \pm 0.04 \pm 0.12 \pm 0.41$
(4.5,5.0]	$6.23 \pm 0.04 \pm 0.10 \pm 0.28$
(5.0,5.5]	$3.96 \pm 0.02 \pm 0.06 \pm 0.18$
(5.5,6.0]	$2.79 \pm 0.03 \pm 0.05 \pm 0.13$
(6.0,7.0]	$1.64 \pm 0.02 \pm 0.05 \pm 0.08$
(7.0,8.0]	$0.80 \pm 0.01 \pm 0.02 \pm 0.04$
(8.0,9.0]	$0.44 \pm 0.01 \pm 0.01 \pm 0.02$
(9.0,10.0]	$0.22 \pm 0.00 \pm 0.01 \pm 0.01$
(10.0,11.0]	$0.13 \pm 0.00 \pm 0.01 \pm 0.01$
(11.0,12.0]	$0.06 \pm 0.00 \pm 0.00 \pm 0.00$
(12.0,13.0]	$0.05 \pm 0.00 \pm 0.00 \pm 0.00$
(13.0,15.0]	$0.03 \pm 0.00 \pm 0.00 \pm 0.00$
(15.0,30.0]	$0.00 \pm 0.00 \pm 0.00 \pm 0.00$

cross-sections measured in pp collisions at the LHC. Then, the modified PDFs of nucleons in the Pb nucleus are introduced in the model to calculate the cross-sections in pPb collisions and to estimate the effect of nPDFs, neglecting other cold and hot nuclear matter effects. Reweighted EPPS16[82] and nCTEQ15[81] nPDF sets, where LHC heavy flavor data[123,143-145] are incorporated by performing a Bayesian-reweighting analysis[225], are used in the calculations, resulting in considerably reduced uncertainties than calculations using the default nPDFs. The uncertainties are dominated by nPDF parameterizations and correspond to a 68% confidence interval. At forward rapidity, the calculations are in general agreement with the data, except for $p_\mathrm{T} < 1\,\mathrm{GeV}/c$ where the predictions are

Table 4.7 One-dimensional cross-sections $\mathrm{d}\sigma/\mathrm{d}p_\mathrm{T}$ for prompt $D^0 + \overline{D}^0$ mesons as a function of p_T in backward rapidity regions, integrated over the common rapidity region of $2.5 < |y^*| < 4.0$. The first uncertainty is statistical, the second is the component of the systematic uncertainty that is uncorrelated between bins and the third is the correlated component.

	Backward
p_T/(GeV/c)	$(\mathrm{d}\sigma/\mathrm{d}p_\mathrm{T})$/(mb/(GeV/$c$))
(0.0,1.0]	$45.58 \pm 0.05 \pm 0.46 \pm 2.67$
(1.0,1.5]	$80.45 \pm 0.12 \pm 0.78 \pm 4.48$
(1.5,2.0]	$74.66 \pm 0.10 \pm 0.72 \pm 4.02$
(2.0,2.5]	$58.62 \pm 0.07 \pm 0.52 \pm 3.13$
(2.5,3.0]	$40.03 \pm 0.06 \pm 0.33 \pm 2.12$
(3.0,3.5]	$27.43 \pm 0.04 \pm 0.25 \pm 1.43$
(3.5,4.0]	$18.23 \pm 0.03 \pm 0.18 \pm 0.94$
(4.0,4.5]	$12.08 \pm 0.03 \pm 0.12 \pm 0.64$
(4.5,5.0]	$8.20 \pm 0.02 \pm 0.09 \pm 0.42$
(5.0,5.5]	$5.56 \pm 0.02 \pm 0.06 \pm 0.29$
(5.5,6.0]	$3.79 \pm 0.02 \pm 0.05 \pm 0.20$
(6.0,7.0]	$2.25 \pm 0.01 \pm 0.03 \pm 0.12$
(7.0,8.0]	$1.21 \pm 0.01 \pm 0.02 \pm 0.07$
(8.0,9.0]	$0.68 \pm 0.00 \pm 0.01 \pm 0.04$
(9.0,10.0]	$0.38 \pm 0.00 \pm 0.00 \pm 0.02$
(10.0,11.0]	$0.23 \pm 0.00 \pm 0.00 \pm 0.02$
(11.0,12.0]	$0.15 \pm 0.00 \pm 0.00 \pm 0.01$
(12.0,13.0]	$0.09 \pm 0.00 \pm 0.00 \pm 0.01$
(13.0,15.0]	$0.05 \pm 0.00 \pm 0.00 \pm 0.01$
(15.0,30.0]	$0.01 \pm 0.00 \pm 0.00 \pm 0.00$

about 2 standard deviations larger than the data. This discrepancy suggests stronger shadowing or additional energy loss at low x. At backward rapidity, for $p_\mathrm{T} > 6\,\mathrm{GeV}/c$ and $-3.5 < y^* < -2.5$ the data are lower than the calculations by $2.0 - 3.8$ standard deviations, indicating a weaker antishadowing effect or possible final-state effects.

The nuclear modification factor is also compared with two calculations based on the CGC effective field theory, CGC1 and CGC2. Since gluon saturation is expected to occur at small x and Q^2, the calculations are applicable for $p_\mathrm{T} < 5\,\mathrm{GeV}/c$ at forward rapidity where saturation effects are relevant. For CGC1 [226-227] the D-meson production is calculated with the color dipole formalism, and the optical Glauber model is used to relate

Table 4.8 One-dimensional cross-sections $\mathrm{d}\sigma/\mathrm{d}y$ for prompt $D^0 + \overline{D}^0$ mesons as a function of y^* in forward rapidity regions, integrated over $p_\mathrm{T} < 30\,\mathrm{GeV}/c$. The first uncertainty is statistical, the second is the component of the systematic uncertainty that is uncorrelated between bins and the third is the correlated component.

	Forward
y^*	$(\mathrm{d}\sigma/\mathrm{d}y)$/mb
(1.50, 1.75]	$135.96 \pm 1.76 \pm 2.64 \pm 6.43$
(1.75, 2.00]	$137.81 \pm 0.24 \pm 1.00 \pm 6.31$
(2.00, 2.25]	$136.81 \pm 0.16 \pm 0.69 \pm 6.04$
(2.25, 2.50]	$133.86 \pm 0.15 \pm 1.05 \pm 5.84$
(2.50, 2.75]	$129.16 \pm 0.15 \pm 0.98 \pm 5.55$
(2.75, 3.00]	$122.74 \pm 0.21 \pm 1.31 \pm 5.32$
(3.00, 3.25]	$115.05 \pm 0.17 \pm 0.96 \pm 5.13$
(3.25, 3.50]	$105.02 \pm 0.25 \pm 1.87 \pm 4.82$
(3.50, 3.75]	$93.99 \pm 0.33 \pm 2.21 \pm 4.38$
(3.75, 4.00]	$79.92 \pm 1.59 \pm 2.32 \pm 4.17$

the initial condition of a nucleus to that of the proton. For CGC2[228] the color dipole approach is combined with a heavy-quark fragmentation function to calculate the cross-sections. The CGC1 predictions have much smaller uncertainties than the CGC2 ones, because the CGC1 uncertainties include only variations of the c quark mass and of the factorization scale, which largely cancel out in the $R_{p\mathrm{Pb}}$ ratio versus p_T. CGC1 is consistent with the upper bound of CGC2 and is slightly higher than the data. CGC2 shows a stronger suppression than HELAC-Onia calculations and gives a better description of the data, especially for $p_\mathrm{T} < 3\,\mathrm{GeV}/c$.

A fourth calculation estimates D^0 suppression caused by medium-induced FCEL[103], a CNM effect where the interference between initial- and final-state gluon radiation results in an energy loss proportional to the incoming parton energy. The FCEL prediction shown in Fig. 4.39 does not consider the modification of nPDFs. The effect is significant for low p_T, suggesting the suppression observed for $p_\mathrm{T} < 1\,\mathrm{GeV}/c$ may be caused by combined effects from nPDFs and FCEL. For $p_\mathrm{T} > 6\,\mathrm{GeV}/c$ the suppression due to FCEL is negligible, thus the discrepancy between the data and HELAC-Onia calculations with nPDFs at backward rapidity cannot be attributed to FCEL effects.

The results are also compared with the LHCb D^0 measurement at $\sqrt{s_\mathrm{NN}} = 5.02\,\mathrm{TeV}$[123]. At forward rapidity the $R_{p\mathrm{Pb}}$ values at the two energies are compatible,

Table 4.9 One-dimensional cross-sections $\mathrm{d}\sigma/\mathrm{d}y$ for prompt D^0 + $\overline{D}^0$ mesons as a function of y^* in backward rapidity regions, integrated over $p_\mathrm{T} < 30\,\mathrm{GeV}/c$. The first uncertainty is statistical, the second is the component of the systematic uncertainty that is uncorrelated between bins and the third is the correlated component.

	Backward
y^*	$(\mathrm{d}\sigma/\mathrm{d}y)$/mb
(-2.75, -2.50]	$145.49 \pm 0.28 \pm 1.80 \pm 8.51$
(-3.00, -2.75]	$152.70 \pm 0.19 \pm 1.25 \pm 8.57$
(-3.25, -3.00]	$151.43 \pm 0.16 \pm 1.17 \pm 8.22$
(-3.50, -3.25]	$147.28 \pm 0.14 \pm 1.01 \pm 7.80$
(-3.75, -3.50]	$136.58 \pm 0.14 \pm 1.18 \pm 7.19$
(-4.00, -3.75]	$127.58 \pm 0.14 \pm 1.21 \pm 6.75$
(-4.25, -4.00]	$119.54 \pm 0.15 \pm 0.94 \pm 6.39$
(-4.50, -4.25]	$107.71 \pm 0.21 \pm 1.92 \pm 5.95$
(-4.75, -4.50]	$92.19 \pm 0.25 \pm 2.47 \pm 5.56$
(-5.00, -4.75]	$80.47 \pm 0.42 \pm 2.52 \pm 5.71$

while at backward rapidity the 8.16 TeV data are significantly lower. The difference could be related to the different Bjorken-x coverage at the two collision energies, while effects related to the Pb-going hemisphere other than nPDFs and FCEL, such as final-state energy loss in a high-particle-density environment, may also show a $\sqrt{s_\mathrm{NN}}$ dependence as more charged hadrons are produced in 8.16 TeV collisions. On the other hand, the model calculations offer limited insights into collision energy dependence. HELAC-Onia predictions based on nPDFs are compatible between the two $\sqrt{s_\mathrm{NN}}$ values due to the large uncertainty of the nPDFs used in the 5.02 TeV calculation. The CGC models show similar values at 5.02 and 8.16 TeV at forward rapidity while they are not applicable at backward. Effects due to FCEL are generally small at backward rapidity.

Figure 4.42 shows $R_{p\mathrm{Pb}}$ as a function of y^* in the full-p_T range (left panel) and for $6 < p_\mathrm{T} < 10\,\mathrm{GeV}/c$ (right panel), where theoretical calculations are also included. The discrepancy in high-p_T regions at backward rapidity can be seen more obviously.

It is essential to study the impact of Bjorken-x coverage in order to interpret the energy dependence observed in the data. However, x and the momemtum transfer Q^2 [72] are partonic quantities that cannot be directly measured in hadronic collisions. Instead,

Table 4.10 Nuclear modification factor $R_{p\mathrm{Pb}}$ for prompt D^0 mesons in intervals of p_{T} and y^* for $p_{\mathrm{T}} < 10\,\mathrm{GeV}/c$. The first uncertainty is statistical and the second is the systematic.

	$R_{p\mathrm{Pb}}$				
p_{T} [GeV/c]\y^*	(2.5, 4.0)	(2.0, 2.5)	(2.5, 3.0)	(3.0, 3.5)	(3.5, 4.0)
(0.0,1.0)	$0.546 \pm 0.002 \pm 0.033$	$0.485 \pm 0.001 \pm 0.041$	$0.525 \pm 0.001 \pm 0.032$	$0.556 \pm 0.002 \pm 0.036$	$0.561 \pm 0.005 \pm 0.039$
(1.0,2.0)	$0.596 \pm 0.002 \pm 0.034$	$0.557 \pm 0.001 \pm 0.037$	$0.591 \pm 0.003 \pm 0.034$	$0.611 \pm 0.002 \pm 0.036$	$0.585 \pm 0.003 \pm 0.038$
(2.0,3.0)	$0.637 \pm 0.001 \pm 0.034$	$0.648 \pm 0.001 \pm 0.036$	$0.637 \pm 0.001 \pm 0.034$	$0.648 \pm 0.001 \pm 0.035$	$0.624 \pm 0.003 \pm 0.037$
(3.0,4.0)	$0.671 \pm 0.001 \pm 0.036$	$0.679 \pm 0.001 \pm 0.038$	$0.676 \pm 0.002 \pm 0.035$	$0.673 \pm 0.002 \pm 0.036$	$0.659 \pm 0.004 \pm 0.044$
(4.0,5.0)	$0.706 \pm 0.002 \pm 0.040$	$0.697 \pm 0.002 \pm 0.042$	$0.719 \pm 0.002 \pm 0.039$	$0.710 \pm 0.003 \pm 0.041$	$0.681 \pm 0.007 \pm 0.048$
(5.0,6.0)	$0.719 \pm 0.005 \pm 0.048$	$0.718 \pm 0.003 \pm 0.056$	$0.722 \pm 0.002 \pm 0.047$	$0.737 \pm 0.004 \pm 0.047$	$0.688 \pm 0.019 \pm 0.064$
(6.0,7.0)	$0.710 \pm 0.014 \pm 0.067$	$0.721 \pm 0.004 \pm 0.056$	$0.769 \pm 0.004 \pm 0.058$	$0.725 \pm 0.006 \pm 0.057$	$0.568 \pm 0.061 \pm 0.169$
(7.0,8.0)	$0.752 \pm 0.005 \pm 0.061$	$0.777 \pm 0.006 \pm 0.067$	$0.783 \pm 0.005 \pm 0.061$	$0.709 \pm 0.010 \pm 0.067$	-
(8.0,9.0)	$0.768 \pm 0.011 \pm 0.073$	$0.717 \pm 0.006 \pm 0.084$	$0.832 \pm 0.008 \pm 0.074$	$0.683 \pm 0.023 \pm 0.078$	-
(9.0,10.0)	$0.784 \pm 0.018 \pm 0.111$	$0.687 \pm 0.007 \pm 0.070$	$0.764 \pm 0.011 \pm 0.086$	$0.814 \pm 0.043 \pm 0.160$	-

Table 4.11 Nuclear modification factor $R_{p\mathrm{Pb}}$ for prompt D^0 mesons in intervals of p_{T} and y^* for $p_{\mathrm{T}} < 10\,\mathrm{GeV}/c$. The first uncertainty is statistical and the second is systematic.

	$R_{p\mathrm{Pb}}$				
p_{T} [GeV/c]\y^*	(-4.0, -2.5)	(-3.0, -2.5)	(-3.5, -3.0)	(-4.0, -3.5)	(-4.5, -4.0)
(0.0,1.0)	$0.691 \pm 0.001 \pm 0.049$	$0.607 \pm 0.002 \pm 0.047$	$0.706 \pm 0.001 \pm 0.049$	$0.781 \pm 0.001 \pm 0.054$	$0.959 \pm 0.002 \pm 0.080$
(1.0,2.0)	$0.803 \pm 0.001 \pm 0.053$	$0.718 \pm 0.001 \pm 0.052$	$0.824 \pm 0.001 \pm 0.054$	$0.891 \pm 0.001 \pm 0.057$	$0.994 \pm 0.002 \pm 0.068$
(2.0,3.0)	$0.891 \pm 0.001 \pm 0.056$	$0.804 \pm 0.002 \pm 0.056$	$0.940 \pm 0.002 \pm 0.056$	$0.960 \pm 0.001 \pm 0.058$	$1.087 \pm 0.002 \pm 0.075$
(3.0,4.0)	$0.917 \pm 0.001 \pm 0.053$	$0.841 \pm 0.003 \pm 0.051$	$0.982 \pm 0.002 \pm 0.056$	$0.952 \pm 0.002 \pm 0.057$	$1.134 \pm 0.003 \pm 0.099$
(4.0,5.0)	$0.916 \pm 0.003 \pm 0.056$	$0.860 \pm 0.008 \pm 0.054$	$0.962 \pm 0.002 \pm 0.058$	$0.948 \pm 0.003 \pm 0.062$	$1.031 \pm 0.004 \pm 0.139$
(5.0,6.0)	$0.894 \pm 0.002 \pm 0.062$	$0.832 \pm 0.005 \pm 0.061$	$0.929 \pm 0.003 \pm 0.060$	$0.956 \pm 0.004 \pm 0.072$	$1.493 \pm 0.010 \pm 0.403$
(6.0,7.0)	$0.884 \pm 0.003 \pm 0.074$	$0.819 \pm 0.005 \pm 0.064$	$0.911 \pm 0.005 \pm 0.073$	$0.974 \pm 0.005 \pm 0.111$	-
(7.0,8.0)	$0.898 \pm 0.004 \pm 0.086$	$0.827 \pm 0.006 \pm 0.067$	$0.881 \pm 0.006 \pm 0.084$	$1.101 \pm 0.009 \pm 0.158$	-
(8.0,9.0)	$0.918 \pm 0.006 \pm 0.118$	$0.861 \pm 0.010 \pm 0.079$	$0.857 \pm 0.008 \pm 0.091$	$1.197 \pm 0.014 \pm 0.352$	-
(9.0,10.0)	$0.867 \pm 0.007 \pm 0.123$	$0.805 \pm 0.010 \pm 0.091$	$0.964 \pm 0.011 \pm 0.181$	-	-

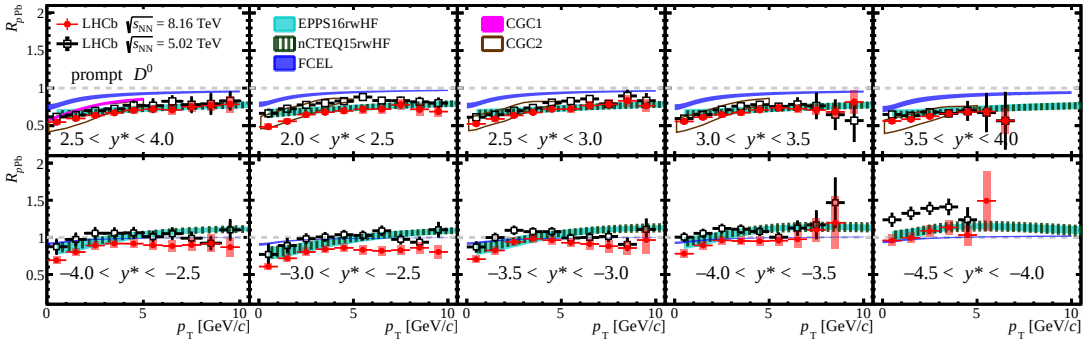

Figure 4.39 Nuclear modification factor as a function of p_T in different y^* intervals for prompt D^0 mesons in the (top) forward and (bottom) backward regions. The error bars show the statistical uncertainties and the boxes show the systematic uncertainties. The LHCb results at $\sqrt{s_{NN}} = 5.02$ TeV[123] and theoretical calculations at $\sqrt{s_{NN}} = 8.16$ TeV from Refs. [81-82,103,227-228] are also shown. For LHCb results at $\sqrt{s_{NN}} = 5.02$ TeV, the error bars show the quadric sum of statistical and systematic uncertainties.

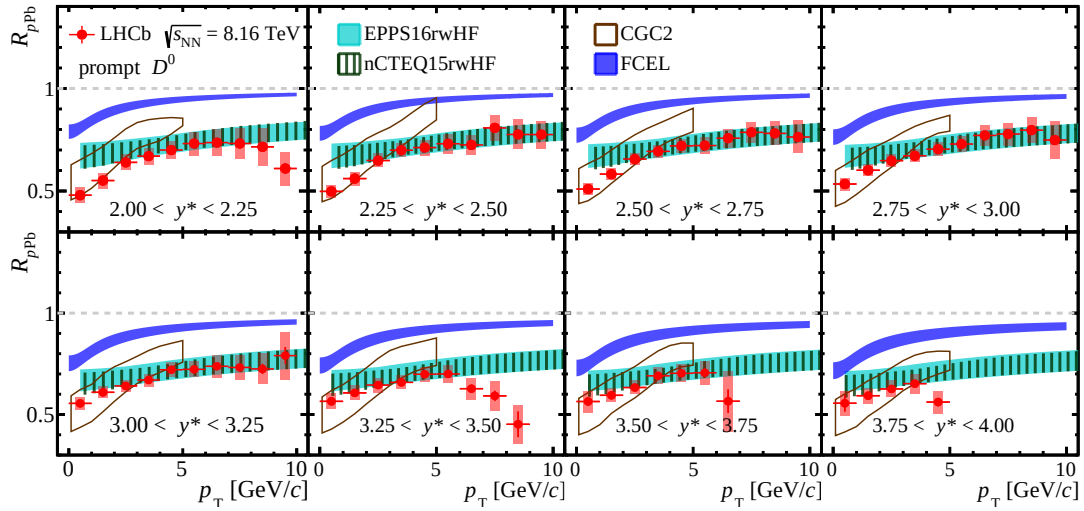

Figure 4.40 Nuclear modification factor as a function of p_T in different y^* intervals with $\Delta y^* = 0.25$ for prompt D^0 mesons in the forward regions for $2.0 < y^* < 4.0$. The error bars show the statistical uncertainties and the boxes show the systematic uncertainties. The theoretical calculations from Refs. [81-82,103,228] are also shown.

experimental proxies x_{exp} and Q^2_{exp}, defined as

$$x_{exp} \equiv 2\frac{\sqrt{p_T^2(D^0) + M^2(D^0)}}{\sqrt{s_{NN}}}e^{-y^*} \text{ and } Q^2_{exp} \equiv p_T^2(D^0) + M^2(D^0), \tag{4.17}$$

are introduced to approximate the variation of R_{pPb} with x and Q^2, where $M(D^0)$ and $p_T(D^0)$ denote the mass and p_T of D^0 mesons, respectively.

Figure 4.43 shows R_{pPb} as a function of x_{exp} in five Q^2_{exp} intervals, for D^0 mesons measured in this work at 8.16 TeV, and at 5.02 TeV from Ref. [123]. The x_{exp} coverage of the 8.16 TeV data extends lower than that of the 5.02 TeV measurements due to the higher

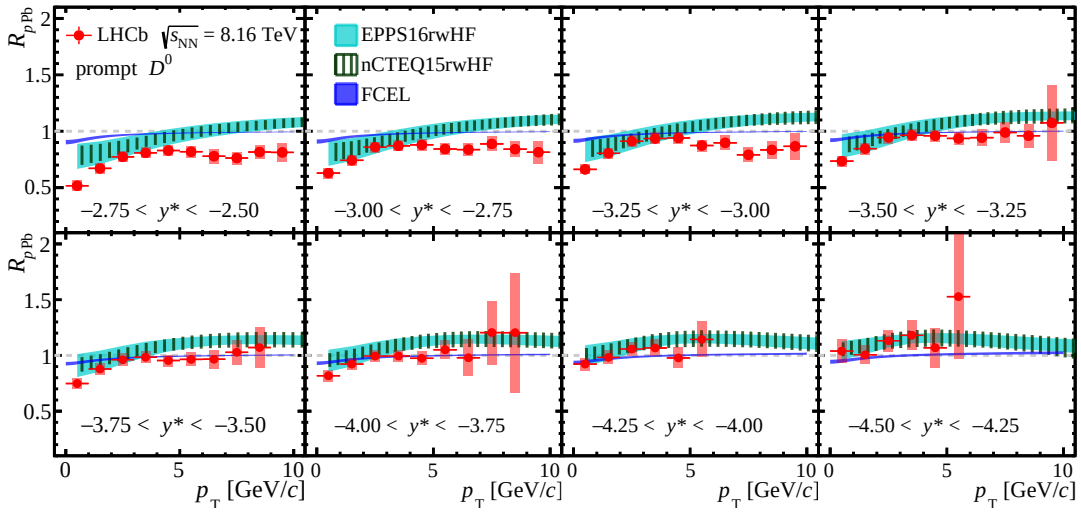

Figure 4.41 Nuclear modification factor as a function of p_T in different y^* intervals with $\Delta y^* = 0.25$ for prompt D^0 mesons in the backward regions for $-4.5 < y^* < -2.5$. The error bars show the statistical uncertainties and the boxes show the systematic uncertainties. The theoretical calculations from Refs. [81-82,103] are also shown.

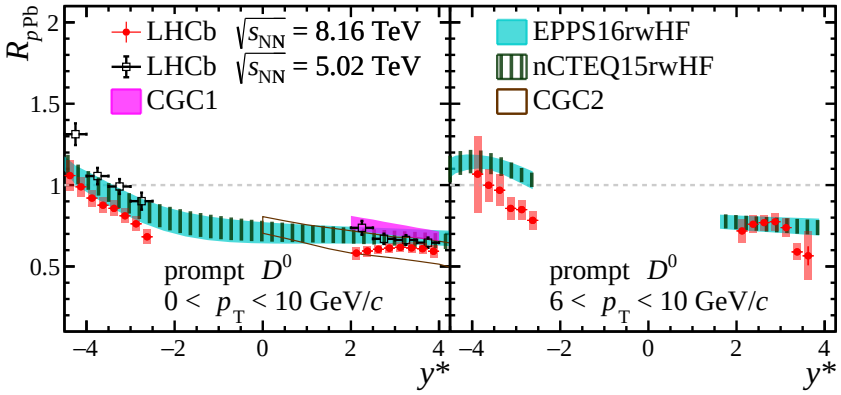

Figure 4.42 Nuclear modification factor for prompt D^0 mesons as a function of y^* in (left) the full-p_T range and (right) the high-p_T range. The error bars show the statistical uncertainties and the boxes show the systematic uncertainties. The LHCb results at $\sqrt{s_{NN}} = 5.02\,\text{TeV}$ [123] and theoretical calculations at $\sqrt{s_{NN}} = 8.16\,\text{TeV}$ from Refs. [81-82,227-228] are also shown. For the LHCb results at $\sqrt{s_{NN}} = 5.02\,\text{TeV}$, the error bars show the quadratic sum of statistical and systematic uncertainties. On the left, the p_T range is $0 < p_T < 15\,\text{GeV}/c$ for the calculations with nPDFs of EPPS16 and nCTEQ15.

$\sqrt{s_{NN}}$ value, reaching down to $x_{exp} \sim 10^{-5}$ in the interval $3.48 < Q^2_{exp} < 7.48\,\text{GeV}^2$, which corresponds to $p_T < 2\,\text{GeV}/c$. The 8.16 TeV data are also more precise. Data from the two energies are in good agreement with each other at common x_{exp} values. The measurements form a consistent trend from the small x_{exp} region corresponding to forward rapidity to the large x_{exp} region corresponding to backward rapidity, for all Q^2_{exp} intervals. The D^0 R_{pPb} ratio at 5.02 TeV at midrapidity [146] measured by the ALICE collaboration

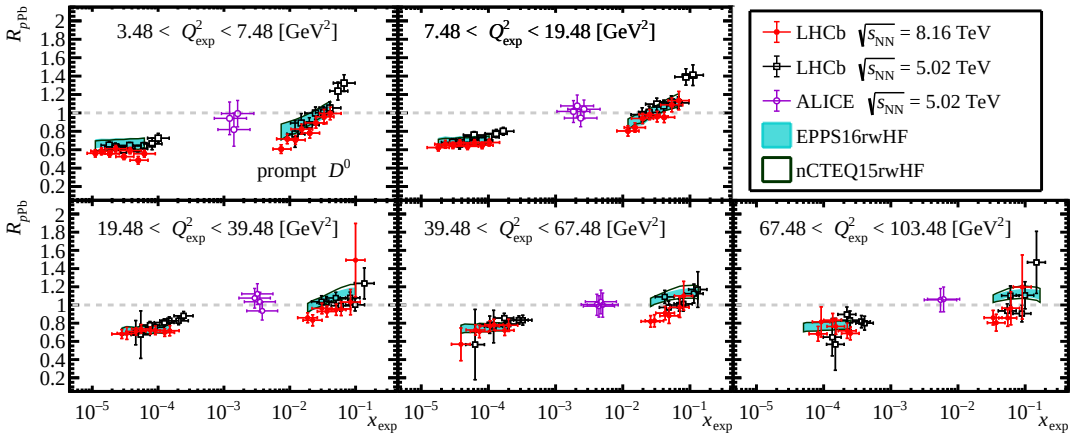

Figure 4.43 Nuclear modification factor as a function of x_{exp} in different Q^2_{exp} intervals for prompt D^0 mesons for LHCb results at $\sqrt{s_{NN}} = 8.16$ TeV and $\sqrt{s_{NN}} = 5.02$ [123] and the ALICE result at $\sqrt{s_{NN}} = 5.02$ TeV [146]. Theoretical calculations at $\sqrt{s_{NN}} = 8.16$ TeV from Refs. [81-82] are also shown. The horizontal error bars account for the maximum and minimum x_{exp} values for a given (p_T, y^*) interval and the vertical error bars show the quadric sum of statistical and systematic uncertainties.

is also added to Fig. 4.43, and is compatible with the trend within uncertainties. The trend suggests that the $\sqrt{s_{NN}}$ dependence observed at backward rapidity in Fig. 4.39 arises from different x coverage in a kinematic region where R_{pPb} depends strongly on x.

The HELAC-Onia predictions are also transformed according to Eq. 4.17 and shown in Fig. 4.43. In the small x_{exp} region, the calculations are in general agreement with the data, except for the interval $3.48 < Q^2_{exp} < 7.48\,\text{GeV}^2$ ($p_T < 2\,\text{GeV}/c$) and $10^{-5} < x_{exp} < 10^{-4}$, where the nPDF expectations are slightly larger than the data and show greater uncertainty. The data hint at a stronger shadowing effect, or other possible effects such as FCEL, that suppresses low-p_T D^0 production at forward rapidity. Moreover, estimations from Ref. [160] suggest gluon saturation may occur in this region. At backward rapidity, the R_{pPb} values from the model are larger than those in the data for $Q^2_{exp} > 19.48\,\text{GeV}^2$ ($p_T > 4\,\text{GeV}/c$) and $10^{-2} < x_{exp} < 10^{-1}$, indicating smaller antishadowing effects in the data if nuclear effects other than nPDFs are negligible. Alternatively it suggests additional suppression mechanisms, such as final-state energy loss, may occur at backward rapidity.

4.6.3 Forward-backward ratio

The forward-backward production ratio is defined as

$$R_{FB}(p_T, y^*) \equiv \frac{d^2\sigma(p_T, |y^*|; y^* > 0)/(dp_T dy^*)}{d^2\sigma(p_T, |y^*|; y^* < 0)/(dp_T dy^*)}\,, \tag{4.18}$$

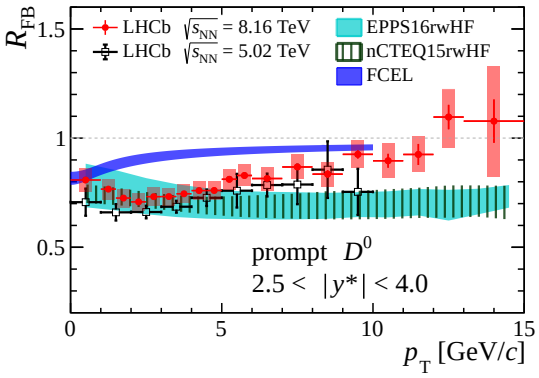

Figure 4.44 Forward-backward production ratio for prompt D^0 mesons as a function of p_T, integrated over the common rapidity range $2.5 < |y^*| < 4.0$. The error bars show the statistical uncertainties and the boxes show the systematic uncertainties. The LHCb results at $\sqrt{s_{NN}} = 5.02$ TeV[123] and theoretical calculations at $\sqrt{s_{NN}} = 8.16$ TeV from Refs. [81-82,103] are also shown. For the LHCb results at $\sqrt{s_{NN}} = 5.02$ TeV, the error bars show the quadratic sum of statistical and systematic uncertainties.

which is calculated in the common $|y^*|$ interval of the forward-backward acceptance, $2.5 < |y^*| < 4$. The measurements of R_{FB} are shown as a function of p_T in Fig. 4.44, along with the LHCb $\sqrt{s_{NN}} = 5.02$ TeV results[123] and the nPDF calculations. The numerical values for R_{FB} are given in Table 4.12. Measurements of R_{FB} *vs.* p_T in $|y^*|$ intervals with $\Delta|y^*| = 0.25$ are shown in Fig. 4.45. Good agreement with nPDF calculations is found at low p_T. However, the data show a clear rising trend with increasing p_T, reaching unity at the highest p_T values, in contrast to the nPDF calculations, which predict $R_{FB} \sim 0.7$ almost independent of p_T. This difference originates from the suppression of high-p_T D^0 mesons at backward rapidity.

4.6.4 Cross-section ratios between 8.16 TeV and 5.02 TeV

The prompt D^0 cross-sections at 8.16 TeV are compared to those at 5.02 TeV by measuring the ratio $\sigma_{8.16\,\text{TeV}}/\sigma_{5.02\,\text{TeV}}$. The ratio of double-differential cross-sections are shown in Fig. 4.46, and the ratio of one-dimensional cross-sections are shown in Figs. 4.47, 4.48 and 4.49. A normalisation is also performed to keep the branching fractions the same. For the uncertainties, the systematic uncertainties from hadronic interaction material budget and branching fraction are considered fully correlated, while other terms are uncorrelated. The numerical values of the cross-section ratios are listed in the Tables 4.13, 4.14, 4.15, 4.17, 4.18 and 4.19 respectively. The ratios all show a rising trend as a function of p_T and $|y^*|$. The results are also compared to the HELAC-Onia calculations with different nPDFs, where the uncertainties from the nPDFs are largely cancelled and the dominate

Table 4.12 Forward-backward production ratio $R_{\rm FB}$ for prompt D^0 mesons as a function of $p_{\rm T}$, integrated over $2.5 < |y^*| < 4.0$. The first uncertainty is statistical, the second is the component of the systematic uncertainty that is uncorrelated across intervals and the third is the correlated component.

$p_{\rm T}$ [GeV/c]	$R_{\rm FB}$
(0.0,1.0)	$0.808 \pm 0.009 \pm 0.019 \pm 0.051$
(1.0,1.5)	$0.766 \pm 0.002 \pm 0.014 \pm 0.044$
(1.5,2.0)	$0.725 \pm 0.002 \pm 0.011 \pm 0.041$
(2.0,2.5)	$0.708 \pm 0.002 \pm 0.011 \pm 0.039$
(2.5,3.0)	$0.732 \pm 0.002 \pm 0.011 \pm 0.040$
(3.0,3.5)	$0.732 \pm 0.002 \pm 0.011 \pm 0.039$
(3.5,4.0)	$0.745 \pm 0.003 \pm 0.013 \pm 0.040$
(4.0,4.5)	$0.760 \pm 0.004 \pm 0.012 \pm 0.042$
(4.5,5.0)	$0.760 \pm 0.006 \pm 0.015 \pm 0.040$
(5.0,5.5)	$0.811 \pm 0.006 \pm 0.016 \pm 0.044$
(5.5,6.0)	$0.829 \pm 0.009 \pm 0.020 \pm 0.045$
(6.0,7.0)	$0.815 \pm 0.010 \pm 0.029 \pm 0.045$
(7.0,8.0)	$0.868 \pm 0.008 \pm 0.024 \pm 0.051$
(8.0,9.0)	$0.835 \pm 0.017 \pm 0.027 \pm 0.050$
(9.0,10.0)	$0.926 \pm 0.019 \pm 0.028 \pm 0.055$
(10.0,11.0)	$0.896 \pm 0.032 \pm 0.050 \pm 0.060$
(11.0,12.0)	$0.925 \pm 0.048 \pm 0.051 \pm 0.063$
(12.0,13.0)	$1.096 \pm 0.056 \pm 0.088 \pm 0.106$
(13.0,15.0)	$1.078 \pm 0.099 \pm 0.178 \pm 0.181$

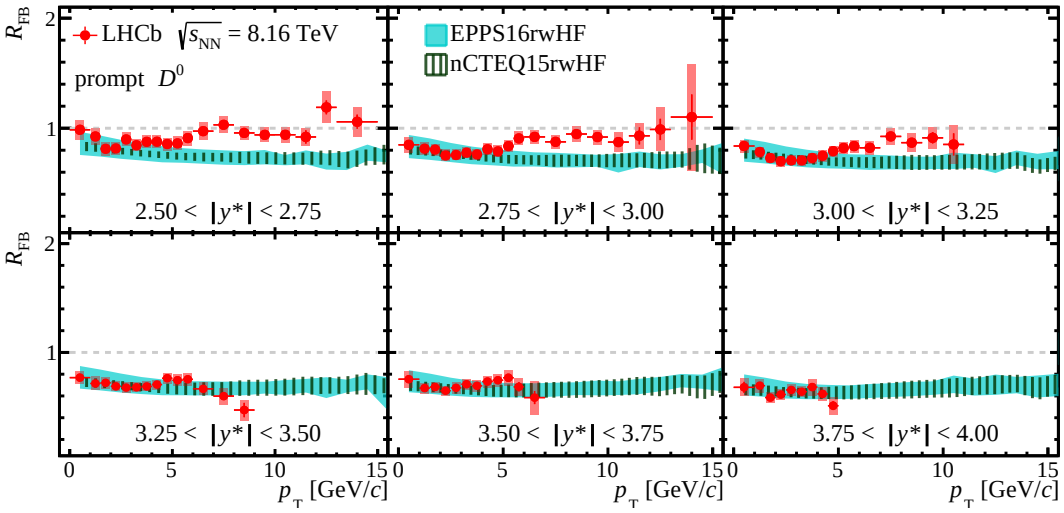

Figure 4.45 Forward and backward production ratio R_{FB} for prompt D^0 mesons as a function of p_T in different $|y^*|$ intervals. The error bars show the statistical uncertainties and the boxes show the systematic uncertainties. The theoretical calculations from Refs. [81-82] are also shown.

term comes from the factorisation scales. An agreement between the measured ratios and HELAC-Onia calculations is observed within uncertainties.

4.7 Summary

This analysis presents the measurement of the prompt D^0 production cross-section at the LHCb experiment in proton-lead collisions at a centre-of-mass energy per nucleon pair of $\sqrt{s_{NN}} = 8.16\,\text{TeV}$. This measurement is performed in a transverse momentum coverage of $0 < p_T < 30\,\text{GeV}/c$, and a rapidity coverage of both forward ($1.5 < y^* < 4.0$) and backward ($-5.0 < y^* < -2.5$) regions. The nuclear modification factors $R_p\text{Pb}$ are derived by comparing the cross-section in pPb collisions to that in pp. A suppression of $R_p\text{Pb}$ compared to unity is observed for both forward and backward rapidities, suggesting the existence of cold nuclear matter effects. The measured results are compared with theoretical predictions from nPDF, CGC and FCEL models. A stronger suppression than the nPDF calculations is observed for the lowest transverse momentum region of $p_T < 1\,\text{GeV}/c$ at forward rapidity, hinting at a stronger shadowing than predicted at Bjorken-$x \sim 10^{-5}$, which can be explained by the FCEL. For the backward rapidity range of $-3.5 < y^* < -2.5$, the $R_{p\text{Pb}}$ values are lower than nPDF calculations at $p_T > 6\,\text{GeV}/c$ with a significance of $2.0-3.8$ standard deviations, indicating a weaker antishadowing effect than the model or additional final-state effects at backward rapidity. The asymmetry between forward and backward D^0 production is also observed, consistent with the expectation

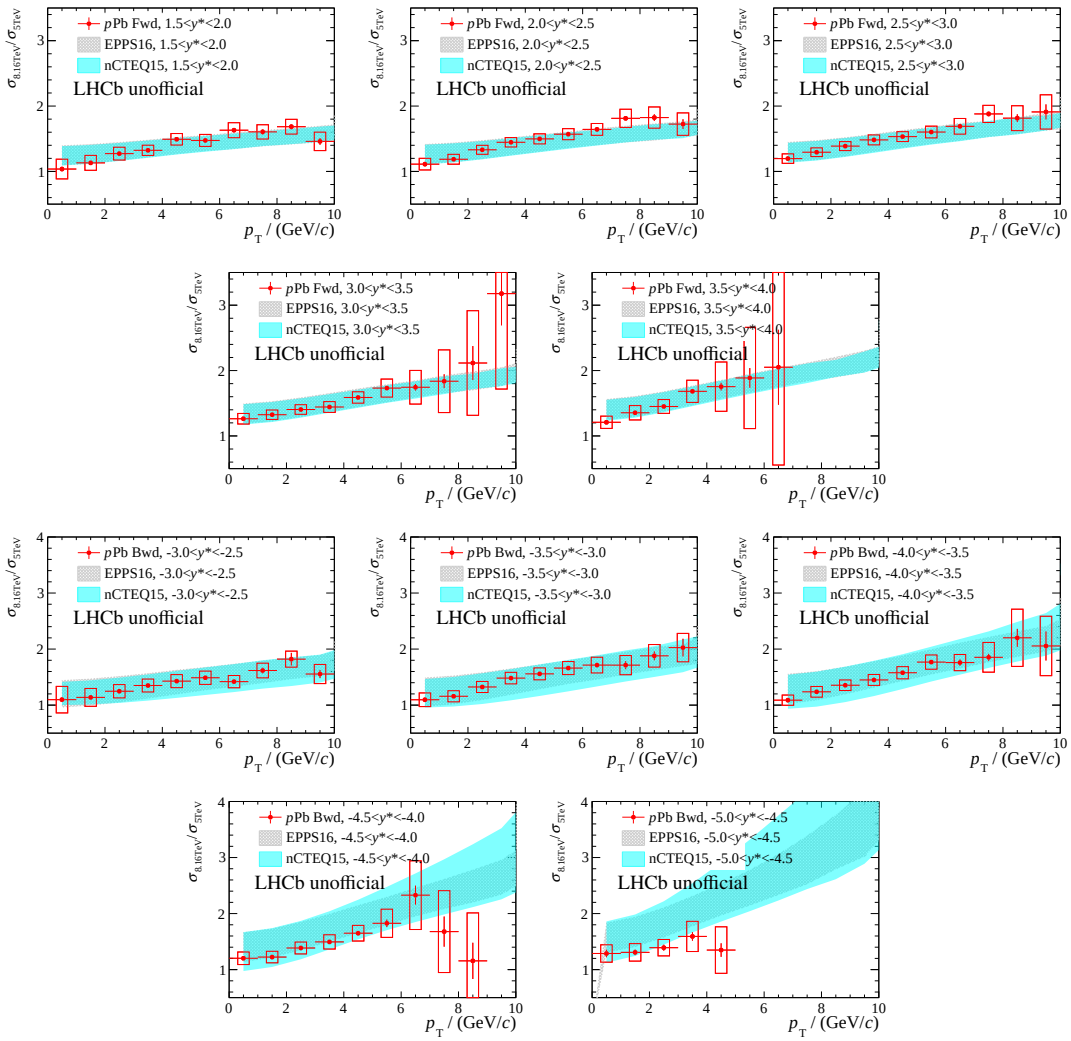

Figure 4.46 Two-dimensional 8.16 TeV/5.02 TeV production ratio $\sigma_{8.16\,\text{TeV}}/\sigma_{5.02\,\text{TeV}}$ as a function of p_T in different y^* bins with $\Delta y^* = 0.5$. Top two rows for forward and bottom two rows for backward. The error bar is the statistical uncertainty while the box is the systematic uncertainty.

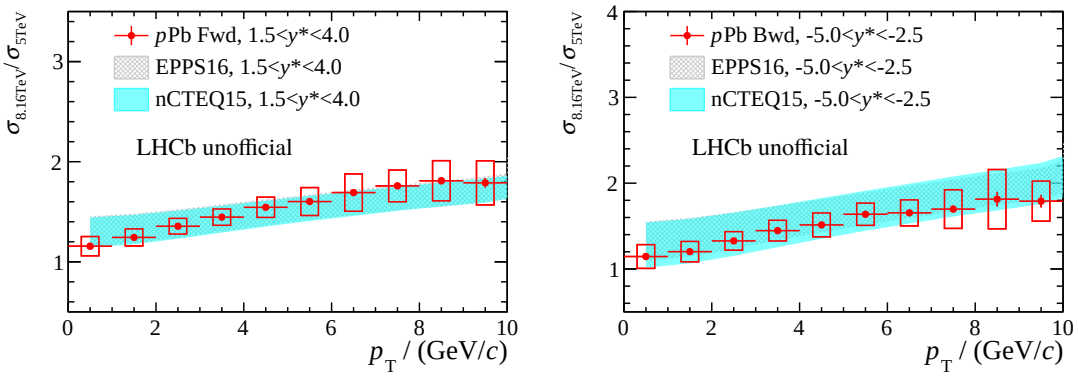

Figure 4.47 One-dimensional 8.16 TeV/5.02 TeV production ratio $\sigma_{8.16\,\text{TeV}}/\sigma_{5.02\,\text{TeV}}$ as a function of p_T, which is integrated over $1.5 < y^* < 4.0$ for forward (left) and $-5.0 < y^* < -2.5$ for backward (right). The error bar is the statistical uncertainty while the box is the systematic uncertainty. The coloured bands mark the theoretical calculations using the HELAC-Onia generator, incorporating nPDFs EPPS16 (grey) and nCTEQ15 (blue).

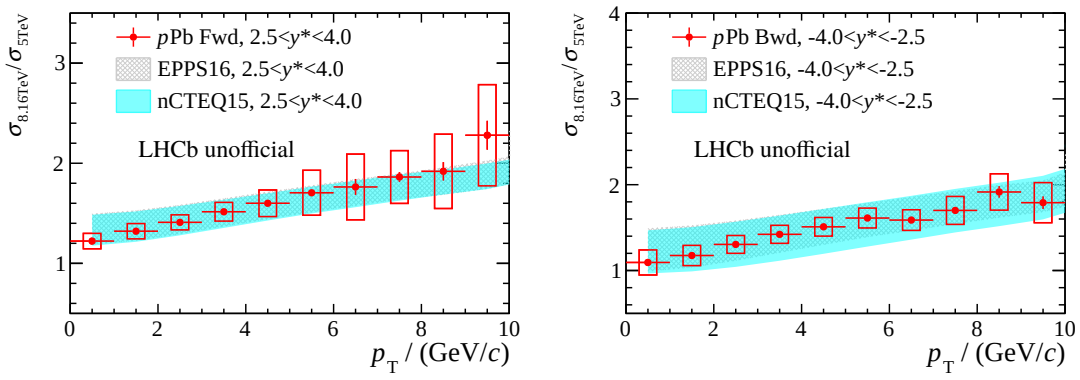

Figure 4.48 One-dimensional 8.16 TeV/5.02 TeV production ratio $\sigma_{8.16\,\text{TeV}}/\sigma_{5.02\,\text{TeV}}$ as a function of p_{T}, which is integrated over $2.5 < y^* < 4.0$ for forward (left) and $-4.0 < y^* < -2.5$ for backward (right). The error bar is the statistical uncertainty while the box is the systematic uncertainty. The coloured bands mark the theoretical calculations using the HELAC-Onia generator, incorporating nPDFs EPPS16 (grey) and nCTEQ15 (blue).

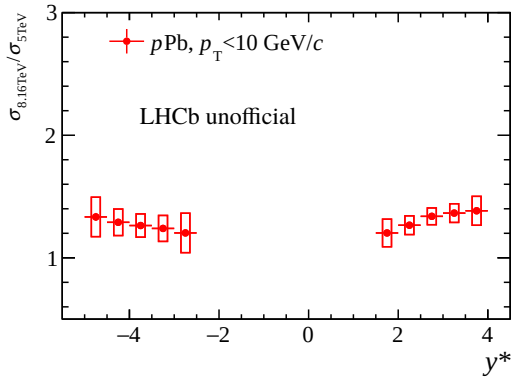

Figure 4.49 One-dimensional 8.16 TeV/5.02 TeV production ratio $\sigma_{8.16\,\text{TeV}}/\sigma_{5.02\,\text{TeV}}$ as a function of y, which is integrated over $p_{\text{T}} < 10\,\text{GeV}/c$. The error bar is the statistical uncertainty while the box is the systematic uncertainty. The coloured bands mark the theoretical calculations using the HELAC-Onia generator, incorporating nPDFs EPPS16 (grey) and nCTEQ15 (blue).

from CNM effects. The D^0 cross-section ratio between 8.16 TeV and 5.02 TeV is also determined, which shows a good agreement with nPDF predictions.

Table 4.13 Two-dimensional $\sigma_{8.16\,\text{TeV}}/\sigma_{5\,\text{TeV}}$ for prompt $D^0 + \overline{D}^0$ mesons in bins of p_T and y^* in forward rapidity regions. The first uncertainty is statistical and the second is the systematic component.

	$\sigma_{8.16\,\text{TeV}}/\sigma_{5\,\text{TeV}}$				
p_T/(GeV/c)\y^*	(1.5, 2.0]	(2.0, 2.5]	(2.5, 3.0]	(3.0, 3.5]	(3.5, 4.0]
(0.0,1.0]	$1.04 \pm 0.01 \pm 0.15$	$1.11 \pm 0.01 \pm 0.09$	$1.20 \pm 0.01 \pm 0.07$	$1.26 \pm 0.01 \pm 0.08$	$1.21 \pm 0.03 \pm 0.09$
(1.0,2.0]	$1.13 \pm 0.01 \pm 0.11$	$1.19 \pm 0.01 \pm 0.08$	$1.29 \pm 0.01 \pm 0.07$	$1.32 \pm 0.01 \pm 0.07$	$1.35 \pm 0.02 \pm 0.11$
(2.0,3.0]	$1.27 \pm 0.01 \pm 0.10$	$1.33 \pm 0.01 \pm 0.07$	$1.39 \pm 0.01 \pm 0.07$	$1.40 \pm 0.01 \pm 0.07$	$1.45 \pm 0.02 \pm 0.11$
(3.0,4.0]	$1.32 \pm 0.01 \pm 0.08$	$1.45 \pm 0.01 \pm 0.07$	$1.48 \pm 0.01 \pm 0.08$	$1.44 \pm 0.01 \pm 0.08$	$1.68 \pm 0.03 \pm 0.17$
(4.0,5.0]	$1.49 \pm 0.02 \pm 0.09$	$1.50 \pm 0.01 \pm 0.08$	$1.53 \pm 0.01 \pm 0.08$	$1.59 \pm 0.02 \pm 0.09$	$1.75 \pm 0.06 \pm 0.38$
(5.0,6.0]	$1.47 \pm 0.02 \pm 0.09$	$1.57 \pm 0.02 \pm 0.08$	$1.60 \pm 0.02 \pm 0.09$	$1.73 \pm 0.03 \pm 0.14$	$1.89 \pm 0.15 \pm 0.77$
(6.0,7.0]	$1.63 \pm 0.03 \pm 0.11$	$1.64 \pm 0.03 \pm 0.09$	$1.69 \pm 0.03 \pm 0.12$	$1.74 \pm 0.05 \pm 0.26$	$2.05 \pm 0.57 \pm 1.50$
(7.0,8.0]	$1.61 \pm 0.04 \pm 0.11$	$1.81 \pm 0.03 \pm 0.14$	$1.88 \pm 0.04 \pm 0.13$	$1.84 \pm 0.11 \pm 0.48$	-
(8.0,9.0]	$1.68 \pm 0.04 \pm 0.11$	$1.82 \pm 0.05 \pm 0.16$	$1.81 \pm 0.06 \pm 0.19$	$2.12 \pm 0.26 \pm 0.80$	-
(9.0,10.0]	$1.46 \pm 0.05 \pm 0.14$	$1.72 \pm 0.07 \pm 0.17$	$1.91 \pm 0.12 \pm 0.26$	$3.18 \pm 0.48 \pm 1.46$	-

Table 4.14 Two-dimensional $\sigma_{8.16\,\mathrm{TeV}}/\sigma_{5\,\mathrm{TeV}}$ for prompt D^0 + $\overline{D}^0$ mesons in bins of p_T and y^* in backward rapidity regions. The first uncertainty is statistical and the second is the systematic component.

	$\sigma_{8.16\,\mathrm{TeV}}/\sigma_{5\,\mathrm{TeV}}$				
p_T/(GeV/c)\y^*	(-3.0, -2.5]	(-3.5, -3.0]	(-4.0, -3.5]	(-4.5, -4.0]	(-5.0, -4.5]
(0.0,1.0]	$1.10 \pm 0.02 \pm 0.24$	$1.10 \pm 0.01 \pm 0.12$	$1.09 \pm 0.01 \pm 0.09$	$1.20 \pm 0.03 \pm 0.11$	$1.29 \pm 0.07 \pm 0.16$
(1.0,2.0]	$1.14 \pm 0.01 \pm 0.16$	$1.16 \pm 0.01 \pm 0.10$	$1.24 \pm 0.01 \pm 0.10$	$1.22 \pm 0.02 \pm 0.10$	$1.31 \pm 0.05 \pm 0.16$
(2.0,3.0]	$1.25 \pm 0.01 \pm 0.12$	$1.32 \pm 0.01 \pm 0.10$	$1.35 \pm 0.01 \pm 0.09$	$1.39 \pm 0.02 \pm 0.11$	$1.39 \pm 0.05 \pm 0.15$
(3.0,4.0]	$1.35 \pm 0.02 \pm 0.12$	$1.48 \pm 0.01 \pm 0.10$	$1.45 \pm 0.02 \pm 0.10$	$1.49 \pm 0.02 \pm 0.13$	$1.59 \pm 0.08 \pm 0.27$
(4.0,5.0]	$1.43 \pm 0.02 \pm 0.12$	$1.56 \pm 0.02 \pm 0.11$	$1.58 \pm 0.02 \pm 0.11$	$1.65 \pm 0.04 \pm 0.14$	$1.35 \pm 0.12 \pm 0.42$
(5.0,6.0]	$1.49 \pm 0.03 \pm 0.12$	$1.66 \pm 0.03 \pm 0.12$	$1.77 \pm 0.04 \pm 0.13$	$1.83 \pm 0.07 \pm 0.25$	-
(6.0,7.0]	$1.42 \pm 0.03 \pm 0.11$	$1.71 \pm 0.04 \pm 0.14$	$1.76 \pm 0.06 \pm 0.14$	$2.33 \pm 0.17 \pm 0.61$	-
(7.0,8.0]	$1.62 \pm 0.05 \pm 0.13$	$1.71 \pm 0.07 \pm 0.17$	$1.85 \pm 0.06 \pm 0.27$	$1.68 \pm 0.27 \pm 0.73$	-
(8.0,9.0]	$1.82 \pm 0.11 \pm 0.14$	$1.88 \pm 0.08 \pm 0.20$	$2.20 \pm 0.16 \pm 0.51$	$1.16 \pm 0.32 \pm 0.86$	-
(9.0,10.0]	$1.56 \pm 0.07 \pm 0.17$	$2.03 \pm 0.16 \pm 0.25$	$2.06 \pm 0.26 \pm 0.53$	-	-

Table 4.15 One-dimensional $\sigma_{8.16\,\mathrm{TeV}}/\sigma_{5\,\mathrm{TeV}}$ for prompt $D^0 + \overline{D}^0$ mesons as a function of p_T in forward rapidity regions, integrated over $1.5 < y^* < 4.0$. The first uncertainty is statistical and the second is the systematic component.

	Forward
$p_\mathrm{T}/(\,\mathrm{GeV}/c)$	$\sigma_{8.16\,\mathrm{TeV}}/\sigma_{5\,\mathrm{TeV}}$
(0.0,1.0]	$1.16 \pm 0.01 \pm 0.10$
(1.0,2.0]	$1.24 \pm 0.00 \pm 0.08$
(2.0,3.0]	$1.36 \pm 0.00 \pm 0.08$
(3.0,4.0]	$1.45 \pm 0.01 \pm 0.08$
(4.0,5.0]	$1.54 \pm 0.01 \pm 0.10$
(5.0,6.0]	$1.60 \pm 0.02 \pm 0.14$
(6.0,7.0]	$1.69 \pm 0.04 \pm 0.19$
(7.0,8.0]	$1.76 \pm 0.02 \pm 0.16$
(8.0,9.0]	$1.81 \pm 0.04 \pm 0.20$
(9.0,10.0]	$1.79 \pm 0.05 \pm 0.22$

Table 4.16 One-dimensional $\sigma_{8.16\,\mathrm{TeV}}/\sigma_{5\,\mathrm{TeV}}$ for prompt $D^0 + \overline{D}^0$ mesons as a function of p_T in backward rapidity regions, integrated over $-5.0 < y^* < -2.5$. The first uncertainty is statistical and the second is the systematic component.

	Backward
$p_\mathrm{T}/(\,\mathrm{GeV}/c)$	$\sigma_{8.16\,\mathrm{TeV}}/\sigma_{5\,\mathrm{TeV}}$
(0.0,1.0]	$1.15 \pm 0.01 \pm 0.14$
(1.0,2.0]	$1.20 \pm 0.01 \pm 0.12$
(2.0,3.0]	$1.33 \pm 0.01 \pm 0.11$
(3.0,4.0]	$1.45 \pm 0.01 \pm 0.12$
(4.0,5.0]	$1.51 \pm 0.02 \pm 0.14$
(5.0,6.0]	$1.64 \pm 0.02 \pm 0.13$
(6.0,7.0]	$1.65 \pm 0.02 \pm 0.15$
(7.0,8.0]	$1.70 \pm 0.04 \pm 0.22$
(8.0,9.0]	$1.81 \pm 0.09 \pm 0.35$
(9.0,10.0]	$1.79 \pm 0.07 \pm 0.23$

Table 4.17 One-dimensional $\sigma_{8.16\,\mathrm{TeV}}/\sigma_{5\,\mathrm{TeV}}$ for prompt $D^0 + \overline{D}^0$ mesons as a function of p_T in forward rapidity regions, integrated over common rapidity region of $2.5 < |y^*| < 4.0$. The first uncertainty is statistical and the second is the systematic component.

	Forward
$p_\mathrm{T}/(\,\mathrm{GeV}/c)$	$\sigma_{8.16\,\mathrm{TeV}}/\sigma_{5\,\mathrm{TeV}}$
(0.0,1.0]	$1.22 \pm 0.01 \pm 0.08$
(1.0,2.0]	$1.32 \pm 0.01 \pm 0.08$
(2.0,3.0]	$1.41 \pm 0.01 \pm 0.08$
(3.0,4.0]	$1.52 \pm 0.01 \pm 0.09$
(4.0,5.0]	$1.60 \pm 0.01 \pm 0.13$
(5.0,6.0]	$1.71 \pm 0.03 \pm 0.22$
(6.0,7.0]	$1.76 \pm 0.08 \pm 0.33$
(7.0,8.0]	$1.86 \pm 0.05 \pm 0.26$
(8.0,9.0]	$1.92 \pm 0.09 \pm 0.37$
(9.0,10.0]	$2.28 \pm 0.14 \pm 0.51$

Table 4.18 One-dimensional $\sigma_{8.16\,\mathrm{TeV}}/\sigma_{5\,\mathrm{TeV}}$ for prompt $D^0 + \overline{D}^0$ mesons as a function of p_T in backward rapidity regions, integrated over common rapidity region of $2.5 < |y^*| < 4.0$. The first uncertainty is statistical and the second is the systematic component.

	Backward
$p_\mathrm{T}/(\,\mathrm{GeV}/c)$	$\sigma_{8.16\,\mathrm{TeV}}/\sigma_{5\,\mathrm{TeV}}$
(0.0,1.0]	$1.09 \pm 0.01 \pm 0.15$
(1.0,2.0]	$1.17 \pm 0.01 \pm 0.12$
(2.0,3.0]	$1.30 \pm 0.01 \pm 0.10$
(3.0,4.0]	$1.42 \pm 0.01 \pm 0.11$
(4.0,5.0]	$1.51 \pm 0.01 \pm 0.11$
(5.0,6.0]	$1.61 \pm 0.02 \pm 0.12$
(6.0,7.0]	$1.59 \pm 0.02 \pm 0.12$
(7.0,8.0]	$1.70 \pm 0.04 \pm 0.16$
(8.0,9.0]	$1.92 \pm 0.07 \pm 0.21$
(9.0,10.0]	$1.79 \pm 0.07 \pm 0.23$

Table 4.19 One-dimensional $\sigma_{8.16\,\mathrm{TeV}}/\sigma_{5\,\mathrm{TeV}}$ for prompt D^0 + $\overline{D}^0$ mesons as a function of y^*, integrated over $p_\mathrm{T} < 10\,\mathrm{GeV}/c$. The first uncertainty is statistical and the second is the systematic component.

y^*	$\sigma_{8.16\,\mathrm{TeV}}/\sigma_{5\,\mathrm{TeV}}$
(-5.0, -4.5]	$1.33 \pm 0.03 \pm 0.16$
(-4.5, -4.0]	$1.29 \pm 0.01 \pm 0.11$
(-4.0, -3.5]	$1.26 \pm 0.01 \pm 0.09$
(-3.5, -3.0]	$1.24 \pm 0.01 \pm 0.11$
(-3.0, -2.5]	$1.20 \pm 0.01 \pm 0.16$
(1.5, 2.0]	$1.20 \pm 0.01 \pm 0.11$
(2.0, 2.5]	$1.27 \pm 0.00 \pm 0.08$
(2.5, 3.0]	$1.34 \pm 0.00 \pm 0.07$
(3.0, 3.5]	$1.36 \pm 0.01 \pm 0.08$
(3.5, 4.0]	$1.38 \pm 0.01 \pm 0.12$

CHAPTER 5 PROMPT D^0 FLOW MEASUREMENT

In this chapter, the collective flow of prompt D^0 mesons are measured via the two-particle correlation method, using the LHCb data in pPb collisions at $\sqrt{s_{\rm NN}} = 8.16\,\text{TeV}$. The $(\Delta\phi, \Delta\eta)$ correlation functions of $D^0 - h$ pairs are obtained in different $p_{\rm T}(D^0)$ intervals and event activities. The elliptic flow and triangle flow are extracted with the Fourier expansion of the long-range correlation function, and results with only statistical uncertainty are presented.

5.1 Data preparation

5.1.1 Event selection and classification

To make sure that the D^0 candidate and the associated tracks are produced from the same PV, each event is required to have only one reconstructed PV. The selection on PV positions is also applied to achieve a better event reconstruction. Since the D^0 data sample is triggered and biased by the real-time reconstructed D^0 candidates, the minimum-bias data sample is used instead to determine the event selection criteria. The distribution of their PV coordinates are shown in Fig. 5.1, and a region within three standard deviations from the mean value $|\text{PV}_i - \mu_{\text{PV}_i}| < 3\sigma_{\text{PV}_i}$ is chosen for the flow measurement, following Ref. [114].

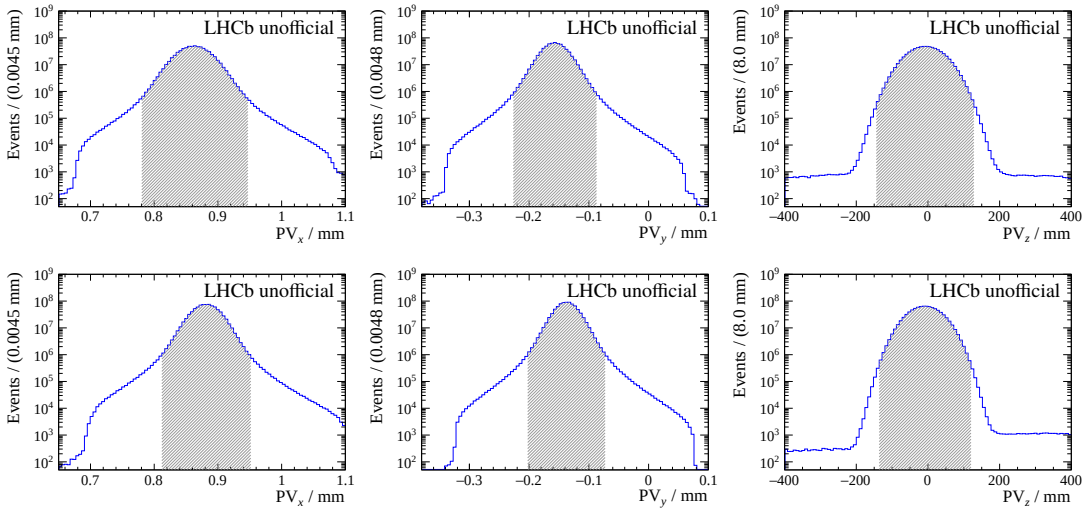

Figure 5.1 Distributions of (left) x, (middle) y and (right) z coordinates of PV in minimum-bias pPb data. Top for the forward and bottom for the backward sample. The shaded areas correspond to the regions within three standard deviations from the mean values.

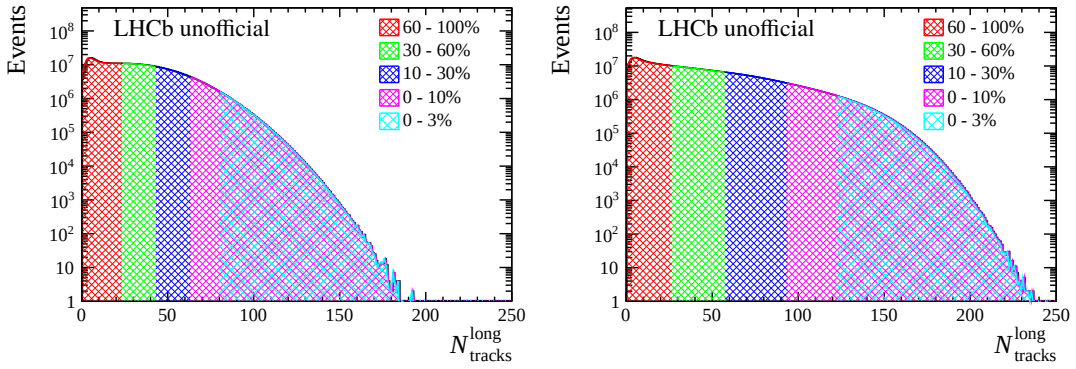

Figure 5.2 Distributions of $N^{\text{long}}_{\text{tracks}}$ and the event classification derived from their quantiles for (left) forward and (right) backward minimum-bias data.

It is essential to classify the events into different event activities, in order to distinguish the high-multiplicity (HM) and low-multiplicity (LM) ones. Here minimum-bias data samples are also employed. As the N_{part} and N_{coll} is hard to determine for pPb collisions, the nLongTracks ($N^{\text{long}}_{\text{tracks}}$) is chosen as the discriminating variable. The $N^{\text{long}}_{\text{tracks}}$ distributions for forward and backward samples are shown in Fig. 5.2. The event classification used in this analysis is derived from the quantiles of the distributions, also shown in Fig. 5.2.

5.1.2 D^0 and h candidate selection

There are two methods to exclude the contribution from the combinatorial background to the signal v_2 measurement. The first method assumes a linear v_2 dependence on invariant mass M for backgrounds, and then fits to the $v_2(M)$ to extract the signal v_2 [157]. Another one applies delicate selections on candidates to achieve a high purity [158-159]. Due to the existence of the online selections listed in Table 3.1, the latter one is more accessible in this analysis. Selections with MVA toolkit [193] are applied instead of the cut-based ones in Table 4.1. The pre-selections of IP(track) < 2 mm and $|M(K\pi) - 1865| < 30\,\text{MeV}/c^2$ are applied to preliminarily subtract the background. Due to very different signal purities between the high and low p_{T} candidates in HM and LM events, the MVA are performed in four different intervals respectively, where the binning schemes are shown in Table 5.1. The samples used for training are the simulated prompt D^0 signals and the sideband background ($|M(K\pi) - 1865\,\text{MeV}/c^2| > 50\,\text{MeV}/c^2$) using the Multi-Layer Perceptron (MLP) method. The training variables are DIRA(D^0), IP(D^0), VD(D^0), χ^2(vtx), VD$_z/\sigma$(VD$_z$), IP(track), χ^2_{IP}(track), p(track), p_{T}(track), χ^2/ndf(track), $\mathcal{P}_{\text{ghost}}$(track) and ProbNNghost(track). The distributions of the input variables for the MVA training are

Table 5.1 p_{T} and multiplicity binning schemes for MVA training.

	Forward	Backward
Low p_{T}	$0 < p_{\mathrm{T}}(D^0) < 2\,\mathrm{GeV}/c$	$0 < p_{\mathrm{T}}(D^0) < 2\,\mathrm{GeV}/c$
High p_{T}	$2 < p_{\mathrm{T}}(D^0) < 20\,\mathrm{GeV}/c$	$2 < p_{\mathrm{T}}(D^0) < 20\,\mathrm{GeV}/c$
LM (10-100% activity)	$N^{\mathrm{long}}_{\mathrm{tracks}} \leq 63$	$N^{\mathrm{long}}_{\mathrm{tracks}} \leq 93$
HM (0-10% activity)	$N^{\mathrm{long}}_{\mathrm{tracks}} > 63$	$N^{\mathrm{long}}_{\mathrm{tracks}} > 93$

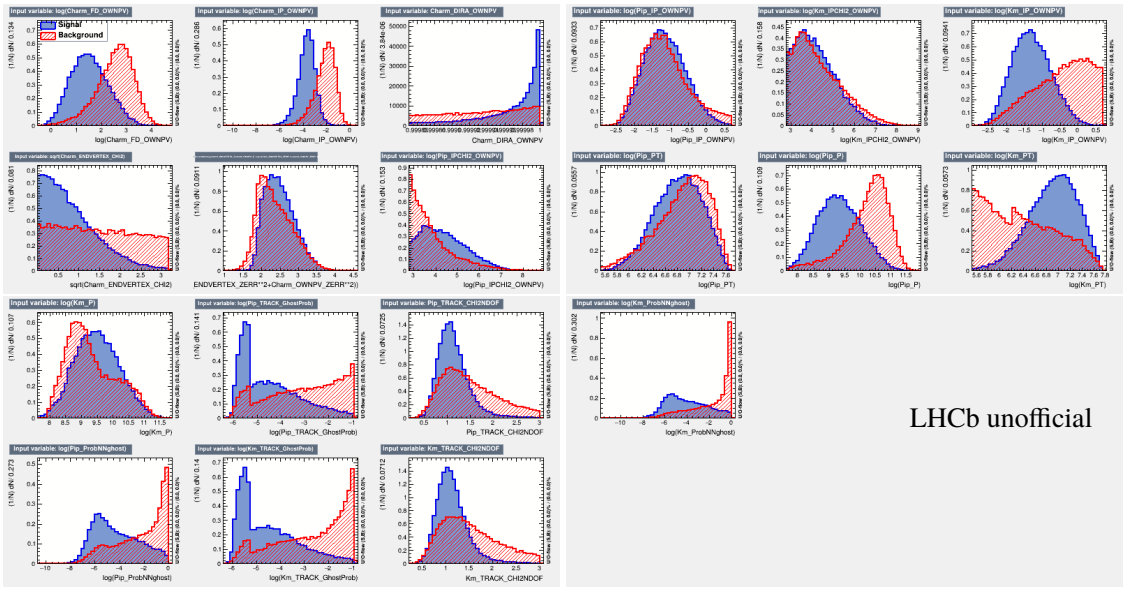

Figure 5.3 Distributions of training variables for (blue) signal and (red shaded) background with $0 < p_{\mathrm{T}}(D^0) < 2\,\mathrm{GeV}/c$ and $N^{\mathrm{long}}_{\mathrm{tracks}} > 93$ at backward rapidity.

shown in Fig. 5.3. The correlation matrix of the input variables are shown in Fig. 5.4 The distributions of the MLP classifier for training and test samples, used for checking possible overtraining, are shown in Fig. 5.5, where a good agreement between training and test samples is found and no overtraining is suggested. The receiver operating characteristic (ROC) curve and cut efficiencies are shown in Fig. 5.6. The optimal cut value for MLP classifier can be obtained by maximising the signal significance $S/\sqrt{S+B}$ shown in the right panel of Fig. 5.6. The training results are only shown for low-p_{T} and HM backward events, which have the worst signal-to-noise ratio. The $M(K\pi)$ and $\log_{10}\left(\chi^2_{\mathrm{IP}}\right)$ distributions before and after the selection are compared in Fig. 5.7. Significant suppression on both combinatorial background and non-prompt D^0 candidates can be seen. The efficiency and signal purity estimated from the fit in Fig. 5.7 are presented in Fig. 5.8 and 5.9 respectively, corresponding to an overall efficiency of 93.3% (92.6%) and purity of 96.1% (94.1%) at forward (backward) rapidity. For the case of Fig. 5.7, the purity increases from

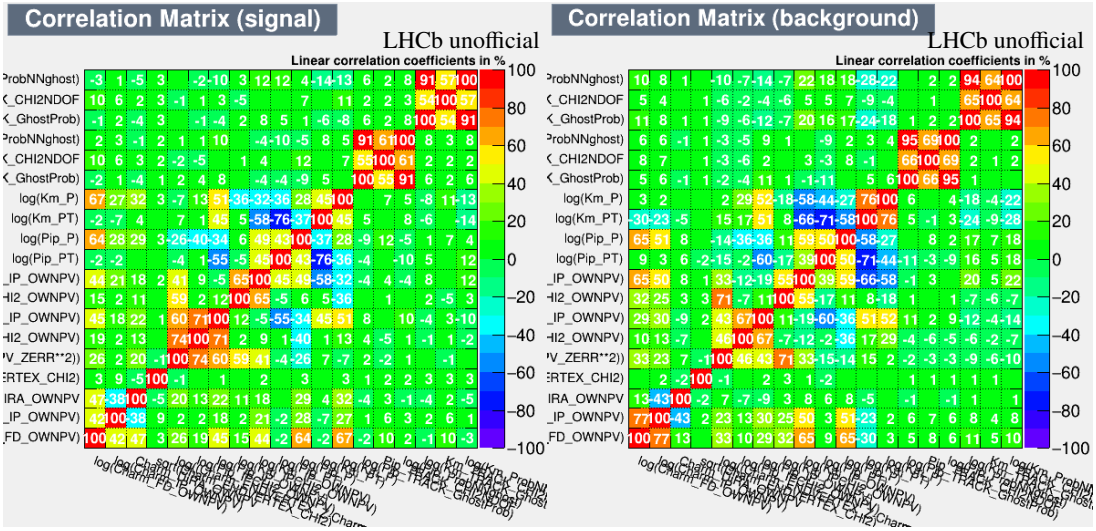

Figure 5.4 Correlation matrices of training variables for (left) signal and (right) background with $0 < p_{\mathrm{T}}(D^0) < 2\,\mathrm{GeV}/c$ and $N^{\mathrm{long}}_{\mathrm{tracks}} > 93$ at backward rapidity.

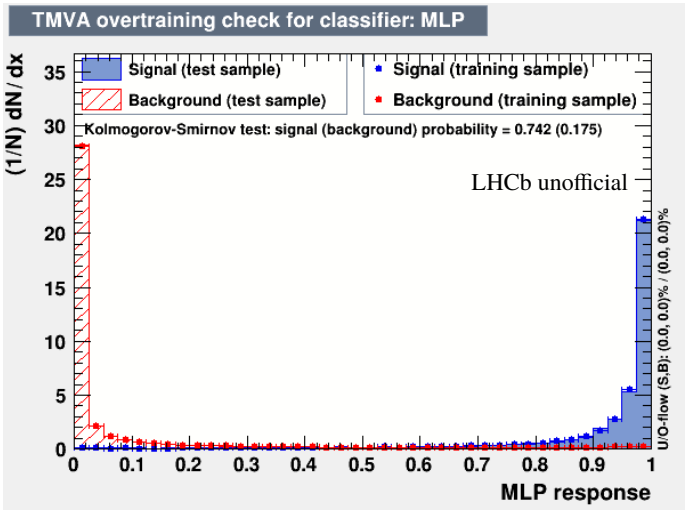

Figure 5.5 MLP classifier distributions for signal and background in training and test samples with $0 < p_{\mathrm{T}}(D^0) < 2\,\mathrm{GeV}/c$ and $N^{\mathrm{long}}_{\mathrm{tracks}} > 93$ at backward rapidity.

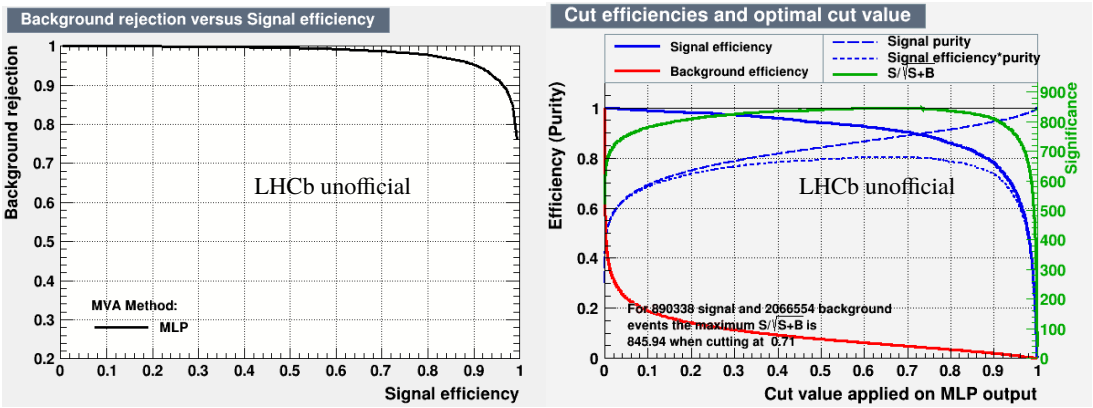

Figure 5.6 (left) Receiver operating characteristic curve and (right) cut efficiencies for the backward sample with $0 < p_{\mathrm{T}}(D^0) < 2\,\mathrm{GeV}/c$ and $N^{\mathrm{long}}_{\mathrm{tracks}} > 93$.

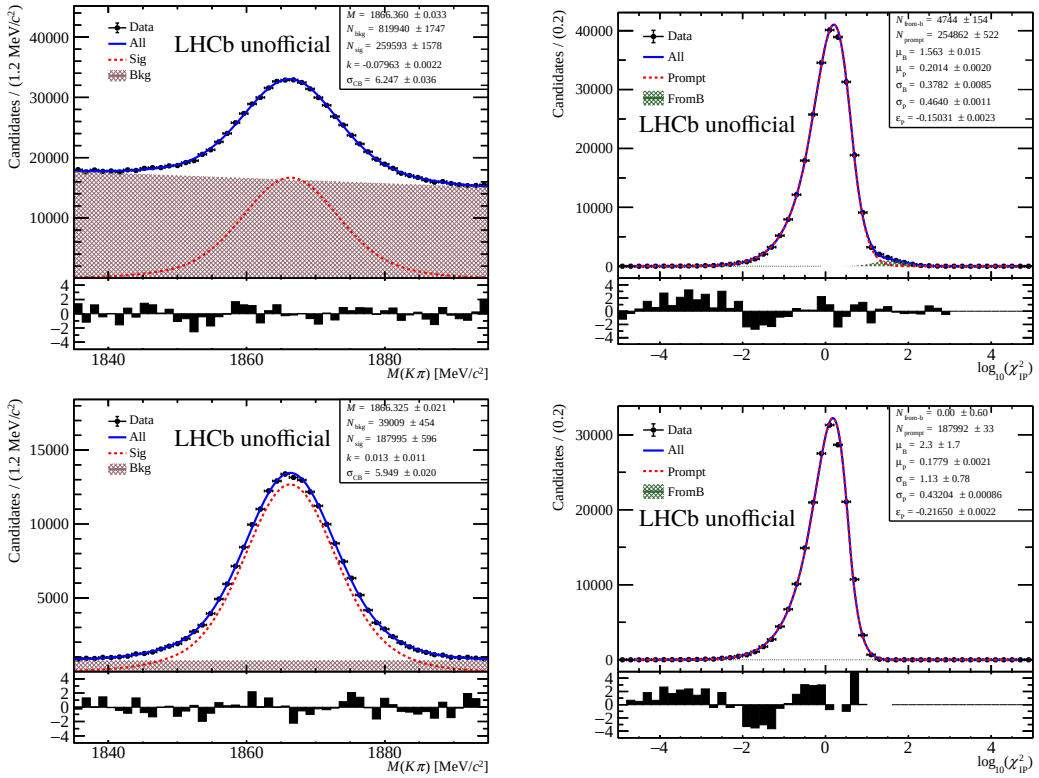

Figure 5.7 (left) $M(K\pi)$ and (right) $\log_{10}\left(\chi^2_{\mathrm{IP}}\right)$ distribution and the fit for backward sample with $0 < p_{\mathrm{T}}(D^0) < 1$ GeV/c and $N^{\mathrm{long}}_{\mathrm{tracks}} > 93$. Top for the sample before selections and bottom for that after selections.

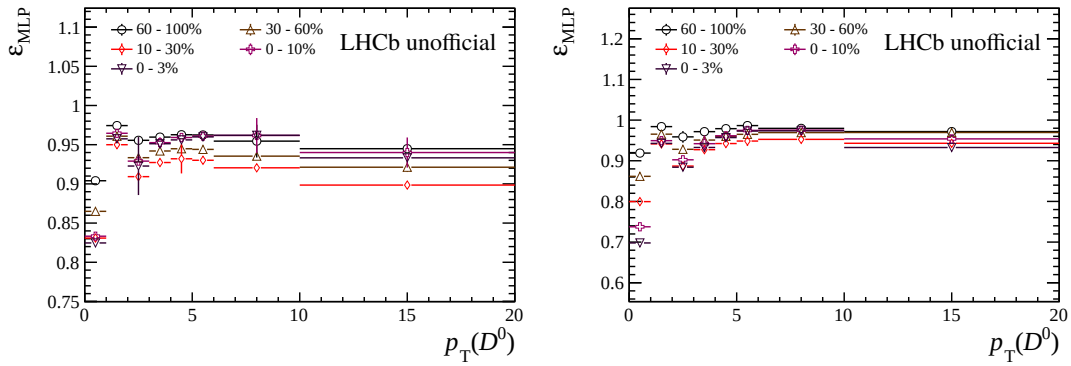

Figure 5.8 Efficiency of the MVA selection with MLP classifier for (left) forward and (right) backward samples. The error bars show the statistical uncertainties.

23.6% to 82.8%, with only 26.2% of signals excluded.

Selections on associated tracks (h) are also applied to subtract non-prompt and fake tracks. The selections are summarised in Table 5.2. Due to the selections on χ^2_{IP}(track) in Tables 5.2 and 3.1 are mutually exclusive, the overlap between h and D^0 final-state tracks are avoided naturally.

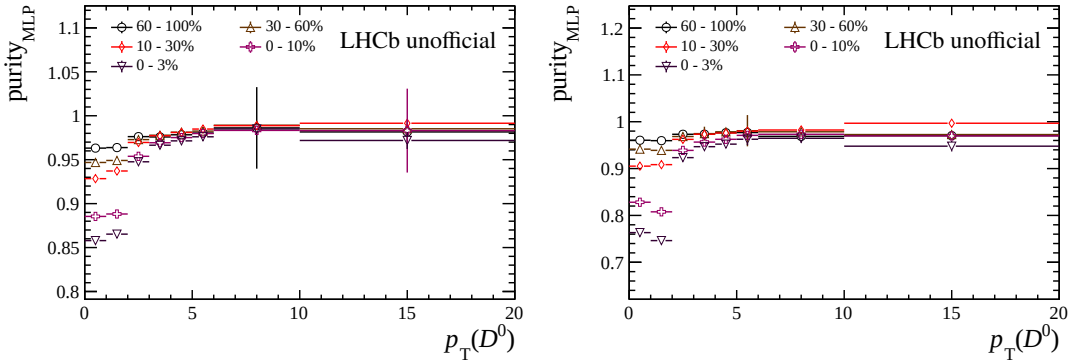

Figure 5.9 Signal purity of the MVA selection with MLP classifier for (left) forward and (right) backward samples. The error bars show the statistical uncertainties

Table 5.2 Selections for charged particle associated to D^0 candidates.

Quantity	Selections
Track type	Long
p_T(track)	$0.8 < p_T < 5$ GeV/c
$\mathcal{P}_{\text{ghost}}$	< 0.4
χ^2/ndf(track)	< 4
χ^2_{IP}(track)	< 16

5.2 Correlation function

To get the correlation function, the azimuthal difference $\Delta\phi = \phi_{D^0} - \phi_h$ and $\Delta\eta = \eta_{D^0} - \eta_h$ are calculated. The $\Delta\phi$ is redefined to obtain a uniform distribution for uncorrelated particle pairs

$$\Delta\phi = \begin{cases} \phi_1 - \phi_2 & , \quad \phi_1 - \phi_2 \in [-\pi, +\pi] \\ (\phi_1 - \phi_2) + 2\pi & , \quad \phi_1 - \phi_2 < -\pi \\ (\phi_1 - \phi_2) - 2\pi & , \quad \phi_1 - \phi_2 > +\pi \end{cases} . \tag{5.1}$$

Because the $\Delta\phi$ distribution is symmetric, the absolute value $|\Delta\phi|$ is used instead. The correlation function, also known as the associated differential yield per trigger particle, can be calculated with

$$\frac{1}{N_{\text{trigger}}} \frac{\mathrm{d}^2 N_{\text{pair}}}{\mathrm{d}\Delta\eta \mathrm{d}\Delta\phi} = B(0,0) \times \frac{S(\Delta\eta, \Delta\phi)}{B(\Delta\eta, \Delta\phi)}. \tag{5.2}$$

The two functions, $S(\Delta\eta, \Delta\phi)$ and $B(\Delta\eta, \Delta\phi)$, are known as the foreground and background and are defined as

$$S(\Delta\eta, \Delta\phi) = \frac{1}{N_{\text{trigger}}} \frac{\mathrm{d}^2 N_{\text{same}}}{\mathrm{d}\Delta\eta \mathrm{d}\Delta\phi} , \tag{5.3}$$

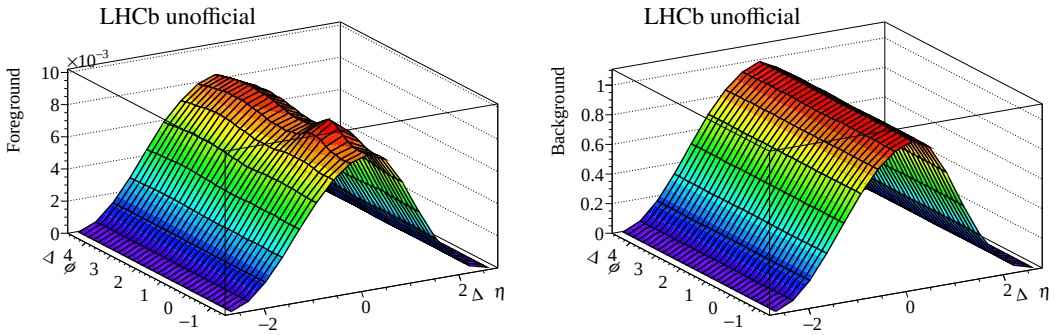

Figure 5.10 Two-dimensional (left) foreground and (right) background distributions (normalised its value at the origin) of $D^0 - h$ pairs for backward sample with $2 < p_{\mathrm{T}}(D^0) < 3\,\mathrm{GeV}/c$ and $N^{\mathrm{long}}_{\mathrm{tracks}} > 93$.

$$B(\Delta\eta, \Delta\phi) = \frac{1}{N_{\mathrm{trigger}}} \frac{\mathrm{d}^2 N_{\mathrm{mix}}}{\mathrm{d}\Delta\eta \mathrm{d}\Delta\phi} \,. \tag{5.4}$$

To be specific, $S(\Delta\eta, \Delta\phi)$ is obtained by combining $D^0 - h$ pairs from the same event, As shown in the left panel of Fig. 5.10, the foreground is dominated by the detector acceptance, especially in the $\Delta\eta$ axis. Thus the background is introduced to suppress this effect and make the correlation *signals* more visible. It is obtained with the *event mixing* technique, where the D^0 candidates are paired with tracks from *similar* events. Here similar events should be in the same p_{T} (D^0) interval and event class. A close PV_z with $\left|\mathrm{PV}_z^{\mathrm{trigger}} - \mathrm{PV}_z^{\mathrm{mix}}\right| < 20\,\mathrm{mm}$ is also required such that the events are reconstructed in a similar way. Ideally the two particles are uncorrelated and the contribution from the detector geometrical acceptance can be described, as shown in the right panel of Fig. 5.10. The two dimensional correlation function can be finally derived from Eq. 5.2. An example is presented in Fig. 5.11, from which the structures of *jet peak*, *near-side ridge* and *away-side ridge* can be seen, as described in Fig. 1.34.

To separate the short-range and long-range components, one-dimensional yields are introduced,

$$\frac{1}{N_{\mathrm{trigger}}} \frac{\mathrm{d}\Delta N_{\mathrm{pair}}}{\mathrm{d}\Delta\phi} = B(0) \times \frac{S(\Delta\phi)}{B(\Delta\phi)} \,, \tag{5.5}$$

where $S(\Delta\phi)$ and $B(\Delta\phi)$ can be obtained from the integration on two-dimensional distributions over regions of $0 < |\Delta\eta| < 1.4$ (short range) or $1.4 < |\Delta\eta| < 2.8$ (long range). The obtained correlation functions are shown in Fig. 5.12. The pedestal of the functions can be removed with the ZYAM method[153-154]. A toy fit with second-order polynomial is performed in $0.4 < \Delta\eta < 1.8$ to determine the minimum value, as represented by

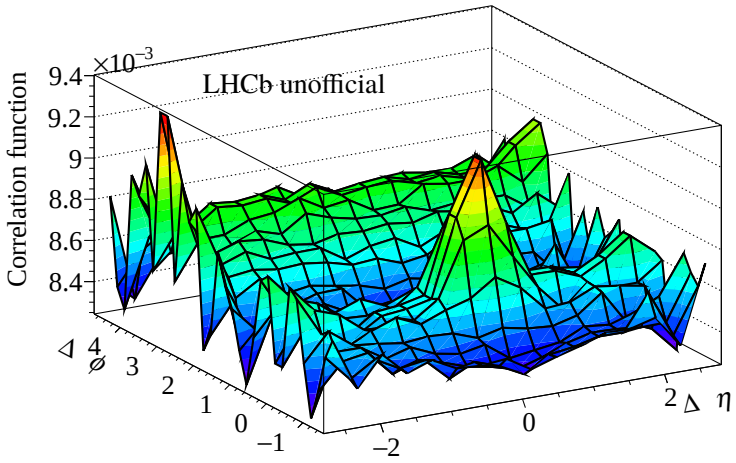

Figure 5.11 Two-dimensional correlation function of $D^0 - h$ pairs for backward sample with $2 < p_{\mathrm{T}}(D^0) < 3\,\mathrm{GeV}/c$ and $N^{\mathrm{long}}_{\mathrm{tracks}} > 93$.

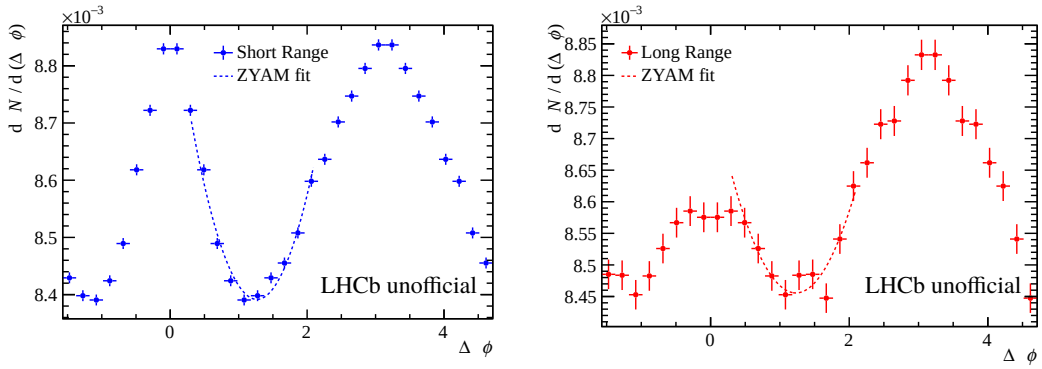

Figure 5.12 One-dimensional (left) short-range ($|\Delta\eta| < 1.4$) and (right) long-range ($|\Delta\eta| > 1.4$) correlation function of $D^0 - h$ pairs for backward sample with $2 < p_{\mathrm{T}}(D^0) < 3\,\mathrm{GeV}/c$ and $N^{\mathrm{long}}_{\mathrm{tracks}} > 93$.

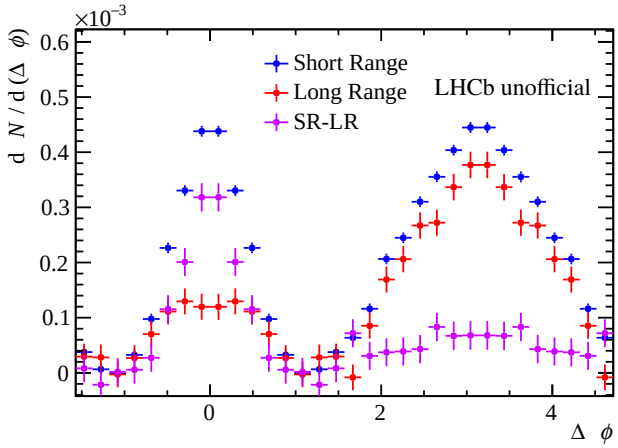

Figure 5.13 One-dimensional short-range and long-range correlation functions of $D^0 - h$ pairs for backward sample with $2 < p_{\mathrm{T}}(D^0) < 3\,\mathrm{GeV}/c$ and $N^{\mathrm{long}}_{\mathrm{tracks}} > 93$. The near-side correlation, obtained by subtracting the long-range correlation function from the short-range one, is also shown.

the dashed curves in Fig. 5.12. The long-range and short range correlation function with pedestals removed are shown in Fig. 5.13. The near-side correlation function can then be derived by subtracting the long-range correlation function from the short-range one, which is also presented in Fig. 5.13. It can be used to determine the *jet yield* afterwards[156].

5.3 Collective flow

The flow harmonics are extracted with the Fourier expansion on the long-range correlation function $f(\Delta\phi) = \frac{1}{N_{\mathrm{trigger}}} \frac{\mathrm{d}\Delta N_{\mathrm{pair}}}{\mathrm{d}\Delta\phi}$,

$$f(\Delta\phi) = G\left\{1 + \sum_{n=1}^{\infty} a_n \cos(n\Delta\phi)\right\}, \tag{5.6}$$

where the contamination from the jet fragmentation is excluded. Examples of the Fourier fit are shown in Fig. 5.14, for the backward region with $2 < p_{\mathrm{T}}(D^0) < 3\,\mathrm{GeV}/c$. The Fourier harmonics a_1, a_2 and a_3 are shown in Fig. 5.15, 5.16 and 5.17. The a_1 has negative values due to the away-side ridge at $\Delta\phi \sim \pi$. The a_2 indicates a decreasing trend versus the increasing event multiplicity, inconsistent with the increasing near-side ridge with multiplicity suggested by Fig. 5.14. It may be attributed to the contribution from the negative a_1 in the near-side region. The a_3 also corresponds to negative values, while a_4 values are not shown due to the large uncertainties.

With further non-flow subtraction[156], the $V_n^{D^0-h}$ values can be obtained, where

$$V_n^{D^0-h} = v_n^{D^0} \cdot v_n^h, \tag{5.7}$$

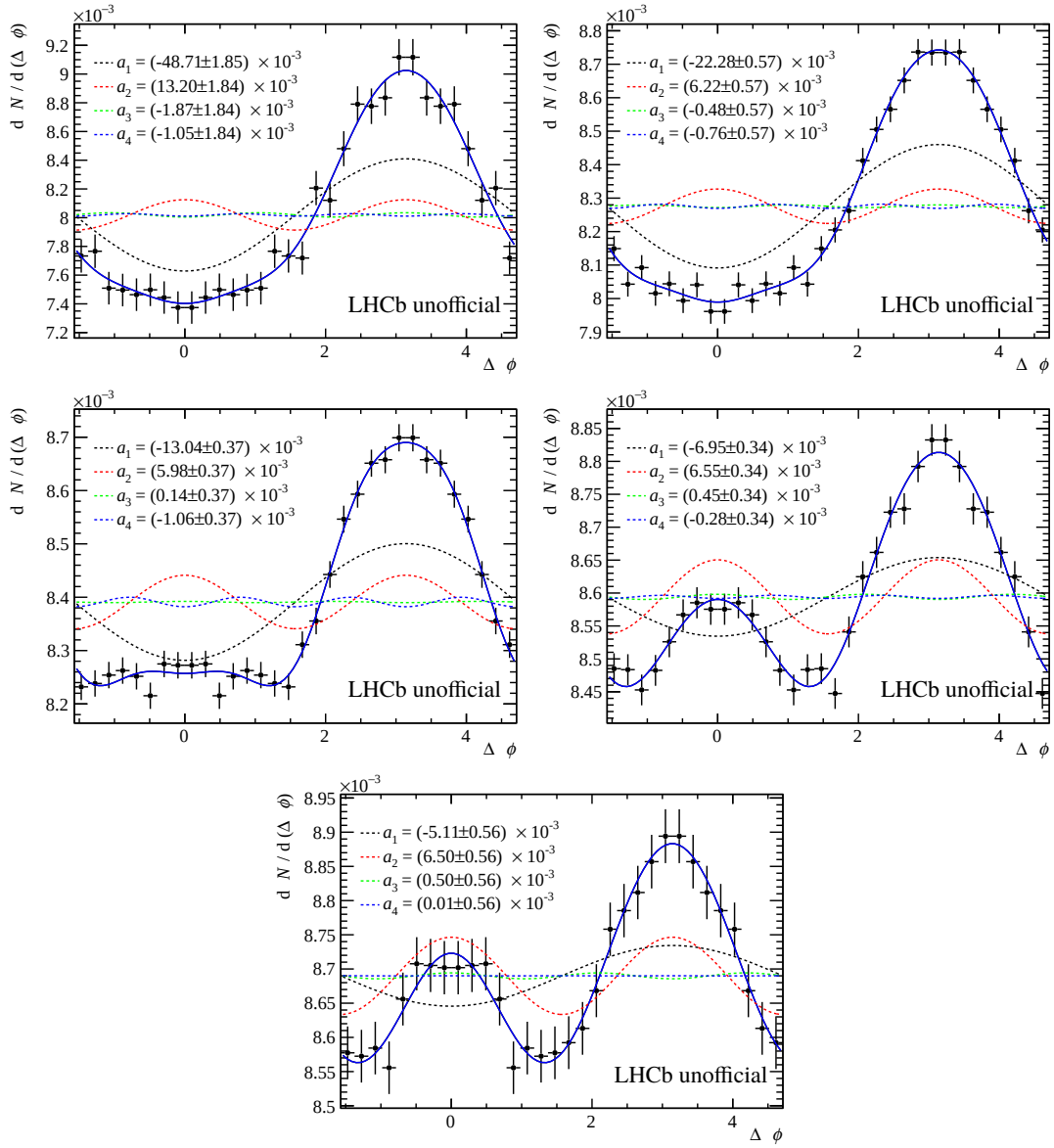

Figure 5.14 Fourier expansion of one-dimensional long-range ($1.4 < |\Delta\eta| < 2.8$) $\Delta\phi$ correlation for backward sample with $2 < p_{\mathrm{T}}(D^0) < 3\,\mathrm{GeV}/c$ from low to high multiplicity ($60-100\%, 30-60\%, 10-30\%, 0-10\%, 0-3\%$ from left to right and top to bottom). The error bars show the statistical uncertainties.

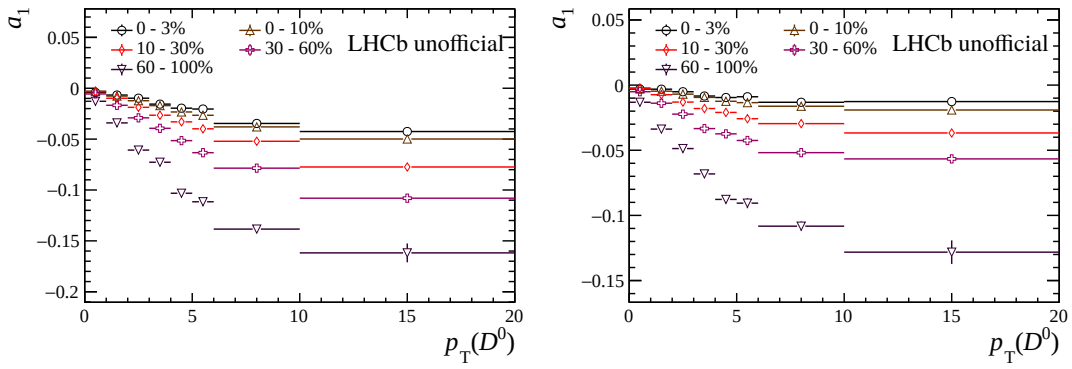

Figure 5.15 Fourier harmonic a_1 of long-range $\Delta\phi$ correlation function for (left) forward and (right) backward rapidities in different p_T (D^0) intervals and event classes. The error bars show the statistical uncertainties.

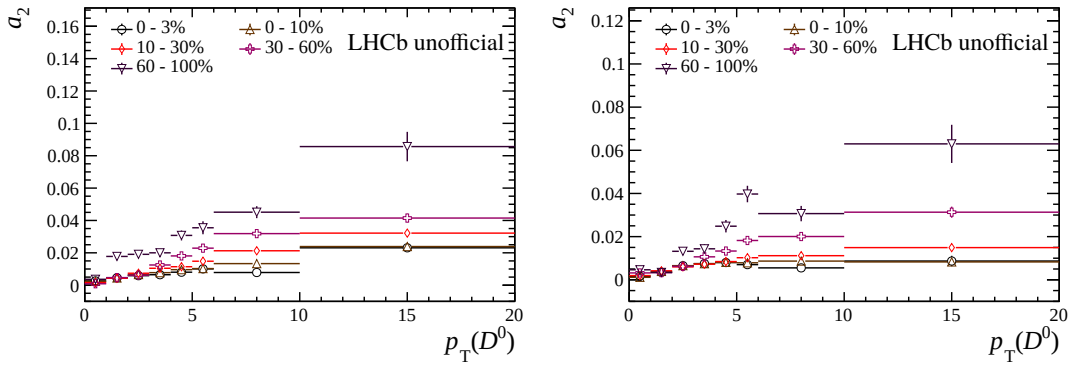

Figure 5.16 Fourier harmonic a_2 of long-range $\Delta\phi$ correlation function for (left) forward and (right) backward rapidities in different p_T (D^0) intervals and event classes. The error bars show the statistical uncertainties.

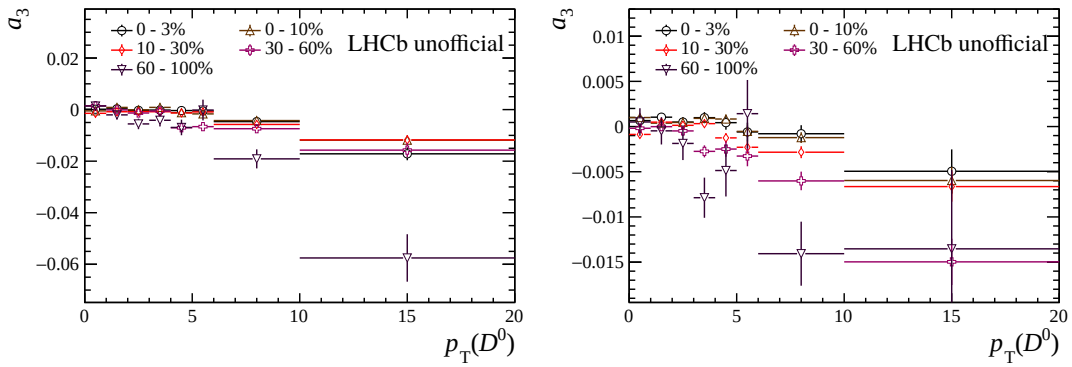

Figure 5.17 Fourier harmonic a_3 of long-range $\Delta\phi$ correlation function for (left) forward and (right) backward rapidities in different p_T (D^0) intervals and event classes. The error bars show the statistical uncertainties.

as Eq. 1.41 suggests. The *CMS method*, which was originally employed in the CMS flow measurement[229], is used in this thesis. The Fourier coefficients a_n in Eq. 5.6 can be separated into flow (c_n) and non-flow terms (d_n). Thus, $f(\Delta\phi)$ can be rewritten as

$$f(\Delta\phi) = G\left\{1 + \sum_{n=1}^{\infty}(c_n + d_n)\cos(n\Delta\phi)\right\} \tag{5.8}$$

$$\equiv J(\Delta\phi) + G\left\{1 + \sum_{n=1}^{\infty} c_n \cos(n\Delta\phi)\right\}\ , \tag{5.9}$$

It can be first assumed that the rational coefficients between HM and LM events $j_n = d_n^{\mathrm{HM}}/d_n^{\mathrm{LM}}$ keep the same for different harmonic numbers as $j_n \equiv j^{\mathrm{CMS}}$. Then the non-flow components for HM and LM can be related as

$$\frac{J^{\mathrm{HM}}(\Delta\phi)}{G^{\mathrm{HM}}} = j^{\mathrm{CMS}}\frac{J^{\mathrm{LM}}(\Delta\phi)}{G^{\mathrm{LM}}}\ . \tag{5.10}$$

Here j^{CMS} can be estimated by comparing the near-side jet yields between HM and LM intervals

$$j^{\mathrm{CMS}} = \frac{G^{\mathrm{LM}}\int_{-1.2}^{1.2}\left[f_{\mathrm{SR}}^{\mathrm{HM}}(\Delta\phi) - f_{\mathrm{LR}}^{\mathrm{HM}}(\Delta\phi)\right]\mathrm{d}\Delta\phi}{G^{\mathrm{HM}}\int_{-1.2}^{1.2}\left[f_{\mathrm{SR}}^{\mathrm{LM}}(\Delta\phi) - f_{\mathrm{LR}}^{\mathrm{LM}}(\Delta\phi)\right]\mathrm{d}\Delta\phi}\ . \tag{5.11}$$

Another reasonable assumption which can be made is that collective flow does not exist for LM events. So, by plugging Eq. 5.10 into Eq. 5.8, the c_n^{HM} can be given as

$$V_n^{\mathrm{HM}} = a_n^{\mathrm{HM}} - j^{\mathrm{CMS}}a_n^{\mathrm{LM}}\ . \tag{5.12}$$

Here, the LM interval is chosen to be $60-100\%$ event activity. After calculating j^{CMS} with the measured near-side correlation in Fig. 5.13, $V_2^{D^0-h}$ and $V_3^{D^0-h}$ are calculated and shown in Fig. 5.18 and 5.19, respectively. The numerical values are also given in Tables 5.3 and 5.4 for $V_2^{D^0-h}$, and in Tables 5.5 and 5.6 for $V_3^{D^0-h}$. The statistical uncertainties shown in this table include uncertainties from the Fourier expansion and the j^{CMS} estimation. The $V_2^{D^0-h}$ results, with only statistical uncertainties considered, show positive values ($> 5\sigma$) for $1 < p_{\mathrm{T}}(D^0) < 5\,\mathrm{GeV}/c$ and event class $< 30\%$ at backward rapidity. At forward rapidity, no significant non-zero results are observed, which probability originates from the smaller event multiplicity in this region. The results from $V_3^{D^0-h}$ are also consistent with zero. It may be due to either the small $V_3^{D^0-h}$ values or the limited statistics.

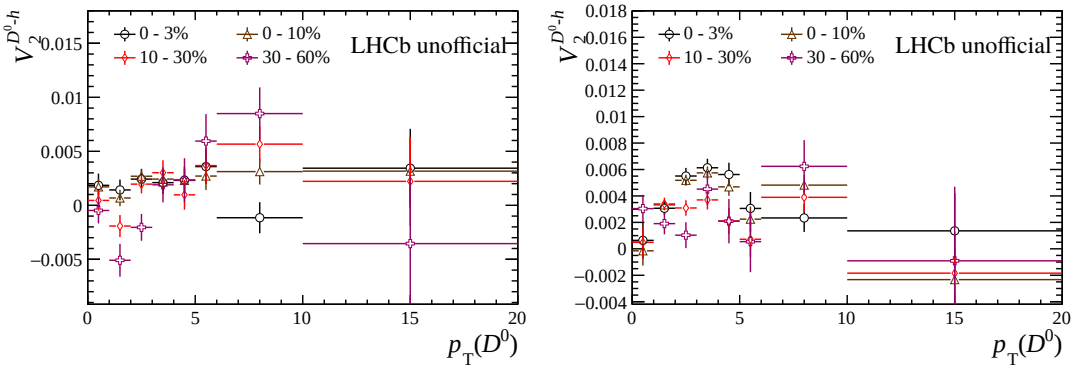

Figure 5.18 $V_2^{D^0-h}$ measured from prompt D^0 and charged track correlation after non-flow subtraction as a function of p_T (D^0) and event class, for (left) forward and (right) backward rapidities. The error bars show the statistical uncertainties.

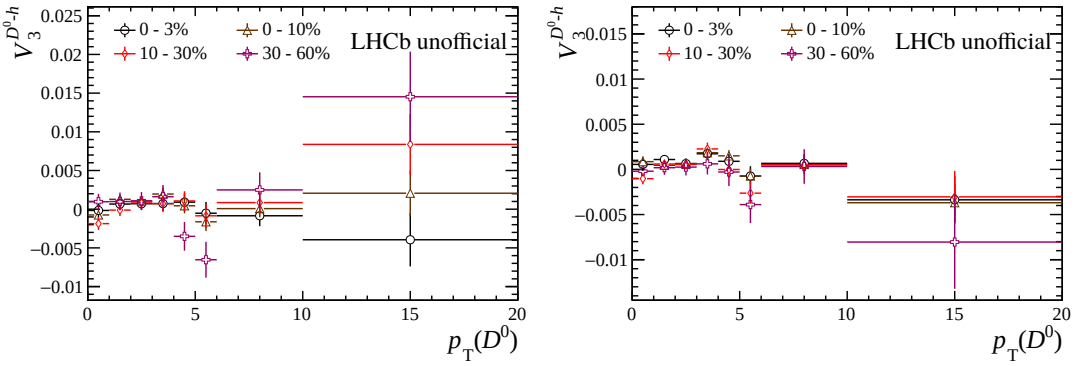

Figure 5.19 $V_3^{D^0-h}$ measured from prompt D^0 and charged track correlation after non-flow subtraction as a function of p_T (D^0) and event class, for (left) forward and (right) backward rapidities. The error bars show the statistical uncertainties.

Table 5.3 $V_2^{D^0-h}$, measured from prompt D^0 and charged track correlation, after non-flow subtraction as a function of p_T (D^0) and event class at forward rapidity.

	$V_2^{D^0-h}$ / 10^{-3}			
p_T (D^0) [GeV/c]\Event class	30 - 60 %	10 - 30 %	0 - 10 %	0 - 3 %
0 - 1 GeV/c	-0.5 ± 1.2	0.5 ± 1.0	1.7 ± 0.8	1.8 ± 1.1
1 - 2 GeV/c	-5.1 ± 1.5	-1.9 ± 1.0	0.7 ± 0.8	1.4 ± 1.0
2 - 3 GeV/c	-2.0 ± 1.2	2.0 ± 0.9	2.7 ± 0.7	2.4 ± 0.9
3 - 4 GeV/c	1.9 ± 1.6	3.0 ± 1.2	2.4 ± 0.9	2.1 ± 1.0
4 - 5 GeV/c	2.3 ± 2.0	1.0 ± 1.4	2.3 ± 1.1	2.3 ± 1.3
5 - 6 GeV/c	5.9 ± 2.5	3.7 ± 1.7	2.7 ± 1.3	3.6 ± 1.6
6 - 10 GeV/c	8.5 ± 2.4	5.7 ± 1.6	3.1 ± 1.2	-1.2 ± 1.4
10 - 20 GeV/c	-3.5 ± 6.2	2.2 ± 4.1	3.2 ± 3.1	3.4 ± 3.6

Table 5.4 $V_2^{D^0-h}$, measured from prompt D^0 and charged track correlation, after non-flow subtraction as a function of p_{T} (D^0) and event class at backward rapidity.

	$V_2^{D^0-h}$ / 10^{-3}			
p_{T} (D^0) [GeV/c]\Event class	30 - 60 %	10 - 30 %	0 - 10 %	0 - 3 %
0 - 1 GeV/c	3.0 ± 1.0	0.5 ± 1.2	-0.2 ± 1.1	0.6 ± 1.4
1 - 2 GeV/c	1.9 ± 0.8	3.4 ± 0.5	3.3 ± 0.4	3.1 ± 0.5
2 - 3 GeV/c	1.0 ± 1.0	3.1 ± 0.6	5.2 ± 0.4	5.5 ± 0.6
3 - 4 GeV/c	4.5 ± 1.2	3.7 ± 0.7	5.7 ± 0.5	6.1 ± 0.7
4 - 5 GeV/c	2.1 ± 1.7	2.1 ± 1.0	4.7 ± 0.7	5.6 ± 0.9
5 - 6 GeV/c	0.5 ± 2.3	0.7 ± 1.3	2.2 ± 1.0	3.1 ± 1.2
6 - 10 GeV/c	6.2 ± 2.0	3.9 ± 1.1	4.8 ± 0.8	2.3 ± 1.1
10 - 20 GeV/c	-0.9 ± 5.6	-1.8 ± 3.1	-2.3 ± 2.3	1.4 ± 2.8

Table 5.5 $V_3^{D^0-h}$, measured from prompt D^0 and charged track correlation, after non-flow subtraction as a function of p_{T} (D^0) and event class at forward rapidity.

	$V_3^{D^0-h}$ / 10^{-3}			
p_{T} (D^0) [GeV/c]\Event class	30 - 60 %	10 - 30 %	0 - 10 %	0 - 3 %
0 - 1 GeV/c	1.0 ± 1.0	-1.9 ± 0.8	-0.7 ± 0.6	-0.2 ± 0.9
1 - 2 GeV/c	1.0 ± 1.2	-0.1 ± 0.8	1.3 ± 0.6	0.7 ± 0.7
2 - 3 GeV/c	1.1 ± 1.1	0.8 ± 0.8	1.1 ± 0.6	0.7 ± 0.8
3 - 4 GeV/c	1.6 ± 1.5	0.7 ± 1.1	2.0 ± 0.8	0.7 ± 1.0
4 - 5 GeV/c	-3.5 ± 1.9	1.1 ± 1.3	0.4 ± 1.0	0.9 ± 1.1
5 - 6 GeV/c	-6.5 ± 2.3	-0.9 ± 1.6	-1.6 ± 1.2	-0.5 ± 1.5
6 - 10 GeV/c	2.5 ± 2.3	0.9 ± 1.5	0.1 ± 1.1	-0.8 ± 1.3
10 - 20 GeV/c	14.5 ± 5.8	8.4 ± 3.9	2.1 ± 2.9	-3.9 ± 3.4

Table 5.6 $V_3^{D^0-h}$, measured from prompt D^0 and charged track correlation, after non-flow subtraction as a function of p_{T} (D^0) and event class at backward rapidity.

	$V_3^{D^0-h}$ / 10^{-3}			
p_{T} (D^0) [GeV/c]\Event class	30 - 60 %	10 - 30 %	0 - 10 %	0 - 3 %
0 - 1 GeV/c	-0.2 ± 0.5	-1.0 ± 0.6	0.9 ± 0.6	0.6 ± 0.7
1 - 2 GeV/c	0.2 ± 0.8	0.6 ± 0.5	0.5 ± 0.4	1.1 ± 0.5
2 - 3 GeV/c	0.3 ± 0.9	0.5 ± 0.5	0.6 ± 0.4	0.6 ± 0.6
3 - 4 GeV/c	0.6 ± 1.2	2.3 ± 0.7	1.8 ± 0.5	1.7 ± 0.7
4 - 5 GeV/c	-0.3 ± 1.6	-0.0 ± 0.9	1.5 ± 0.6	0.9 ± 0.8
5 - 6 GeV/c	-3.9 ± 2.0	-2.6 ± 1.2	-0.7 ± 0.8	-0.7 ± 1.1
6 - 10 GeV/c	0.3 ± 1.9	0.5 ± 1.1	0.5 ± 0.7	0.7 ± 1.0
10 - 20 GeV/c	-8.0 ± 5.2	-3.0 ± 2.9	-3.7 ± 2.1	-3.4 ± 2.6

5.4 Summary and outlook

This analysis presents the first measurement of D^0 flow in LHCb experiment. The $(\Delta\eta, \Delta\phi)$ correlation functions of D^0 meson and charged particles pairs are obtained, in which the structures of jet peak, near-side ridge and away-side ridge can be observed. By extracting the long-range component, the flow harmonics are calculated via Fourier expansion, with only statistical uncertainties included. The measured $V_2^{D^0-h}$ results indicate positive values, especially for high-multiplicity events at backward rapidity. This can be interpreted by the collective behaviour of charm quarks. The $V_3^{D^0}$ values are too small to be determined.

Several sources of systematic uncertainties are to be considered in the next steps for this measurement. The first one comes from the combinatorial background from-b as indicated in Fig 5.9. Due to the small statistics of these components, it may be difficult to directly reduce their contribution on the measured $V_n^{D^0-h}$ by estimating V_n^{B-h} and $V_n^{\mathrm{bkg}-h}$. Alternatively, they can be considered by changing the cut-based or MLP selection to see how the $V_n^{D^0-h}$ values vary. The boundary for separating short-range and long-range correlation is chosen to be $|\Delta\eta| = 1.4$. By varying the boundary, the systematic uncertainties from its choice can be evaluated. It is also essential to investigate whether an effective cancellation on detector efficiency is achieved with event-mixing method. In the fitting procedure, the binning scheme, as well as the order of the Fourier expansion, may also influence the extracted flow.

There may be other several aspects to be improved possibly. The event class (central-

ity) estimators used is the detector occupancy $N_{\text{tracks}}^{\text{long}}$ currently. It will be more convenient for comparisons with theoretical predictions if the occupancy variables can be related to the collision geometry. And an improved $p_{\text{T}}(D^0)$ binning will also be considered. The v_n^h values are also needed for the final $v_n^{D^0}$ results as Eq. 5.7 indicates, which is another ongoing analysis.

CHAPTER 6 CONCLUSION AND PROSPECTS

6.1 Conclusion

QGP is an import topic that connects the minimum (QCD) and the maximum (Big Bang theory) in the Universe. Heavy-ion collisions provide unique opportunities to produce and study it in the laboratory. Throughout the evolution of heavy-ion collsions, the particle production may be affected by different kinds of nuclear matter effects. These effects can be classified into HNM effects, induced by the QGP, and CNM effects, related to the intrinsic properties of heavy nuclei and multiple scatterings between nucleons. The have been many signatures in experiments for investigating these effects, which help to achieve a full knowledge of the properties of QGP. The pA collisions are usually considered as a baseline for AA collisions. The measurements in pA collisions are important for the investigation of CNM effects, since HNM effects are not expected to dominate. However, as more and more QGP-like signatures, such as collective flow and strangeness enhancement, are gradually observed in such small systems, it worth further confirming whether a small droplet of QGP is created in pA collisions.

The LHCb detector is a delicate instrumentation for heavy-flavour measurements. It collected pPb data at $\sqrt{s_{\mathrm{NN}}} = 8.16\,\mathrm{TeV}$ for both forward and backward rapidity regions in 2016, corresponding to integrated luminosities of $12.2 \pm 0.3\,\mathrm{nb}^{-1}$ and $18.6 \pm 0.5\,\mathrm{nb}^{-1}$ respectively. The D^0 candidates are efficiently reconstructed online and are recorded with large statistics. In this thesis, the measurements on prompt D^0 production cross-section and collective flow are performed with these data samples.

In the first analysis, the prompt D^0 production cross-section is measured for both forward ($1.5 < y^* < 4.0$) and backward ($-5.0 < y^* < -2.5$) rapidities, where the LHCb detector provides excellent reconstruction and prompt / non-prompt discrimination for D^0 mesons. The D^0 production cross-section is measured down to $p_{\mathrm{T}} \sim 0\,\mathrm{GeV}/c$ with the highest precision achieved ever in heavy-ion experiments. The total cross-sections are $297.6 \pm 0.6 \pm 14.0\,\mathrm{mb}$ and $315.2 \pm 0.2 \pm 17.8\,\mathrm{mb}$ in the kinematic range of $0 < p_{\mathrm{T}} < 30\,\mathrm{GeV}/c$ for forward and backward rapidities respectively. The nuclear modification factors are derived incorporating LHCb results in pp collisions. It shows a significant suppression at forward rapidity, confirming the existence of strong cold nuclear matter effects there. An even stronger suppression than the predictions of nPDF calcula-

tions is observed for the lowest transverse momentum region of $p_{\mathrm{T}} < 1\,\mathrm{GeV}/c$ at forward rapidity, hinting at a stronger shadowing than predicted at Bjorken-$x \sim 10^{-5}$, or additional energy loss at play. For the backward rapidity range of $-3.5 < y^* < -2.5$, the $R_{p\mathrm{Pb}}$ values are lower than nPDF calculations at $p_{\mathrm{T}} > 6\,\mathrm{GeV}/c$ with a significance of $2.0 - 3.8$ standard deviations, indicating a weaker anti-shadowing effect than the model predictions or additional final-state effects at backward rapidity. The measured forward-backward ratio also suggests a strong production asymmetry for two different regions, consistent with the results from the nuclear modification factor. The production ratio between LHCb 8.16 TeV and 5.02 TeV pPb collisions, in which uncertainties from nPDF parametrisation are canceled, is also measured and compared with theoretical calculation. A good agreement between data and theories is found. This measurement presents the most precise measurement of the prompt D^0 production in pPb collisions to date, providing unique constraints to improve nPDF parameterization down to $x \sim 10^{-5}$.

The measurement of the D^0 collective flow is also performed with these data. It is among one of the first flow analyses in LHCb experiment. The two-particle correlation method is employed in this analysis. The near-side ridge, considered as the signature of the QGP, is observed in the $D^0 - h$ $(\Delta\eta, \Delta\phi)$ correlation function. By extracting the near-side $(\Delta\phi)$ correlation function and further subtracting the non-flow contribution from back-to-back jets, the $V_n^{D^0-h}$ is obtained for different p_{T} intervals and event classes, which involves the contributions from $v_2^{D^0}$ and v_2^h. Positive V_2 values ($> 5\sigma$ with only statistic uncertainties considered) are observed for D^0 mesons with $1 < p_{\mathrm{T}} < 5\,\mathrm{GeV}/c$ in high-multiplicity events, hinting at the collectivity of charm quarks in pPb collisions. Estimation on systematic uncertainties and the measurement of charged particle flow are in progress. This result will ideally validates the results from other experiments and provides more knowledge of small collision systems in the forward region.

6.2 Prospects

There have been large varieties of heavy-ion data samples collected by the LHCb detector, as summarised in Fig. 2.3, while only a few measurements have been conducted till now. With the current data sets in Run1 and Run2, more measurements can be expected. Take for instance the heavy-flavour production related to this thesis, the measurements of excited charm hadrons, such as D^* mesons and Σ_c baryons, have not been carried out. Taking the pp data into consideration, there will be significant improvements both in statis-

tics and reconstruction quality. Thus, more particles of interests, such as double-stranged Ω_c baryons, can be investigated in (very) high-multiplicity pp samples. When it comes to the flow measurements, there have been no published results in LHCb experiment yet. So more measurements on particle flow can also be performed soon. As more interests have been arisen in the flow of heavy-flavour particle in pp collisions, it is also worth investigating them, especially for B hadrons for which the pPb data are facing lack of statistics.

The LHC has began its Run3 operation at the end of last year. For a near future, more heavy-ion data will be taken in Run3. For collision configurations, the energy will be improved and more importantly, the centrality of PbPb collisions can reach $< 30\%$ ($> 60\%$ in Run2), with the upgraded tracking systems[230]. This will make more measurements possible, such as collective flow in PbPb and nuclear modification factor R_{AA}. The fixed-target experiment in LHCb has been upgraded to SMOG2[174], which allows a simultaneous data taking with pp and PbPb runs, as well as wider choices in gas species. About $10^3\times$ more statistics are expected for all kinds of heavy-flavour particles, providing more possibilities in LHCb fixed-target measurements.

REFERENCES

[1] Wikipedia contributors. Standard model — Wikipedia, the free encyclopedia[EB/OL]. 2021. https://en.wikipedia.org/w/index.php?title=Standard_Model&oldid=1029913027.

[2] Gell-Mann M. A Schematic Model of Baryons and Mesons[J/OL]. Phys. Lett., 1964, 8: 214-215. DOI: 10.1016/S0031-9163(64)92001-3.

[3] Zweig G. An SU_3 model for strong interaction symmetry and its breaking; Version 2: CERN-TH-412[EB/OL]. 1964. http://cds.cern.ch/record/570209.

[4] Aubert J J, et al. Experimental Observation of a Heavy Particle J[J/OL]. Phys. Rev. Lett., 1974, 33: 1404-1406. DOI: 10.1103/PhysRevLett.33.1404.

[5] Augustin J E, et al. Discovery of a Narrow Resonance in e^+e^- Annihilation[J/OL]. Phys. Rev. Lett., 1974, 33: 1406-1408. DOI: 10.1103/PhysRevLett.33.1406.

[6] Herb S W, et al. Observation of a Dimuon Resonance at 9.5-GeV in 400-GeV Proton-Nucleus Collisions[J/OL]. Phys. Rev. Lett., 1977, 39: 252-255. DOI: 10.1103/PhysRevLett.39.252.

[7] Abe F, et al. Observation of top quark production in $\bar{p}p$ collisions[J/OL]. Phys. Rev. Lett., 1995, 74: 2626-2631. DOI: 10.1103/PhysRevLett.74.2626.

[8] Fukuda Y, et al. Evidence for oscillation of atmospheric neutrinos[J/OL]. Phys. Rev. Lett., 1998, 81: 1562-1567. DOI: 10.1103/PhysRevLett.81.1562.

[9] Thomson M. Modern particle physics[M]. Cambridge University Press, 2013.

[10] Schael S, et al. Precision electroweak measurements on the Z resonance[J/OL]. Phys. Rept., 2006, 427: 257-454. DOI: 10.1016/j.physrep.2005.12.006.

[11] Englert F, Brout R. Broken Symmetry and the Mass of Gauge Vector Mesons[J/OL]. Phys. Rev. Lett., 1964, 13: 321-323. DOI: 10.1103/PhysRevLett.13.321.

[12] Higgs P W. Broken symmetries, massless particles and gauge fields[J/OL]. Phys. Lett., 1964, 12: 132-133. DOI: 10.1016/0031-9163(64)91136-9.

[13] Higgs P W. Broken Symmetries and the Masses of Gauge Bosons[J/OL]. Phys. Rev. Lett., 1964, 13: 508-509. DOI: 10.1103/PhysRevLett.13.508.

[14] Guralnik G S, Hagen C R, Kibble T W B. Global Conservation Laws and Massless Particles [J/OL]. Phys. Rev. Lett., 1964, 13: 585-587. DOI: 10.1103/PhysRevLett.13.585.

[15] Higgs P W. Spontaneous Symmetry Breakdown without Massless Bosons[J/OL]. Phys. Rev., 1966, 145: 1156-1163. DOI: 10.1103/PhysRev.145.1156.

[16] Kibble T W B. Symmetry breaking in nonAbelian gauge theories[J/OL]. Phys. Rev., 1967, 155: 1554-1561. DOI: 10.1103/PhysRev.155.1554.

[17] Aad G, et al. Observation of a new particle in the search for the Standard Model Higgs boson with the ATLAS detector at the LHC[J/OL]. Phys. Lett. B, 2012, 716: 1-29. DOI: 10.1016/j.physletb.2012.08.020.

[18] Chatrchyan S, et al. Observation of a New Boson at a Mass of 125 GeV with the CMS Experiment at the LHC[J/OL]. Phys. Lett. B, 2012, 716: 30-61. DOI: 10.1016/j.physletb.2012.08.021.

[19] Friedman J I, Kendall H W. Deep inelastic electron scattering[J/OL]. Ann. Rev. Nucl. Part. Sci., 1972, 22: 203-254. DOI: 10.1146/annurev.ns.22.120172.001223.

[20] Bodek A, et al. Experimental Studies of the Neutron and Proton Electromagnetic Structure Functions[J/OL]. Phys. Rev. D, 1979, 20: 1471-1552. DOI: 10.1103/PhysRevD.20.1471.

[21] Choi S K, et al. Observation of a narrow charmonium-like state in exclusive $B^{\pm} \to K^{\pm}\pi^{+}\pi^{-}J/\psi$ decays[J/OL]. Phys. Rev. Lett., 2003, 91: 262001. DOI: 10.1103/PhysRevLett.91.262001.

[22] Aaij R, et al. Observation of $J/\psi p$ resonances consistent with pentaquark states in $\Lambda_b^0 \to J/\psi p K^{-}$ decays[J/OL]. Phys. Rev. Lett., 2015, 115: 072001. DOI: 10.1103/PhysRevLett.115.072001.

[23] Workman R L, et al. Review of Particle Physics[J/OL]. PTEP, 2022, 2022: 083C01. DOI: 10.1093/ptep/ptac097.

[24] Wilson K G. Confinement of Quarks[J/OL]. Phys. Rev. D, 1974, 10: 2445-2459. DOI: 10.1103/PhysRevD.10.2445.

[25] Chodos A, Jaffe R L, Johnson K, et al. A New Extended Model of Hadrons[J/OL]. Phys. Rev. D, 1974, 9: 3471-3495. DOI: 10.1103/PhysRevD.9.3471.

[26] DeTar C E, Donoghue J F. BAG MODELS OF HADRONS[J/OL]. Ann. Rev. Nucl. Part. Sci., 1983, 33: 235-264. DOI: 10.1146/annurev.ns.33.120183.001315.

[27] Akiba Y, et al. The Hot QCD White Paper: Exploring the Phases of QCD at RHIC and the LHC [A]. 2015. arXiv: 1502.02730.

[28] Bazavov A, et al. The chiral and deconfinement aspects of the QCD transition[J/OL]. Phys. Rev. D, 2012, 85: 054503. DOI: 10.1103/PhysRevD.85.054503.

[29] Fodor Z, Katz S D. Critical point of QCD at finite T and mu, lattice results for physical quark masses[J/OL]. JHEP, 2004, 04: 050. DOI: 10.1088/1126-6708/2004/04/050.

[30] Shen C, Heinz U. The road to precision: Extraction of the specific shear viscosity of the quark-gluon plasma[J/OL]. Nucl. Phys. News, 2015, 25(2): 6-11. DOI: 10.1080/10619127.2015.1006502.

[31] Yagi K, Hatsuda T, Miake Y. Quark-gluon plasma: From big bang to little bang: volume 23 [M]. Cambridge University Press, 2005.

[32] Miller M L, Reygers K, Sanders S J, et al. Glauber modeling in high energy nuclear collisions [J/OL]. Ann. Rev. Nucl. Part. Sci., 2007, 57: 205-243. DOI: 10.1146/annurev.nucl.57.090506.123020.

[33] Gatoff G, Kerman A K, Matsui T. The Flux Tube Model for Ultrarelativistic Heavy Ion Collisions: Electrohydrodynamics of a Quark Gluon Plasma[J/OL]. Phys. Rev. D, 1987, 36: 114. DOI: 10.1103/PhysRevD.36.114.

[34] Schwinger J S. On gauge invariance and vacuum polarization[J/OL]. Phys. Rev., 1951, 82: 664-679. DOI: 10.1103/PhysRev.82.664.

[35] Wang X N. pQCD based approach to parton production and equilibration in high-energy nuclear collisions[J/OL]. Phys. Rept., 1997, 280: 287-371. DOI: 10.1016/S0370-1573(96)00022-1.

[36] Gyulassy M, Wang X N. HIJING 1.0: A Monte Carlo program for parton and particle production in high-energy hadronic and nuclear collisions[J/OL]. Comput. Phys. Commun., 1994, 83: 307. DOI: 10.1016/0010-4655(94)90057-4.

[37] Bjorken J D. Highly Relativistic Nucleus-Nucleus Collisions: The Central Rapidity Region [J/OL]. Phys. Rev. D, 1983, 27: 140-151. DOI: 10.1103/PhysRevD.27.140.

[38] Song H, Heinz U W. Suppression of elliptic flow in a minimally viscous quark-gluon plasma [J/OL]. Phys. Lett. B, 2008, 658: 279-283. DOI: 10.1016/j.physletb.2007.11.019.

[39] Song H, Heinz U W. Causal viscous hydrodynamics in 2+1 dimensions for relativistic heavy-ion collisions[J/OL]. Phys. Rev. C, 2008, 77: 064901. DOI: 10.1103/PhysRevC.77.064901.

[40] Shen C, Qiu Z, Song H, et al. The iEBE-VISHNU code package for relativistic heavy-ion collisions[J/OL]. Comput. Phys. Commun., 2016, 199: 61-85. DOI: 10.1016/j.cpc.2015.08.039.

[41] Andersson B, Gustafson G, Ingelman G, et al. Parton Fragmentation and String Dynamics [J/OL]. Phys. Rept., 1983, 97: 31-145. DOI: 10.1016/0370-1573(83)90080-7.

[42] Webber B R. A QCD Model for Jet Fragmentation Including Soft Gluon Interference[J/OL]. Nucl. Phys. B, 1984, 238: 492-528. DOI: 10.1016/0550-3213(84)90333-X.

[43] Brock R, et al. Handbook of perturbative QCD: Version 1.0[J/OL]. Rev. Mod. Phys., 1995, 67: 157-248. DOI: 10.1103/RevModPhys.67.157.

[44] Fries R J, Muller B, Nonaka C, et al. Hadronization in heavy ion collisions: Recombination and fragmentation of partons[J/OL]. Phys. Rev. Lett., 2003, 90: 202303. DOI: 10.1103/PhysRevLett.90.202303.

[45] Greco V, Ko C M, Levai P. Parton coalescence and anti-proton / pion anomaly at RHIC[J/OL]. Phys. Rev. Lett., 2003, 90: 202302. DOI: 10.1103/PhysRevLett.90.202302.

[46] Bleicher M, et al. Relativistic hadron hadron collisions in the ultrarelativistic quantum molecular dynamics model[J/OL]. J. Phys. G, 1999, 25: 1859-1896. DOI: 10.1088/0954-3899/25/9/308.

[47] Rapp R, van Hees H. Thermal Dileptons as Fireball Thermometer and Chronometer[J/OL]. Phys. Lett. B, 2016, 753: 586-590. DOI: 10.1016/j.physletb.2015.12.065.

[48] Baier R, Schiff D, Zakharov B G. Energy loss in perturbative QCD[J/OL]. Ann. Rev. Nucl. Part. Sci., 2000, 50: 37-69. DOI: 10.1146/annurev.nucl.50.1.37.

[49] Gyulassy M, Levai P, Vitev I. Jet tomography of Au+Au reactions including multigluon fluctuations[J/OL]. Phys. Lett. B, 2002, 538: 282-288. DOI: 10.1016/S0370-2693(02)01990-1.

[50] Bjorken J D. Energy Loss of Energetic Partons in Quark - Gluon Plasma: Possible Extinction of High p(t) Jets in Hadron - Hadron Collisions[Z]. 1982.

[51] Dokshitzer Y L, Kharzeev D E. Heavy quark colorimetry of QCD matter[J/OL]. Phys. Lett. B, 2001, 519: 199-206. DOI: 10.1016/S0370-2693(01)01130-3.

[52] Armesto N, Dainese A, Salgado C A, et al. Testing the color charge and mass dependence of parton energy loss with heavy-to-light ratios at RHIC and CERN LHC[J/OL]. Phys. Rev. D, 2005, 71: 054027. DOI: 10.1103/PhysRevD.71.054027.

[53] Peigne S, Peshier A. Collisional energy loss of a fast heavy quark in a quark-gluon plasma [J/OL]. Phys. Rev. D, 2008, 77: 114017. DOI: 10.1103/PhysRevD.77.114017.

[54] Wroblewski A. ON THE STRANGE QUARK SUPPRESSION FACTOR IN HIGH-ENERGY COLLISIONS[J]. Acta Phys. Polon. B, 1985, 16: 379-392.

[55] Rafelski J, Muller B. Strangeness Production in the Quark - Gluon Plasma[J/OL]. Phys. Rev. Lett., 1982, 48: 1066. DOI: 10.1103/PhysRevLett.48.1066.

[56] Matsui T, Satz H. J/ψ Suppression by Quark-Gluon Plasma Formation[J/OL]. Phys. Lett. B, 1986, 178: 416-422. DOI: 10.1016/0370-2693(86)91404-8.

[57] Kanaya K, Satz H. Correlation and Screening in Finite Temperature SU(2) Gauge Theory[J/OL]. Phys. Rev. D, 1986, 34: 3193. DOI: 10.1103/PhysRevD.34.3193.

[58] Vogt R, Jackson A. The Charmonium and D Mesons at Finite Temperature[J/OL]. Phys. Lett. B, 1988, 206: 333-338. DOI: 10.1016/0370-2693(88)91516-X.

[59] Siemens P J, Rasmussen J O. Evidence for a blast wave from compress nuclear matter[J/OL]. Phys. Rev. Lett., 1979, 42: 880-887. DOI: 10.1103/PhysRevLett.42.880.

[60] Ollitrault J Y. Anisotropy as a signature of transverse collective flow[J/OL]. Phys. Rev. D, 1992, 46: 229-245. DOI: 10.1103/PhysRevD.46.229.

[61] Snellings R. Elliptic Flow: A Brief Review[J/OL]. New J. Phys., 2011, 13: 055008. DOI: 10.1088/1367-2630/13/5/055008.

[62] Voloshin S, Zhang Y. Flow study in relativistic nuclear collisions by Fourier expansion of Azimuthal particle distributions[J/OL]. Z. Phys. C, 1996, 70: 665-672. DOI: 10.1007/s00288 0050141.

[63] Becattini F, Inghirami G, Rolando V, et al. A study of vorticity formation in high energy nuclear collisions[J/OL]. Eur. Phys. J. C, 2015, 75(9): 406. DOI: 10.1140/epjc/s10052-015-3624-1.

[64] Serenone W M, Barbon J a G P, Chinellato D D, et al. Λ polarization from thermalized jet energy[J/OL]. Phys. Lett. B, 2021, 820: 136500. DOI: 10.1016/j.physletb.2021.136500.

[65] Molnar D, Voloshin S A. Elliptic flow at large transverse momenta from quark coalescence [J/OL]. Phys. Rev. Lett., 2003, 91: 092301. DOI: 10.1103/PhysRevLett.91.092301.

[66] Wong C Y. INITIAL ENERGY DENSITY OF QUARK GLUON PLASMA IN RELATIVISTIC HEAVY ION COLLISIONS[J/OL]. Phys. Rev. D, 1984, 30: 961-971. DOI: 10.1103/PhysRe vD.30.961.

[67] Nikolaev N N, Zakharov V I. Parton Model and Deep Inelastic Scattering on Nuclei[J/OL]. Phys. Lett. B, 1975, 55: 397-399. DOI: 10.1016/0370-2693(75)90368-8.

[68] Krzywicki A. Anomalous Nuclear Enhancement of Inclusive Spectra at Large Transverse Momentum[J/OL]. Phys. Rev. D, 1976, 14: 152. DOI: 10.1103/PhysRevD.14.152.

[69] Aubert J J, et al. The ratio of the nucleon structure functions $F2_n$ for iron and deuterium[J/OL]. Phys. Lett. B, 1983, 123: 275-278. DOI: 10.1016/0370-2693(83)90437-9.

[70] Eskola K J, Paukkunen H, Salgado C A. EPS09: A New Generation of NLO and LO Nuclear Parton Distribution Functions[J/OL]. JHEP, 2009, 04: 065. DOI: 10.1088/1126-6708/2009/0 4/065.

[71] Brodsky S J, Close F E, Gunion J F. Phenomenology of Photon Processes, Vector Dominance and Crucial Tests for Parton Models[J/OL]. Phys. Rev. D, 1972, 6: 177. DOI: 10.1103/PhysRe vD.6.177.

[72] Armesto N. Nuclear shadowing[J/OL]. J. Phys. G, 2006, 32: R367-R394. DOI: 10.1088/0954 -3899/32/11/R01.

[73] Llewellyn Smith C H. A Possible Explanation of the Difference Between the Structure Functions of Iron and Deuterium[J/OL]. Phys. Lett. B, 1983, 128: 107-111. DOI: 10.1016/0370-2693(83)90084-9.

[74] Ericson M, Thomas A W. Pionic Corrections and the EMC Enhancement of the Sea in Iron [J/OL]. Phys. Lett. B, 1983, 128: 112-116. DOI: 10.1016/0370-2693(83)90085-0.

[75] Hendry A W, Lichtenberg D B, Predazzi E. Ratio of the Nucleon Structure Function F2 for Heavy Nuclei and Free Nucleons[J/OL]. Phys. Lett. B, 1984, 136: 433-436. DOI: 10.1016/0370-2693(84)92035-5.

[76] Bodek A, Ritchie J L. Fermi Motion Effects in Deep Inelastic Lepton Scattering from Nuclear Targets[J/OL]. Phys. Rev. D, 1981, 23: 1070. DOI: 10.1103/PhysRevD.23.1070.

[77] Saito K, Uchiyama T. Effect of the Fermi Motion on Nuclear Structure Functions and the Emc Effect[J/OL]. Z. Phys. A, 1985, 322: 299. DOI: 10.1007/BF01411895.

[78] Dokshitzer Y L. Calculation of the Structure Functions for Deep Inelastic Scattering and e+ e- Annihilation by Perturbation Theory in Quantum Chromodynamics.[J]. Sov. Phys. JETP, 1977, 46: 641-653.

[79] Gribov V N, Lipatov L N. Deep inelastic e p scattering in perturbation theory[J]. Sov. J. Nucl. Phys., 1972, 15: 438-450.

[80] Altarelli G, Parisi G. Asymptotic Freedom in Parton Language[J/OL]. Nucl. Phys. B, 1977, 126: 298-318. DOI: 10.1016/0550-3213(77)90384-4.

[81] Kovarik K, et al. nCTEQ15 - Global analysis of nuclear parton distributions with uncertainties in the CTEQ framework[J/OL]. Phys. Rev. D, 2016, 93(8): 085037. DOI: 10.1103/PhysRevD.93.085037.

[82] Eskola K J, Paakkinen P, Paukkunen H, et al. EPPS16: Nuclear parton distributions with LHC data[J/OL]. Eur. Phys. J. C, 2017, 77(3): 163. DOI: 10.1140/epjc/s10052-017-4725-9.

[83] Eskola K J, Paakkinen P, Paukkunen H, et al. EPPS21: a global QCD analysis of nuclear PDFs [J/OL]. Eur. Phys. J. C, 2022, 82(5): 413. DOI: 10.1140/epjc/s10052-022-10359-0.

[84] Ball R D, et al. Parton distributions from high-precision collider data[J/OL]. Eur. Phys. J. C, 2017, 77(10): 663. DOI: 10.1140/epjc/s10052-017-5199-5.

[85] Abdul Khalek R, Gauld R, Giani T, et al. nNNPDF3.0: evidence for a modified partonic structure in heavy nuclei[J/OL]. Eur. Phys. J. C, 2022, 82(6): 507. DOI: 10.1140/epjc/s10052-022-10417-7.

[86] Iancu E, Venugopalan R. The Color glass condensate and high-energy scattering in QCD [M/OL]. 2003: 249-3363. DOI: 10.1142/9789812795533_0005.

[87] Gribov L V, Levin E M, Ryskin M G. Semihard Processes in QCD[J/OL]. Phys. Rept., 1983, 100: 1-150. DOI: 10.1016/0370-1573(83)90022-4.

[88] Mueller A H, Qiu J w. Gluon Recombination and Shadowing at Small Values of x[J/OL]. Nucl. Phys. B, 1986, 268: 427-452. DOI: 10.1016/0550-3213(86)90164-1.

[89] Lipatov L N. Reggeization of the Vector Meson and the Vacuum Singularity in Nonabelian Gauge Theories[J]. Sov. J. Nucl. Phys., 1976, 23: 338-345.

[90] Kuraev E A, Lipatov L N, Fadin V S. The Pomeranchuk Singularity in Nonabelian Gauge Theories[J]. Sov. Phys. JETP, 1977, 45: 199-204.

[91] Balitsky I I, Lipatov L N. The Pomeranchuk Singularity in Quantum Chromodynamics[J]. Sov. J. Nucl. Phys., 1978, 28: 822-829.

[92] Balitsky I. Operator expansion for high-energy scattering[J/OL]. Nucl. Phys. B, 1996, 463: 99-160. DOI: 10.1016/0550-3213(95)00638-9.

[93] Kovchegov Y V. Small x F(2) structure function of a nucleus including multiple pomeron exchanges[J/OL]. Phys. Rev. D, 1999, 60: 034008. DOI: 10.1103/PhysRevD.60.034008.

[94] Cronin J W, Frisch H J, Shochet M J, et al. Production of hadrons with large transverse momentum at 200, 300, and 400 GeV[J/OL]. Phys. Rev. D, 1975, 11: 3105-3123. DOI: 10.1103/PhysRevD.11.3105.

[95] Accardi A. Cronin effect in proton nucleus collisions: A Survey of theoretical models[A]. 2002. arXiv: hep-ph/0212148.

[96] Wang X N. Systematic study of high p_T hadron spectra in pp, p A and A A collisions from SPS to RHIC energies[J/OL]. Phys. Rev. C, 2000, 61: 064910. DOI: 10.1103/PhysRevC.61.064910.

[97] Zhang Y, Fai G I, Papp G, et al. High p_T pion and kaon production in relativistic nuclear collisions[J/OL]. Phys. Rev. C, 2002, 65: 034903. DOI: 10.1103/PhysRevC.65.034903.

[98] Kopeliovich B Z, Nemchik J, Schafer A, et al. Cronin effect in hadron production off nuclei [J/OL]. Phys. Rev. Lett., 2002, 88: 232303. DOI: 10.1103/PhysRevLett.88.232303.

[99] Accardi A, Treleani D. Minijet transverse spectrum in high-energy hadron nucleus collisions [J/OL]. Phys. Rev. D, 2001, 64: 116004. DOI: 10.1103/PhysRevD.64.116004.

[100] Vitev I, Gyulassy M. High p_T tomography of d + Au and Au+Au at SPS, RHIC, and LHC [J/OL]. Phys. Rev. Lett., 2002, 89: 252301. DOI: 10.1103/PhysRevLett.89.252301.

[101] Vitev I, Goldman J T, Johnson M B, et al. Open charm tomography of cold nuclear matter [J/OL]. Phys. Rev. D, 2006, 74: 054010. DOI: 10.1103/PhysRevD.74.054010.

[102] Vitev I. Non-Abelian energy loss in cold nuclear matter[J/OL]. Phys. Rev. C, 2007, 75: 064906. DOI: 10.1103/PhysRevC.75.064906.

[103] Arleo F, Jackson G, Peigné S. Impact of fully coherent energy loss on heavy meson production in pA collisions[J/OL]. JHEP, 2022, 01: 164. DOI: 10.1007/JHEP01(2022)164.

[104] Kang Z B, Vitev I, Wang E, et al. Multiple scattering effects on heavy meson production in p+A collisions at backward rapidity[J/OL]. Phys. Lett. B, 2015, 740: 23-29. DOI: 10.1016/j.physletb.2014.11.024.

[105] Khachatryan V, et al. Observation of Long-Range Near-Side Angular Correlations in Proton-Proton Collisions at the LHC[J/OL]. JHEP, 2010, 09: 091. DOI: 10.1007/JHEP09(2010)091.

[106] Chatrchyan S, et al. Observation of Long-Range Near-Side Angular Correlations in Proton-Lead Collisions at the LHC[J/OL]. Phys. Lett. B, 2013, 718: 795-814. DOI: 10.1016/j.physletb.2012.11.025.

[107] Abelev B, et al. Long-range angular correlations on the near and away side in p-Pb collisions at $\sqrt{s_{NN}} = 5.02$ TeV[J/OL]. Phys. Lett. B, 2013, 719: 29-41. DOI: 10.1016/j.physletb.2013.01.012.

[108] Aad G, et al. Observation of Associated Near-Side and Away-Side Long-Range Correlations in $\sqrt{s_{NN}}$=5.02 TeV Proton-Lead Collisions with the ATLAS Detector[J/OL]. Phys. Rev. Lett., 2013, 110(18): 182302. DOI: 10.1103/PhysRevLett.110.182302.

[109] Adare A, et al. Measurement of long-range angular correlation and quadrupole anisotropy of pions and (anti)protons in central d+Au collisions at $\sqrt{s_{_{NN}}}$=200 GeV[J/OL]. Phys. Rev. Lett., 2015, 114(19): 192301. DOI: 10.1103/PhysRevLett.114.192301.

[110] Adamczyk L, et al. Long-range pseudorapidity dihadron correlations in d+Au collisions at $\sqrt{s_{\rm NN}}$ = 200 GeV[J/OL]. Phys. Lett. B, 2015, 747: 265-271. DOI: 10.1016/j.physletb.2015.05.075.

[111] Adare A, et al. Measurements of elliptic and triangular flow in high-multiplicity ^{3}He+Au collisions at $\sqrt{s_{_{NN}}}$ = 200 GeV[J/OL]. Phys. Rev. Lett., 2015, 115(14): 142301. DOI: 10.1103/PhysRevLett.115.142301.

[112] Aad G, et al. Observation of Long-Range Elliptic Azimuthal Anisotropies in $\sqrt{s}$ =13 and 2.76 TeV pp Collisions with the ATLAS Detector[J/OL]. Phys. Rev. Lett., 2016, 116(17): 172301. DOI: 10.1103/PhysRevLett.116.172301.

[113] Khachatryan V, et al. Measurement of long-range near-side two-particle angular correlations in pp collisions at $\sqrt{s}$ =13 TeV[J/OL]. Phys. Rev. Lett., 2016, 116(17): 172302. DOI: 10.1103/PhysRevLett.116.172302.

[114] Aaij R, et al. Measurements of long-range near-side angular correlations in $\sqrt{s_{\rm NN}}$ =5 TeV proton-lead collisions in the forward region[J/OL]. Phys. Lett., 2016, B762: 473. DOI: 10.1016/j.physletb.2016.09.064.

[115] Zhao W, Ko C M, Liu Y X, et al. Probing the Partonic Degrees of Freedom in High-Multiplicity $p-Pb$ collisions at $\sqrt{s_{NN}}$ = 5.02 TeV[J/OL]. Phys. Rev. Lett., 2020, 125(7): 072301. DOI: 10.1103/PhysRevLett.125.072301.

[116] Lisa M A, Barbon J a G P, Chinellato D D, et al. Vortex rings from high energy central p+A collisions[J/OL]. Phys. Rev. C, 2021, 104(1): 011901. DOI: 10.1103/PhysRevC.104.L011901.

[117] Schlichting S, Tribedy P. Collectivity in Small Collision Systems: An Initial-State Perspective [J/OL]. Adv. High Energy Phys., 2016, 2016: 8460349. DOI: 10.1155/2016/8460349.

[118] Zhang C, Marquet C, Qin G Y, et al. Elliptic Flow of Heavy Quarkonia in pA Collisions[J/OL]. Phys. Rev. Lett., 2019, 122(17): 172302. DOI: 10.1103/PhysRevLett.122.172302.

[119] Workman R L, et al. Review of Particle Physics[J/OL]. PTEP, 2022, 2022: 083C01. DOI: 10.1093/ptep/ptac097.

[120] Collins J C, Soper D E, Sterman G F. Factorization of Hard Processes in QCD[J/OL]. Adv. Ser. Direct. High Energy Phys., 1989, 5: 1-91. DOI: 10.1142/9789814503266_0001.

[121] Gauld R, Rojo J, Rottoli L, et al. Charm production in the forward region: constraints on the small-x gluon and backgrounds for neutrino astronomy[J/OL]. JHEP, 2015, 11: 009. DOI: 10.1007/JHEP11(2015)009.

[122] Gauld R. Forward D predictions for pPb collisions, and sensitivity to cold nuclear matter effects [J/OL]. Phys. Rev. D, 2016, 93(1): 014001. DOI: 10.1103/PhysRevD.93.014001.

[123] Aaij R, et al. Study of prompt D^0 meson production in pPb collisions at $\sqrt{s_{\rm NN}}$ =5 TeV[J/OL]. JHEP, 2017, 10: 090. DOI: 10.1007/JHEP10(2017)090.

[124] Fujii H, Watanabe K. Leptons from heavy-quark semileptonic decay in p A collisions within the CGC framework[J/OL]. Nucl. Phys. A, 2016, 951: 45-59. DOI: 10.1016/j.nuclphysa.2016 .03.045.

[125] Fujii H, Watanabe K. Heavy quark pair production in high energy pA collisions: Open heavy flavors[J/OL]. Nucl. Phys. A, 2013, 920: 78-93. DOI: 10.1016/j.nuclphysa.2013.10.006.

[126] Aaij R, et al. Observation of double charm production involving open charm in pp collisions at $\sqrt{s}$ =7 TeV[J/OL]. JHEP, 2012, 06: 141. DOI: 10.1007/JHEP06(2012)141.

[127] Aaij R, et al. Observation of enhanced double parton scattering in proton-lead collisions at $\sqrt{s_{\rm NN}}$ = 8.16 TeV[J/OL]. Phys. Rev. Lett., 2020, 125: 212001. DOI: 10.1103/PhysRevLett.12 5.212001.

[128] Evidence for modification of b quark hadronization in high-multiplicity pp collisions at $\sqrt{s}$ = 13 TeV[A]. 2022. arXiv: 2204.13042.

[129] Aaij R, et al. Modification of $\chi_{c1}(3872)$ and $\psi(2S)$ production in pp collisions at $\sqrt{s}$ = 8 TeV [J/OL]. Phys. Rev. Lett., 2021, 126: 092001. DOI: 10.1103/PhysRevLett.126.092001.

[130] Modification of $\chi_{c1}(3872)$ and $\psi(2S)$ production in pPb collisions at $\sqrt{s_{NN}}$ = 8.16 TeV[Z]. 2022.

[131] Aaij R, et al. Prompt Λ_c^+ production in pPb collisions at $\sqrt{s_{\rm NN}}$ = 5.02 TeV[J/OL]. JHEP, 2019, 02: 102. DOI: 10.1007/JHEP02(2019)102.

[132] Alves Jr. A A, et al. The LHCb detector at the LHC[J/OL]. JINST, 2008, 3(LHCb-DP-2008-001): S08005. DOI: 10.1088/1748-0221/3/08/S08005.

[133] Aaij R, et al. LHCb detector performance[J/OL]. Int. J. Mod. Phys., 2015, A30: 1530022. DOI: 10.1142/S0217751X15300227.

[134] Aaij R, et al. Study of J/ψ production and cold nuclear matter effects in pPb collisions at $\sqrt{s_{\rm NN}}$ =5 TeV[J/OL]. JHEP, 2014, 02: 072. DOI: 10.1007/JHEP02(2014)072.

[135] Aaij R, et al. Study of $\psi(2S)$ production cross-sections and cold nuclear matter effects in pPb collisions at $\sqrt{s_{\rm NN}}$ =5 TeV[J/OL]. JHEP, 2016, 03: 133. DOI: 10.1007/JHEP03(2016)133.

[136] Aaij R, et al. Measurement of J/ψ production cross-sections in pp collisions at $\sqrt{s}$ = 5 TeV [J/OL]. JHEP, 2021, 11: 181. DOI: 10.1007/JHEP11(2021)181.

[137] Albacete J L, et al. Predictions for p+Pb Collisions at sqrt s_NN = 5 TeV[J/OL]. Int. J. Mod. Phys. E, 2013, 22: 1330007. DOI: 10.1142/S0218301313300075.

[138] Arleo F, Peigne S. Heavy-quarkonium suppression in p-A collisions from parton energy loss in cold QCD matter[J/OL]. JHEP, 2013, 03: 122. DOI: 10.1007/JHEP03(2013)122.

[139] Aaij R, et al. Prompt and nonprompt J/ψ production and nuclear modification in pPb collisions at $\sqrt{s_{\rm NN}}$ =8.16 TeV[J/OL]. Phys. Lett., 2017, B774: 159. DOI: 10.1016/j.physletb.2017.09.058.

[140] Aaij R, et al. Measurement of B^+, B^0 and Λ_b^0 production in pPb collisions at $\sqrt{s_{\rm NN}}$ =8.16 TeV [J/OL]. Phys. Rev., 2019, D99: 052011. DOI: 10.1103/PhysRevD.99.052011.

[141] Eskola K J, Helenius I, Paakkinen P, et al. A QCD analysis of LHCb D-meson data in p+Pb collisions[J/OL]. JHEP, 2020, 05: 037. DOI: 10.1007/JHEP05(2020)037.

[142] Acharya S, et al. Λ_c^+ production in pp collisions at $\sqrt{s}$ = 7 TeV and in p-Pb collisions at $\sqrt{s_{\rm NN}}$ = 5.02 TeV[J/OL]. JHEP, 2018, 04: 108. DOI: 10.1007/JHEP04(2018)108.

[143] Abelev B B, et al. Measurement of prompt D-meson production in $p-Pb$ collisions at $\sqrt{s_{NN}}$ = 5.02 TeV[J/OL]. Phys. Rev. Lett., 2014, 113(23): 232301. DOI: 10.1103/PhysRevLett.113.232301.

[144] Adam J, et al. Measurement of D-meson production versus multiplicity in p-Pb collisions at $\sqrt{\rm s_{NN}}$ = 5.02 TeV[J/OL]. JHEP, 2016, 08: 078. DOI: 10.1007/JHEP08(2016)078.

[145] Adam J, et al. D-meson production in p-Pb collisions at $\sqrt{s_{\rm NN}}$ =5.02 TeV and in pp collisions at $\sqrt{s}$ =7 TeV[J/OL]. Phys. Rev. C, 2016, 94(5): 054908. DOI: 10.1103/PhysRevC.94.054908.

[146] Acharya S, et al. Measurement of prompt $\rm D^0$, $\rm D^+$, $\rm D^{*+}$, and $\rm D_S^+$ production in p–Pb collisions at $\sqrt{\rm s_{NN}}$ = 5.02 TeV[J/OL]. JHEP, 2019, 12: 092. DOI: 10.1007/JHEP12(2019)092.

[147] Adams J, et al. The STAR Event Plane Detector[J/OL]. Nucl. Instrum. Meth. A, 2020, 968: 163970. DOI: 10.1016/j.nima.2020.163970.

[148] Borghini N, Dinh P M, Ollitrault J Y. A New method for measuring azimuthal distributions in nucleus-nucleus collisions[J/OL]. Phys. Rev. C, 2001, 63: 054906. DOI: 10.1103/PhysRevC.63.054906.

[149] Borghini N, Dinh P M, Ollitrault J Y. Flow analysis from multiparticle azimuthal correlations [J/OL]. Phys. Rev. C, 2001, 64: 054901. DOI: 10.1103/PhysRevC.64.054901.

[150] Bilandzic A, Snellings R, Voloshin S. Flow analysis with cumulants: Direct calculations[J/OL]. Phys. Rev. C, 2011, 83: 044913. DOI: 10.1103/PhysRevC.83.044913.

[151] Chatrchyan S, et al. Long-range and short-range dihadron angular correlations in central PbPb collisions at a nucleon-nucleon center of mass energy of 2.76 TeV[J/OL]. JHEP, 2011, 07: 076. DOI: 10.1007/JHEP07(2011)076.

[152] Aad G, et al. Measurement of the azimuthal anisotropy for charged particle production in $\sqrt{s_{NN}}$ = 2.76 TeV lead-lead collisions with the ATLAS detector[J/OL]. Phys. Rev. C, 2012, 86: 014907. DOI: 10.1103/PhysRevC.86.014907.

[153] Adler C, et al. Disappearance of back-to-back high p_T hadron correlations in central Au+Au collisions at $\sqrt{s_{NN}}$ = 200-GeV[J/OL]. Phys. Rev. Lett., 2003, 90: 082302. DOI: 10.1103/PhysRevLett.90.082302.

[154] Ajitanand N N, Alexander J M, Chung P, et al. Decomposition of harmonic and jet contributions to particle-pair correlations at ultra-relativistic energies[J/OL]. Phys. Rev. C, 2005, 72: 011902. DOI: 10.1103/PhysRevC.72.011902.

[155] Alver B, et al. System size dependence of cluster properties from two-particle angular correlations in Cu+Cu and Au+Au collisions at s(NN)**(1/2) = 200-GeV[J/OL]. Phys. Rev. C, 2010, 81: 024904. DOI: 10.1103/PhysRevC.81.024904.

[156] Lim S H, Hu Q, Belmont R, et al. Examination of flow and nonflow factorization methods in small collision systems[J/OL]. Phys. Rev. C, 2019, 100(2): 024908. DOI: 10.1103/PhysRevC.100.024908.

[157] Sirunyan A M, et al. Elliptic flow of charm and strange hadrons in high-multiplicity pPb collisions at $\sqrt{s_{\rm NN}}$ = 8.16 TeV[J/OL]. Phys. Rev. Lett., 2018, 121(8): 082301. DOI: 10.1103/PhysRevLett.121.082301.

[158] Sirunyan A M, et al. Measurement of prompt D^0 meson azimuthal anisotropy in Pb-Pb collisions at $\sqrt{s_{NN}}$ = 5.02 TeV[J/OL]. Phys. Rev. Lett., 2018, 120(20): 202301. DOI: 10.1103/PhysRevLett.120.202301.

[159] Khachatryan V, et al. Long-range two-particle correlations of strange hadrons with charged particles in pPb and PbPb collisions at LHC energies[J/OL]. Phys. Lett. B, 2015, 742: 200-224. DOI: 10.1016/j.physletb.2015.01.034.

[160] Kowalski H, Lappi T, Venugopalan R. Nuclear enhancement of universal dynamics of high parton densities[J/OL]. Phys. Rev. Lett., 2008, 100: 022303. DOI: 10.1103/PhysRevLett.100.022303.

[161] Romatschke P. Do nuclear collisions create a locally equilibrated quark–gluon plasma?[J/OL]. Eur. Phys. J. C, 2017, 77(1): 21. DOI: 10.1140/epjc/s10052-016-4567-x.

[162] Weller R D, Romatschke P. One fluid to rule them all: viscous hydrodynamic description of event-by-event central p+p, p+Pb and Pb+Pb collisions at $\sqrt{s} = 5.02$ TeV[J/OL]. Phys. Lett. B, 2017, 774: 351-356. DOI: 10.1016/j.physletb.2017.09.077.

[163] LHC Machine[J/OL]. JINST, 2008, 3: S08001. DOI: 10.1088/1748-0221/3/08/S08001.

[164] LHC Guide[EB/OL]. 2017. https://cds.cern.ch/record/2255762.

[165] Aad G, et al. The ATLAS Experiment at the CERN Large Hadron Collider[J/OL]. JINST, 2008, 3: S08003. DOI: 10.1088/1748-0221/3/08/S08003.

[166] Chatrchyan S, et al. The CMS Experiment at the CERN LHC[J/OL]. JINST, 2008, 3: S08004. DOI: 10.1088/1748-0221/3/08/S08004.

[167] Adriani O, et al. The LHCf detector at the CERN Large Hadron Collider[J/OL]. JINST, 2008, 3: S08006. DOI: 10.1088/1748-0221/3/08/S08006.

[168] Anelli G, et al. The TOTEM experiment at the CERN Large Hadron Collider[J/OL]. JINST, 2008, 3: S08007. DOI: 10.1088/1748-0221/3/08/S08007.

[169] LHC Programme Coordination. Lhc programme coordination[EB/OL]. 2022. https://lpc.web.cern.ch.

[170] Elsässer C. $\bar{b}b$ production angle plots[EB/OL]. https://lhcb.web.cern.ch/lhcb/speakersbureau/html/bb_ProductionAngles.html.

[171] Aaij R, et al. Performance of the LHCb Vertex Locator[J/OL]. JINST, 2014, 9: P09007. DOI: 10.1088/1748-0221/9/09/P09007.

[172] LHCb VELO (VErtex LOcator): Technical Design Report: CERN-LHCC-2001-011[Z]. Geneva: CERN, 2001.

[173] Aaij R, et al. Precision measurement of the B_s^0–$\overline{B}_s^0$ oscillation frequency in the decay $B_s^0 \to D_s^- \pi^+$[J/OL]. New J. Phys., 2013, 15: 053021. DOI: 10.1088/1367-2630/15/5/053021.

[174] Bursche A, Dembinski H P, Di Nezza P, et al. Physics opportunities with the fixed-target program of the LHCb experiment using an unpolarized gas target[R/OL]. Geneva: CERN, 2018. https://cds.cern.ch/record/2649878.

[175] Ferro-Luzzi M. Proposal for an absolute luminosity determination in colliding beam experiments using vertex detection of beam-gas interactions[J/OL]. Nucl. Instrum. Meth., 2005, A553: 388-399. DOI: 10.1016/j.nima.2005.07.010.

[176] Barschel C. Precision luminosity measurement at LHCb with beam-gas imaging[EB/OL]. 2014. https://cds.cern.ch/record/1693671.

[177] Aaij R, et al. Precision luminosity measurements at LHCb[J/OL]. JINST, 2014, 9: P12005. DOI: 10.1088/1748-0221/9/12/P12005.

[178] Brodsky S J, Fleuret F, Hadjidakis C, et al. Physics Opportunities of a Fixed-Target Experiment using the LHC Beams[J/OL]. Phys. Rept., 2013, 522: 239-255. DOI: 10.1016/j.physrep.2012.10.001.

[179] Hadjidakis C, et al. A fixed-target programme at the LHC: Physics case and projected performances for heavy-ion, hadron, spin and astroparticle studies[J/OL]. Phys. Rept., 2021, 911: 1-83. DOI: 10.1016/j.physrep.2021.01.002.

[180] Arink R, et al. Performance of the LHCb Outer Tracker[J/OL]. JINST, 2014, 9: P01002. DOI: 10.1088/1748-0221/9/01/P01002.

[181] Callot O, Hansmann-Menzemer S. The Forward Tracking: Algorithm and Performance Studies [Z]. 2007.

[182] Needham M, Van Tilburg J. Performance of the track matching[Z]. 2007.

[183] Fruhwirth R. Application of Kalman filtering to track and vertex fitting[J/OL]. Nucl. Instrum. Meth. A, 1987, 262: 444-450. DOI: 10.1016/0168-9002(87)90887-4.

[184] De Cian M, Farry S, Seyfert P, et al. Fast neural-net based fake track rejection in the LHCb reconstruction: LHCb-PUB-2017-011[EB/OL]. Geneva: CERN, 2017. http://cds.cern.ch/record/2255039.

[185] Jaeger A, Seyfert P, De Cian M, et al. Measurement of the track finding efficiency[Z]. 2012.

[186] Aaij R, et al. Measurement of the track reconstruction efficiency at LHCb[J/OL]. JINST, 2015, 10: P02007. DOI: 10.1088/1748-0221/10/02/P02007.

[187] Adinolfi M, et al. Performance of the LHCb RICH detector at the LHC[J/OL]. Eur. Phys. J., 2013, C73: 2431. DOI: 10.1140/epjc/s10052-013-2431-9.

[188] Forty R. Ring imaging Cherenkov detectors for LHC-B[J/OL]. Nucl. Instrum. Meth. A, 1996, 384: 167-174. DOI: 10.1016/S0168-9002(96)00951-5.

[189] Abellan Beteta C, et al. Calibration and performance of the LHCb calorimeters in Run 1 and 2 at the LHC[A]. 2020. arXiv: 2008.11556.

[190] Aaij R, et al. Measurement of the relative rate of prompt χ_{c0}, χ_{c1} and χ_{c2} production at $\sqrt{s}$ =7 TeV[J/OL]. JHEP, 2013, 10: 115. DOI: 10.1007/JHEP10(2013)115.

[191] Alves Jr. A A, et al. Performance of the LHCb muon system[J/OL]. JINST, 2013, 8: P02022. DOI: 10.1088/1748-0221/8/02/P02022.

[192] Archilli F, et al. Performance of the muon identification at LHCb[J/OL]. JINST, 2013, 8: P10020. DOI: 10.1088/1748-0221/8/10/P10020.

[193] Voss H, Hoecker A, Stelzer J, et al. TMVA - Toolkit for Multivariate Data Analysis with ROOT [J/OL]. PoS, 2007, ACAT: 040. DOI: 10.22323/1.050.0040.

[194] Quagliani R. Novel real-time alignment and calibration of LHCb detector for Run II and tracking for the upgrade.[J/OL]. J. Phys. Conf. Ser., 2016, 762(1): 012046. DOI: 10.1088/1742-6596/762/1/012046.

[195] Aaij R, et al. Performance of the LHCb trigger and full real-time reconstruction in Run 2 of the LHC[J/OL]. JINST, 2019, 14(LHCb-DP-2019-001): P04013. DOI: 10.1088/1748-0221/14/04/P04013.

[196] Aaij R, et al. Absolute luminosity measurements with the LHCb detector at the LHC[J/OL]. JINST, 2012, 7: P01010. DOI: 10.1088/1748-0221/7/01/P01010.

[197] Aaij R, et al. Tesla: an application for real-time data analysis in High Energy Physics[J/OL]. Comput. Phys. Commun., 2016, 208: 35-42. DOI: 10.1016/j.cpc.2016.07.022.

[198] Aaij R, et al. A comprehensive real-time analysis model at the LHCb experiment[J/OL]. JINST, 2019, 14: P04006. DOI: 10.1088/1748-0221/14/04/P04006.

[199] Corti G, Cattaneo M, Charpentier P, et al. Software for the LHCb experiment[J/OL]. IEEE Trans. Nucl. Sci., 2006, 53: 1323-1328. DOI: 10.1109/TNS.2006.872627.

[200] Barrand G, et al. GAUDI - A software architecture and framework for building HEP data processing applications[J/OL]. Comput. Phys. Commun., 2001, 140: 45-55. DOI: 10.1016/S0010-4655(01)00254-5.

[201] Dujany G, Storaci B. Real-time alignment and calibration of the LHCb Detector in Run II[J/OL]. J. Phys. Conf. Ser., 2015, 664: 082010. DOI: 10.1088/1742-6596/664/8/082010.

[202] Sjöstrand T, Mrenna S, Skands P. PYTHIA 6.4 physics and manual[J/OL]. JHEP, 2006, 05: 026. DOI: 10.1088/1126-6708/2006/05/026.

[203] Sjöstrand T, Mrenna S, Skands P. A brief introduction to PYTHIA 8.1[J/OL]. Comput. Phys. Commun., 2008, 178: 852-867. DOI: 10.1016/j.cpc.2008.01.036.

[204] Belyaev I, et al. Handling of the generation of primary events in Gauss, the LHCb simulation framework[J/OL]. J. Phys. Conf. Ser., 2011, 331: 032047. DOI: 10.1088/1742-6596/331/3/032047.

[205] Lange D J. The EvtGen particle decay simulation package[J/OL]. Nucl. Instrum. Meth., 2001, A462: 152-155. DOI: 10.1016/S0168-9002(01)00089-4.

[206] Golonka P, Was Z. PHOTOS Monte Carlo: A precision tool for QED corrections in Z and W decays[J/OL]. Eur. Phys. J., 2006, C45: 97-107. DOI: 10.1140/epjc/s2005-02396-4.

[207] Allison J, Amako K, Apostolakis J, et al. Geant4 developments and applications[J/OL]. IEEE Trans.Nucl.Sci., 2006, 53: 270. DOI: 10.1109/TNS.2006.869826.

[208] Agostinelli S, et al. Geant4: A simulation toolkit[J/OL]. Nucl. Instrum. Meth., 2003, A506: 250. DOI: 10.1016/S0168-9002(03)01368-8.

[209] Clemencic M, et al. The LHCb simulation application, Gauss: Design, evolution and experience [J/OL]. J. Phys. Conf. Ser., 2011, 331: 032023. DOI: 10.1088/1742-6596/331/3/032023.

[210] Pierog T, Karpenko I, Katzy J M, et al. EPOS LHC: Test of collective hadronization with data measured at the CERN Large Hadron Collider[J/OL]. Phys. Rev. C, 2015, 92(3): 034906. DOI: 10.1103/PhysRevC.92.034906.

[211] Skwarnicki T. A study of the radiative cascade transitions between the Upsilon-prime and Upsilon resonances[D]. Institute of Nuclear Physics, Krakow, 1986.

[212] Pivk M, Le Diberder F R. sPlot: A statistical tool to unfold data distributions[J/OL]. Nucl. Instrum. Meth., 2005, A555: 356-369. DOI: 10.1016/j.nima.2005.08.106.

[213] Bukin A D. Fitting function for asymmetric peaks[A]. 2007. arXiv: 0711.4449.

[214] Aaij R, et al. Measurements of prompt charm production cross-sections in pp collisions at $\sqrt{s}$ =13 TeV[J/OL]. JHEP, 2016, 03: 159. DOI: 10.1007/JHEP03(2016)159.

[215] Aaij R, et al. Measurement of forward J/ψ production cross-sections in pp collisions at $\sqrt{s}$ =13 TeV[J/OL]. JHEP, 2015, 10: 172. DOI: 10.1007/JHEP10(2015)172.

[216] Jaeger A, Seyfert P, De Cian M, et al. Measurement of the track finding efficiency[Z]. 2012.

[217] Aaij R, et al. Study of beauty hadron decays into pairs of charm hadrons[J/OL]. Phys. Rev. Lett., 2014, 112: 202001. DOI: 10.1103/PhysRevLett.112.202001.

[218] Aaij R, et al. Selection and processing of calibration samples to measure the particle identification performance of the LHCb experiment in Run 2[J/OL]. Eur. Phys. J. Tech. Instr., 2019, 6: 1. DOI: 10.1140/epjti/s40485-019-0050-z.

[219] Tolk S, Albrecht J, Dettori F, et al. Data driven trigger efficiency determination at LHCb: LHCb-PUB-2014-039[Z]. 2014.

[220] Cranmer K S. Kernel estimation in high-energy physics[J/OL]. Comput. Phys. Commun., 2001, 136: 198-207. DOI: 10.1016/S0010-4655(00)00243-5.

[221] Aaij R, et al. Measurements of prompt charm production cross-sections in pp collisions at $\sqrt{s}$ =5 TeV[J/OL]. JHEP, 2017, 06: 147. DOI: 10.1007/JHEP06(2017)147.

[222] Shao H S. HELAC-Onia: An automatic matrix element generator for heavy quarkonium physics [J/OL]. Comput. Phys. Commun., 2013, 184: 2562-2570. DOI: 10.1016/j.cpc.2013.05.023.

[223] Shao H S. HELAC-Onia 2.0: an upgraded matrix-element and event generator for heavy quarkonium physics[J/OL]. Comput. Phys. Commun., 2016, 198: 238-259. DOI: 10.1016/j.cpc.2015.09.011.

[224] Lansberg J P, Shao H S. Towards an automated tool to evaluate the impact of the nuclear modification of the gluon density on quarkonium, D and B meson production in proton–nucleus collisions[J/OL]. Eur. Phys. J., 2017, C77(1): 1. DOI: 10.1140/epjc/s10052-016-4575-x.

[225] Kusina A, Lansberg J P, Schienbein I, et al. Gluon shadowing in heavy-flavor production at the lhc[J/OL]. Phys. Rev. Lett., 2018, 121: 052004. https://link.aps.org/doi/10.1103/PhysRevLett.121.052004.

[226] Ducloué B, Lappi T, Mäntysaari H. Forward J/ψ production in proton-nucleus collisions at high energy[J/OL]. Phys. Rev. D, 2015, 91(11): 114005. DOI: 10.1103/PhysRevD.91.114005.

[227] Ducloué B, Lappi T, Mäntysaari H. Forward J/ψ and D meson nuclear suppression at the LHC [J/OL]. Nucl. Part. Phys. Proc., 2017, 289-290: 309-312. DOI: 10.1016/j.nuclphysbps.2017.05.071.

[228] Ma Y Q, Tribedy P, Venugopalan R, et al. Event engineering studies for heavy flavor production and hadronization in high multiplicity hadron-hadron and hadron-nucleus collisions[J/OL]. Phys. Rev. D, 2018, 98(7): 074025. DOI: 10.1103/PhysRevD.98.074025.

[229] Khachatryan V, et al. Evidence for collectivity in pp collisions at the LHC[J/OL]. Phys. Lett. B, 2017, 765: 193-220. DOI: 10.1016/j.physletb.2016.12.009.

[230] Di Nezza P. LHC Run 3 and Run 4 prospects for heavy-ion physics with LHCb[J/OL]. Nucl. Phys. A, 2021, 1005: 121872. DOI: 10.1016/j.nuclphysa.2020.121872.

APPENDIX A APPENDIX

A.1 Efficiency tables

The efficiencies tables for ε_{acc} are listed in Tables A.1 and A.2. The efficiencies tables for $\varepsilon_{\text{rec\&sel}}$ are listed in Tables A.3 and A.4. The efficiencies tables for ε_{PID} are listed in Tables A.5 and A.6. The efficiencies tables for $\varepsilon_{\text{trigger}}$ are listed in Tables A.7 and A.8. The efficiencies tables for ε_{tot} are listed in Tables A.9 and A.10. Statistical uncertainties only.

Table A.1 $\varepsilon_{\mathrm{acc}}$ in bins of D^0 p_{T} and y^* in forward rapidity regions. Statistical uncertaities only.

p_{T}/(GeV/c)\y^*	(1.50, 1.75]	(1.75, 2.00]	(2.00, 2.25]	(2.25, 2.50]	(2.50, 2.75]
(0.0,1.0]	0.649 ± 0.004	0.829 ± 0.003	0.896 ± 0.002	0.929 ± 0.002	0.950 ± 0.002
(1.0,1.5]	0.683 ± 0.004	0.845 ± 0.003	0.907 ± 0.003	0.943 ± 0.002	0.960 ± 0.002
(1.5,2.0]	0.717 ± 0.004	0.875 ± 0.003	0.931 ± 0.002	0.959 ± 0.002	0.977 ± 0.001
(2.0,2.5]	0.752 ± 0.004	0.904 ± 0.003	0.949 ± 0.002	0.968 ± 0.002	0.985 ± 0.001
(2.5,3.0]	0.799 ± 0.005	0.923 ± 0.003	0.962 ± 0.002	0.978 ± 0.002	0.988 ± 0.001
(3.0,3.5]	0.834 ± 0.005	0.937 ± 0.003	0.969 ± 0.002	0.986 ± 0.002	0.994 ± 0.001
(3.5,4.0]	0.864 ± 0.005	0.953 ± 0.003	0.982 ± 0.002	0.995 ± 0.001	0.996 ± 0.001
(4.0,4.5]	0.881 ± 0.006	0.960 ± 0.004	0.988 ± 0.002	0.997 ± 0.001	0.996 ± 0.001
(4.5,5.0]	0.905 ± 0.006	0.966 ± 0.004	0.990 ± 0.002	0.998 ± 0.001	0.998 ± 0.001
(5.0,5.5]	0.924 ± 0.006	0.981 ± 0.003	0.996 ± 0.002	0.999 ± 0.001	0.999 ± 0.001
(5.5,6.0]	0.946 ± 0.006	0.979 ± 0.004	0.999 ± 0.001	0.998 ± 0.001	1.000 ± 0.000
(6.0,7.0]	0.942 ± 0.006	0.984 ± 0.003	0.998 ± 0.001	0.999 ± 0.001	1.000 ± 0.000
(7.0,8.0]	0.960 ± 0.006	0.990 ± 0.003	1.000 ± 0.000	0.999 ± 0.001	1.000 ± 0.000
(8.0,9.0]	0.979 ± 0.006	1.000 ± 0.000	1.000 ± 0.000	1.000 ± 0.000	0.998 ± 0.002
(9.0,10.0]	0.988 ± 0.005	0.995 ± 0.004	1.000 ± 0.000	1.000 ± 0.000	1.000 ± 0.000
(10.0,11.0]	0.982 ± 0.008	1.000 ± 0.000	1.000 ± 0.000	1.000 ± 0.000	1.000 ± 0.000
(11.0,12.0]	0.994 ± 0.006	1.000 ± 0.000	1.000 ± 0.000	1.000 ± 0.000	1.000 ± 0.000
(12.0,13.0]	0.983 ± 0.012	1.000 ± 0.000	1.000 ± 0.000	1.000 ± 0.000	1.000 ± 0.000
(13.0,15.0]	0.993 ± 0.007	1.000 ± 0.000	1.000 ± 0.000	1.000 ± 0.000	1.000 ± 0.000
(15.0,30.0]	1.000 ± 0.000	1.000 ± 0.000	1.000 ± 0.000	1.000 ± 0.000	1.000 ± 0.000
p_{T}/(GeV/c)\y^*	(2.75, 3.00]	(3.00, 3.25]	(3.25, 3.50]	(3.50, 3.75]	(3.75, 4.00]
(0.0,1.0]	0.955 ± 0.002	0.940 ± 0.002	0.898 ± 0.003	0.837 ± 0.003	0.739 ± 0.004
(1.0,1.5]	0.968 ± 0.002	0.949 ± 0.002	0.919 ± 0.003	0.862 ± 0.004	0.779 ± 0.005
(1.5,2.0]	0.974 ± 0.002	0.961 ± 0.002	0.939 ± 0.003	0.887 ± 0.004	0.810 ± 0.005
(2.0,2.5]	0.978 ± 0.002	0.967 ± 0.002	0.948 ± 0.003	0.906 ± 0.004	0.844 ± 0.005
(2.5,3.0]	0.981 ± 0.002	0.973 ± 0.002	0.955 ± 0.003	0.924 ± 0.004	0.860 ± 0.005
(3.0,3.5]	0.987 ± 0.002	0.981 ± 0.002	0.967 ± 0.003	0.938 ± 0.004	0.897 ± 0.006
(3.5,4.0]	0.994 ± 0.001	0.988 ± 0.002	0.975 ± 0.003	0.953 ± 0.004	0.928 ± 0.006
(4.0,4.5]	0.997 ± 0.001	0.992 ± 0.002	0.985 ± 0.003	0.979 ± 0.003	0.939 ± 0.006
(4.5,5.0]	0.999 ± 0.001	0.994 ± 0.002	0.991 ± 0.002	0.987 ± 0.003	0.962 ± 0.006
(5.0,5.5]	0.998 ± 0.001	0.997 ± 0.002	0.993 ± 0.003	0.990 ± 0.003	0.983 ± 0.005
(5.5,6.0]	0.999 ± 0.001	0.995 ± 0.002	0.991 ± 0.003	0.991 ± 0.004	0.984 ± 0.006
(6.0,7.0]	0.998 ± 0.001	1.000 ± 0.000	0.996 ± 0.002	0.994 ± 0.003	0.986 ± 0.005
(7.0,8.0]	1.000 ± 0.000	1.000 ± 0.000	0.998 ± 0.002	0.995 ± 0.003	0.986 ± 0.006
(8.0,9.0]	1.000 ± 0.000	0.997 ± 0.003	0.989 ± 0.006	0.992 ± 0.006	1.000 ± 0.000
(9.0,10.0]	1.000 ± 0.000	1.000 ± 0.000	1.000 ± 0.000	0.993 ± 0.007	1.000 ± 0.000
(10.0,11.0]	1.000 ± 0.000	0.982 ± 0.013	1.000 ± 0.000	1.000 ± 0.000	0.988 ± 0.012
(11.0,12.0]	0.990 ± 0.010	1.000 ± 0.000	1.000 ± 0.000	1.000 ± 0.000	1.000 ± 0.000
(12.0,13.0]	1.000 ± 0.000	1.000 ± 0.000	1.000 ± 0.000	0.946 ± 0.037	1.000 ± 0.000
(13.0,15.0]	1.000 ± 0.000	1.000 ± 0.000	1.000 ± 0.000	1.000 ± 0.000	1.000 ± 0.000
(15.0,30.0]	1.000 ± 0.000	1.000 ± 0.000	1.000 ± 0.000	1.000 ± 0.000	1.000 ± 0.000

Table A.2 $\varepsilon_{\mathrm{acc}}$ in bins of D^0 p_{T} and y^* in backward rapidity regions. Statistical uncertaities only.

p_{T}/(GeV/c)\y^*	(-2.75, -2.50]	(-3.00, -2.75]	(-3.25, -3.00]	(-3.50, -3.25]	(-3.75, -3.50]
(0.0,1.0]	0.712 ± 0.003	0.857 ± 0.003	0.907 ± 0.002	0.936 ± 0.002	0.953 ± 0.002
(1.0,1.5]	0.746 ± 0.004	0.869 ± 0.003	0.919 ± 0.002	0.946 ± 0.002	0.966 ± 0.002
(1.5,2.0]	0.780 ± 0.004	0.897 ± 0.003	0.937 ± 0.002	0.966 ± 0.002	0.979 ± 0.001
(2.0,2.5]	0.811 ± 0.004	0.921 ± 0.003	0.956 ± 0.002	0.974 ± 0.002	0.987 ± 0.001
(2.5,3.0]	0.848 ± 0.004	0.934 ± 0.003	0.971 ± 0.002	0.982 ± 0.002	0.986 ± 0.001
(3.0,3.5]	0.872 ± 0.004	0.956 ± 0.003	0.972 ± 0.002	0.990 ± 0.001	0.992 ± 0.001
(3.5,4.0]	0.900 ± 0.005	0.963 ± 0.003	0.986 ± 0.002	0.997 ± 0.001	0.996 ± 0.001
(4.0,4.5]	0.912 ± 0.005	0.972 ± 0.003	0.991 ± 0.002	0.999 ± 0.001	0.996 ± 0.001
(4.5,5.0]	0.927 ± 0.005	0.974 ± 0.003	0.994 ± 0.002	0.999 ± 0.001	0.998 ± 0.001
(5.0,5.5]	0.945 ± 0.005	0.987 ± 0.003	0.997 ± 0.001	0.999 ± 0.001	0.998 ± 0.001
(5.5,6.0]	0.959 ± 0.005	0.987 ± 0.003	0.999 ± 0.001	0.999 ± 0.001	1.000 ± 0.000
(6.0,7.0]	0.961 ± 0.005	0.989 ± 0.002	0.999 ± 0.001	0.999 ± 0.001	1.000 ± 0.000
(7.0,8.0]	0.971 ± 0.005	0.996 ± 0.002	0.999 ± 0.001	1.000 ± 0.000	1.000 ± 0.000
(8.0,9.0]	0.984 ± 0.005	1.000 ± 0.000	1.000 ± 0.000	1.000 ± 0.000	0.998 ± 0.002
(9.0,10.0]	0.986 ± 0.006	1.000 ± 0.000	1.000 ± 0.000	1.000 ± 0.000	1.000 ± 0.000
(10.0,11.0]	0.986 ± 0.007	1.000 ± 0.000	1.000 ± 0.000	1.000 ± 0.000	1.000 ± 0.000
(11.0,12.0]	0.994 ± 0.006	1.000 ± 0.000	1.000 ± 0.000	1.000 ± 0.000	1.000 ± 0.000
(12.0,13.0]	0.991 ± 0.009	1.000 ± 0.000	1.000 ± 0.000	1.000 ± 0.000	1.000 ± 0.000
(13.0,15.0]	1.000 ± 0.000	1.000 ± 0.000	1.000 ± 0.000	1.000 ± 0.000	1.000 ± 0.000
(15.0,30.0]	1.000 ± 0.000	1.000 ± 0.000	1.000 ± 0.000	1.000 ± 0.000	1.000 ± 0.000
p_{T}/(GeV/c)\y^*	(-4.00, -3.75]	(-4.25, -4.00]	(-4.50, -4.25]	(-4.75, -4.50]	(-5.00, -4.75]
(0.0,1.0]	0.954 ± 0.002	0.931 ± 0.002	0.882 ± 0.003	0.817 ± 0.004	0.702 ± 0.004
(1.0,1.5]	0.966 ± 0.002	0.943 ± 0.002	0.903 ± 0.003	0.842 ± 0.004	0.751 ± 0.005
(1.5,2.0]	0.971 ± 0.002	0.957 ± 0.002	0.927 ± 0.003	0.865 ± 0.004	0.787 ± 0.005
(2.0,2.5]	0.973 ± 0.002	0.961 ± 0.002	0.942 ± 0.003	0.889 ± 0.004	0.822 ± 0.005
(2.5,3.0]	0.980 ± 0.002	0.966 ± 0.002	0.952 ± 0.003	0.907 ± 0.004	0.842 ± 0.006
(3.0,3.5]	0.985 ± 0.002	0.977 ± 0.002	0.961 ± 0.003	0.931 ± 0.004	0.879 ± 0.006
(3.5,4.0]	0.993 ± 0.001	0.984 ± 0.002	0.973 ± 0.003	0.946 ± 0.005	0.913 ± 0.006
(4.0,4.5]	0.996 ± 0.001	0.991 ± 0.002	0.983 ± 0.003	0.969 ± 0.004	0.928 ± 0.007
(4.5,5.0]	0.996 ± 0.001	0.993 ± 0.002	0.992 ± 0.002	0.981 ± 0.004	0.956 ± 0.007
(5.0,5.5]	0.998 ± 0.001	0.997 ± 0.002	0.990 ± 0.003	0.990 ± 0.003	0.972 ± 0.006
(5.5,6.0]	0.999 ± 0.001	0.995 ± 0.002	0.988 ± 0.004	0.987 ± 0.005	0.982 ± 0.006
(6.0,7.0]	0.998 ± 0.001	1.000 ± 0.000	0.993 ± 0.003	0.995 ± 0.003	0.979 ± 0.006
(7.0,8.0]	1.000 ± 0.000	0.998 ± 0.002	0.998 ± 0.002	0.997 ± 0.003	0.980 ± 0.007
(8.0,9.0]	1.000 ± 0.000	0.992 ± 0.005	0.997 ± 0.003	0.991 ± 0.007	1.000 ± 0.000
(9.0,10.0]	1.000 ± 0.000	1.000 ± 0.000	1.000 ± 0.000	0.992 ± 0.008	1.000 ± 0.000
(10.0,11.0]	1.000 ± 0.000	0.981 ± 0.013	1.000 ± 0.000	0.989 ± 0.011	1.000 ± 0.000
(11.0,12.0]	0.989 ± 0.010	1.000 ± 0.000	1.000 ± 0.000	1.000 ± 0.000	1.000 ± 0.000
(12.0,13.0]	1.000 ± 0.000	1.000 ± 0.000	0.970 ± 0.030	0.977 ± 0.023	1.000 ± 0.000
(13.0,15.0]	1.000 ± 0.000	1.000 ± 0.000	1.000 ± 0.000	1.000 ± 0.000	1.000 ± 0.000
(15.0,30.0]	1.000 ± 0.000	1.000 ± 0.000	1.000 ± 0.000	1.000 ± 0.000	1.000 ± 0.000

Table A.3 ε_{sel} in bins of D^0 p_{T} and y^* in forward rapidity regions. Statistical uncertaities only.

p_{T}/(GeV/c)\y^*	(1.50, 1.75]	(1.75, 2.00]	(2.00, 2.25]	(2.25, 2.50]	(2.50, 2.75]
(0.0,1.0]	0.005 ± 0.000	0.019 ± 0.000	0.034 ± 0.000	0.043 ± 0.000	0.046 ± 0.000
(1.0,1.5]	0.005 ± 0.000	0.022 ± 0.000	0.039 ± 0.000	0.048 ± 0.001	0.050 ± 0.001
(1.5,2.0]	0.008 ± 0.000	0.029 ± 0.000	0.047 ± 0.001	0.056 ± 0.001	0.059 ± 0.001
(2.0,2.5]	0.010 ± 0.000	0.039 ± 0.001	0.063 ± 0.001	0.073 ± 0.001	0.072 ± 0.001
(2.5,3.0]	0.014 ± 0.000	0.051 ± 0.001	0.081 ± 0.001	0.090 ± 0.001	0.090 ± 0.001
(3.0,3.5]	0.017 ± 0.000	0.070 ± 0.001	0.100 ± 0.001	0.109 ± 0.001	0.110 ± 0.001
(3.5,4.0]	0.023 ± 0.001	0.084 ± 0.001	0.118 ± 0.001	0.120 ± 0.001	0.120 ± 0.001
(4.0,4.5]	0.027 ± 0.001	0.093 ± 0.001	0.125 ± 0.002	0.130 ± 0.002	0.130 ± 0.002
(4.5,5.0]	0.032 ± 0.001	0.100 ± 0.002	0.132 ± 0.002	0.138 ± 0.002	0.142 ± 0.002
(5.0,5.5]	0.035 ± 0.001	0.114 ± 0.002	0.141 ± 0.002	0.144 ± 0.002	0.149 ± 0.003
(5.5,6.0]	0.039 ± 0.001	0.119 ± 0.002	0.141 ± 0.003	0.151 ± 0.003	0.154 ± 0.003
(6.0,7.0]	0.045 ± 0.001	0.130 ± 0.002	0.146 ± 0.002	0.162 ± 0.003	0.157 ± 0.003
(7.0,8.0]	0.049 ± 0.002	0.138 ± 0.003	0.154 ± 0.003	0.154 ± 0.003	0.164 ± 0.004
(8.0,9.0]	0.055 ± 0.001	0.140 ± 0.002	0.157 ± 0.002	0.167 ± 0.002	0.166 ± 0.002
(9.0,10.0]	0.062 ± 0.001	0.149 ± 0.002	0.162 ± 0.002	0.172 ± 0.002	0.165 ± 0.002
(10.0,11.0]	0.068 ± 0.002	0.151 ± 0.003	0.166 ± 0.003	0.178 ± 0.003	0.148 ± 0.003
(11.0,12.0]	0.069 ± 0.002	0.161 ± 0.003	0.176 ± 0.004	0.173 ± 0.004	0.126 ± 0.003
(12.0,13.0]	0.075 ± 0.003	0.156 ± 0.004	0.182 ± 0.004	0.169 ± 0.004	0.089 ± 0.004
(13.0,15.0]	0.080 ± 0.003	0.167 ± 0.004	0.174 ± 0.004	0.142 ± 0.004	0.064 ± 0.003
(15.0,30.0]	0.094 ± 0.002	0.164 ± 0.003	0.126 ± 0.003	0.070 ± 0.003	0.018 ± 0.002

p_{T}/(GeV/c)\y^*	(2.75, 3.00]	(3.00, 3.25]	(3.25, 3.50]	(3.50, 3.75]	(3.75, 4.00]
(0.0,1.0]	0.045 ± 0.000	0.041 ± 0.000	0.034 ± 0.000	0.026 ± 0.000	0.020 ± 0.000
(1.0,1.5]	0.048 ± 0.001	0.043 ± 0.001	0.038 ± 0.001	0.029 ± 0.000	0.020 ± 0.000
(1.5,2.0]	0.055 ± 0.001	0.051 ± 0.001	0.042 ± 0.001	0.033 ± 0.001	0.023 ± 0.001
(2.0,2.5]	0.070 ± 0.001	0.066 ± 0.001	0.056 ± 0.001	0.044 ± 0.001	0.028 ± 0.001
(2.5,3.0]	0.092 ± 0.001	0.085 ± 0.001	0.072 ± 0.001	0.056 ± 0.001	0.030 ± 0.001
(3.0,3.5]	0.106 ± 0.001	0.102 ± 0.001	0.088 ± 0.001	0.063 ± 0.001	0.029 ± 0.001
(3.5,4.0]	0.123 ± 0.001	0.116 ± 0.002	0.104 ± 0.002	0.067 ± 0.001	0.023 ± 0.001
(4.0,4.5]	0.134 ± 0.002	0.128 ± 0.002	0.110 ± 0.002	0.059 ± 0.002	0.018 ± 0.001
(4.5,5.0]	0.142 ± 0.002	0.134 ± 0.002	0.105 ± 0.002	0.050 ± 0.002	0.008 ± 0.001
(5.0,5.5]	0.149 ± 0.003	0.144 ± 0.003	0.094 ± 0.002	0.033 ± 0.002	0.001 ± 0.000
(5.5,6.0]	0.153 ± 0.003	0.138 ± 0.003	0.081 ± 0.003	0.019 ± 0.001	-
(6.0,7.0]	0.158 ± 0.003	0.125 ± 0.003	0.062 ± 0.002	0.006 ± 0.001	-
(7.0,8.0]	0.151 ± 0.004	0.090 ± 0.003	0.030 ± 0.002	0.000 ± 0.000	-
(8.0,9.0]	0.125 ± 0.002	0.057 ± 0.001	0.007 ± 0.001	-	-
(9.0,10.0]	0.101 ± 0.002	0.032 ± 0.001	0.000 ± 0.000	-	-
(10.0,11.0]	0.077 ± 0.002	0.014 ± 0.001	-	-	-
(11.0,12.0]	0.048 ± 0.002	0.002 ± 0.001	-	-	-
(12.0,13.0]	0.031 ± 0.002	-	-	-	-
(13.0,15.0]	0.007 ± 0.001	-	-	-	-
(15.0,30.0]	-	-	-	-	-

Table A.4 $\varepsilon_{\mathrm{sel}}$ in bins of D^0 p_{T} and y^* in backward rapidity regions. Statistical uncertaities only.

p_{T}/(GeV/c)\y^*	(-2.75, -2.50]	(-3.00, -2.75]	(-3.25, -3.00]	(-3.50, -3.25]	(-3.75, -3.50]
(0.0,1.0]	0.007 ± 0.000	0.020 ± 0.000	0.033 ± 0.000	0.039 ± 0.000	0.042 ± 0.000
(1.0,1.5]	0.008 ± 0.000	0.025 ± 0.000	0.037 ± 0.000	0.043 ± 0.000	0.044 ± 0.000
(1.5,2.0]	0.011 ± 0.000	0.031 ± 0.000	0.044 ± 0.000	0.051 ± 0.001	0.052 ± 0.001
(2.0,2.5]	0.015 ± 0.000	0.041 ± 0.001	0.059 ± 0.001	0.066 ± 0.001	0.066 ± 0.001
(2.5,3.0]	0.022 ± 0.000	0.058 ± 0.001	0.078 ± 0.001	0.084 ± 0.001	0.086 ± 0.001
(3.0,3.5]	0.027 ± 0.001	0.073 ± 0.001	0.093 ± 0.001	0.098 ± 0.001	0.100 ± 0.001
(3.5,4.0]	0.035 ± 0.001	0.089 ± 0.001	0.108 ± 0.001	0.112 ± 0.001	0.112 ± 0.001
(4.0,4.5]	0.042 ± 0.001	0.100 ± 0.001	0.117 ± 0.002	0.118 ± 0.002	0.122 ± 0.002
(4.5,5.0]	0.049 ± 0.001	0.106 ± 0.002	0.121 ± 0.002	0.127 ± 0.002	0.134 ± 0.002
(5.0,5.5]	0.055 ± 0.001	0.117 ± 0.002	0.132 ± 0.002	0.130 ± 0.002	0.140 ± 0.003
(5.5,6.0]	0.062 ± 0.002	0.127 ± 0.003	0.131 ± 0.003	0.135 ± 0.003	0.133 ± 0.003
(6.0,7.0]	0.071 ± 0.002	0.132 ± 0.002	0.135 ± 0.002	0.141 ± 0.003	0.146 ± 0.003
(7.0,8.0]	0.082 ± 0.002	0.130 ± 0.003	0.147 ± 0.003	0.138 ± 0.004	0.145 ± 0.004
(8.0,9.0]	0.081 ± 0.001	0.133 ± 0.001	0.143 ± 0.001	0.148 ± 0.002	0.145 ± 0.002
(9.0,10.0]	0.090 ± 0.001	0.139 ± 0.002	0.143 ± 0.002	0.145 ± 0.002	0.133 ± 0.002
(10.0,11.0]	0.095 ± 0.002	0.148 ± 0.002	0.154 ± 0.003	0.146 ± 0.003	0.112 ± 0.003
(11.0,12.0]	0.090 ± 0.002	0.139 ± 0.003	0.148 ± 0.003	0.149 ± 0.003	0.080 ± 0.003
(12.0,13.0]	0.106 ± 0.003	0.144 ± 0.003	0.150 ± 0.004	0.126 ± 0.004	0.076 ± 0.004
(13.0,15.0]	0.107 ± 0.003	0.148 ± 0.003	0.151 ± 0.004	0.105 ± 0.003	0.043 ± 0.003
(15.0,30.0]	0.118 ± 0.003	0.131 ± 0.003	0.105 ± 0.003	0.037 ± 0.002	0.007 ± 0.001
p_{T}/(GeV/c)\y^*	(-4.00, -3.75]	(-4.25, -4.00]	(-4.50, -4.25]	(-4.75, -4.50]	(-5.00, -4.75]
(0.0,1.0]	0.040 ± 0.000	0.035 ± 0.000	0.029 ± 0.000	0.022 ± 0.000	0.016 ± 0.000
(1.0,1.5]	0.043 ± 0.000	0.038 ± 0.000	0.032 ± 0.000	0.024 ± 0.000	0.016 ± 0.000
(1.5,2.0]	0.049 ± 0.001	0.045 ± 0.001	0.038 ± 0.001	0.028 ± 0.001	0.017 ± 0.001
(2.0,2.5]	0.065 ± 0.001	0.059 ± 0.001	0.048 ± 0.001	0.036 ± 0.001	0.019 ± 0.001
(2.5,3.0]	0.084 ± 0.001	0.076 ± 0.001	0.064 ± 0.001	0.047 ± 0.001	0.022 ± 0.001
(3.0,3.5]	0.098 ± 0.001	0.094 ± 0.001	0.076 ± 0.001	0.053 ± 0.001	0.019 ± 0.001
(3.5,4.0]	0.111 ± 0.002	0.104 ± 0.002	0.090 ± 0.002	0.054 ± 0.002	0.013 ± 0.001
(4.0,4.5]	0.123 ± 0.002	0.120 ± 0.002	0.091 ± 0.002	0.045 ± 0.002	0.008 ± 0.001
(4.5,5.0]	0.128 ± 0.002	0.125 ± 0.003	0.085 ± 0.002	0.034 ± 0.002	0.002 ± 0.001
(5.0,5.5]	0.129 ± 0.003	0.126 ± 0.003	0.074 ± 0.003	0.020 ± 0.002	-
(5.5,6.0]	0.139 ± 0.003	0.117 ± 0.004	0.063 ± 0.003	0.015 ± 0.002	-
(6.0,7.0]	0.151 ± 0.003	0.101 ± 0.003	0.035 ± 0.002	0.001 ± 0.001	-
(7.0,8.0]	0.129 ± 0.004	0.059 ± 0.004	0.012 ± 0.002	-	-
(8.0,9.0]	0.099 ± 0.002	0.040 ± 0.001	0.002 ± 0.000	-	-
(9.0,10.0]	0.077 ± 0.002	0.017 ± 0.001	-	-	-
(10.0,11.0]	0.057 ± 0.002	0.004 ± 0.001	-	-	-
(11.0,12.0]	0.028 ± 0.002	-	-	-	-
(12.0,13.0]	0.015 ± 0.002	-	-	-	-
(13.0,15.0]	0.002 ± 0.001	-	-	-	-
(15.0,30.0]	-	-	-	-	-

Table A.5 $\varepsilon_{\mathrm{PID}}$ in bins of D^0 p_{T} and y^* in forward rapidity regions. Statistical uncertaities only.

p_{T}/(GeV/c)\y^*	(1.50, 1.75]	(1.75, 2.00]	(2.00, 2.25]	(2.25, 2.50]	(2.50, 2.75]
(0.0,1.0]	0.893 ± 0.009	0.889 ± 0.002	0.885 ± 0.002	0.894 ± 0.001	0.898 ± 0.001
(1.0,1.5]	0.889 ± 0.006	0.885 ± 0.002	0.892 ± 0.002	0.902 ± 0.001	0.905 ± 0.001
(1.5,2.0]	0.886 ± 0.004	0.887 ± 0.002	0.899 ± 0.001	0.911 ± 0.001	0.913 ± 0.001
(2.0,2.5]	0.886 ± 0.004	0.894 ± 0.002	0.907 ± 0.001	0.920 ± 0.001	0.921 ± 0.001
(2.5,3.0]	0.894 ± 0.004	0.901 ± 0.002	0.918 ± 0.001	0.928 ± 0.001	0.928 ± 0.001
(3.0,3.5]	0.901 ± 0.003	0.910 ± 0.002	0.928 ± 0.001	0.935 ± 0.001	0.934 ± 0.001
(3.5,4.0]	0.907 ± 0.003	0.921 ± 0.002	0.935 ± 0.001	0.939 ± 0.001	0.935 ± 0.001
(4.0,4.5]	0.915 ± 0.004	0.930 ± 0.002	0.938 ± 0.001	0.938 ± 0.001	0.933 ± 0.001
(4.5,5.0]	0.924 ± 0.004	0.937 ± 0.002	0.939 ± 0.002	0.932 ± 0.002	0.928 ± 0.002
(5.0,5.5]	0.931 ± 0.004	0.941 ± 0.002	0.936 ± 0.002	0.922 ± 0.002	0.918 ± 0.002
(5.5,6.0]	0.936 ± 0.004	0.942 ± 0.002	0.930 ± 0.002	0.910 ± 0.002	0.906 ± 0.003
(6.0,7.0]	0.941 ± 0.003	0.941 ± 0.002	0.916 ± 0.002	0.884 ± 0.002	0.877 ± 0.003
(7.0,8.0]	0.942 ± 0.004	0.933 ± 0.002	0.890 ± 0.003	0.840 ± 0.004	0.823 ± 0.004
(8.0,9.0]	0.938 ± 0.005	0.919 ± 0.003	0.856 ± 0.004	0.781 ± 0.005	0.761 ± 0.006
(9.0,10.0]	0.930 ± 0.006	0.899 ± 0.005	0.818 ± 0.006	0.719 ± 0.007	0.710 ± 0.008
(10.0,11.0]	0.921 ± 0.008	0.877 ± 0.006	0.779 ± 0.008	0.652 ± 0.009	0.674 ± 0.010
(11.0,12.0]	0.906 ± 0.010	0.849 ± 0.009	0.732 ± 0.012	0.600 ± 0.011	0.623 ± 0.015
(12.0,13.0]	0.890 ± 0.013	0.825 ± 0.012	0.677 ± 0.015	0.563 ± 0.015	0.584 ± 0.020
(13.0,15.0]	0.857 ± 0.013	0.788 ± 0.012	0.630 ± 0.015	0.519 ± 0.015	0.519 ± 0.023
(15.0,30.0]	0.770 ± 0.015	0.703 ± 0.015	0.535 ± 0.018	0.422 ± 0.020	0.402 ± 0.040

p_{T}/(GeV/c)\y^*	(2.75, 3.00]	(3.00, 3.25]	(3.25, 3.50]	(3.50, 3.75]	(3.75, 4.00]
(0.0,1.0]	0.895 ± 0.001	0.872 ± 0.002	0.818 ± 0.002	0.732 ± 0.003	0.629 ± 0.005
(1.0,1.5]	0.897 ± 0.001	0.873 ± 0.002	0.819 ± 0.002	0.724 ± 0.003	0.560 ± 0.006
(1.5,2.0]	0.903 ± 0.001	0.876 ± 0.002	0.817 ± 0.002	0.703 ± 0.003	0.490 ± 0.006
(2.0,2.5]	0.908 ± 0.001	0.875 ± 0.002	0.804 ± 0.002	0.645 ± 0.004	0.438 ± 0.005
(2.5,3.0]	0.911 ± 0.001	0.869 ± 0.002	0.772 ± 0.002	0.574 ± 0.004	0.400 ± 0.006
(3.0,3.5]	0.911 ± 0.001	0.856 ± 0.002	0.722 ± 0.003	0.526 ± 0.004	0.355 ± 0.007
(3.5,4.0]	0.907 ± 0.002	0.832 ± 0.002	0.665 ± 0.003	0.488 ± 0.005	0.295 ± 0.008
(4.0,4.5]	0.898 ± 0.002	0.792 ± 0.003	0.621 ± 0.004	0.437 ± 0.006	0.225 ± 0.010
(4.5,5.0]	0.881 ± 0.002	0.743 ± 0.003	0.585 ± 0.005	0.381 ± 0.008	0.196 ± 0.019
(5.0,5.5]	0.852 ± 0.003	0.700 ± 0.004	0.548 ± 0.006	0.319 ± 0.011	-
(5.5,6.0]	0.810 ± 0.004	0.658 ± 0.005	0.506 ± 0.008	0.280 ± 0.016	-
(6.0,7.0]	0.751 ± 0.004	0.618 ± 0.005	0.439 ± 0.009	0.246 ± 0.026	-
(7.0,8.0]	0.687 ± 0.005	0.553 ± 0.008	0.344 ± 0.017	-	-
(8.0,9.0]	0.639 ± 0.008	0.461 ± 0.014	0.304 ± 0.048	-	-
(9.0,10.0]	0.592 ± 0.012	0.390 ± 0.023	-	-	-
(10.0,11.0]	0.526 ± 0.018	0.322 ± 0.045	-	-	-
(11.0,12.0]	0.461 ± 0.027	-	-	-	-
(12.0,13.0]	0.381 ± 0.040	-	-	-	-
(13.0,15.0]	0.371 ± 0.084	-	-	-	-
(15.0,30.0]	-	-	-	-	-

Table A.6 $\varepsilon_{\mathrm{PID}}$ in bins of D^0 p_{T} and y^* in backward rapidity regions. Statistical uncertaities only.

p_{T}/(GeV/c)\y^*	(-2.75, -2.50]	(-3.00, -2.75]	(-3.25, -3.00]	(-3.50, -3.25]	(-3.75, -3.50]
(0.0,1.0]	0.862 ± 0.005	0.818 ± 0.002	0.791 ± 0.002	0.799 ± 0.001	0.813 ± 0.001
(1.0,1.5]	0.856 ± 0.003	0.816 ± 0.002	0.804 ± 0.002	0.816 ± 0.001	0.822 ± 0.001
(1.5,2.0]	0.851 ± 0.003	0.819 ± 0.002	0.820 ± 0.001	0.829 ± 0.001	0.834 ± 0.001
(2.0,2.5]	0.847 ± 0.003	0.828 ± 0.001	0.839 ± 0.001	0.846 ± 0.001	0.847 ± 0.001
(2.5,3.0]	0.848 ± 0.003	0.841 ± 0.001	0.856 ± 0.001	0.862 ± 0.001	0.860 ± 0.001
(3.0,3.5]	0.853 ± 0.003	0.856 ± 0.001	0.871 ± 0.001	0.877 ± 0.001	0.869 ± 0.001
(3.5,4.0]	0.860 ± 0.003	0.871 ± 0.002	0.883 ± 0.001	0.888 ± 0.001	0.872 ± 0.002
(4.0,4.5]	0.872 ± 0.003	0.883 ± 0.002	0.893 ± 0.002	0.893 ± 0.002	0.871 ± 0.002
(4.5,5.0]	0.882 ± 0.003	0.893 ± 0.002	0.898 ± 0.002	0.891 ± 0.002	0.865 ± 0.002
(5.0,5.5]	0.892 ± 0.003	0.902 ± 0.002	0.900 ± 0.002	0.885 ± 0.002	0.852 ± 0.003
(5.5,6.0]	0.900 ± 0.003	0.907 ± 0.002	0.896 ± 0.002	0.878 ± 0.003	0.835 ± 0.003
(6.0,7.0]	0.910 ± 0.003	0.910 ± 0.002	0.888 ± 0.002	0.861 ± 0.003	0.800 ± 0.003
(7.0,8.0]	0.918 ± 0.003	0.904 ± 0.003	0.872 ± 0.003	0.826 ± 0.004	0.740 ± 0.005
(8.0,9.0]	0.920 ± 0.004	0.877 ± 0.004	0.845 ± 0.005	0.781 ± 0.006	0.682 ± 0.007
(9.0,10.0]	0.903 ± 0.006	0.847 ± 0.006	0.809 ± 0.007	0.724 ± 0.008	0.637 ± 0.010
(10.0,11.0]	0.875 ± 0.008	0.805 ± 0.009	0.775 ± 0.009	0.667 ± 0.012	0.600 ± 0.015
(11.0,12.0]	0.841 ± 0.011	0.759 ± 0.012	0.716 ± 0.013	0.616 ± 0.015	0.544 ± 0.021
(12.0,13.0]	0.798 ± 0.015	0.682 ± 0.027	0.656 ± 0.018	0.589 ± 0.019	0.513 ± 0.031
(13.0,15.0]	0.736 ± 0.018	0.524 ± 0.027	0.594 ± 0.017	0.529 ± 0.021	0.434 ± 0.038
(15.0,30.0]	0.510 ± 0.025	0.467 ± 0.032	0.490 ± 0.022	0.411 ± 0.031	-
p_{T}/(GeV/c)\y^*	(-4.00, -3.75]	(-4.25, -4.00]	(-4.50, -4.25]	(-4.75, -4.50]	(-5.00, -4.75]
(0.0,1.0]	0.811 ± 0.002	0.780 ± 0.002	0.710 ± 0.003	0.619 ± 0.004	0.515 ± 0.006
(1.0,1.5]	0.811 ± 0.002	0.774 ± 0.002	0.701 ± 0.003	0.594 ± 0.004	0.440 ± 0.007
(1.5,2.0]	0.818 ± 0.001	0.775 ± 0.002	0.694 ± 0.003	0.555 ± 0.004	0.391 ± 0.007
(2.0,2.5]	0.824 ± 0.001	0.771 ± 0.002	0.669 ± 0.003	0.506 ± 0.004	0.342 ± 0.006
(2.5,3.0]	0.828 ± 0.001	0.758 ± 0.002	0.627 ± 0.003	0.448 ± 0.004	0.310 ± 0.007
(3.0,3.5]	0.829 ± 0.002	0.737 ± 0.002	0.574 ± 0.003	0.409 ± 0.004	0.264 ± 0.008
(3.5,4.0]	0.823 ± 0.002	0.704 ± 0.003	0.524 ± 0.004	0.366 ± 0.005	0.207 ± 0.011
(4.0,4.5]	0.808 ± 0.002	0.664 ± 0.003	0.490 ± 0.004	0.321 ± 0.007	0.174 ± 0.018
(4.5,5.0]	0.783 ± 0.003	0.617 ± 0.004	0.447 ± 0.006	0.264 ± 0.010	-
(5.0,5.5]	0.753 ± 0.004	0.581 ± 0.005	0.403 ± 0.008	0.214 ± 0.014	-
(5.5,6.0]	0.711 ± 0.005	0.547 ± 0.006	0.367 ± 0.011	0.191 ± 0.025	-
(6.0,7.0]	0.659 ± 0.005	0.506 ± 0.007	0.307 ± 0.012	-	-
(7.0,8.0]	0.608 ± 0.007	0.440 ± 0.012	0.239 ± 0.028	-	-
(8.0,9.0]	0.557 ± 0.011	0.353 ± 0.021	-	-	-
(9.0,10.0]	0.487 ± 0.017	0.280 ± 0.038	-	-	-
(10.0,11.0]	0.423 ± 0.028	-	-	-	-
(11.0,12.0]	0.395 ± 0.052	-	-	-	-
(12.0,13.0]	-	-	-	-	-
(13.0,15.0]	-	-	-	-	-
(15.0,30.0]	-	-	-	-	-

Table A.7 $\varepsilon_{\text{trigger}}$ in bins of D^0 p_{T} and y^* in forward rapidity regions. Statistical uncertaities only.

p_{T}/(GeV/c)\y^*	(1.50, 1.75]	(1.75, 2.00]	(2.00, 2.25]	(2.25, 2.50]	(2.50, 2.75]
(0.0,1.0]	0.263 ± 0.017	0.891 ± 0.005	0.966 ± 0.002	0.981 ± 0.001	0.990 ± 0.001
(1.0,1.5]	0.708 ± 0.018	0.953 ± 0.004	0.974 ± 0.002	0.982 ± 0.002	0.986 ± 0.001
(1.5,2.0]	0.865 ± 0.012	0.977 ± 0.002	0.982 ± 0.002	0.987 ± 0.001	0.990 ± 0.001
(2.0,2.5]	0.917 ± 0.009	0.985 ± 0.002	0.989 ± 0.001	0.990 ± 0.001	0.992 ± 0.001
(2.5,3.0]	0.932 ± 0.008	0.985 ± 0.002	0.989 ± 0.001	0.993 ± 0.001	0.993 ± 0.001
(3.0,3.5]	0.964 ± 0.006	0.988 ± 0.002	0.992 ± 0.001	0.993 ± 0.001	0.995 ± 0.001
(3.5,4.0]	0.970 ± 0.005	0.992 ± 0.001	0.994 ± 0.001	0.997 ± 0.001	0.996 ± 0.001
(4.0,4.5]	0.982 ± 0.004	0.992 ± 0.002	0.997 ± 0.001	0.996 ± 0.001	0.997 ± 0.001
(4.5,5.0]	0.980 ± 0.005	0.994 ± 0.001	0.995 ± 0.001	0.996 ± 0.001	0.994 ± 0.001
(5.0,5.5]	0.980 ± 0.005	0.995 ± 0.001	0.995 ± 0.001	0.996 ± 0.001	0.997 ± 0.001
(5.5,6.0]	0.988 ± 0.005	0.997 ± 0.001	0.996 ± 0.001	0.997 ± 0.001	0.996 ± 0.001
(6.0,7.0]	0.985 ± 0.004	0.996 ± 0.001	0.998 ± 0.001	0.997 ± 0.001	0.994 ± 0.002
(7.0,8.0]	0.995 ± 0.003	0.995 ± 0.002	0.997 ± 0.001	0.999 ± 0.001	0.997 ± 0.001
(8.0,9.0]	0.992 ± 0.002	0.997 ± 0.001	0.998 ± 0.001	0.997 ± 0.001	0.997 ± 0.001
(9.0,10.0]	0.992 ± 0.002	0.998 ± 0.001	0.998 ± 0.001	0.997 ± 0.001	0.996 ± 0.001
(10.0,11.0]	0.994 ± 0.002	0.999 ± 0.001	0.998 ± 0.001	0.996 ± 0.001	0.998 ± 0.001
(11.0,12.0]	0.998 ± 0.002	0.998 ± 0.001	0.999 ± 0.001	0.997 ± 0.001	0.996 ± 0.002
(12.0,13.0]	0.997 ± 0.002	0.998 ± 0.001	0.999 ± 0.001	0.997 ± 0.002	0.998 ± 0.002
(13.0,15.0]	0.996 ± 0.002	0.996 ± 0.002	0.997 ± 0.001	0.996 ± 0.002	1.000 ± 0.000
(15.0,30.0]	0.994 ± 0.002	0.998 ± 0.001	0.998 ± 0.001	0.998 ± 0.002	1.000 ± 0.000
p_{T}/(GeV/c)\y^*	(2.75, 3.00]	(3.00, 3.25]	(3.25, 3.50]	(3.50, 3.75]	(3.75, 4.00]
(0.0,1.0]	0.993 ± 0.001	0.993 ± 0.001	0.995 ± 0.001	0.996 ± 0.001	0.991 ± 0.002
(1.0,1.5]	0.986 ± 0.001	0.986 ± 0.002	0.992 ± 0.001	0.989 ± 0.002	0.982 ± 0.003
(1.5,2.0]	0.992 ± 0.001	0.991 ± 0.001	0.993 ± 0.001	0.992 ± 0.002	0.989 ± 0.002
(2.0,2.5]	0.993 ± 0.001	0.993 ± 0.001	0.995 ± 0.001	0.994 ± 0.001	0.995 ± 0.002
(2.5,3.0]	0.995 ± 0.001	0.994 ± 0.001	0.996 ± 0.001	0.996 ± 0.001	0.999 ± 0.001
(3.0,3.5]	0.995 ± 0.001	0.997 ± 0.001	0.996 ± 0.001	0.997 ± 0.001	0.993 ± 0.002
(3.5,4.0]	0.996 ± 0.001	0.997 ± 0.001	0.996 ± 0.001	0.998 ± 0.001	1.000 ± 0.000
(4.0,4.5]	0.997 ± 0.001	0.997 ± 0.001	0.997 ± 0.001	0.997 ± 0.002	0.997 ± 0.003
(4.5,5.0]	0.998 ± 0.001	0.996 ± 0.001	0.997 ± 0.001	0.999 ± 0.001	1.000 ± 0.000
(5.0,5.5]	0.996 ± 0.001	0.998 ± 0.001	1.000 ± 0.000	0.997 ± 0.003	1.000 ± 0.000
(5.5,6.0]	0.998 ± 0.001	0.997 ± 0.002	1.000 ± 0.000	1.000 ± 0.000	-
(6.0,7.0]	0.995 ± 0.001	0.999 ± 0.001	1.000 ± 0.000	1.000 ± 0.000	-
(7.0,8.0]	0.998 ± 0.001	0.998 ± 0.002	1.000 ± 0.000	1.000 ± 0.000	-
(8.0,9.0]	0.997 ± 0.001	0.999 ± 0.001	0.995 ± 0.005	-	-
(9.0,10.0]	0.998 ± 0.001	1.000 ± 0.000	1.000 ± 0.000	-	-
(10.0,11.0]	0.997 ± 0.002	1.000 ± 0.000	-	-	-
(11.0,12.0]	1.000 ± 0.000	1.000 ± 0.000	-	-	-
(12.0,13.0]	1.000 ± 0.000	-	-	-	-
(13.0,15.0]	1.000 ± 0.000	-	-	-	-
(15.0,30.0]	-	-	-	-	-

Table A.8 $\varepsilon_{\text{trigger}}$ in bins of D^0 p_{T} and y^* in backward rapidity regions. Statistical uncertaities only.

p_{T}/(GeV/c)\y^*	(-2.75, -2.50]	(-3.00, -2.75]	(-3.25, -3.00]	(-3.50, -3.25]	(-3.75, -3.50]
(0.0,1.0]	0.540 ± 0.014	0.939 ± 0.004	0.973 ± 0.002	0.980 ± 0.002	0.987 ± 0.001
(1.0,1.5]	0.844 ± 0.010	0.957 ± 0.003	0.973 ± 0.002	0.979 ± 0.002	0.984 ± 0.001
(1.5,2.0]	0.899 ± 0.008	0.969 ± 0.003	0.979 ± 0.002	0.983 ± 0.001	0.987 ± 0.001
(2.0,2.5]	0.933 ± 0.006	0.979 ± 0.002	0.983 ± 0.001	0.988 ± 0.001	0.988 ± 0.001
(2.5,3.0]	0.957 ± 0.004	0.985 ± 0.002	0.987 ± 0.001	0.988 ± 0.001	0.990 ± 0.001
(3.0,3.5]	0.973 ± 0.004	0.989 ± 0.001	0.992 ± 0.001	0.993 ± 0.001	0.991 ± 0.001
(3.5,4.0]	0.979 ± 0.003	0.990 ± 0.001	0.991 ± 0.001	0.993 ± 0.001	0.993 ± 0.001
(4.0,4.5]	0.984 ± 0.003	0.991 ± 0.002	0.992 ± 0.001	0.993 ± 0.001	0.995 ± 0.001
(4.5,5.0]	0.987 ± 0.003	0.993 ± 0.002	0.990 ± 0.002	0.993 ± 0.002	0.995 ± 0.001
(5.0,5.5]	0.983 ± 0.004	0.991 ± 0.002	0.992 ± 0.002	0.993 ± 0.002	0.993 ± 0.002
(5.5,6.0]	0.991 ± 0.003	0.995 ± 0.002	0.993 ± 0.002	0.992 ± 0.002	0.994 ± 0.002
(6.0,7.0]	0.994 ± 0.002	0.996 ± 0.001	0.992 ± 0.002	0.994 ± 0.002	0.992 ± 0.002
(7.0,8.0]	0.990 ± 0.003	0.995 ± 0.002	0.991 ± 0.003	0.995 ± 0.002	0.990 ± 0.003
(8.0,9.0]	0.986 ± 0.002	0.988 ± 0.001	0.989 ± 0.001	0.987 ± 0.001	0.990 ± 0.002
(9.0,10.0]	0.987 ± 0.002	0.989 ± 0.002	0.989 ± 0.002	0.989 ± 0.002	0.989 ± 0.002
(10.0,11.0]	0.987 ± 0.002	0.988 ± 0.002	0.990 ± 0.002	0.992 ± 0.002	0.991 ± 0.003
(11.0,12.0]	0.987 ± 0.003	0.989 ± 0.002	0.981 ± 0.003	0.988 ± 0.003	0.994 ± 0.003
(12.0,13.0]	0.989 ± 0.003	0.990 ± 0.003	0.987 ± 0.004	0.986 ± 0.004	0.993 ± 0.005
(13.0,15.0]	0.981 ± 0.004	0.987 ± 0.003	0.991 ± 0.003	0.988 ± 0.004	0.979 ± 0.010
(15.0,30.0]	0.988 ± 0.003	0.987 ± 0.003	0.990 ± 0.003	0.996 ± 0.004	1.000 ± 0.000
p_{T}/(GeV/c)\y^*	(-4.00, -3.75]	(-4.25, -4.00]	(-4.50, -4.25]	(-4.75, -4.50]	(-5.00, -4.75]
(0.0,1.0]	0.989 ± 0.001	0.993 ± 0.001	0.991 ± 0.001	0.987 ± 0.002	0.992 ± 0.002
(1.0,1.5]	0.983 ± 0.002	0.989 ± 0.001	0.985 ± 0.002	0.989 ± 0.002	0.971 ± 0.005
(1.5,2.0]	0.990 ± 0.001	0.987 ± 0.002	0.989 ± 0.002	0.990 ± 0.002	0.978 ± 0.005
(2.0,2.5]	0.989 ± 0.001	0.990 ± 0.001	0.993 ± 0.001	0.992 ± 0.002	0.993 ± 0.003
(2.5,3.0]	0.991 ± 0.001	0.988 ± 0.002	0.992 ± 0.002	0.994 ± 0.002	0.981 ± 0.005
(3.0,3.5]	0.993 ± 0.001	0.992 ± 0.001	0.992 ± 0.002	0.994 ± 0.002	0.995 ± 0.004
(3.5,4.0]	0.994 ± 0.001	0.992 ± 0.002	0.994 ± 0.002	1.000 ± 0.000	0.989 ± 0.008
(4.0,4.5]	0.992 ± 0.002	0.993 ± 0.002	0.993 ± 0.002	0.996 ± 0.002	0.986 ± 0.013
(4.5,5.0]	0.993 ± 0.002	0.993 ± 0.002	0.997 ± 0.002	0.993 ± 0.005	1.000 ± 0.000
(5.0,5.5]	0.993 ± 0.002	0.996 ± 0.002	0.993 ± 0.004	1.000 ± 0.000	-
(5.5,6.0]	0.992 ± 0.003	0.991 ± 0.003	0.997 ± 0.003	1.000 ± 0.000	-
(6.0,7.0]	0.990 ± 0.003	0.995 ± 0.002	0.995 ± 0.004	1.000 ± 0.000	-
(7.0,8.0]	0.999 ± 0.001	0.996 ± 0.004	0.968 ± 0.032	-	-
(8.0,9.0]	0.991 ± 0.002	0.987 ± 0.004	1.000 ± 0.000	-	-
(9.0,10.0]	0.990 ± 0.003	1.000 ± 0.000	-	-	-
(10.0,11.0]	0.995 ± 0.004	1.000 ± 0.000	-	-	-
(11.0,12.0]	0.984 ± 0.011	-	-	-	-
(12.0,13.0]	1.000 ± 0.000	-	-	-	-
(13.0,15.0]	1.000 ± 0.000	-	-	-	-
(15.0,30.0]	-	-	-	-	-

Table A.9 $\varepsilon_{\mathrm{tot}}$ in bins of D^0 p_{T} and y^* in forward rapidity regions. Statistical uncertaities only.

p_{T}/(GeV/c)\y^*	(1.50, 1.75]	(1.75, 2.00]	(2.00, 2.25]	(2.25, 2.50]	(2.50, 2.75]
(0.0,1.0]	0.001 ± 0.000	0.013 ± 0.000	0.026 ± 0.000	0.035 ± 0.000	0.039 ± 0.000
(1.0,1.5]	0.002 ± 0.000	0.016 ± 0.000	0.030 ± 0.000	0.040 ± 0.001	0.042 ± 0.001
(1.5,2.0]	0.004 ± 0.000	0.022 ± 0.000	0.039 ± 0.001	0.049 ± 0.001	0.052 ± 0.001
(2.0,2.5]	0.006 ± 0.000	0.031 ± 0.001	0.053 ± 0.001	0.065 ± 0.001	0.065 ± 0.001
(2.5,3.0]	0.009 ± 0.000	0.042 ± 0.001	0.071 ± 0.001	0.081 ± 0.001	0.082 ± 0.001
(3.0,3.5]	0.012 ± 0.000	0.059 ± 0.001	0.089 ± 0.001	0.099 ± 0.001	0.101 ± 0.001
(3.5,4.0]	0.017 ± 0.001	0.073 ± 0.001	0.108 ± 0.001	0.112 ± 0.002	0.111 ± 0.002
(4.0,4.5]	0.021 ± 0.001	0.083 ± 0.002	0.116 ± 0.002	0.121 ± 0.002	0.120 ± 0.002
(4.5,5.0]	0.026 ± 0.001	0.090 ± 0.002	0.122 ± 0.002	0.127 ± 0.002	0.131 ± 0.002
(5.0,5.5]	0.030 ± 0.001	0.104 ± 0.002	0.131 ± 0.003	0.132 ± 0.003	0.137 ± 0.003
(5.5,6.0]	0.034 ± 0.002	0.109 ± 0.003	0.131 ± 0.003	0.137 ± 0.003	0.139 ± 0.003
(6.0,7.0]	0.039 ± 0.001	0.120 ± 0.002	0.133 ± 0.003	0.143 ± 0.003	0.136 ± 0.003
(7.0,8.0]	0.044 ± 0.002	0.127 ± 0.003	0.137 ± 0.003	0.129 ± 0.003	0.134 ± 0.004
(8.0,9.0]	0.050 ± 0.001	0.128 ± 0.002	0.134 ± 0.002	0.130 ± 0.002	0.125 ± 0.002
(9.0,10.0]	0.056 ± 0.001	0.133 ± 0.002	0.132 ± 0.002	0.123 ± 0.002	0.117 ± 0.002
(10.0,11.0]	0.061 ± 0.002	0.133 ± 0.003	0.129 ± 0.003	0.115 ± 0.003	0.099 ± 0.003
(11.0,12.0]	0.062 ± 0.002	0.136 ± 0.003	0.128 ± 0.003	0.104 ± 0.003	0.078 ± 0.003
(12.0,13.0]	0.065 ± 0.003	0.128 ± 0.004	0.123 ± 0.004	0.095 ± 0.004	0.052 ± 0.003
(13.0,15.0]	0.068 ± 0.003	0.131 ± 0.004	0.109 ± 0.004	0.073 ± 0.003	0.033 ± 0.002
(15.0,30.0]	0.072 ± 0.002	0.115 ± 0.003	0.067 ± 0.003	0.029 ± 0.002	0.007 ± 0.001

p_{T}/(GeV/c)\y^*	(2.75, 3.00]	(3.00, 3.25]	(3.25, 3.50]	(3.50, 3.75]	(3.75, 4.00]
(0.0,1.0]	0.038 ± 0.000	0.033 ± 0.000	0.025 ± 0.000	0.016 ± 0.000	0.009 ± 0.000
(1.0,1.5]	0.041 ± 0.001	0.035 ± 0.001	0.028 ± 0.000	0.018 ± 0.000	0.009 ± 0.000
(1.5,2.0]	0.048 ± 0.001	0.043 ± 0.001	0.032 ± 0.001	0.020 ± 0.000	0.009 ± 0.000
(2.0,2.5]	0.062 ± 0.001	0.055 ± 0.001	0.042 ± 0.001	0.026 ± 0.001	0.010 ± 0.000
(2.5,3.0]	0.081 ± 0.001	0.071 ± 0.001	0.053 ± 0.001	0.029 ± 0.001	0.010 ± 0.000
(3.0,3.5]	0.095 ± 0.001	0.085 ± 0.001	0.061 ± 0.001	0.031 ± 0.001	0.009 ± 0.000
(3.5,4.0]	0.111 ± 0.002	0.095 ± 0.001	0.067 ± 0.001	0.031 ± 0.001	0.006 ± 0.000
(4.0,4.5]	0.120 ± 0.002	0.100 ± 0.002	0.067 ± 0.001	0.025 ± 0.001	0.004 ± 0.000
(4.5,5.0]	0.124 ± 0.002	0.098 ± 0.002	0.061 ± 0.002	0.019 ± 0.001	0.002 ± 0.000
(5.0,5.5]	0.126 ± 0.003	0.100 ± 0.002	0.051 ± 0.002	0.010 ± 0.001	-
(5.5,6.0]	0.124 ± 0.003	0.090 ± 0.003	0.041 ± 0.002	0.005 ± 0.001	-
(6.0,7.0]	0.118 ± 0.003	0.077 ± 0.002	0.027 ± 0.001	0.001 ± 0.000	-
(7.0,8.0]	0.104 ± 0.003	0.050 ± 0.002	0.010 ± 0.001	-	-
(8.0,9.0]	0.080 ± 0.002	0.026 ± 0.001	0.002 ± 0.000	-	-
(9.0,10.0]	0.059 ± 0.002	0.012 ± 0.001	-	-	-
(10.0,11.0]	0.040 ± 0.002	0.004 ± 0.001	-	-	-
(11.0,12.0]	0.022 ± 0.002	-	-	-	-
(12.0,13.0]	0.012 ± 0.002	-	-	-	-
(13.0,15.0]	0.003 ± 0.001	-	-	-	-
(15.0,30.0]	-	-	-	-	-

Table A.10 $\varepsilon_{\mathrm{tot}}$ in bins of D^0 p_{T} and y^* in backward rapidity regions. Statistical uncertaities only.

p_{T}/(GeV/c)\y^*	(-2.75, -2.50]	(-3.00, -2.75]	(-3.25, -3.00]	(-3.50, -3.25]	(-3.75, -3.50]
(0.0,1.0]	0.002 ± 0.000	0.013 ± 0.000	0.023 ± 0.000	0.028 ± 0.000	0.032 ± 0.000
(1.0,1.5]	0.004 ± 0.000	0.017 ± 0.000	0.026 ± 0.000	0.032 ± 0.000	0.035 ± 0.000
(1.5,2.0]	0.007 ± 0.000	0.022 ± 0.000	0.033 ± 0.000	0.041 ± 0.001	0.042 ± 0.001
(2.0,2.5]	0.010 ± 0.000	0.031 ± 0.000	0.047 ± 0.001	0.054 ± 0.001	0.055 ± 0.001
(2.5,3.0]	0.015 ± 0.000	0.045 ± 0.001	0.064 ± 0.001	0.070 ± 0.001	0.072 ± 0.001
(3.0,3.5]	0.020 ± 0.001	0.059 ± 0.001	0.078 ± 0.001	0.084 ± 0.001	0.086 ± 0.001
(3.5,4.0]	0.027 ± 0.001	0.074 ± 0.001	0.093 ± 0.001	0.099 ± 0.001	0.097 ± 0.002
(4.0,4.5]	0.033 ± 0.001	0.085 ± 0.002	0.103 ± 0.002	0.104 ± 0.002	0.105 ± 0.002
(4.5,5.0]	0.039 ± 0.001	0.091 ± 0.002	0.107 ± 0.002	0.113 ± 0.002	0.115 ± 0.002
(5.0,5.5]	0.045 ± 0.002	0.104 ± 0.002	0.118 ± 0.003	0.114 ± 0.003	0.118 ± 0.003
(5.5,6.0]	0.053 ± 0.002	0.113 ± 0.003	0.117 ± 0.003	0.118 ± 0.003	0.110 ± 0.003
(6.0,7.0]	0.062 ± 0.002	0.118 ± 0.003	0.119 ± 0.003	0.121 ± 0.003	0.116 ± 0.003
(7.0,8.0]	0.073 ± 0.003	0.117 ± 0.003	0.127 ± 0.004	0.114 ± 0.004	0.107 ± 0.004
(8.0,9.0]	0.072 ± 0.001	0.116 ± 0.002	0.119 ± 0.002	0.114 ± 0.002	0.098 ± 0.002
(9.0,10.0]	0.079 ± 0.002	0.116 ± 0.002	0.114 ± 0.002	0.104 ± 0.002	0.084 ± 0.002
(10.0,11.0]	0.081 ± 0.002	0.118 ± 0.003	0.118 ± 0.003	0.096 ± 0.003	0.067 ± 0.003
(11.0,12.0]	0.074 ± 0.003	0.104 ± 0.003	0.104 ± 0.004	0.091 ± 0.004	0.043 ± 0.003
(12.0,13.0]	0.083 ± 0.004	0.097 ± 0.005	0.097 ± 0.004	0.073 ± 0.004	0.038 ± 0.004
(13.0,15.0]	0.077 ± 0.003	0.077 ± 0.005	0.089 ± 0.004	0.055 ± 0.003	0.018 ± 0.002
(15.0,30.0]	0.060 ± 0.003	0.060 ± 0.005	0.051 ± 0.003	0.015 ± 0.002	-
p_{T}/(GeV/c)\y^*	(-4.00, -3.75]	(-4.25, -4.00]	(-4.50, -4.25]	(-4.75, -4.50]	(-5.00, -4.75]
(0.0,1.0]	0.030 ± 0.000	0.025 ± 0.000	0.018 ± 0.000	0.011 ± 0.000	0.006 ± 0.000
(1.0,1.5]	0.033 ± 0.000	0.027 ± 0.000	0.020 ± 0.000	0.012 ± 0.000	0.005 ± 0.000
(1.5,2.0]	0.039 ± 0.001	0.033 ± 0.001	0.024 ± 0.000	0.013 ± 0.000	0.005 ± 0.000
(2.0,2.5]	0.052 ± 0.001	0.043 ± 0.001	0.030 ± 0.001	0.016 ± 0.000	0.005 ± 0.000
(2.5,3.0]	0.068 ± 0.001	0.055 ± 0.001	0.038 ± 0.001	0.019 ± 0.001	0.006 ± 0.000
(3.0,3.5]	0.080 ± 0.001	0.067 ± 0.001	0.042 ± 0.001	0.020 ± 0.001	0.004 ± 0.000
(3.5,4.0]	0.091 ± 0.002	0.072 ± 0.001	0.046 ± 0.001	0.019 ± 0.001	0.002 ± 0.000
(4.0,4.5]	0.098 ± 0.002	0.078 ± 0.002	0.044 ± 0.001	0.014 ± 0.001	0.001 ± 0.000
(4.5,5.0]	0.099 ± 0.002	0.076 ± 0.002	0.037 ± 0.001	0.009 ± 0.001	-
(5.0,5.5]	0.096 ± 0.003	0.073 ± 0.002	0.029 ± 0.001	0.004 ± 0.001	-
(5.5,6.0]	0.098 ± 0.003	0.063 ± 0.003	0.023 ± 0.002	0.003 ± 0.001	-
(6.0,7.0]	0.098 ± 0.003	0.051 ± 0.002	0.011 ± 0.001	-	-
(7.0,8.0]	0.078 ± 0.003	0.026 ± 0.002	0.003 ± 0.001	-	-
(8.0,9.0]	0.055 ± 0.002	0.014 ± 0.001	-	-	-
(9.0,10.0]	0.037 ± 0.002	0.005 ± 0.001	-	-	-
(10.0,11.0]	0.024 ± 0.002	-	-	-	-
(11.0,12.0]	0.011 ± 0.002	-	-	-	-
(12.0,13.0]	-	-	-	-	-
(13.0,15.0]	-	-	-	-	-
(15.0,30.0]	-	-	-	-	-

A.2 Yields and fractions

The raw yields of D^0 candidates from $M(D^0)$ fit are listed in Tables A.11 and A.12. The prompt yields of D^0 signal from $\log_{10}\left(\chi^2_{\mathrm{IP}}\right)$ fit are listed in Tables A.13 and A.14. The fractions of prompt D^0 mesons are listed in Tables A.15 and A.16. Statistical uncertainties only.

A.3 Double-differential cross-sections

The numerical values for D^0 production cross-section are listed in Tables A.17 and A.18.

Table A.11 Raw yield of D^0 candidates in bins of p_T and y^* in forward rapidity regions. Statistical uncertainties only.

	(Raw yield/($\Delta p_T \Delta y$)) / (10^4/(GeV/c))				
p_T/(GeV/c)\y^*	(1.50, 1.75]	(1.75, 2.00]	(2.00, 2.25]	(2.25, 2.50]	(2.50, 2.75]
(0.0,1.0]	0.90 ± 0.02	15.17 ± 0.09	32.78 ± 0.14	44.82 ± 0.18	50.62 ± 0.18
(1.0,1.5]	5.07 ± 0.08	36.30 ± 0.20	69.13 ± 0.27	89.27 ± 0.30	98.29 ± 0.37
(1.5,2.0]	8.55 ± 0.09	47.33 ± 0.58	83.91 ± 0.30	105.06 ± 0.34	108.13 ± 0.35
(2.0,2.5]	10.72 ± 0.10	54.44 ± 0.22	94.76 ± 0.32	112.36 ± 0.35	111.09 ± 0.39
(2.5,3.0]	11.87 ± 0.10	57.46 ± 0.24	96.09 ± 0.32	108.01 ± 0.35	103.25 ± 0.29
(3.0,3.5]	11.65 ± 0.11	54.77 ± 0.21	85.04 ± 0.28	93.14 ± 0.32	89.47 ± 0.33
(3.5,4.0]	11.03 ± 0.11	48.57 ± 0.21	70.49 ± 0.28	73.48 ± 0.25	70.32 ± 0.29
(4.0,4.5]	9.93 ± 0.09	40.84 ± 0.21	55.12 ± 0.25	55.82 ± 0.23	52.95 ± 0.23
(4.5,5.0]	8.52 ± 0.09	33.17 ± 0.19	41.41 ± 0.22	41.88 ± 0.20	40.14 ± 0.23
(5.0,5.5]	7.18 ± 0.08	25.73 ± 0.15	31.67 ± 0.19	31.12 ± 0.18	29.65 ± 0.20
(5.5,6.0]	5.91 ± 0.08	20.33 ± 0.14	23.33 ± 0.16	22.76 ± 0.15	21.98 ± 0.17
(6.0,7.0]	4.53 ± 0.05	14.03 ± 0.08	15.58 ± 0.09	15.31 ± 0.10	14.13 ± 0.09
(7.0,8.0]	3.11 ± 0.04	8.61 ± 0.06	8.72 ± 0.06	8.63 ± 0.07	7.99 ± 0.08
(8.0,9.0]	2.09 ± 0.03	5.24 ± 0.05	5.08 ± 0.05	5.04 ± 0.05	4.37 ± 0.05
(9.0,10.0]	1.37 ± 0.03	3.19 ± 0.04	2.94 ± 0.04	3.01 ± 0.04	2.42 ± 0.05
(10.0,11.0]	0.96 ± 0.02	2.07 ± 0.03	1.77 ± 0.03	1.85 ± 0.03	1.32 ± 0.03
(11.0,12.0]	0.67 ± 0.02	1.28 ± 0.03	1.07 ± 0.02	1.14 ± 0.02	0.65 ± 0.02
(12.0,13.0]	0.48 ± 0.02	0.81 ± 0.02	0.69 ± 0.02	0.65 ± 0.02	0.33 ± 0.01
(13.0,15.0]	0.29 ± 0.01	0.41 ± 0.01	0.35 ± 0.01	0.30 ± 0.01	0.11 ± 0.01
(15.0,30.0]	0.04 ± 0.00	0.05 ± 0.00	0.03 ± 0.00	0.02 ± 0.00	0.00 ± 0.00
p_T/(GeV/c)\y^*	(2.75, 3.00]	(3.00, 3.25]	(3.25, 3.50]	(3.50, 3.75]	(3.75, 4.00]
(0.0,1.0]	50.26 ± 0.22	44.73 ± 0.74	33.25 ± 0.28	20.33 ± 0.22	10.88 ± 0.12
(1.0,1.5]	93.32 ± 0.41	80.76 ± 0.43	59.88 ± 0.39	35.58 ± 0.37	16.59 ± 0.47
(1.5,2.0]	100.58 ± 0.30	85.20 ± 0.41	62.18 ± 0.38	36.27 ± 0.39	14.36 ± 0.20
(2.0,2.5]	102.25 ± 0.38	85.20 ± 0.36	61.93 ± 0.39	33.36 ± 0.34	11.71 ± 0.22
(2.5,3.0]	94.38 ± 0.33	78.40 ± 0.36	53.57 ± 0.36	27.44 ± 0.21	8.38 ± 0.16
(3.0,3.5]	79.05 ± 0.30	65.31 ± 0.34	42.42 ± 0.24	20.35 ± 0.20	4.59 ± 0.08
(3.5,4.0]	62.34 ± 0.39	49.31 ± 0.20	31.22 ± 0.16	12.77 ± 0.13	2.17 ± 0.07
(4.0,4.5]	47.29 ± 0.20	36.24 ± 0.23	21.27 ± 0.16	7.08 ± 0.10	0.76 ± 0.05
(4.5,5.0]	34.81 ± 0.17	26.23 ± 0.22	13.66 ± 0.29	3.41 ± 0.05	0.17 ± 0.01
(5.0,5.5]	25.28 ± 0.16	17.80 ± 0.17	7.75 ± 0.10	1.34 ± 0.04	-
(5.5,6.0]	18.03 ± 0.16	11.72 ± 0.13	4.18 ± 0.06	0.43 ± 0.02	-
(6.0,7.0]	11.08 ± 0.07	5.94 ± 0.05	1.52 ± 0.03	0.06 ± 0.01	-
(7.0,8.0]	5.48 ± 0.05	2.05 ± 0.01	0.27 ± 0.01	-	-
(8.0,9.0]	2.45 ± 0.03	0.63 ± 0.02	0.03 ± 0.00	-	-
(9.0,10.0]	1.01 ± 0.02	0.16 ± 0.01	-	-	-
(10.0,11.0]	0.40 ± 0.01	0.03 ± 0.00	-	-	-
(11.0,12.0]	0.15 ± 0.01	-	-	-	-
(12.0,13.0]	0.05 ± 0.00	-	-	-	-
(13.0,15.0]	0.01 ± 0.00	-	-	-	-
(15.0,30.0]	-	-	-	-	-

Table A.12 Raw yield of D^0 candidates in bins of p_{T} and y^* in backward rapidity regions. Statistical uncertainties only.

	(Raw yield/($\Delta p_{\mathrm{T}} \Delta y$)) / ($10^4$/(GeV/$c$))				
p_{T}/(GeV/c)\y^*	(-2.75, -2.50]	(-3.00, -2.75]	(-3.25, -3.00]	(-3.50, -3.25]	(-3.75, -3.50]
(0.0,1.0]	4.27 ± 0.05	30.49 ± 0.14	52.30 ± 0.17	68.58 ± 0.24	73.79 ± 0.31
(1.0,1.5]	16.44 ± 0.14	68.32 ± 0.85	110.27 ± 0.37	134.95 ± 0.43	139.84 ± 0.47
(1.5,2.0]	24.82 ± 0.19	82.95 ± 0.29	128.89 ± 0.38	152.33 ± 0.44	152.34 ± 0.54
(2.0,2.5]	29.81 ± 0.21	96.33 ± 0.30	143.69 ± 0.40	159.49 ± 0.44	151.94 ± 0.46
(2.5,3.0]	30.83 ± 0.16	97.43 ± 0.32	139.34 ± 0.39	144.91 ± 0.44	135.07 ± 0.37
(3.0,3.5]	29.73 ± 0.17	88.87 ± 0.30	117.99 ± 0.34	119.33 ± 0.34	108.94 ± 0.37
(3.5,4.0]	27.37 ± 0.15	75.61 ± 0.32	92.40 ± 0.29	91.36 ± 0.32	82.06 ± 0.29
(4.0,4.5]	23.42 ± 0.16	58.36 ± 0.24	68.57 ± 0.25	64.83 ± 0.23	57.76 ± 0.28
(4.5,5.0]	19.63 ± 0.14	45.05 ± 0.20	49.62 ± 0.24	46.59 ± 0.21	40.85 ± 0.22
(5.0,5.5]	15.83 ± 0.14	34.33 ± 0.19	35.73 ± 0.18	33.09 ± 0.18	28.48 ± 0.15
(5.5,6.0]	12.74 ± 0.12	25.39 ± 0.15	25.54 ± 0.16	23.22 ± 0.16	19.93 ± 0.16
(6.0,7.0]	8.99 ± 0.07	16.58 ± 0.10	15.82 ± 0.09	14.51 ± 0.10	11.71 ± 0.08
(7.0,8.0]	5.70 ± 0.06	9.70 ± 0.07	8.41 ± 0.06	7.71 ± 0.08	5.71 ± 0.07
(8.0,9.0]	3.62 ± 0.04	5.29 ± 0.05	4.64 ± 0.04	4.07 ± 0.05	2.90 ± 0.06
(9.0,10.0]	2.36 ± 0.04	3.00 ± 0.04	2.56 ± 0.03	2.24 ± 0.03	1.36 ± 0.03
(10.0,11.0]	1.54 ± 0.03	1.76 ± 0.03	1.50 ± 0.03	1.28 ± 0.03	0.65 ± 0.04
(11.0,12.0]	1.02 ± 0.02	1.10 ± 0.03	0.89 ± 0.02	0.72 ± 0.02	0.30 ± 0.01
(12.0,13.0]	0.61 ± 0.02	0.64 ± 0.02	0.56 ± 0.02	0.42 ± 0.01	0.12 ± 0.01
(13.0,15.0]	0.36 ± 0.01	0.30 ± 0.01	0.26 ± 0.01	0.16 ± 0.01	0.04 ± 0.00
(15.0,30.0]	0.04 ± 0.00	0.03 ± 0.00	0.02 ± 0.00	0.01 ± 0.00	-
p_{T}/(GeV/c)\y^*	(-4.00, -3.75]	(-4.25, -4.00]	(-4.50, -4.25]	(-4.75, -4.50]	(-5.00, -4.75]
(0.0,1.0]	71.04 ± 0.19	59.72 ± 0.32	42.23 ± 0.83	24.04 ± 1.40	12.07 ± 0.39
(1.0,1.5]	128.47 ± 0.44	105.75 ± 0.60	71.36 ± 0.45	37.00 ± 0.45	15.00 ± 0.36
(1.5,2.0]	136.60 ± 0.46	106.45 ± 0.42	70.74 ± 0.39	34.80 ± 0.42	12.02 ± 0.58
(2.0,2.5]	133.68 ± 0.49	102.95 ± 0.49	65.20 ± 0.37	29.70 ± 0.34	8.39 ± 0.16
(2.5,3.0]	115.09 ± 0.31	86.85 ± 0.28	52.23 ± 0.22	21.30 ± 0.22	4.48 ± 0.11
(3.0,3.5]	89.58 ± 0.36	66.46 ± 0.24	36.45 ± 0.18	13.56 ± 0.15	2.09 ± 0.06
(3.5,4.0]	66.00 ± 0.28	46.21 ± 0.26	23.17 ± 0.14	7.04 ± 0.09	0.72 ± 0.02
(4.0,4.5]	46.71 ± 0.20	30.54 ± 0.20	14.31 ± 0.11	3.19 ± 0.06	0.18 ± 0.01
(4.5,5.0]	31.37 ± 0.16	19.38 ± 0.16	7.58 ± 0.08	1.14 ± 0.03	-
(5.0,5.5]	21.17 ± 0.13	11.85 ± 0.12	3.75 ± 0.06	0.38 ± 0.02	-
(5.5,6.0]	13.91 ± 0.11	7.16 ± 0.09	1.66 ± 0.04	0.10 ± 0.01	-
(6.0,7.0]	7.69 ± 0.06	3.07 ± 0.05	0.50 ± 0.02	-	-
(7.0,8.0]	3.20 ± 0.04	0.82 ± 0.02	0.05 ± 0.00	-	-
(8.0,9.0]	1.17 ± 0.02	0.18 ± 0.01	-	-	-
(9.0,10.0]	0.41 ± 0.01	0.04 ± 0.00	-	-	-
(10.0,11.0]	0.13 ± 0.01	-	-	-	-
(11.0,12.0]	0.03 ± 0.00	-	-	-	-
(12.0,13.0]	-	-	-	-	-
(13.0,15.0]	-	-	-	-	-
(15.0,30.0]	-	-	-	-	-

Table A.13 Prompt yield of D^0 candidates in bins of p_{T} and y^* in forward rapidity regions. Statistical uncertainties only.

	(Prompt yield/($\Delta p_{\mathrm{T}} \Delta y$)) / ($10^4$/(GeV/$c$))				
p_{T}/(GeV/c)\y^*	(1.50, 1.75]	(1.75, 2.00]	(2.00, 2.25]	(2.25, 2.50]	(2.50, 2.75]
(0.0,1.0]	0.90 ± 0.06	15.12 ± 0.08	32.56 ± 0.11	44.20 ± 0.13	49.33 ± 0.14
(1.0,1.5]	5.06 ± 0.02	36.18 ± 0.17	68.63 ± 0.24	87.88 ± 0.27	95.20 ± 0.28
(1.5,2.0]	8.54 ± 0.03	47.15 ± 0.20	83.03 ± 0.19	102.79 ± 0.30	103.69 ± 0.30
(2.0,2.5]	10.69 ± 0.11	54.04 ± 0.21	93.46 ± 0.29	109.23 ± 0.32	106.47 ± 0.30
(2.5,3.0]	11.81 ± 0.10	56.90 ± 0.22	94.22 ± 0.30	103.75 ± 0.31	98.19 ± 0.38
(3.0,3.5]	11.56 ± 0.10	54.08 ± 0.44	82.71 ± 0.27	89.72 ± 0.33	83.71 ± 0.37
(3.5,4.0]	10.94 ± 0.10	47.58 ± 0.20	67.83 ± 0.31	69.87 ± 0.31	65.07 ± 0.30
(4.0,4.5]	9.76 ± 0.10	39.64 ± 0.48	52.70 ± 0.31	51.97 ± 0.33	48.35 ± 0.22
(4.5,5.0]	8.33 ± 0.09	31.89 ± 0.17	39.68 ± 0.21	38.49 ± 0.26	35.82 ± 0.22
(5.0,5.5]	6.94 ± 0.09	24.44 ± 0.20	29.83 ± 0.20	28.16 ± 0.22	26.25 ± 0.19
(5.5,6.0]	5.72 ± 0.08	19.64 ± 0.14	21.67 ± 0.19	20.70 ± 0.17	19.24 ± 0.15
(6.0,7.0]	4.25 ± 0.04	13.14 ± 0.13	14.07 ± 0.12	13.53 ± 0.10	12.12 ± 0.09
(7.0,8.0]	2.96 ± 0.04	7.95 ± 0.08	7.64 ± 0.09	7.38 ± 0.06	6.81 ± 0.06
(8.0,9.0]	1.98 ± 0.03	4.72 ± 0.06	4.55 ± 0.05	4.27 ± 0.05	3.66 ± 0.04
(9.0,10.0]	1.19 ± 0.05	2.86 ± 0.04	2.51 ± 0.04	2.54 ± 0.04	2.00 ± 0.03
(10.0,11.0]	0.84 ± 0.05	1.78 ± 0.05	1.49 ± 0.03	1.53 ± 0.03	1.09 ± 0.02
(11.0,12.0]	0.59 ± 0.03	1.10 ± 0.03	0.90 ± 0.02	0.92 ± 0.03	0.54 ± 0.02
(12.0,13.0]	0.43 ± 0.01	0.64 ± 0.03	0.58 ± 0.02	0.53 ± 0.02	0.28 ± 0.01
(13.0,15.0]	0.24 ± 0.01	0.35 ± 0.01	0.28 ± 0.01	0.24 ± 0.01	0.09 ± 0.00
(15.0,30.0]	0.03 ± 0.00	0.04 ± 0.00	0.02 ± 0.00	0.02 ± 0.00	0.00 ± 0.00
p_{T}/(GeV/c)\y^*	(2.75, 3.00]	(3.00, 3.25]	(3.25, 3.50]	(3.50, 3.75]	(3.75, 4.00]
(0.0,1.0]	47.93 ± 0.27	41.97 ± 0.13	30.24 ± 0.18	17.94 ± 0.15	9.21 ± 0.68
(1.0,1.5]	88.37 ± 0.35	75.27 ± 0.26	53.90 ± 0.36	30.98 ± 0.29	14.56 ± 0.17
(1.5,2.0]	94.71 ± 0.29	78.27 ± 0.36	55.91 ± 0.31	31.49 ± 0.25	11.94 ± 0.19
(2.0,2.5]	95.54 ± 0.36	76.99 ± 0.34	55.04 ± 0.28	28.92 ± 0.17	10.10 ± 0.12
(2.5,3.0]	87.41 ± 0.34	70.89 ± 0.30	47.00 ± 0.25	23.60 ± 0.17	7.21 ± 0.10
(3.0,3.5]	72.06 ± 0.32	58.22 ± 0.27	36.88 ± 0.21	17.47 ± 0.15	4.06 ± 0.07
(3.5,4.0]	55.91 ± 0.28	43.55 ± 0.22	27.11 ± 0.18	11.29 ± 0.11	1.89 ± 0.06
(4.0,4.5]	42.27 ± 0.22	31.72 ± 0.18	18.35 ± 0.14	6.16 ± 0.08	0.66 ± 0.02
(4.5,5.0]	30.60 ± 0.18	22.74 ± 0.16	11.82 ± 0.12	2.98 ± 0.05	0.15 ± 0.01
(5.0,5.5]	22.12 ± 0.15	15.39 ± 0.12	6.69 ± 0.08	1.15 ± 0.04	-
(5.5,6.0]	15.59 ± 0.13	9.97 ± 0.00	3.63 ± 0.06	0.38 ± 0.02	-
(6.0,7.0]	9.40 ± 0.07	5.09 ± 0.05	1.29 ± 0.03	0.05 ± 0.00	-
(7.0,8.0]	4.62 ± 0.05	1.79 ± 0.03	0.24 ± 0.01	-	-
(8.0,9.0]	2.05 ± 0.03	0.51 ± 0.02	0.02 ± 0.00	-	-
(9.0,10.0]	0.82 ± 0.02	0.14 ± 0.01	-	-	-
(10.0,11.0]	0.31 ± 0.01	0.03 ± 0.00	-	-	-
(11.0,12.0]	0.12 ± 0.01	-	-	-	-
(12.0,13.0]	0.05 ± 0.00	-	-	-	-
(13.0,15.0]	0.01 ± 0.00	-	-	-	-
(15.0,30.0]	-	-	-	-	-

Table A.14 Prompt yield of D^0 candidates in bins of p_{T} and y^* in backward rapidity regions. Statistical uncertainties only.

(Prompt yield/($\Delta p_{\mathrm{T}} \Delta y$)) / ($10^4$/(GeV/$c$))					
p_{T}/(GeV/c)\y^*	(-2.75, -2.50]	(-3.00, -2.75]	(-3.25, -3.00]	(-3.50, -3.25]	(-3.75, -3.50]
(0.0,1.0]	4.27 ± 0.01	30.43 ± 0.11	51.96 ± 0.14	67.72 ± 0.17	72.23 ± 0.18
(1.0,1.5]	16.41 ± 0.11	68.07 ± 0.24	109.58 ± 0.30	133.06 ± 0.33	136.73 ± 0.36
(1.5,2.0]	24.78 ± 0.13	82.62 ± 0.26	127.85 ± 0.33	149.72 ± 0.37	147.76 ± 0.37
(2.0,2.5]	29.75 ± 0.15	95.65 ± 0.28	141.98 ± 0.00	155.94 ± 0.36	145.96 ± 0.38
(2.5,3.0]	30.74 ± 0.16	96.54 ± 0.29	137.01 ± 0.71	140.67 ± 0.32	130.46 ± 0.42
(3.0,3.5]	29.54 ± 0.15	87.71 ± 0.34	115.21 ± 0.31	114.60 ± 0.30	103.52 ± 0.35
(3.5,4.0]	27.05 ± 0.15	74.25 ± 0.25	89.41 ± 0.54	87.88 ± 0.33	77.65 ± 0.29
(4.0,4.5]	23.03 ± 0.26	56.90 ± 0.25	66.30 ± 0.29	61.86 ± 0.26	53.88 ± 0.25
(4.5,5.0]	19.21 ± 0.13	43.52 ± 0.29	47.88 ± 0.22	43.72 ± 0.22	37.87 ± 0.19
(5.0,5.5]	15.40 ± 0.12	33.18 ± 0.24	33.69 ± 0.26	30.79 ± 0.19	26.09 ± 0.16
(5.5,6.0]	12.33 ± 0.16	23.87 ± 0.23	23.54 ± 0.20	21.25 ± 0.15	17.95 ± 0.13
(6.0,7.0]	8.59 ± 0.11	15.65 ± 0.13	14.55 ± 0.10	13.11 ± 0.09	10.47 ± 0.07
(7.0,8.0]	5.44 ± 0.06	9.04 ± 0.06	7.51 ± 0.08	6.88 ± 0.06	5.06 ± 0.05
(8.0,9.0]	3.35 ± 0.07	4.78 ± 0.05	4.09 ± 0.05	3.60 ± 0.04	2.55 ± 0.04
(9.0,10.0]	2.19 ± 0.03	2.67 ± 0.05	2.23 ± 0.04	1.95 ± 0.03	1.19 ± 0.02
(10.0,11.0]	1.43 ± 0.03	1.58 ± 0.01	1.32 ± 0.03	1.11 ± 0.02	0.57 ± 0.02
(11.0,12.0]	0.85 ± 0.05	0.91 ± 0.04	0.78 ± 0.02	0.62 ± 0.02	0.26 ± 0.01
(12.0,13.0]	0.56 ± 0.02	0.57 ± 0.02	0.48 ± 0.02	0.36 ± 0.01	0.12 ± 0.01
(13.0,15.0]	0.32 ± 0.01	0.26 ± 0.01	0.22 ± 0.01	0.14 ± 0.01	0.03 ± 0.00
(15.0,30.0]	0.04 ± 0.00	0.02 ± 0.00	0.02 ± 0.00	0.01 ± 0.00	-
p_{T}/(GeV/c)\y^*	(-4.00, -3.75]	(-4.25, -4.00]	(-4.50, -4.25]	(-4.75, -4.50]	(-5.00, -4.75]
(0.0,1.0]	68.51 ± 0.16	57.47 ± 0.16	40.44 ± 0.14	22.46 ± 0.14	11.45 ± 0.07
(1.0,1.5]	124.15 ± 0.37	100.65 ± 0.31	66.58 ± 0.40	34.50 ± 0.21	13.69 ± 0.13
(1.5,2.0]	132.03 ± 0.36	101.57 ± 0.30	66.20 ± 0.28	32.24 ± 0.20	10.74 ± 0.19
(2.0,2.5]	127.59 ± 0.41	96.98 ± 0.32	60.59 ± 0.26	27.36 ± 0.00	7.52 ± 0.13
(2.5,3.0]	109.15 ± 0.34	81.18 ± 0.31	47.53 ± 0.26	19.71 ± 0.14	4.19 ± 0.07
(3.0,3.5]	83.79 ± 0.32	61.32 ± 0.26	33.52 ± 0.18	12.45 ± 0.11	1.91 ± 0.04
(3.5,4.0]	61.40 ± 0.25	42.32 ± 0.21	21.24 ± 0.15	6.45 ± 0.08	0.63 ± 0.03
(4.0,4.5]	42.89 ± 0.21	27.54 ± 0.16	13.09 ± 0.11	2.97 ± 0.05	0.18 ± 0.01
(4.5,5.0]	28.14 ± 0.19	17.58 ± 0.13	6.87 ± 0.08	1.04 ± 0.03	-
(5.0,5.5]	19.12 ± 0.14	10.69 ± 0.10	3.45 ± 0.05	0.31 ± 0.02	-
(5.5,6.0]	12.44 ± 0.10	6.45 ± 0.08	1.51 ± 0.00	0.10 ± 0.01	-
(6.0,7.0]	6.82 ± 0.06	2.76 ± 0.04	0.43 ± 0.02	-	-
(7.0,8.0]	2.81 ± 0.04	0.71 ± 0.02	0.05 ± 0.00	-	-
(8.0,9.0]	1.04 ± 0.02	0.16 ± 0.01	-	-	-
(9.0,10.0]	0.35 ± 0.02	0.03 ± 0.00	-	-	-
(10.0,11.0]	0.12 ± 0.01	-	-	-	-
(11.0,12.0]	0.03 ± 0.00	-	-	-	-
(12.0,13.0]	-	-	-	-	-
(13.0,15.0]	-	-	-	-	-
(15.0,30.0]	-	-	-	-	-

Table A.15 Prompt fraction of D^0 candidates in bins of p_T and y^* in forward rapidity regions. Statistical uncertainties only.

	Prompt fraction				
p_T/(GeV/c)\y^*	(1.50, 1.75]	(1.75, 2.00]	(2.00, 2.25]	(2.25, 2.50]	(2.50, 2.75]
(0.0,1.0]	1.00 ± 0.06	1.00 ± 0.00	0.99 ± 0.00	0.99 ± 0.00	0.97 ± 0.00
(1.0,1.5]	1.00 ± 0.01	1.00 ± 0.00	0.99 ± 0.00	0.98 ± 0.00	0.97 ± 0.00
(1.5,2.0]	1.00 ± 0.01	1.00 ± 0.01	0.99 ± 0.00	0.98 ± 0.00	0.96 ± 0.00
(2.0,2.5]	1.00 ± 0.00	0.99 ± 0.00	0.99 ± 0.00	0.97 ± 0.00	0.96 ± 0.00
(2.5,3.0]	1.00 ± 0.00	0.99 ± 0.00	0.98 ± 0.00	0.96 ± 0.00	0.95 ± 0.00
(3.0,3.5]	0.99 ± 0.00	0.99 ± 0.01	0.97 ± 0.00	0.96 ± 0.00	0.94 ± 0.00
(3.5,4.0]	0.99 ± 0.00	0.98 ± 0.00	0.96 ± 0.00	0.95 ± 0.00	0.93 ± 0.00
(4.0,4.5]	0.98 ± 0.00	0.97 ± 0.01	0.96 ± 0.00	0.93 ± 0.00	0.91 ± 0.00
(4.5,5.0]	0.98 ± 0.00	0.96 ± 0.00	0.96 ± 0.00	0.92 ± 0.00	0.89 ± 0.00
(5.0,5.5]	0.97 ± 0.00	0.95 ± 0.00	0.94 ± 0.00	0.90 ± 0.00	0.89 ± 0.00
(5.5,6.0]	0.97 ± 0.01	0.97 ± 0.00	0.93 ± 0.00	0.91 ± 0.00	0.88 ± 0.00
(6.0,7.0]	0.94 ± 0.00	0.94 ± 0.01	0.90 ± 0.00	0.88 ± 0.00	0.86 ± 0.00
(7.0,8.0]	0.95 ± 0.01	0.92 ± 0.00	0.88 ± 0.01	0.86 ± 0.00	0.85 ± 0.01
(8.0,9.0]	0.95 ± 0.01	0.90 ± 0.01	0.90 ± 0.00	0.85 ± 0.00	0.84 ± 0.01
(9.0,10.0]	0.87 ± 0.03	0.90 ± 0.01	0.85 ± 0.00	0.84 ± 0.01	0.83 ± 0.01
(10.0,11.0]	0.87 ± 0.04	0.86 ± 0.01	0.84 ± 0.00	0.83 ± 0.00	0.82 ± 0.01
(11.0,12.0]	0.87 ± 0.03	0.86 ± 0.01	0.84 ± 0.00	0.80 ± 0.01	0.83 ± 0.01
(12.0,13.0]	0.89 ± 0.02	0.79 ± 0.02	0.84 ± 0.00	0.82 ± 0.01	0.85 ± 0.01
(13.0,15.0]	0.85 ± 0.03	0.84 ± 0.00	0.80 ± 0.01	0.82 ± 0.01	0.84 ± 0.02
(15.0,30.0]	0.82 ± 0.03	0.83 ± 0.01	0.84 ± 0.01	0.87 ± 0.02	0.86 ± 0.03
p_T/(GeV/c)\y^*	(2.75, 3.00]	(3.00, 3.25]	(3.25, 3.50]	(3.50, 3.75]	(3.75, 4.00]
(0.0,1.0]	0.95 ± 0.00	0.94 ± 0.02	0.91 ± 0.01	0.88 ± 0.01	0.85 ± 0.05
(1.0,1.5]	0.95 ± 0.00	0.93 ± 0.00	0.90 ± 0.00	0.87 ± 0.01	0.88 ± 0.02
(1.5,2.0]	0.94 ± 0.00	0.92 ± 0.00	0.90 ± 0.00	0.87 ± 0.01	0.83 ± 0.01
(2.0,2.5]	0.93 ± 0.00	0.90 ± 0.00	0.89 ± 0.00	0.87 ± 0.01	0.86 ± 0.01
(2.5,3.0]	0.93 ± 0.00	0.90 ± 0.00	0.88 ± 0.00	0.86 ± 0.00	0.86 ± 0.01
(3.0,3.5]	0.91 ± 0.00	0.89 ± 0.00	0.87 ± 0.00	0.86 ± 0.01	0.88 ± 0.01
(3.5,4.0]	0.90 ± 0.00	0.88 ± 0.00	0.87 ± 0.00	0.88 ± 0.01	0.87 ± 0.01
(4.0,4.5]	0.89 ± 0.00	0.88 ± 0.00	0.86 ± 0.00	0.87 ± 0.01	0.87 ± 0.04
(4.5,5.0]	0.88 ± 0.00	0.87 ± 0.01	0.86 ± 0.02	0.87 ± 0.00	0.90 ± 0.02
(5.0,5.5]	0.88 ± 0.00	0.86 ± 0.01	0.86 ± 0.01	0.86 ± 0.01	-
(5.5,6.0]	0.86 ± 0.01	0.85 ± 0.01	0.87 ± 0.00	0.87 ± 0.02	-
(6.0,7.0]	0.85 ± 0.00	0.86 ± 0.00	0.85 ± 0.00	0.78 ± 0.03	-
(7.0,8.0]	0.84 ± 0.00	0.87 ± 0.01	0.90 ± 0.02	-	-
(8.0,9.0]	0.84 ± 0.00	0.82 ± 0.00	0.80 ± 0.07	-	-
(9.0,10.0]	0.81 ± 0.01	0.89 ± 0.02	-	-	-
(10.0,11.0]	0.79 ± 0.01	0.84 ± 0.04	-	-	-
(11.0,12.0]	0.80 ± 0.00	-	-	-	-
(12.0,13.0]	0.91 ± 0.05	-	-	-	-
(13.0,15.0]	0.78 ± 0.10	-	-	-	-
(15.0,30.0]	-	-	-	-	-

Table A.16 Prompt fraction of D^0 candidates in bins of p_T and y^* in backward rapidity regions. Statistical uncertainties only.

	Prompt fraction				
p_T/(GeV/c)\y^*	(-2.75, -2.50]	(-3.00, -2.75]	(-3.25, -3.00]	(-3.50, -3.25]	(-3.75, -3.50]
(0.0,1.0]	1.00 ± 0.01	1.00 ± 0.00	0.99 ± 0.00	0.99 ± 0.00	0.98 ± 0.00
(1.0,1.5]	1.00 ± 0.01	1.00 ± 0.01	0.99 ± 0.00	0.99 ± 0.00	0.98 ± 0.00
(1.5,2.0]	1.00 ± 0.01	1.00 ± 0.00	0.99 ± 0.00	0.98 ± 0.00	0.97 ± 0.00
(2.0,2.5]	1.00 ± 0.00	0.99 ± 0.00	0.99 ± 0.00	0.98 ± 0.00	0.96 ± 0.00
(2.5,3.0]	1.00 ± 0.00	0.99 ± 0.00	0.98 ± 0.00	0.97 ± 0.00	0.97 ± 0.00
(3.0,3.5]	0.99 ± 0.00	0.99 ± 0.00	0.98 ± 0.00	0.96 ± 0.00	0.95 ± 0.00
(3.5,4.0]	0.99 ± 0.00	0.98 ± 0.00	0.97 ± 0.00	0.96 ± 0.00	0.95 ± 0.00
(4.0,4.5]	0.98 ± 0.01	0.98 ± 0.00	0.97 ± 0.00	0.95 ± 0.00	0.93 ± 0.00
(4.5,5.0]	0.98 ± 0.00	0.97 ± 0.00	0.96 ± 0.00	0.94 ± 0.00	0.93 ± 0.00
(5.0,5.5]	0.97 ± 0.00	0.97 ± 0.00	0.94 ± 0.00	0.93 ± 0.00	0.92 ± 0.00
(5.5,6.0]	0.97 ± 0.01	0.94 ± 0.01	0.92 ± 0.00	0.92 ± 0.00	0.90 ± 0.00
(6.0,7.0]	0.96 ± 0.01	0.94 ± 0.01	0.92 ± 0.00	0.90 ± 0.00	0.89 ± 0.00
(7.0,8.0]	0.95 ± 0.01	0.93 ± 0.00	0.89 ± 0.01	0.89 ± 0.01	0.89 ± 0.01
(8.0,9.0]	0.93 ± 0.01	0.90 ± 0.00	0.88 ± 0.00	0.88 ± 0.01	0.88 ± 0.01
(9.0,10.0]	0.93 ± 0.00	0.89 ± 0.01	0.87 ± 0.01	0.87 ± 0.00	0.87 ± 0.01
(10.0,11.0]	0.93 ± 0.01	0.90 ± 0.01	0.88 ± 0.00	0.87 ± 0.01	0.88 ± 0.05
(11.0,12.0]	0.83 ± 0.03	0.83 ± 0.02	0.88 ± 0.01	0.85 ± 0.01	0.85 ± 0.01
(12.0,13.0]	0.92 ± 0.00	0.89 ± 0.01	0.86 ± 0.01	0.86 ± 0.02	0.95 ± 0.02
(13.0,15.0]	0.87 ± 0.02	0.86 ± 0.01	0.83 ± 0.01	0.86 ± 0.02	0.92 ± 0.03
(15.0,30.0]	0.85 ± 0.01	0.87 ± 0.01	0.88 ± 0.02	0.85 ± 0.04	-
p_T/(GeV/c)\y^*	(-4.00, -3.75]	(-4.25, -4.00]	(-4.50, -4.25]	(-4.75, -4.50]	(-5.00, -4.75]
(0.0,1.0]	0.96 ± 0.00	0.96 ± 0.00	0.96 ± 0.02	0.93 ± 0.05	0.95 ± 0.03
(1.0,1.5]	0.97 ± 0.00	0.95 ± 0.00	0.93 ± 0.00	0.93 ± 0.01	0.91 ± 0.02
(1.5,2.0]	0.97 ± 0.00	0.95 ± 0.00	0.94 ± 0.00	0.93 ± 0.01	0.89 ± 0.04
(2.0,2.5]	0.95 ± 0.00	0.94 ± 0.00	0.93 ± 0.00	0.92 ± 0.01	0.90 ± 0.01
(2.5,3.0]	0.95 ± 0.00	0.93 ± 0.00	0.91 ± 0.00	0.93 ± 0.01	0.93 ± 0.02
(3.0,3.5]	0.94 ± 0.00	0.92 ± 0.00	0.92 ± 0.00	0.92 ± 0.01	0.92 ± 0.02
(3.5,4.0]	0.93 ± 0.00	0.92 ± 0.00	0.92 ± 0.00	0.92 ± 0.00	0.88 ± 0.02
(4.0,4.5]	0.92 ± 0.00	0.90 ± 0.00	0.91 ± 0.00	0.93 ± 0.01	0.96 ± 0.05
(4.5,5.0]	0.90 ± 0.00	0.91 ± 0.00	0.91 ± 0.00	0.92 ± 0.01	-
(5.0,5.5]	0.90 ± 0.00	0.90 ± 0.00	0.92 ± 0.00	0.83 ± 0.03	-
(5.5,6.0]	0.89 ± 0.00	0.90 ± 0.00	0.91 ± 0.02	0.98 ± 0.05	-
(6.0,7.0]	0.89 ± 0.00	0.90 ± 0.01	0.88 ± 0.01	-	-
(7.0,8.0]	0.88 ± 0.01	0.86 ± 0.01	0.90 ± 0.05	-	-
(8.0,9.0]	0.89 ± 0.01	0.86 ± 0.01	-	-	-
(9.0,10.0]	0.85 ± 0.01	0.82 ± 0.05	-	-	-
(10.0,11.0]	0.90 ± 0.03	-	-	-	-
(11.0,12.0]	0.78 ± 0.04	-	-	-	-
(12.0,13.0]	-	-	-	-	-
(13.0,15.0]	-	-	-	-	-
(15.0,30.0]	-	-	-	-	-

Table A.17 Double-differential cross-sections for prompt D^0 mesons in intervals of p_{T} and y^* in forward rapidity regions. The first uncertainty is statistical, the second is the component of the systematic uncertainty that is uncorrelated across intervals and the third is the correlated component.

	$\mathrm{d}^2\sigma/(\mathrm{d}p_{\mathrm{T}}\mathrm{d}y)$ [mb/(GeV/c)]				
p_{T} [GeV/c]\y^*	(1.50, 1.75)	(1.75, 2.00)	(2.00, 2.25)	(2.25, 2.50)	(2.50, 2.75)
(0.0,1.0)	$26.049 \pm 1.734 \pm 1.961 \pm 4.494$	$25.059 \pm 0.128 \pm 0.594 \pm 1.304$	$25.716 \pm 0.090 \pm 0.327 \pm 1.205$	$26.194 \pm 0.079 \pm 0.455 \pm 1.208$	$26.046 \pm 0.075 \pm 0.607 \pm 1.162$
(1.0,1.5)	$47.452 \pm 0.229 \pm 2.317 \pm 4.304$	$47.375 \pm 0.222 \pm 0.870 \pm 2.639$	$46.707 \pm 0.160 \pm 0.630 \pm 2.243$	$45.091 \pm 0.137 \pm 1.369 \pm 2.000$	$46.465 \pm 0.138 \pm 0.780 \pm 1.999$
(1.5,2.0)	$42.066 \pm 0.153 \pm 1.760 \pm 2.658$	$44.164 \pm 0.188 \pm 0.962 \pm 2.054$	$44.574 \pm 0.103 \pm 0.564 \pm 1.952$	$43.939 \pm 0.129 \pm 0.876 \pm 2.220$	$41.657 \pm 0.120 \pm 0.852 \pm 1.793$
(2.0,2.5)	$34.993 \pm 0.350 \pm 1.535 \pm 1.662$	$35.978 \pm 0.140 \pm 0.653 \pm 1.709$	$36.344 \pm 0.112 \pm 0.546 \pm 1.558$	$35.023 \pm 0.103 \pm 0.550 \pm 1.541$	$33.970 \pm 0.095 \pm 0.659 \pm 1.413$
(2.5,3.0)	$26.858 \pm 0.227 \pm 0.865 \pm 1.295$	$28.324 \pm 0.109 \pm 0.440 \pm 1.250$	$27.658 \pm 0.089 \pm 0.358 \pm 1.336$	$26.622 \pm 0.080 \pm 0.554 \pm 1.151$	$24.771 \pm 0.095 \pm 0.536 \pm 1.062$
(3.0,3.5)	$19.321 \pm 0.165 \pm 0.615 \pm 0.963$	$19.133 \pm 0.155 \pm 0.295 \pm 0.817$	$19.185 \pm 0.062 \pm 0.381 \pm 0.828$	$18.717 \pm 0.069 \pm 0.251 \pm 0.822$	$17.124 \pm 0.076 \pm 0.345 \pm 0.737$
(3.5,4.0)	$12.973 \pm 0.114 \pm 0.409 \pm 0.563$	$13.543 \pm 0.057 \pm 0.282 \pm 0.578$	$13.060 \pm 0.059 \pm 0.336 \pm 0.672$	$12.918 \pm 0.057 \pm 0.354 \pm 0.542$	$12.153 \pm 0.056 \pm 0.248 \pm 0.531$
(4.0,4.5)	$9.619 \pm 0.098 \pm 0.379 \pm 0.449$	$9.947 \pm 0.120 \pm 0.222 \pm 0.432$	$9.450 \pm 0.055 \pm 0.189 \pm 0.405$	$8.918 \pm 0.057 \pm 0.234 \pm 0.386$	$8.350 \pm 0.038 \pm 0.205 \pm 0.360$
(4.5,5.0)	$6.639 \pm 0.075 \pm 0.323 \pm 0.341$	$7.358 \pm 0.039 \pm 0.205 \pm 0.323$	$6.747 \pm 0.036 \pm 0.137 \pm 0.292$	$6.269 \pm 0.042 \pm 0.170 \pm 0.267$	$5.691 \pm 0.036 \pm 0.145 \pm 0.239$
(5.0,5.5)	$4.851 \pm 0.063 \pm 0.194 \pm 0.212$	$4.857 \pm 0.040 \pm 0.151 \pm 0.215$	$4.723 \pm 0.032 \pm 0.114 \pm 0.200$	$4.430 \pm 0.035 \pm 0.126 \pm 0.194$	$3.983 \pm 0.028 \pm 0.105 \pm 0.177$
(5.5,6.0)	$3.492 \pm 0.051 \pm 0.163 \pm 0.148$	$3.726 \pm 0.027 \pm 0.088 \pm 0.168$	$3.437 \pm 0.029 \pm 0.088 \pm 0.146$	$3.142 \pm 0.025 \pm 0.121 \pm 0.132$	$2.877 \pm 0.022 \pm 0.087 \pm 0.130$
(6.0,7.0)	$2.230 \pm 0.023 \pm 0.104 \pm 0.099$	$2.275 \pm 0.022 \pm 0.058 \pm 0.097$	$2.196 \pm 0.019 \pm 0.061 \pm 0.097$	$1.964 \pm 0.014 \pm 0.053 \pm 0.086$	$1.842 \pm 0.013 \pm 0.049 \pm 0.081$
(7.0,8.0)	$1.395 \pm 0.021 \pm 0.063 \pm 0.060$	$1.297 \pm 0.013 \pm 0.037 \pm 0.056$	$1.161 \pm 0.014 \pm 0.044 \pm 0.050$	$1.188 \pm 0.009 \pm 0.049 \pm 0.053$	$1.052 \pm 0.009 \pm 0.032 \pm 0.048$
(8.0,9.0)	$0.818 \pm 0.013 \pm 0.022 \pm 0.036$	$0.764 \pm 0.010 \pm 0.018 \pm 0.032$	$0.702 \pm 0.008 \pm 0.014 \pm 0.031$	$0.682 \pm 0.008 \pm 0.022 \pm 0.031$	$0.605 \pm 0.007 \pm 0.015 \pm 0.028$
(9.0,10.0)	$0.438 \pm 0.019 \pm 0.032 \pm 0.020$	$0.446 \pm 0.007 \pm 0.009 \pm 0.019$	$0.394 \pm 0.006 \pm 0.012 \pm 0.018$	$0.428 \pm 0.006 \pm 0.010 \pm 0.020$	$0.355 \pm 0.006 \pm 0.009 \pm 0.018$
(10.0,11.0)	$0.284 \pm 0.016 \pm 0.015 \pm 0.013$	$0.278 \pm 0.007 \pm 0.010 \pm 0.012$	$0.239 \pm 0.005 \pm 0.007 \pm 0.028$	$0.276 \pm 0.005 \pm 0.008 \pm 0.014$	$0.227 \pm 0.005 \pm 0.008 \pm 0.012$
(11.0,12.0)	$0.196 \pm 0.009 \pm 0.008 \pm 0.008$	$0.168 \pm 0.005 \pm 0.007 \pm 0.008$	$0.145 \pm 0.004 \pm 0.005 \pm 0.007$	$0.184 \pm 0.005 \pm 0.009 \pm 0.011$	$0.143 \pm 0.005 \pm 0.006 \pm 0.008$
(12.0,13.0)	$0.136 \pm 0.005 \pm 0.006 \pm 0.006$	$0.103 \pm 0.005 \pm 0.008 \pm 0.005$	$0.098 \pm 0.003 \pm 0.004 \pm 0.005$	$0.116 \pm 0.004 \pm 0.006 \pm 0.007$	$0.110 \pm 0.004 \pm 0.006 \pm 0.006$
(13.0,15.0)	$0.074 \pm 0.004 \pm 0.004 \pm 0.004$	$0.055 \pm 0.002 \pm 0.003 \pm 0.002$	$0.053 \pm 0.002 \pm 0.002 \pm 0.003$	$0.069 \pm 0.002 \pm 0.003 \pm 0.005$	$0.059 \pm 0.003 \pm 0.004 \pm 0.004$
(15.0,30.0)	$(9.1 \pm 0.5 \pm 0.5 \pm 0.5) \times 10^{-3}$	$(6.8 \pm 0.3 \pm 0.3 \pm 0.3) \times 10^{-3}$	$(7.4 \pm 0.3 \pm 0.4 \pm 0.8) \times 10^{-3}$	$(10.7 \pm 0.5 \pm 0.7 \pm 0.9) \times 10^{-3}$	$(9.3 \pm 1.1 \pm 1.3 \pm 0.7) \times 10^{-3}$
p_{T}[GeV/c]\y^*	(2.75, 3.00)	(3.00, 3.25)	(3.25, 3.50)	(3.50, 3.75)	(3.75, 4.00)
(0.0,1.0)	$26.300 \pm 0.149 \pm 0.840 \pm 1.169$	$26.038 \pm 0.083 \pm 0.662 \pm 1.191$	$24.968 \pm 0.147 \pm 1.061 \pm 1.189$	$23.157 \pm 0.196 \pm 1.842 \pm 1.157$	$20.817 \pm 1.548 \pm 1.918 \pm 1.093$
(1.0,1.5)	$44.909 \pm 0.177 \pm 1.057 \pm 1.965$	$44.107 \pm 0.152 \pm 0.649 \pm 1.959$	$39.851 \pm 0.269 \pm 2.554 \pm 1.807$	$36.184 \pm 0.336 \pm 1.706 \pm 1.688$	$35.092 \pm 0.401 \pm 1.848 \pm 1.984$
(1.5,2.0)	$41.222 \pm 0.124 \pm 1.261 \pm 1.769$	$37.934 \pm 0.172 \pm 0.827 \pm 1.668$	$36.200 \pm 0.203 \pm 1.124 \pm 1.708$	$32.475 \pm 0.262 \pm 1.177 \pm 1.541$	$27.126 \pm 0.421 \pm 1.168 \pm 1.492$
(2.0,2.5)	$31.966 \pm 0.121 \pm 0.963 \pm 1.501$	$28.923 \pm 0.127 \pm 0.644 \pm 1.291$	$27.061 \pm 0.139 \pm 0.855 \pm 1.342$	$23.492 \pm 0.139 \pm 0.796 \pm 1.048$	$20.558 \pm 0.243 \pm 1.053 \pm 1.147$
(2.5,3.0)	$22.247 \pm 0.087 \pm 0.451 \pm 0.977$	$20.647 \pm 0.087 \pm 0.412 \pm 0.918$	$18.474 \pm 0.097 \pm 0.814 \pm 0.812$	$16.646 \pm 0.123 \pm 0.755 \pm 0.779$	$14.379 \pm 0.208 \pm 0.637 \pm 0.811$
(3.0,3.5)	$15.693 \pm 0.070 \pm 0.332 \pm 0.708$	$14.210 \pm 0.066 \pm 0.308 \pm 0.631$	$12.554 \pm 0.072 \pm 0.365 \pm 0.573$	$11.648 \pm 0.101 \pm 0.451 \pm 0.563$	$9.117 \pm 0.152 \pm 0.424 \pm 0.501$
(3.5,4.0)	$10.468 \pm 0.052 \pm 0.246 \pm 0.459$	$9.542 \pm 0.048 \pm 0.260 \pm 0.425$	$8.336 \pm 0.055 \pm 0.285 \pm 0.370$	$7.540 \pm 0.072 \pm 0.303 \pm 0.409$	$6.285 \pm 0.185 \pm 0.525 \pm 0.406$
(4.0,4.5)	$7.317 \pm 0.038 \pm 0.159 \pm 0.317$	$6.576 \pm 0.037 \pm 0.174 \pm 0.304$	$5.675 \pm 0.043 \pm 0.155 \pm 0.258$	$5.108 \pm 0.068 \pm 0.204 \pm 0.253$	$3.678 \pm 0.138 \pm 0.273 \pm 0.219$
(4.5,5.0)	$5.108 \pm 0.030 \pm 0.116 \pm 0.234$	$4.799 \pm 0.033 \pm 0.136 \pm 0.216$	$4.029 \pm 0.040 \pm 0.121 \pm 0.188$	$3.322 \pm 0.061 \pm 0.149 \pm 0.167$	$1.971 \pm 0.154 \pm 0.269 \pm 0.139$
(5.0,5.5)	$3.645 \pm 0.025 \pm 0.088 \pm 0.166$	$3.189 \pm 0.026 \pm 0.081 \pm 0.147$	$2.725 \pm 0.034 \pm 0.108 \pm 0.139$	$2.307 \pm 0.082 \pm 0.158 \pm 0.119$	-
(5.5,6.0)	$2.611 \pm 0.021 \pm 0.074 \pm 0.114$	$2.296 \pm 0.024 \pm 0.068 \pm 0.111$	$1.847 \pm 0.030 \pm 0.077 \pm 0.093$	$1.510 \pm 0.094 \pm 0.152 \pm 0.080$	-
(6.0,7.0)	$1.656 \pm 0.013 \pm 0.052 \pm 0.073$	$1.372 \pm 0.014 \pm 0.056 \pm 0.064$	$0.983 \pm 0.023 \pm 0.049 \pm 0.049$	$0.717 \pm 0.073 \pm 0.180 \pm 0.039$	-
(7.0,8.0)	$0.924 \pm 0.010 \pm 0.033 \pm 0.042$	$0.746 \pm 0.012 \pm 0.034 \pm 0.035$	$0.493 \pm 0.021 \pm 0.044 \pm 0.030$	-	-
(8.0,9.0)	$0.533 \pm 0.009 \pm 0.018 \pm 0.025$	$0.405 \pm 0.014 \pm 0.025 \pm 0.021$	$0.202 \pm 0.028 \pm 0.038 \pm 0.011$	-	-
(9.0,10.0)	$0.287 \pm 0.008 \pm 0.010 \pm 0.014$	$0.243 \pm 0.013 \pm 0.018 \pm 0.013$	-	-	-
(10.0,11.0)	$0.161 \pm 0.007 \pm 0.011 \pm 0.008$	$0.129 \pm 0.015 \pm 0.024 \pm 0.008$	-	-	-
(11.0,12.0)	$0.110 \pm 0.008 \pm 0.009 \pm 0.007$	-	-	-	-
(12.0,13.0)	$0.079 \pm 0.007 \pm 0.011 \pm 0.005$	-	-	-	-
(13.0,15.0)	$0.051 \pm 0.009 \pm 0.017 \pm 0.004$	-	-	-	-
(15.0,30.0)	-	-	-	-	-

Table A.18 Double-differential cross-sections for prompt D^0 mesons in intervals of p_{T} and y^* in backward rapidity regions. The first uncertainty is statistical, the second is the component of the systematic uncertainty that is uncorrelated across intervals and the third is the correlated component.

	$\mathrm{d}^2\sigma/(\mathrm{d}p_{\mathrm{T}}\mathrm{d}y)$ [mb/(GeV/c)]				
p_{T} [GeV/c]\y^*	(-2.75, -2.50)	(-3.00, -2.75)	(-3.25, -3.00)	(-3.50, -3.25)	(-3.75, -3.50)
(0.0,1.0)	$26.423 \pm 0.077 \pm 1.135 \pm 2.046$	$30.978 \pm 0.110 \pm 0.658 \pm 2.272$	$31.059 \pm 0.086 \pm 0.746 \pm 1.764$	$32.488 \pm 0.079 \pm 0.575 \pm 1.859$	$30.706 \pm 0.075 \pm 0.555 \pm 1.731$
(1.0,1.5)	$50.258 \pm 0.329 \pm 1.766 \pm 3.570$	$55.180 \pm 0.193 \pm 1.433 \pm 3.295$	$56.266 \pm 0.152 \pm 1.055 \pm 3.169$	$55.760 \pm 0.139 \pm 0.959 \pm 2.935$	$53.809 \pm 0.143 \pm 0.971 \pm 2.852$
(1.5,2.0)	$51.254 \pm 0.277 \pm 1.579 \pm 3.222$	$51.164 \pm 0.162 \pm 0.940 \pm 2.918$	$52.039 \pm 0.133 \pm 1.058 \pm 2.768$	$50.232 \pm 0.125 \pm 0.751 \pm 2.968$	$47.612 \pm 0.121 \pm 1.373 \pm 2.535$
(2.0,2.5)	$41.615 \pm 0.211 \pm 1.109 \pm 2.506$	$42.476 \pm 0.126 \pm 1.047 \pm 2.332$	$41.267 \pm 0.099 \pm 0.490 \pm 2.482$	$39.322 \pm 0.092 \pm 0.618 \pm 2.022$	$36.252 \pm 0.094 \pm 1.045 \pm 1.873$
(2.5,3.0)	$27.597 \pm 0.140 \pm 0.693 \pm 1.672$	$29.397 \pm 0.089 \pm 0.468 \pm 1.603$	$29.188 \pm 0.150 \pm 0.490 \pm 1.570$	$27.301 \pm 0.062 \pm 0.725 \pm 1.417$	$24.672 \pm 0.080 \pm 0.394 \pm 1.389$
(3.0,3.5)	$20.272 \pm 0.106 \pm 0.478 \pm 1.148$	$20.175 \pm 0.079 \pm 0.294 \pm 1.079$	$20.078 \pm 0.055 \pm 0.590 \pm 1.055$	$18.466 \pm 0.049 \pm 0.464 \pm 0.946$	$16.460 \pm 0.056 \pm 0.292 \pm 0.805$
(3.5,4.0)	$13.875 \pm 0.078 \pm 0.362 \pm 0.737$	$13.732 \pm 0.046 \pm 0.269 \pm 0.727$	$13.085 \pm 0.079 \pm 0.394 \pm 0.678$	$12.130 \pm 0.046 \pm 0.221 \pm 0.637$	$10.876 \pm 0.041 \pm 0.303 \pm 0.544$
(4.0,4.5)	$9.523 \pm 0.109 \pm 0.258 \pm 0.517$	$9.049 \pm 0.040 \pm 0.232 \pm 0.515$	$8.776 \pm 0.039 \pm 0.182 \pm 0.488$	$8.053 \pm 0.034 \pm 0.160 \pm 0.407$	$6.978 \pm 0.032 \pm 0.145 \pm 0.359$
(4.5,5.0)	$6.647 \pm 0.044 \pm 0.182 \pm 0.363$	$6.474 \pm 0.043 \pm 0.190 \pm 0.325$	$6.065 \pm 0.028 \pm 0.132 \pm 0.294$	$5.284 \pm 0.026 \pm 0.124 \pm 0.269$	$4.464 \pm 0.022 \pm 0.105 \pm 0.216$
(5.0,5.5)	$4.622 \pm 0.035 \pm 0.153 \pm 0.247$	$4.353 \pm 0.032 \pm 0.106 \pm 0.228$	$3.888 \pm 0.030 \pm 0.093 \pm 0.202$	$3.662 \pm 0.023 \pm 0.089 \pm 0.184$	$3.006 \pm 0.019 \pm 0.091 \pm 0.150$
(5.5,6.0)	$3.160 \pm 0.041 \pm 0.115 \pm 0.172$	$2.878 \pm 0.028 \pm 0.089 \pm 0.158$	$2.741 \pm 0.024 \pm 0.086 \pm 0.133$	$2.454 \pm 0.017 \pm 0.068 \pm 0.125$	$2.209 \pm 0.016 \pm 0.064 \pm 0.114$
(6.0,7.0)	$1.893 \pm 0.023 \pm 0.098 \pm 0.105$	$1.798 \pm 0.015 \pm 0.044 \pm 0.094$	$1.669 \pm 0.012 \pm 0.047 \pm 0.084$	$1.478 \pm 0.010 \pm 0.037 \pm 0.087$	$1.225 \pm 0.009 \pm 0.039 \pm 0.066$
(7.0,8.0)	$1.021 \pm 0.012 \pm 0.034 \pm 0.055$	$1.055 \pm 0.007 \pm 0.030 \pm 0.054$	$0.807 \pm 0.009 \pm 0.027 \pm 0.044$	$0.824 \pm 0.007 \pm 0.026 \pm 0.054$	$0.646 \pm 0.006 \pm 0.021 \pm 0.039$
(8.0,9.0)	$0.632 \pm 0.014 \pm 0.014 \pm 0.033$	$0.562 \pm 0.006 \pm 0.020 \pm 0.029$	$0.467 \pm 0.006 \pm 0.011 \pm 0.029$	$0.429 \pm 0.005 \pm 0.008 \pm 0.030$	$0.355 \pm 0.005 \pm 0.010 \pm 0.022$
(9.0,10.0)	$0.377 \pm 0.006 \pm 0.010 \pm 0.019$	$0.312 \pm 0.006 \pm 0.008 \pm 0.017$	$0.266 \pm 0.005 \pm 0.007 \pm 0.017$	$0.256 \pm 0.004 \pm 0.007 \pm 0.020$	$0.194 \pm 0.004 \pm 0.006 \pm 0.013$
(10.0,11.0)	$0.241 \pm 0.005 \pm 0.008 \pm 0.013$	$0.184 \pm 0.003 \pm 0.006 \pm 0.011$	$0.151 \pm 0.003 \pm 0.004 \pm 0.011$	$0.157 \pm 0.003 \pm 0.005 \pm 0.014$	$0.117 \pm 0.003 \pm 0.008 \pm 0.009$
(11.0,12.0)	$0.155 \pm 0.009 \pm 0.007 \pm 0.008$	$0.118 \pm 0.006 \pm 0.006 \pm 0.008$	$0.102 \pm 0.003 \pm 0.004 \pm 0.010$	$0.092 \pm 0.003 \pm 0.004 \pm 0.011$	$0.080 \pm 0.003 \pm 0.005 \pm 0.006$
(12.0,13.0)	$0.093 \pm 0.003 \pm 0.007 \pm 0.006$	$0.080 \pm 0.003 \pm 0.004 \pm 0.010$	$0.067 \pm 0.002 \pm 0.004 \pm 0.008$	$0.067 \pm 0.002 \pm 0.003 \pm 0.008$	$0.041 \pm 0.002 \pm 0.004 \pm 0.004$
(13.0,15.0)	$0.056 \pm 0.002 \pm 0.002 \pm 0.005$	$0.046 \pm 0.002 \pm 0.003 \pm 0.012$	$0.033 \pm 0.001 \pm 0.001 \pm 0.005$	$0.033 \pm 0.002 \pm 0.002 \pm 0.005$	$0.024 \pm 0.002 \pm 0.003 \pm 0.002$
(15.0,30.0)	$(8.6 \pm 0.3 \pm 0.6 \pm 2.4) \times 10^{-3}$	$(5.5 \pm 0.2 \pm 0.4 \pm 1.5) \times 10^{-3}$	$(4.6 \pm 0.2 \pm 0.3 \pm 0.9) \times 10^{-3}$	$(6.1 \pm 0.4 \pm 0.6 \pm 1.1) \times 10^{-3}$	-
p_{T} [GeV/c]\y^*	(-4.00, -3.75)	(-4.25, -4.00)	(-4.50, -4.25)	(-4.75, -4.50)	(-5.00, -4.75)
(0.0,1.0)	$30.648 \pm 0.072 \pm 0.728 \pm 1.785$	$30.899 \pm 0.087 \pm 0.480 \pm 1.646$	$30.195 \pm 0.102 \pm 1.591 \pm 1.724$	$27.540 \pm 0.167 \pm 2.236 \pm 1.559$	$27.064 \pm 0.176 \pm 1.855 \pm 1.897$
(1.0,1.5)	$50.516 \pm 0.149 \pm 1.295 \pm 2.628$	$49.920 \pm 0.154 \pm 1.026 \pm 2.753$	$45.676 \pm 0.273 \pm 1.648 \pm 2.581$	$39.963 \pm 0.244 \pm 1.630 \pm 2.396$	$37.309 \pm 0.360 \pm 2.581 \pm 2.781$
(1.5,2.0)	$46.320 \pm 0.125 \pm 1.204 \pm 2.395$	$42.339 \pm 0.125 \pm 1.000 \pm 2.246$	$36.955 \pm 0.155 \pm 1.076 \pm 2.017$	$33.341 \pm 0.208 \pm 0.936 \pm 2.091$	$29.194 \pm 0.518 \pm 1.784 \pm 2.086$
(2.0,2.5)	$33.509 \pm 0.107 \pm 0.558 \pm 1.718$	$30.329 \pm 0.102 \pm 0.515 \pm 1.557$	$27.392 \pm 0.119 \pm 0.550 \pm 1.415$	$22.942 \pm 0.159 \pm 0.702 \pm 1.405$	$19.056 \pm 0.326 \pm 1.006 \pm 1.649$
(2.5,3.0)	$21.950 \pm 0.069 \pm 0.390 \pm 1.114$	$20.166 \pm 0.078 \pm 0.350 \pm 1.076$	$17.099 \pm 0.093 \pm 0.526 \pm 1.266$	$13.958 \pm 0.096 \pm 0.359 \pm 0.918$	$10.073 \pm 0.161 \pm 0.579 \pm 0.860$
(3.0,3.5)	$14.270 \pm 0.055 \pm 0.262 \pm 0.720$	$12.483 \pm 0.054 \pm 0.235 \pm 0.681$	$10.923 \pm 0.060 \pm 0.233 \pm 0.656$	$8.404 \pm 0.075 \pm 0.256 \pm 0.580$	$5.923 \pm 0.129 \pm 0.373 \pm 0.566$
(3.5,4.0)	$9.224 \pm 0.037 \pm 0.187 \pm 0.462$	$8.029 \pm 0.040 \pm 0.239 \pm 0.453$	$6.325 \pm 0.044 \pm 0.186 \pm 0.394$	$4.711 \pm 0.058 \pm 0.172 \pm 0.368$	$3.459 \pm 0.169 \pm 0.395 \pm 0.339$
(4.0,4.5)	$5.943 \pm 0.029 \pm 0.119 \pm 0.306$	$4.791 \pm 0.028 \pm 0.114 \pm 0.295$	$4.084 \pm 0.035 \pm 0.116 \pm 0.272$	$2.899 \pm 0.050 \pm 0.177 \pm 0.231$	$1.790 \pm 0.116 \pm 0.282 \pm 0.188$
(4.5,5.0)	$3.863 \pm 0.026 \pm 0.098 \pm 0.208$	$3.150 \pm 0.024 \pm 0.094 \pm 0.196$	$2.502 \pm 0.030 \pm 0.088 \pm 0.165$	$1.621 \pm 0.048 \pm 0.135 \pm 0.142$	-
(5.0,5.5)	$2.708 \pm 0.019 \pm 0.076 \pm 0.154$	$1.993 \pm 0.019 \pm 0.070 \pm 0.131$	$1.598 \pm 0.025 \pm 0.082 \pm 0.122$	$1.001 \pm 0.072 \pm 0.117 \pm 0.093$	-
(5.5,6.0)	$1.722 \pm 0.015 \pm 0.053 \pm 0.098$	$1.389 \pm 0.016 \pm 0.052 \pm 0.087$	$0.895 \pm 0.021 \pm 0.058 \pm 0.066$	$0.458 \pm 0.049 \pm 0.086 \pm 0.040$	-
(6.0,7.0)	$0.945 \pm 0.008 \pm 0.031 \pm 0.063$	$0.736 \pm 0.010 \pm 0.027 \pm 0.054$	$0.550 \pm 0.023 \pm 0.048 \pm 0.046$	-	-
(7.0,8.0)	$0.489 \pm 0.007 \pm 0.020 \pm 0.032$	$0.371 \pm 0.010 \pm 0.026 \pm 0.028$	$0.241 \pm 0.023 \pm 0.053 \pm 0.024$	-	-
(8.0,9.0)	$0.258 \pm 0.005 \pm 0.009 \pm 0.018$	$0.153 \pm 0.010 \pm 0.011 \pm 0.012$	-	-	-
(9.0,10.0)	$0.128 \pm 0.006 \pm 0.007 \pm 0.010$	$0.083 \pm 0.013 \pm 0.014 \pm 0.007$	-	-	-
(10.0,11.0)	$0.069 \pm 0.004 \pm 0.006 \pm 0.006$	-	-	-	-
(11.0,12.0)	$0.033 \pm 0.004 \pm 0.005 \pm 0.003$	-	-	-	-
(12.0,13.0)	-	-	-	-	-
(13.0,15.0)	-	-	-	-	-
(15.0,30.0)	-	-	-	-	-

A.4 Results of re-calculated double-differential cross-sections

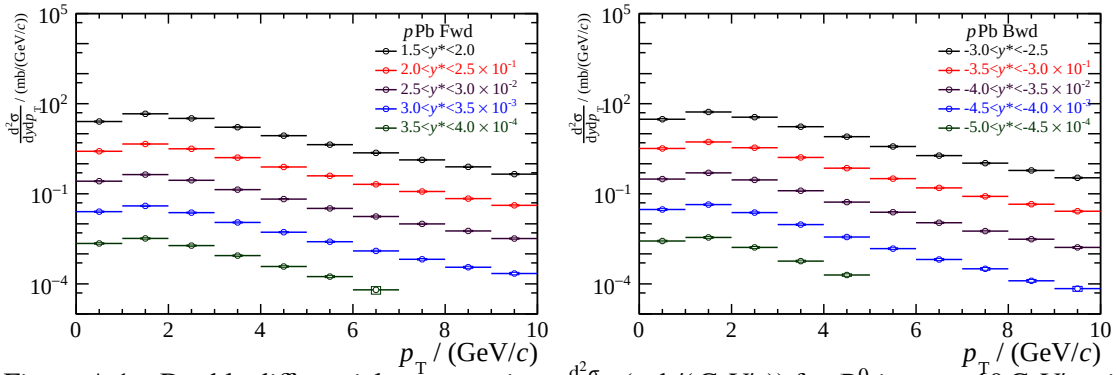

Figure A.1 Double differential cross-section $\frac{\mathrm{d}^2\sigma}{\mathrm{d}p_\mathrm{T}\mathrm{d}y^*}$ (mb/(GeV/c)) for D^0 in $p_\mathrm{T} < 10$ GeV/c with $\Delta pt = 1$ GeV/c and $\Delta y^* = 0.5$. Left for Fwd and right for Bwd.

ACKNOWLEDGEMENTS

首先感谢我的导师朱相雷老师。朱老师知识渊博，治学严谨，平易近人，在这五年里给了我各方面的帮助，以身作则教我如何做科研。感谢北大高原宁院士，杨振伟教授，他们带领我了解并进入了物理学这一领域。感谢近代物理实验室的小伙伴，陪我度过了本科和博士的美好时光，帮我解决了许多科研上的问题，我们一起学习一起进步一起吹牛，特别感谢王梦臻，许傲，陈晨师兄，孙佳音师姐，张舒楠，许立，牟宏杰，沈志宏，秦凝，他们给了我很多帮助。也感谢 LHCb 实验组的其他老师同学，艳席，Giulia 和 Matt 老师，Benjamin 和 Sam 小哥，在物理分析的过程中给我传授了很多经验和知识。

感谢我的父母，他们一直在全力支持我，给了我坚定的信念。感谢我的其他亲戚朋友，尤其是黄立舅舅，在生活上给了我各种帮助。感谢我的好友们，特别是王学知、耿婧、茅泽坤，他们在我遇到困难的时候一直耐心地安慰我，劝告我，陪我玩游戏、打球，让我能一直有一个好的心情。

再次感谢各位，希望我也能成为你们这样的人。

声 明

本人郑重声明：所呈交的学位论文，是本人在导师指导下，独立进行研究工作所取得的成果。尽我所知，除文中已经注明引用的内容外，本学位论文的研究成果不包含任何他人享有著作权的内容。对本论文所涉及的研究工作做出贡献的其他个人和集体，均已在文中以明确方式标明。

签 名：王剑桥 日 期：2023.5.22

RESUME

Jianqiao Wang was born on 29th November 1996 in Taizhou, Jiangsu, China.

He began his bachelor's study in the Department of Engineering Physics, Tsinghua University in September 2014, majoring in engineering physics, and got a Bachelor of Engineering degree in July 2018.

He has started to pursue a doctor's degree in Physics in the Department of Engineering Physics, Tsinghua University since September 2018. During this period, he has made academic achievements as follows.

Journal article

[1] LHCb Collaboration. Measurement of the prompt D^0 nuclear modification factor in pPb collisions at. $\sqrt{s_{\mathrm{NN}}} = 8.16\,\mathrm{TeV}$ (arXiv: 2205.03936, accepted by Physics Review Letter)

[2] Jianqiao Wang for LHCb Collaboration. Heavy flavor and exotic production at LHCb.

[3] Jianqiao Wang for LHCb Collaboration. Open heavy-flavor production in pPb collisions at LHCb.

[4] LHCb Collaboration. Study of prompt D^0 meson production in pPb at $\sqrt{s_{\mathrm{NN}}} = 8.16\,\mathrm{TeV}$ at LHCb.

COMMENTS FROM THESIS SUPERVISOR

显粲强子是高能重离子碰撞中产生的退禁闭物态性质的重要实验探针，对理解夸克胶子等离子体输运特性具有重要科学意义。而在高能质子-核碰撞中精确测量瞬发显粲强子产生是定量限定重离子碰撞中影响粲强子产生的冷核物质效应的重要实验手段。

王剑桥基于 LHCb Run2 的每核子对质心系能量为 8.16 TeV 的质子-铅核碰撞数据系统测量了D^0 介子在前向和后向快度区的产生截面和方位角各向异性集体流。该论文的实验数据分析工作，包括D^0 的信号优化和拟合、瞬发信号提取、探测器接受度和重建选择效率估计、截面计算、系统误差分析、核修正因子和截面比的计算、集体流的测量等都由王剑桥独立完成。在分析工作过程中，王剑桥还解决了质子-铅核模拟数据在较低动量下的寻迹效率修正问题，为 LHCb 相关物理分析提供了支持。他的结果是质子-铅核碰撞中对D^0 产生的最精确实验测量，并且覆盖了对冷核物质效应更敏感的前向和后向快度区，为限定核部分子分布函数和色玻璃凝聚等冷核物质效应理论计算提供了重要实验参考。他得到的高横动量下的D^0 的前向后向比或者后向快度区的核修正因子测量结果，对基于核部分子分布函数的理论计算提出了挑战。王剑桥还首次利用二粒子关联方法在前向和后向快度区测量了D^0 介子和带电粒子的关联函数，并通过对长程关联函数的傅立叶展开得到了椭圆流和三角流。结果显示在后向高多重数事例的中等横动量区存在显著的D^0 介子椭圆流，这为研究小碰撞系统中可能存在的热核物质效应提供了重要实验参考。该论文表述清晰，内容详实，是一篇优秀的博士论文。

RESOLUTION OF THESIS DEFENSE COMMITTEE

粲强子是研究重离子碰撞中核物质效应的敏感探针。论文基于 LHCb 采集的核子核子质心系能量 8.16 TeV 的质子-铅核对撞数据，研究影响粲介子产生的冷核物质效应以及小碰撞系统中的粲介子集体流，选题具有重要科学意义。

论文的主要工作和创新性成果为:

1. 精确测量了瞬发 D^0 介子产生截面。在前向快度区，核修正因子显著小于 1，证实了冷核物质效应的存在，与核部分子分布函数和色玻璃凝聚等冷核物质理论计算结果一致; 在后向快度区，核修正因子在高横动量区间低于冷核物质理论的计算，表明了热核或其它核物质效应存在的迹象。

2. 利用二粒子关联方法测量了瞬发 D^0 介子的集体流。在后向快度区高多重数事例中，发现 D^0 介子和带电粒子的长程关联现象，并观测到作为热核物质效应信号的 D^0 介子椭圆流。

论文写作规范、数据详实、叙述清晰，反映出作者具有扎实的专业基础知识和实验技能，具备独立从事科学研究的能力。

答辩过程表达清楚，回答问题正确。经答辩委员会表决，一致同意通过博士学位论文答辩，建议授予王剑桥同学理学博士学位，并推荐参评优秀博士论文。